



# Development of a Versatile High-Brightness Electron Impact Ion Source for Nano-Machining, Nano-Imaging and Nano-Analysis

Olivier De Castro

## ► To cite this version:

Olivier De Castro. Development of a Versatile High-Brightness Electron Impact Ion Source for Nano-Machining, Nano-Imaging and Nano-Analysis. Accelerator Physics [physics.acc-ph]. Université Paris Saclay (COMUE), 2016. English. NNT : 2016SACLS468 . tel-01480952

**HAL Id: tel-01480952**

**<https://theses.hal.science/tel-01480952>**

Submitted on 2 Mar 2017

**HAL** is a multi-disciplinary open access archive for the deposit and dissemination of scientific research documents, whether they are published or not. The documents may come from teaching and research institutions in France or abroad, or from public or private research centers.

L'archive ouverte pluridisciplinaire **HAL**, est destinée au dépôt et à la diffusion de documents scientifiques de niveau recherche, publiés ou non, émanant des établissements d'enseignement et de recherche français ou étrangers, des laboratoires publics ou privés.

NNT: 2016SACLS468

THÈSE DE DOCTORAT  
DE L'UNIVERSITÉ PARIS-SACLAY,  
préparée à "L'UNIVERSITÉ PARIS SUD"

ÉCOLE DOCTORALE N° 576  
Particules, Hadrons, Énergie et Noyaux:  
Instrumentation, Imagerie, Cosmos et Simulation  
(PHENIICS)

Spécialité de doctorat: Physique des accélérateurs

Par

**M. Olivier De Castro**

**Development of a Versatile High-Brightness Electron Impact Ion  
Source for Nano-Machining , Nano-Imaging and Nano-Analysis**

**Thèse présentée et soutenue à Belvaux, Luxembourg le 07.12.2016**

**Composition du jury:**

Dr. Alain Brunelle	ICSN – CNRS, Gif-sur-Yvette, France	Président - Examineur
Prof. Emile A. Schweikert	Texas A&M University, College Station, USA	Rapporteur
Dr. Gérard BenAssayag	CEMES – CNRS, Toulouse, France	Rapporteur
Dr. Michael Wiedenbeck	GFZ Helmholtz Centre, Potsdam, Germany	Examineur
Dr. David Dowsett	LIST, Esch-sur-Alzette, Luxembourg	Examineur
Dr. Serge Della Negra	IPNO – UPSUD, Orsay, France	Directeur de thèse
Dr. Tom Wirtz	LIST, Esch-sur-Alzette, Luxembourg	Co-directeur de thèse





## Acknowledgments

I would like to address my first thanks to my thesis supervisors Dr. Tom Wirtz and Dr. Serge Della Negra. By giving me the opportunity to do my PhD within his group, Dr. Tom Wirtz allowed me to go through an experience during the last four years that was sometimes quite challenging but very often enriching on the professional and personal level. He let me find my own way to develop ideas and concepts but when needed gave me very helpful advices and support to keep me on track to reach the goals of my PhD work. I am so thankful to have had a supervisor that I could go to and freely talk to about any issue that came up during my thesis.

A big acknowledgement goes to Dr. Serge Della Negra. Even if we did not see each other on a day to day basis to discuss about the progress of my PhD work, he gave me a lot of helpful advices, made the right comments when needed and asked the correct critical questions at the right moment.

I would like to thank as well Prof. Emile A. Schweikert, Dr. Gérard BenAssayag, Dr. Alain Brunelle and Dr. Michael Wiedenbeck for being a member of my PhD thesis defence committee.

To Dr. David Dowsett I need to express many thanks. He was always available to discuss about instrument development issues and taught me a lot about charged particle optics theory, simulations and design. Furthermore, on the experimental side he shared his experience with me about prototyping, trouble shooting of equipment and general instrumentation aspects.

I also have to express my gratitude to Mr Mathieu Gerard and Mr Olivier Bouton. Without their expertise and work done in the areas of mechanical development/assemblage and electronics conception the realisation of the prototype ion source designed during my PhD work would not have been possible. By close collaboration with them both I was able to develop some skills in their respective field of expertise.

My thanks also need to go to my AINA group colleagues at LIST (past and present) for all the discussions we had during our group meetings, for any support that they provided to me and for many other things. I think that getting feedback from many different points of view and to work as a team to group up many different skills are both powerful tools that help you to succeed. Thanks to those of them who became good friends of mine over the last years.

To Samir Menaouli, Jean Furgala, Asmaa El Moul, Anaïs Chauvière and Yannick Rault from the support team of the MRT department at LIST I would also like to address my thanks. They were always available to perform equipment related repairs or changes, to provide chemical substances, to organise the delivery of goods or to deal with general laboratory related issues.

To Mr Christophe Joly from the Nuclear Physics Institute in Orsay France, whose advice and expertise in the field of radio frequency electronics did help me and my colleague Olivier Bouton to complete the electronics system related to the prototype development.

To all those employees of LIST (past and present) that I did not mention yet but helped and supported me in any way during the last years, I also need to express my gratitude to them.

Last but not least, I need to express many thanks to my family and my girlfriend Déborah for their support and encouragement that they gave to me during the last years. Without them the pathway to finish my PhD work would have been far more difficult.



# Contents

<b>1</b>	<b>Introduction and objectives</b>	<b>1</b>
<b>2</b>	<b>Focused ion beam systems</b>	<b>3</b>
2.1	General overview . . . . .	3
2.2	Ion sources . . . . .	4
2.2.1	Electron impact ion sources . . . . .	6
2.2.2	Gas field ion sources . . . . .	10
2.2.3	Liquid metal ion sources . . . . .	12
2.2.4	Plasma ion sources . . . . .	13
2.2.5	Laser ion sources . . . . .	14
2.3	Instrumentation . . . . .	15
2.4	Applications . . . . .	16
2.4.1	FIB machining . . . . .	16
2.4.2	FIB imaging . . . . .	18
2.4.3	FIB analysis . . . . .	19
2.5	Summary and conclusions . . . . .	21
<b>3</b>	<b>Theoretical concepts and simulation software</b>	<b>23</b>
3.1	Charged particle optics . . . . .	23
3.1.1	Theoretical concepts . . . . .	23
3.1.2	Simulation software SIMION . . . . .	31
3.2	Radio frequency ion guiding and funnelling structures . . . . .	35
3.3	Vacuum technology and gas conductance simulations . . . . .	39
3.3.1	Theoretical concepts . . . . .	39
3.3.2	Simulation software Molflow+ . . . . .	43
3.4	Electron ranges and SREM simulation software . . . . .	44
3.5	Summary and conclusions . . . . .	48
<b>4</b>	<b>Miniature ionisation volume electron impact ion source</b>	<b>49</b>
4.1	Ion source concept . . . . .	49
4.2	Electron column CPO simulations and design . . . . .	51
4.2.1	Filament and triode extraction setup . . . . .	51
4.2.2	Estimation of the extracted electron beam current . . . . .	54
4.2.3	Beam collimation . . . . .	55
4.2.4	Beam focalisation within the ionisation region . . . . .	57
4.3	Brightness of the ion source . . . . .	63
4.3.1	Ion beam generation and current estimation . . . . .	63
4.3.2	Ion beam reduced brightness calculation . . . . .	67
4.3.3	Energy distributions . . . . .	72
4.4	Technical considerations . . . . .	74
4.4.1	Gas conductance simulations . . . . .	74
4.4.2	Experimental gas conductance and electron beam transmission tests . . .	77
4.5	Summary and conclusions . . . . .	87

<b>5</b>	<b>Electron impact radio frequency ion source</b>	<b>89</b>
5.1	Ion source concept . . . . .	89
5.2	CPO simulations . . . . .	92
5.2.1	Electron column investigations . . . . .	92
5.2.2	Ion generation and ion carpet extraction . . . . .	97
5.3	Brightness of the ion source . . . . .	103
5.3.1	Ion current calculation . . . . .	103
5.3.2	Brightness calculation . . . . .	104
5.3.3	Energy distributions . . . . .	108
5.4	Technical considerations . . . . .	110
5.4.1	Gas conductance calculations for the e-Column . . . . .	110
5.4.2	Molecular flow simulations for the ion column . . . . .	113
5.5	Experimental investigations . . . . .	116
5.5.1	Mechanical assembly . . . . .	116
5.5.2	Electron column characterisation . . . . .	119
5.5.3	Ion current generation within the ionisation region . . . . .	123
5.5.4	Ion carpet incorporation and ion extraction tests . . . . .	125
5.6	Summary and conclusions . . . . .	131
<b>6</b>	<b>Conclusions and Outlook</b>	<b>133</b>
6.1	Conclusions . . . . .	133
6.1.1	Miniature ionisation volume electron impact ion source . . . . .	133
6.1.2	Electron impact radio frequency ion source . . . . .	135
6.1.3	General conclusions . . . . .	137
6.2	Outlook . . . . .	138
<b>7</b>	<b>Appendices</b>	<b>140</b>
7.1	Appendix A: General theory and simulation software . . . . .	140
7.2	Appendix B: Miniature ionisation volume EI - ion source . . . . .	142
7.3	Appendix C: EIRFIS . . . . .	156
7.4	Appendix D: Résumé français de la thèse . . . . .	170
7.4.1	Introduction et objectifs . . . . .	170
7.4.2	Source d'ions à impact électronique et volume d'ionisation micrométrique . . . . .	171
7.4.3	Source d'ions radio-fréquence à impact électronique . . . . .	174
7.4.4	Conclusions finales et perspectives . . . . .	178
<b>8</b>	<b>Glossary</b>	<b>180</b>
<b>9</b>	<b>List of Tables</b>	<b>190</b>
<b>10</b>	<b>List of Figures</b>	<b>191</b>
<b>11</b>	<b>References</b>	<b>198</b>

# 1 Introduction and objectives

Nano-scales techniques that are based on finely focused ion beams can be split in three major groups: **Focused Ion Beam (FIB) machining, imaging** (no chemical information) and **analysis** (chemical information).

In nano-machining applications a FIB is used for example as tool to manufacture small devices by milling, to perform ion lithography, to functionalize surfaces with specific properties or to create nano-materials [1, 2, 3]. Moreover, nano-analytics use FIB-machining as a sample preparation tool, e.g. for Transmission Electron Microscopy (TEM) [4, 5].

FIBs are also used in nano-imaging in order to perform three-dimensional sample investigations at the nanoscale. A well-established tool in this application field is the ORION Helium Ion Microscope (HIM). It uses  $\text{He}^+$  and  $\text{Ne}^+$  beams to perform high resolution ion-microscopy [6, 7, 8].

For analytical purposes, Secondary Ion Mass Spectrometry (SIMS) represents a widely used and extremely powerful technique in order to perform chemical analysis of specimens. In SIMS a focused primary ion beam is used to sputter material from a specimen and create localised secondary ion emission which can be analysed by different kinds of spectrometers [9, 10].  $\text{Cs}^+$ ,  $\text{O}_2^+$  or  $\text{O}^-$  ions represent typical reactive primary ion species used by SIMS as they enhance the emission of positive or negative secondary ions, respectively [11].

A common aspect of all of these afore mentioned **FIB nano-applications** is that they **need high-brightness ion sources** to provide finely focused ion beams for a high lateral resolution while having sufficiently high ion beam currents to obtain reasonable erosion rates as well as acceptable secondary electron/ion yields. Furthermore, the energy spread of the generated ions should be kept as small as possible in order to minimise possible chromatic aberrations<sup>1</sup> within the ion focussing column. The achievable ion probe size would be considerably increased by such chromatic aberrations. Another important fact is that the used ion species has a strong impact on many different parameters in all three afore mentioned application areas. For example, in ion beam machining applications the ion species has a strong influence on etching effects [12], on the generation of surface roughness [13], as well as on milling rates which are related to the achieved sputtering yields [14]. By implanting a given ion species into a substrate a local modification of that substrate material can be achieved [3, 15]. In ion nano-imaging the produced secondary electron yields [16], as well as the resolution of the image which is closely related to the generated collision cascades within the sample, are influenced by the chosen ion species [14]. Moreover, for analytical applications such as SIMS the ionisation efficiency of the sputtered matter and therefore the sensitivity of the performed analysis is strongly related to the choice of the used primary ion species [17, 18, 19].

The most used high-brightness ion source for FIB-applications is the Liquid Metal Ion Source (LMIS). For high-resolution imaging, such as for HIM, the Gas Field Ion Source (GFIS) is used to provide high-brightness ion beams. Both sources can provide ion beams with reasonable lifetimes but unfortunately are limited in the choice of ion species (non-reactive species). Ion sources with more versatility regarding the choice of ion species are Electron Impact (EI) or plasma ion sources. Unfortunately, so far these sources do not provide high-brightness ion beams comparable to the LMIS or GFIS. More detailed information about the different kinds of ion sources can be found in section 2.2.

---

<sup>1</sup>Chromatic aberrations are explained in more detail in section 3.1.1.

Many attempts have been made to develop a high-brightness low energy spread noble gas ion source providing a broad flexibility in the ion species choice [20]. Moreover, in the literature some attempts have been reported about the creation of high-brightness EI ion sources for FIB-applications. Barth et al. suggested in 1985 that while keeping a high ionising electron beam current and simultaneously reducing the ionisation volume size to the micron scale it should be possible to considerably increase the brightness of EI ion sources [21]. An EI ion source of nanometre dimensions using the electron beam of a Scanning Electron Microscope (SEM) for the ionisation was proposed in 2010/2011 by Kruit et al. [22, 23]. Recently (2015/2016), in close relation with Kruit et al. investigations related to a slightly modified nanometre dimension EI ion source within an environmental SEM are reported by Khursheed and van Kan et al. [24, 25].

**The objectives of the here presented thesis** are therefore the following:

- **The development of a high-brightness gaseous ion source based on the electron impact ionisation process.** This allows the technical requirements for the ion source operation to be kept at a realistic level. The targeted range for the reduced brightness of the ion source is  $10^3 - 10^4 \text{ A m}^{-2} \text{ sr}^{-1} \text{ V}^{-1}$ .
- **The generation of low energy spread ion beams** to minimise the beam broadening related to chromatic aberrations when the ion source is used in FIB applications. The targeted value of the ion source energy spread is  $\Delta E \lesssim 1 \text{ eV}$ .
- **A versatile choice in provided ion species**, obtained by basically only changing the gas feed to the source.
- **A mechanical ion source design as compact as possible** in order to facilitate its use as an add-on tool for existing FIB instruments.

In section 2 of this manuscript more detailed explanations are given about FIB systems in general, the used ion sources, related instrumentation aspects and application fields. This section is then followed in section 3 by background on Charged Particle Optics (CPO), the CPO simulation software SIMION, the theory for gas conductance calculations/simulations and as well by theoretical background needed for the understanding of the ion source developments investigated during this PhD thesis. The ion sources we developed during this work are described in detail in section 4 and 5. For each investigated ion source concept the main tasks consisted in creating the basic concept ideas, performing CPO simulations, gas conductance calculations/simulations and related experimental investigations. Furthermore, the construction of a prototype ion source, including the mechanical and electronics design and its experimental characterisation, is described in section 5.

## 2 Focused ion beam systems

### 2.1 General overview

In a **FIB instrument** an ion beam is produced within the **ion source** and is guided by the means of an **ion column** towards the **sample region** where it interacts with the sample (see Figure 2.1) [26]. **Different effects occur as a result of the bombardment of the sample with the energetic primary ion beam** as shown in figure 2.2. One kind of particle that results from the interaction are **backscattered primary ions** which can e. g. be used for imaging purposes of the sample surface. Another generated particle species that is also often used for imaging purposes are **secondary electrons** ejected from the sample material. Furthermore, **photons** can be produced due to the primary ion bombardment and can be analysed in order to extract specific chemical information about the investigated sample. As shown in figure 2.2, in the generated **collision cascade** within the sample material a series of elastic collisions can provide enough energy to a sample atom/molecule in order to overcome the surface binding energy. These particles leaving the sample are called **sputtered particles**, most of which are of neutral nature and only a small fraction is charged; these are the so called **secondary ions**. The sputtered particles can be used for analytical purposes as they reflect the chemical composition of the bombarded sample. The secondary ions can for example be collected and analysed by specialised mass filtering devices, the mass spectrometers. The **sputtering yield**  $Y_S$  (number of removed atoms/incident primary ion) is dependent on parameters such as the primary ion energy and mass, the angle of incidence<sup>2</sup>  $\alpha_{Inc}$ , mass of the target atoms and the surface binding energies. At normal incidence the energy of the primary ions needs to be in general above a threshold of about 20 eV to 40 eV in order that sputtering occurs.  $Y_S$  increases with increasing primary energy and shows between 5 keV and 50 keV a broad maximum. The highest values for  $Y_S$  can be reached at incidence angles  $\alpha_{Inc}$  of 70° to 80° and lie in the range of  $10^{-1}$  to  $10^2$  for typical FIB energies (depending on target material and  $\alpha_{Inc}$ ) [26, 27]. Another effect that occurs due to ion bombardment is the **implantation of primary ions** within the sample material which can lead to undesired defects or to a desired change in sample properties.

**The ion source plays a crucial role in the overall performance of a complete FIB system.** Many different processes can be used to generate ions and in section 2.2 a few kinds of ion sources are described in more detail as they are used for FIB applications [15]. Due to the different effects related to the ion bombardment of a sample as described above, FIB systems can be used as sample preparation tool for Transmission Electron Microscopy (TEM), as implantation tool for devices, as surface patterning tool or as a tool for the deposition of selected materials. Moreover, as already mentioned, imaging can be done with a FIB system by using the generated secondary electron or ion signal. One has to keep in mind that when imaging with an ion beam the image formation is always accompanied by removal of material from the analysed specimen. A last application field is SIMS in order to obtain chemical information with high spatial resolution [15]. Some of these application fields will be described in more detail in section 2.4.

---

<sup>2</sup> $\alpha_{Inc}$  is defined as the angle between the surface normal and the primary ion beam axis.



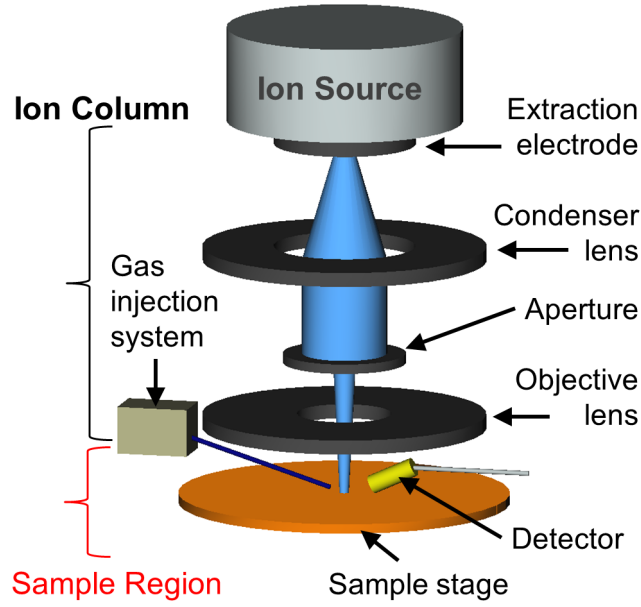


Figure 2.1: Schematic of a typical FIB instrument setup.

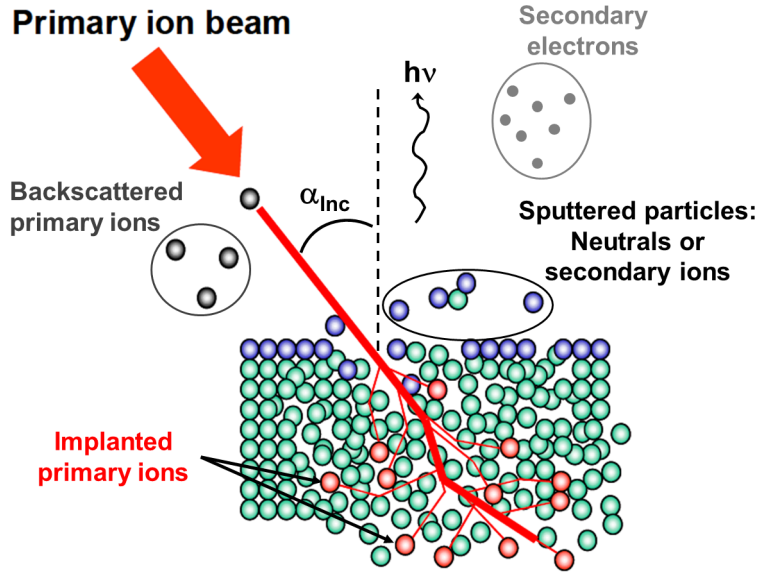


Figure 2.2: Illustration of the interaction between an energetic ion beam and a solid (modified from [28]).

## 2.2 Ion sources

The **key elements of every ion source** design can be explained as follows: Neutral particles (atoms/molecules) need to be fed into the source, within which they are ionised by a chosen process. After that the ionisation takes place the created ions are extracted from the source by the application of electrical fields. As illustrated in figure 2.3 the extracted ion beam has different geometrical parameters with which it can be characterised. The extracted beam has a certain source size  $A_{Source}$  and spreads into the half opening beam angle  $\alpha_{Ion-beam}$  which can be used to determine the occupied solid angle by  $\Omega = 2\pi(1 - \cos(\alpha_{Ion-beam}))$ . In the case of a small  $\alpha_{Ion-beam}$  the solid angle can be approximated by  $\Omega \approx \pi \cdot \alpha_{Ion-beam}^2$  (paraxial beam). Another parameter that characterises the ion beam is the contained current  $I_{Ion-beam}$  and the beam current density (current per unit area)  $J_{Ion-beam}$ .

In order to evaluate the quality of an ion beam the **emittance**  $\varepsilon$  and the **brightness**  $B$  can be used. The emittance represents a mathematical model to describe a group of charged particles in the phase space of their positions and momentums ( $x, y, z + p_x, p_y, p_z$ ). When evaluating the transportation of the ion beam by optical systems the emittances in the phase space transverse to the main ion beam motion direction (taken here as the  $z$ -direction) are the most important quantities. In order to compare the **transverse emittances** of different ion sources at different beam energies they can be defined **in their normalised form** by [29, 30]:

$$\varepsilon_{x,\text{norm}} = \sqrt{E_{\text{Beam}}} \frac{1}{\pi} \int \int dx d\alpha_x \quad \text{and} \quad \varepsilon_{y,\text{norm}} = \sqrt{E_{\text{Beam}}} \frac{1}{\pi} \int \int dy d\alpha_y \quad . \quad (2.1)$$

Where the transverse beam angles are given by  $\alpha_x$  and  $\alpha_y$ ,  $E_{\text{Beam}}$  is the beam energy and the unit in which the emittances are expressed most often is  $\pi \cdot \text{mm} \cdot \text{mrad} \cdot \sqrt{\text{MeV}}$ . In equation 2.1 the integrals can be performed by only taking a certain fraction of the total ion beam into account (e. g. 50 %, 90 %, etc.). In an optical system at the location of the ion beam focus the emittance can be taken as the simple product of the beam spot size and the corresponding angular spread [31]. Small values for  $\varepsilon_{x,\text{norm}}$  and  $\varepsilon_{y,\text{norm}}$  are desired as this means that the transverse beam size/angular spread is small which is favourable to minimise beam broadening effects at the sample location related to spherical aberrations<sup>3</sup> produced by the optical elements within the ion column.

The **brightness**  $B$  as other ion beam quality proving quantity can be defined as current density per unit solid angle [29] and can be calculated on the source side by:

$$B = \frac{I_{\text{Ion-beam}}}{A_{\text{Source}} \cdot \Omega} \approx \frac{4 \cdot I_{\text{Ion-beam}}}{\pi^2 \cdot d_{\text{Source}}^2 \cdot \alpha_{\text{Ion-beam}}^2} \quad . \quad (2.2)$$

Where  $d_{\text{Source}}$  is the ion beam source diameter. The **normalised or reduced brightness**  $B_r$  is defined as [20, 32, 33]:

$$B_r = \frac{B}{V_{\text{Beam}}} \approx \frac{4 \cdot I_{\text{Ion-beam}}}{\pi^2 \cdot d_{\text{Source}}^2 \cdot \alpha_{\text{Ion-beam}}^2 \cdot V_{\text{Beam}}} \quad . \quad (2.3)$$

Where  $V_{\text{Beam}}$  is the beam potential.  $B_r$  is used in order to compare the performance of different ion sources to each other and the unit in which it is most often expressed is  $\text{A m}^{-2} \text{sr}^{-1} \text{V}^{-1}$ .

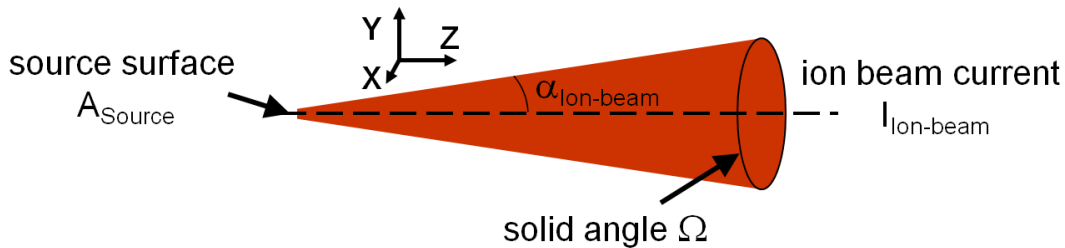


Figure 2.3: Illustration of the characteristic geometrical parameters of an ion beam.

<sup>3</sup>Spherical aberrations are explained in detail in section 3.1.1.

For FIB applications ion sources with high  $B_r$  values are desired as they allow to obtain finely focused ion beams at the sample location (high lateral resolution) combined with sufficiently high beam currents in order to get good sputtering yields (erosion rates) and/or high secondary electron/ion yields.

Another important characteristic quantity of the ion source performance is the **energy spread**  $\Delta E$  of the generated ion beam. The beam spot size at the sample location can be broadened up due to chromatic aberrations within the ion column, which are proportional to the **relative energy spread**  $\Delta E/E_{\text{Beam}}$ . Therefore,  $\Delta E$  or  $\Delta E/E_{\text{Beam}}$  should be kept as small as possible in order to minimise this broadening effect.  $\Delta E$  can have different physical causes as collisional effects (e. g. in a plasma ion source), thermal effects (e. g. in a surface ionisation or electron impact (EI) ion source), different local potentials at the generation sites of the ions, oscillating fields/potentials within the ionisation region, as well as an unstable extraction potential. Further parameters that are characteristic for an ion source are the **charge/mass spectra** of the ion beam as well as its **stability**. On the more practical side parameters as the ion source **cost**, its **ease of operation/maintenance** as well as its **lifetime** are of interest [29, 30, 34].

Many different processes can be used to perform the primary ionisation. In the following sections more explanations are given about plasma, field ionisation, field evaporation, photo ionisation and EI-ionisation sources as these are the types of high brightness sources used for different FIB applications. A more detailed description is given for EI-ionisation sources as this represents the type of ion source chosen for the investigated designs in section 4 and 5.

### 2.2.1 Electron impact ion sources

EI ion sources are based on the simple principle of using an electron beam (e-beam) to rip off atomic electrons from target gas particles and create in this way positive charged ions [35]. Many **conventional EI ion sources** are based on the **Nier type EI ion source** where a heated filament is used to generate an e-beam by thermionic emission, see figure 2.4. This e-beam then passes through an ionisation chamber at low gas pressure ( $\leq 10^{-6}$  mbar) and the created ions are extracted perpendicular to the e-beam axis by applying a positive voltage to the repeller. In these designs two permanent magnets are used to create an external magnetic field confining the electrons into a narrow beam with spiral trajectories directed towards the electron trap. In some cases instead of an electron trap a reflector is used so that in addition the e-beam oscillates between filament and reflector. In this way the electron path length is considerably increased and a higher ionisation efficiency is obtained. Ion beams with currents in the range of  $10^{-3}$  up to a few tens of mA can be obtained, having an energy spread  $\Delta E$  in the order of 1 - 10 eV [29, 30, 36, 37, 38]. Typical ion species created by EI ion sources are rare gas ions as well as cluster ions such as  $C_{60}^+$  or  $Ar_{4000}^+$  [22, 39].

#### Electron emitters

The ionising electrons in EI ion sources are generated most commonly by thermionic emission from **directly heated filaments** (cathodes). The **thermionic emission current density** can be expressed by the **Richardson-Dushman equation** defined as [29]:

$$J_{e,\text{thermionic}} = A_R \cdot f_M \cdot T^2 \cdot \exp\left(\frac{-\phi}{k_B T}\right) \quad \text{and} \quad A_R = \frac{4\pi \cdot m_e \cdot k_B \cdot e}{h^3} \quad . \quad (2.4)$$

$A_R$  is known as Richardson constant and is equal to  $120.4 \text{ A}/(\text{cm}^2 \text{ K}^2)$  where  $m_e$ ,  $e$ ,  $h$  and  $k_B$  are the electron mass, the elementary charge, the Planck constant and the Boltzmann constant, respectively. The temperature of the cathode is expressed by  $T$  and its work function by  $\phi$ . The factor  $f_M$  scales the parameter  $A_R$  depending on the kind of material used, see table 2.1 for values of  $A_R \cdot f_M$  and  $\phi$  for various materials (many more can be found in [29]). The work function at the surface of a cathode can be changed by deposition of a contaminant layer. An electropositive or electronegative contaminant decreases (activation) and increases (poisoning)  $\phi$ , respectively. In practice a good cathode should have a sufficiently high emission at a temperature at which the evaporation rate is not too high. One kind of **directly heated cathode** that is very often used is made from tungsten (W), having a  $T_{\text{Operating}}$  in the range of 2500 - 3000 K. This quite high operating temperature has the advantage that absorbed layers of electronegative gases are removed quite fast and a satisfactory operation in relatively poor vacuum is possible. In order to keep similar emission characteristics at a lower  $T_{\text{Operating}}$ , which reduces the evaporation and increases the cathode lifetime, a reduction of  $\phi$  is needed. This can for example be done in the case of W-cathodes by contaminating them with Thorium dioxide ( $\text{ThO}_2$ ), leading to a diffusion of Thorium to the cathode surface where it forms a monolayer with the effect of reducing  $\phi$  from about 4.5 eV to 2.6 - 2.7 eV. Another kind of cathode that has lower values of  $T_{\text{Operating}}$  and  $\phi$  compared to W-cathodes are Lanthanum hexaboride  $\text{LaB}_6$  cathodes (1400 - 2000 K, 2.7 - 2.8 eV). They have the slight disadvantage that they need a vacuum level below  $10^{-6}$  mbar for their operation, which is two orders of magnitude lower compared to W-cathodes with  $p \leq 10^{-4}$  mbar [29, 34, 40, 41, 42]. For more information about indirectly heated cathodes also used in EI ion source designs please refer to the literature. Our ion source development concepts presented in sections 4 and 5 make use of directly heated cathodes.

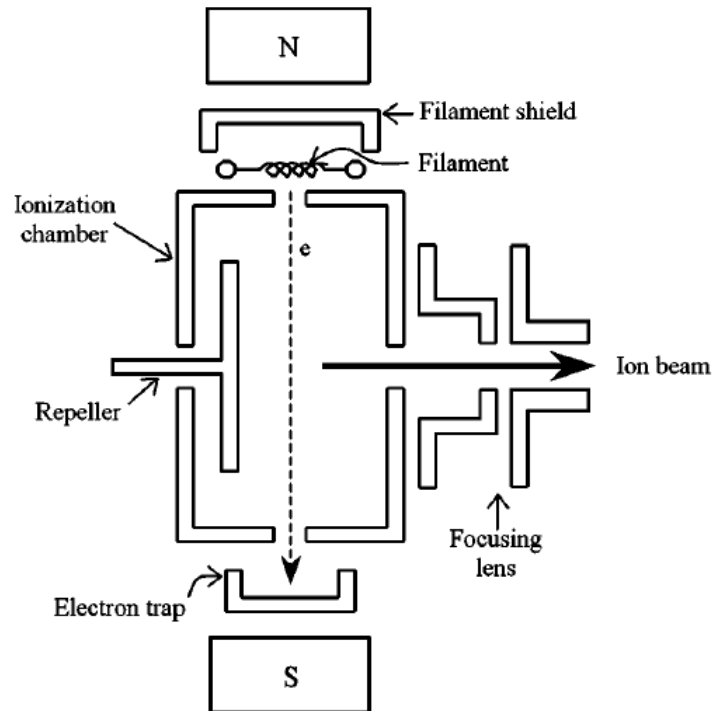


Figure 2.4: Schematic of a conventional Nier-type ion source (taken from [38]).

Material	$A_R \cdot f_M \text{ [A cm}^{-2} \text{ K}^{-2}]$	$\phi \text{ [eV]}$
Tungsten	60	4.54
Barium	60	2.11
Iridium	170	5.4
Thorium on tungsten	3	2.63
Lanthanum hexaboride LaB <sub>6</sub>	29	2.7

Table 2.1: Product  $A_R \cdot f_M$  and work function  $\phi$  for various materials [29].

### Electron impact ionisation process

An e-beam is capable of creating ions from neutral particles if its energy is at least equal to the **first ionisation potential**  $\Phi_{1,i}$  of the corresponding neutral species. For example for many kinds of gases  $\Phi_{1,i}$  is about 15 eV. The target electrons that can be removed most easily are those from the outermost electron shells as they have the lowest binding energies to the atomic core [29, 34, 43]. When the **EI ionisation process** is approximated in a semi-empirical/semi-classical model as a two-body collision process (binary accouter approximation) the **counting cross section**  $\sigma_C$  is defined as the simple sum of the **individual (partial) cross sections**  $\sigma_{\text{Individual}}$ :

$$\sigma_C = \sum \sigma_{\text{Individual}} \quad . \quad (2.5)$$

The individual cross sections represent the cases of the creation of a n-times charged ion by a single collision. In experimental setups it is often very difficult to directly measure values for  $\sigma_C$  as for this purpose it is mandatory to exactly determine the number of occurring ionisation events. Therefore, most often values for  $\sigma_{\text{Individual}}$  or the **total (gross) cross section**  $\sigma_t$  are experimentally determined by measuring the total produced ion current through all existing ionisation channels. By definition  $\sigma_t$  is the sum of the different  $\sigma_{\text{Individual}}$  weighted by the corresponding charge  $q_n$  of the individual produced kinds of ions [35, 43, 44]:

$$\sigma_t = \sum q_n \cdot \sigma_{\text{Individual}} \quad . \quad (2.6)$$

In general ionisation cross sections represent a measure of the ionisation probability and are dependent on the ionising e-beam energy. In the case of rare gases single and multiple ionisation occurs and for He, Ne, Ar, Kr and Xe;  $\sigma_t$  reaches its maximum in the range of 80 - 110 eV and is dominated by the contribution of the singly charged ions [45]. The cross section studies performed by Rapp and Englander-Golden [46] are used very often as standards when experimental values for the EI ionisation cross sections  $\sigma_{\text{EI}}$  of different gases are needed. The correctness of these studies has been verified by the authors of [45, 47] and [48], who found very good agreement with the results from [46]. Therefore, the  $\sigma_{\text{EI}}$  results stated in [45, 47] and [48] will be used in this manuscript as standard values. Many different theoretical models exist to describe and calculate  $\sigma_{\text{EI}}$ , please refer to [35, 49, 50] and [51] for more detailed information.

When considering in a setup the ionising e-beam as parallel, mono-energetic and if the gas particle density  $n_{\text{Gas}}$  is so dilute that the **single collision condition** (SCC)  $n_{\text{Gas}} \cdot \sigma_t \cdot L_{\text{Gen}} \leq 0.01$  is fulfilled, the **total generated ion current** can be calculated by [35, 46]:

$$I_{\text{Ion,total}} = I_e \cdot n_{\text{Gas}} \cdot \sigma_t \cdot L_{\text{Gen}} \quad . \quad (2.7)$$

Where  $L_{\text{Gen}}$  is the effective length along which the ions are created (e. g. length of the ionisation volume) and  $I_e$  the ionising e-beam current. When  $\sigma_t$  is replaced in equation 2.7 by  $\sigma_{\text{Individual}}$  the individual ion currents for each generated ion species can be determined. As already seen before, conventional EI ion sources very often use thermionic cathodes with large electron emission areas leading to large (mm-dimensions) ionisation volumes and therefore to large ion beam source sizes which is not favourable for high brightness values.

### High brightness EI ion sources

Conventional EI ion sources reach reduced brightness values of  $B_r \approx 1 \text{ A m}^{-2} \text{ sr}^{-1} \text{ V}^{-1}$ . In the literature it has been stated that by reducing the ionisation volume size to the micron scale while keeping a quite high ionising e-beam current it should be feasible to considerably increase  $B_r$  [21]. One example of an attempt to design a **high brightness EI ion source** for FIB applications is the development by the group of P. Kruit (TU Delft) [22, 52, 53]. As can be seen in figure 2.5a they introduced a small parallel plate chip as ionisation cell into a Scanning Electron Microscope (SEM) and focused the e-beam into the ionisation region through a small circular opening with a diameter of 1 to 2  $\mu\text{m}$ . The intended spacing of the parallel plates is only a few hundreds of nanometres but after the dry etching/lithography fabrication process (details can be found in [52]) the real spacing is determined to be in the range of 1 to a few  $\mu\text{m}$ . The achievable  $B_r$  of the ion source is claimed to be directly proportional to the current density of the used Schottky electron emitter  $J_{e,\text{Schottky}}$ , as well as to  $\sigma_{\text{EI}}$  and inversely proportional to the molecular diameter  $d_m$  of the corresponding gas species ( $B_{r,\text{Ion-beam}} \sim J_{e,\text{Schottky}} \cdot \sigma_{\text{EI}}/d_m$ ). Mainly thanks to the high value of  $J_{e,\text{Schottky}}$  in the range of 1 - 20  $\text{A m}^{-2}$  the estimated values of  $B_r$  lie in the range of 0.5 to 4  $\cdot 10^7 \text{ A m}^{-2} \text{ sr}^{-1} \text{ V}^{-1}$  depending on the rare gas ion species used (singly charged) and on the e-beam energy, see figure 2.5b. Experimental investigations have shown that the extracted ion current ranges from a few tens to a few hundreds of pA, again depending on the considered ion species.

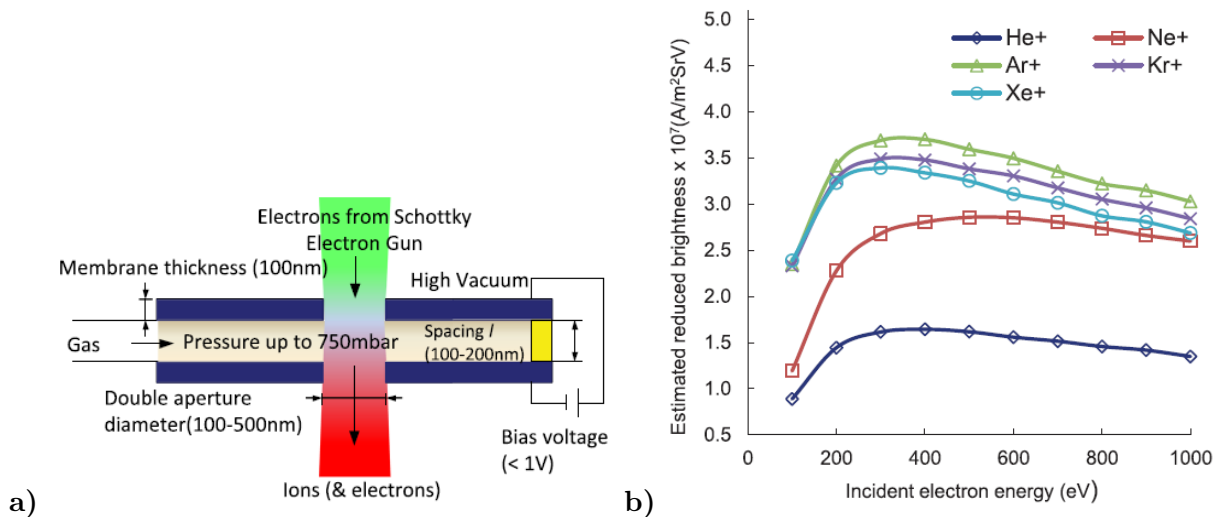


Figure 2.5: a) NAIS: microchip as ionisation cell in SEM (taken from [22]).

b) Estimated achievable  $B_r$  values by the NAIS from TU Delft (taken from [22]).

The used e-beam has a current of about 14 nA at 1 keV, the gas inlet pressure  $p_{\text{Inlet}}$  goes up to a few hundreds of mbar and a voltage drop of only a few volts at maximum is used across the ionisation cell creating high ion extraction fields of a few  $10^6 \text{ V m}^{-2}$  within the cell (for example for  $\text{Ar}^+$ : 180 pA at about 310 mbar of  $p_{\text{Inlet}}$  have been extracted). In [54] more details can be found about first FIB applications that have been performed with this ion source concept named **Nano Aperture Ion Source (NAIS)**. The experimentally deduced  $B_r$  values of the NAIS are stated by the author in the range of  $10^3$  to  $10^4 \text{ A m}^{-2} \text{ sr}^{-1} \text{ V}^{-1}$  for an argon ion beam. A further system optimisation is expected to raise the  $B_r$  to about  $10^6 \text{ A m}^{-2} \text{ sr}^{-1} \text{ V}^{-1}$  which is closer to the estimated  $B_r$  value for the NAIS concept. The development of a complete stand-alone NAIS system, by combining the tiny parallel plate chips with a small Schottky emitter electron column (not any more integrated into an SEM), has been started by the TU Delft group, see [54] for more details.

Recently Liu et al. from the University of Singapore published experimental results obtained by a slightly modified ion source design compared to the NAIS [24, 25]. They introduced their own version of sub-micron ionisation chamber as well into a field emission SEM. An e-beam of about 4 nA and 1 keV ionised argon gas injected at a  $p_{\text{Inlet}}$ <sup>4</sup> of 700 mbar and a total extracted Argon ion current of about 200 pA was measured. Charged particle optics simulations were used to perform ion trajectory back tracing to find the virtual ion beam source size  $d_{\text{VS, simul}}$  and position. At a chip plate potential difference of 18 V a maximum value of  $B_{r, \text{Ar}} \approx 750 \text{ A m}^{-2} \text{ sr}^{-1} \text{ V}^{-1}$  has been calculated, where  $d_{\text{VS, simul}} \approx 400 \text{ nm}$  (defined as Full Width 50, FW50<sup>5</sup>) and  $I_{a, \text{Ar}} \approx 40 - 50 \text{ pA}$  (axial beam current) have been used. A lower value for the maximum achievable  $B_{r, \text{Ar}}$  of about  $280 \text{ A m}^{-2} \text{ sr}^{-1} \text{ V}^{-1}$  has been deduced by the authors when the ion beam source size is assumed to be equal to the e-beam focus of  $1.3 \mu\text{m}$  (defined as Full Width Half Maximum, FWHM). According to the authors the e-beam  $B_r$  with  $880 \text{ A m}^{-2} \text{ sr}^{-1} \text{ V}^{-1}$  during these experimental tests was not yet optimised. They claim that the value of  $B_{r, \text{Ar}}$  can in the future still be increased by a factor of at least  $10^4$  with an optimised e-beam  $B_r$  value.

### 2.2.2 Gas field ion sources

The ionisation mechanism by which ions are created within a GFIS is the **field ionisation process**. For this purpose it is necessary to create high electrical fields  $\geq 10^{10} \text{ V/m}$  close to a metal surface within a gas ionisation region. In this way the gas atoms present in the vicinity of the surface are polarised, the potential barrier for electrons to tunnel from the gas atoms into the metal is lowered and gaseous ions are created which can be extracted [20, 29]. The critical distance for this process to take place can be approximated as [29]:

$$D_C \approx \frac{\Phi_{1,i} - \phi}{E_{\text{field}}} \quad . \quad (2.8)$$

Where  $\Phi_{1,i}$  and  $\phi$  correspond as already stated before to the first ionisation potential of the gas atoms and work function of the metal surface respectively. The electric field magnitude is expressed by  $E_{\text{field}}$ . The high values of  $E_{\text{field}}$  are most often created by using a sharp tip with a radius of 100 nm up to a few hundreds of nm to which a high voltage is applied. Only at the extremely sharp tip end the electric field values exceed the threshold for field ionisation and

<sup>4</sup>In both NAIS designs (TU Delft and University of Singapore) the inlet pressure is measured quite far away from the actual ionisation region so that the pressure within it should be lower than  $p_{\text{Inlet}}$ .

<sup>5</sup>The FW50 represents the beam diameter within which 50 % of the total beam current is contained.

only at this location ions are created which leads in an optimal configuration to sub-nanometre virtual source sizes of the extracted ion beams. The injection pressure into the ionisation region of a GFIS is in the range of  $10^{-3}$  to  $10^{-2}$  mbar. Most often the metal needle is cooled to temperatures below 77 K as it has been shown that the ionisation probability strongly increases at lower temperatures due to a higher gas density at the needle tip. This kind of GFIS is often referred to as **GFIS with cold-finger**. Another kind of GFIS are capillary based sources where the gas is fed through a hollow capillary set to high voltages and the ionisation takes place at the open end of the capillary. Unfortunately, GFIS very often do not allow stable operation conditions and therefore are not widely used for FIB applications [20, 29].

A needle type GFIS without cold finger that is used to produce a  $H^+$  ion beam is described in [55]. An ion current up to 20 nA has been measured at 20 keV by using a polycrystalline Iridium needle as ioniser. The reduced brightness that can be achieved by this source lies in the order of  $10^7 \text{ A m}^{-2} \text{ sr}^{-1} \text{ V}^{-1}$ . A **supertip GFIS** is expected to even have a much higher  $B_r$  value reaching the range of  $10^{11} \text{ A m}^{-2} \text{ sr}^{-1} \text{ V}^{-1}$  [56, 20]. This kind of source uses as ionisation location a nanometric protrusion at the end of the tip used in a conventional GFIS, see figure 2.6. According to Kalbitzer [56] it is expected to considerably reduce the ion source half-opening beam angle to about  $1^\circ$  and lead to a virtual source size of about 0.1 nm. With a similar ion beam current of about 10 nA compared to the conventional GFIS,  $B_r$  is clearly increased and Kalbitzer states a value of  $3 \cdot 10^{11} \text{ A m}^{-2} \text{ sr}^{-1} \text{ V}^{-1}$  for a  $He^+$  ion beam having a  $\Delta E$  of 1 eV.

One of the high performance GFIS currently used for high resolution ion microscopy is the Atomic Level Ion Source **ALIS** within the HIM, as already mentioned in section 1. This source uses a cryo-refrigerator to cool down the ionisation region so that for example Helium of about 77 K surrounds the ionising tungsten needle. The emitter tip consists of a pyramid of only 3 atoms and each of these atoms can provide up to a few tens of pA of He ion beam current. In order to perform ion beam imaging the extracted ion beam from one of those atomic emission locations is chosen and the ion source reduced brightness is stated in the order of  $10^9 \text{ A m}^{-2} \text{ sr}^{-1} \text{ V}^{-1}$  with  $\Delta E$  of 1 eV or below. The ion imaging resolution that is obtained with the ALIS source is as low as 0.35 nm with up to a few pA of ion probe current. In addition to Helium also Neon is used in the ALIS as gas species. Unfortunately, the use of Ne caused at the beginning some ion source stability problems and the developers are still working on completely solving this issue [6, 8, 57, 58, 59].

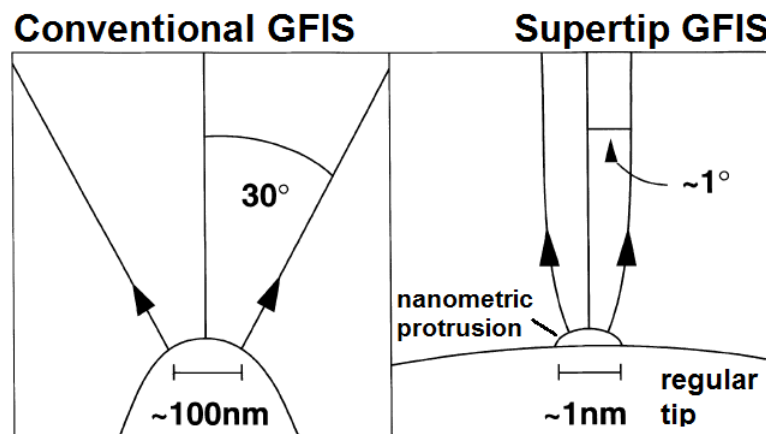


Figure 2.6: Emitter tip of a conventional GFIS on the left and a supertip GFIS with a nanometric protrusion on top of a regular emitter on the right (modified from [56]).



Another developed high performance GFIS system uses  $N_2^+$  ions at 25 keV for the purpose of photomask repair technology with a minimum ion beam dimension of about 10 nm for the repair process. Moreover, ion imaging can be performed and a feature size of 4 nm could be resolved by using the 25 keV/0.1 pA  $N_2^+$  ion beam. This system can as well be operated with hydrogen ions ( $H_2^+$ ) at 15 keV [60, 61].

### 2.2.3 Liquid metal ion sources

Another kind of ion source that uses sharp needles (most often tungsten) for the purpose of ionisation is the LMIS. In contrast to the afore described GFIS, the needle is not any more surrounded by a gas to be ionised but a metal reservoir is in contact with it, see figure 2.7. By heating up both the needle and the metal reservoir to the melting point temperature  $T_{MP}$  of the metal, a thin film of liquid metal flows over the needle surface towards its tip end having a radius of up to 10  $\mu m$ . By setting the needle to high voltages, typically up to 10 kV, the high electric fields at the tip end ( $\geq 10^{10}$  V/m) pull the liquid metal into a so called **Taylor cone**. The emission of ions occurs due to the **process of field evaporation** at the rounded apex of the Taylor cone with a radius of about 5 nm. An electrode at ground is placed close to the needle at high potential in order to extract the created ions [26, 29, 62, 63]. LMIS are very widely used in high resolution FIB-applications mainly due to their long life time and reliable/stable operation. The ion currents that can be created by a LMIS span over the range of a few up to several 100  $\mu A$  by the use of a single needle. In sources using an array of needle emitters the current can even be increased to several tens of mA [26, 29, 62, 63]. **Most common is the use of Gallium** as metal<sup>6</sup> (low  $T_{MP} \sim 300$  K and low vapour pressure) and an extracted  $Ga^+$  ion beam to reach typically an ion probe resolution at the specimen of about 10 nm at 30 keV. This resolution is mainly limited by chromatic aberration effects related to the quite large  $\Delta E$  of 5 - 10 eV. The reduced brightness achieved by a LMIS is stated to be in the range of  $10^6 - 10^7$   $A m^{-2} sr^{-1} V^{-1}$  [20, 29]. Beside ion implantation or sample properties modification techniques, major drawbacks related to the use of  $Ga^+$  ions are sample contamination, swelling or unwanted properties change of the analysed specimens [15, 64, 65].

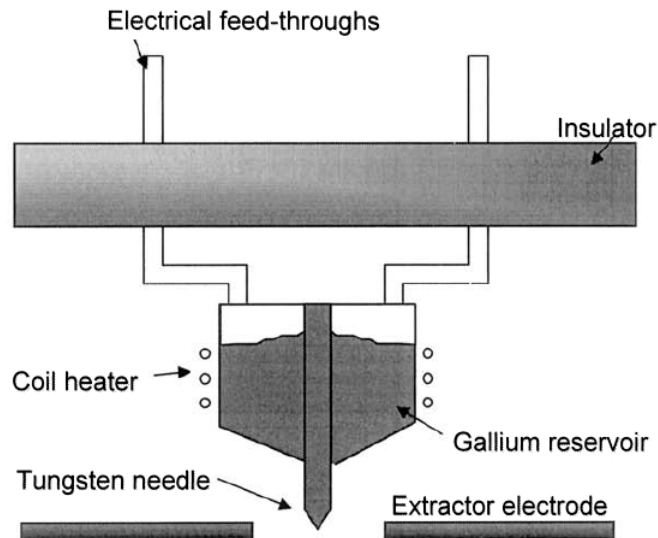


Figure 2.7: Illustration of the sharp tungsten needle and the attached metal reservoir within a LMIS (modified from [26]).

<sup>6</sup>Many other metals have been used in LMIS: Al, Au, B, Be, Cs, Cu, Fe, Ge, Li, Pb, Si, U and many more [29].

Therefore, as can be seen in sections 2.2.1, 2.2.2, 2.2.4 and 2.2.5, several attempts have been done and still are ongoing to create high brightness reliable noble gas ion sources to avoid this contamination effects and replace the LMIS as the most common used source. More details about the theory of the field evaporation and the LMIS principle in general can be found in [29] and [62]. In a simple explanation, the strong influence of the external electric fields on the potential well of the metal surface atoms leads to a higher probability of thermal escape of ions over the energy barrier for ionisation.

### 2.2.4 Plasma ion sources

Another process with which an ion source can be created is the generation of a stable plasma which consists of electrons, ions as well as neutral particles (the overall charge is zero). Many different kinds of plasma ion sources exist and a lot of details can be found in [29] and [30]. A few of those concepts will be shortly described here. The **duoplasmatron** is widely used e. g. for SIMS purposes. It mainly consists of four components: the cathode (to create primary ionising electrons), the intermediate electrode, the anode and the extraction electrode, see figure 2.8a. Two different plasma regions exist. The lower-density<sup>7</sup> region between cathode and intermediate electrode which leaks through an opening into the region in front the anode where a high-density region is created by a further compression due to the presence of an axial magnetic field. This has the effect that higher ion beam currents can be extracted. In order to generate at the end again lower beam densities and therefore facilitate the beam transport very often an expansion cup is placed at the beam exit side of the anode. The duoplasmatron's  $B_r$  lies in the range of  $10^2 - 10^3 \text{ A m}^{-2} \text{ sr}^{-1} \text{ V}^{-1}$  [66, 67]. Pillatsch et al. [66] report about the extraction of negatively charged halogen ion beams ( $\text{F}^-$ ,  $\text{Cl}^-$ ,  $\text{Br}^-$  and  $\text{I}^-$ ). For the  $\text{F}^-$  beam they state  $B_r = 200 \text{ A m}^{-2} \text{ sr}^{-1} \text{ V}^{-1}$  with 55 nA of beam current. Duoplasmatron sources are also used to create positive ions as reported by Coathe and Long in [68]. They state that their maximum  $B_r$  for an  $\text{Ar}^+$  ion beam is about  $1.1 \cdot 10^3 \text{ A m}^{-2} \text{ sr}^{-1} \text{ V}^{-1}$  with a beam current close to 100 nA.

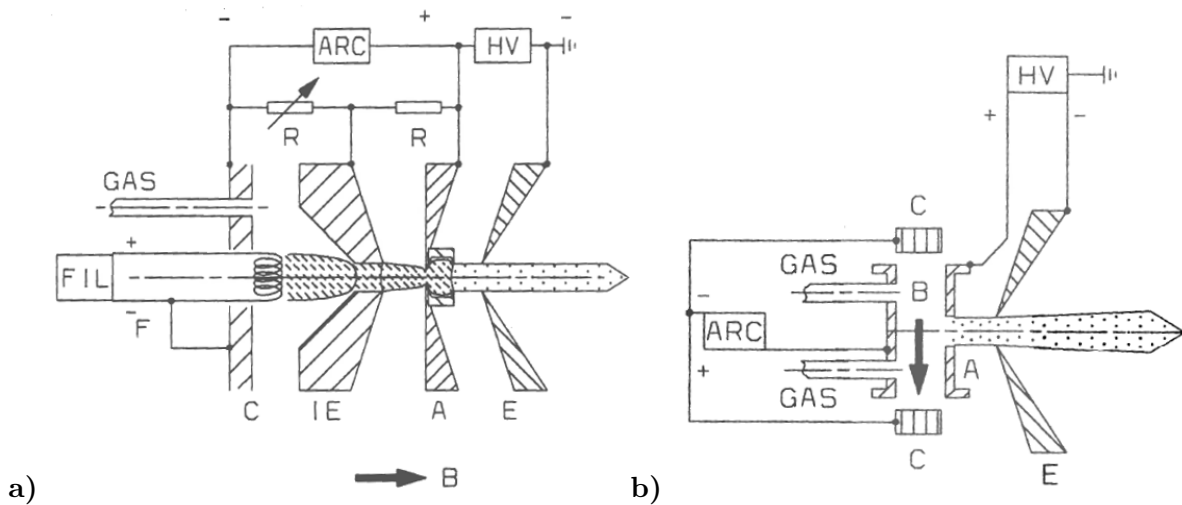


Figure 2.8: a) Schematic of a duoplasmatron ion source with expansion cup (taken from [29]);  
b) Schematic of a cold cathode Penning type ion source (taken from [29]).

<sup>7</sup>The term of plasma density is very often not well defined, but in many cases it is identified as the electron density within the plasma [30].

Another kind of plasma ion source is the **Penning type source** as can be seen in figure 2.8b. The anode forms a hollow cylindrical plasma chamber and has at each of its open ends a cathode. The design in figure 2.8b is a cold cathode Penning source (other designs use a hot cathode opposite of a cold anticathode, see [29]). The source can be operated in two discharge modes defined as the low,  $10^{-8} - 10^{-2}$  mbar, and high pressure regime,  $10^{-3} - 1$  mbar. Most important for applications is the later one. The gas ionisation is done by primary emitted electrons performing several oscillations between the cathodes during which they are thermalised, but also secondary electrons at low energies within the discharge contribute to the ionisation process. The ion beam extraction can be either done through an opening in the anode or in one of the cathodes. Singly charged ion beams can reach a few mA of current by using cathode extraction [29]. Guharay et al. report about the use of a Penning source in a pulsed mode (1 ms pulse time, 12 Hz repetition rate) [69]. They report about the extraction of  $H^-$  and  $O^-$  with  $B_r = 10^5 \text{ A m}^{-2} \text{ sr}^{-1} \text{ V}^{-1}$ , beam currents close to 1 mA and  $\Delta E = 3 \text{ eV}$ .

A last plasma source mentioned here is the **Hyperion source** (Oregon Physics) [67, 70]. It is based on the principle of a **RF plasma source** and can be operated in many different modes. The authors report about a Xe beam  $B_r$  of  $10^4 \text{ A m}^{-2} \text{ sr}^{-1} \text{ V}^{-1}$  and  $\approx 3 \cdot 10^3 \text{ A m}^{-2} \text{ sr}^{-1} \text{ V}^{-1}$  for the operation with  $O_2^+$  with an axial energy spread close to 5 eV. Ion beam probe sizes of 42 nm (FW50) containing 10 pA and 22 nm containing 1 pA at 30 keV have been determined. The source can be used with reactive and inert gases for many applications (e. g.  $O_2^+$  and  $O^-$  for SIMS,  $Xe^+$  for FIB and  $He^+/Ne^+/Ar^+$  for low energy ion scattering (LEIS)) [71, 72].

### 2.2.5 Laser ion sources

Gas particles can also be ionised by the use of a laser beam if the energy of the generated photons is above the first ionisation potential of the specific gas species [29]. One high brightness ion source that is based on **laser ionisation** is the **magneto-optical trap ion source** (MOTIS). As can be seen in figure 2.9, this ion source uses two MOT lasers to trap neutral atoms at very low temperatures ( $< 1 \text{ K}$ ) within a small ionisation volume (cylindrical dimensions in  $\mu\text{m}$  range) in between two parallel plates.

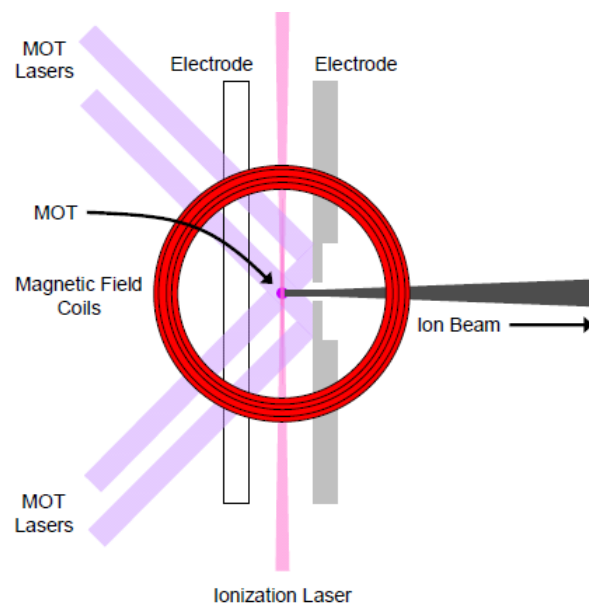


Figure 2.9: Illustration of the MOTIS working principle (taken from [31]).

An ionising laser is focused onto the MOT and the generated ions are extracted through an aperture (diameter can be a few mm) in orthogonal direction to the ionising laser beam axis. This ion source can produce very low divergent ion beams by a combination of a resistive tube within the extraction column having a very weak lens effect on the ion beam and the very low ion temperatures within the MOT resulting in very low transverse ion energies at the source location. Furthermore, very low ion beam energy spreads below 100 meV can be achieved by the MOTIS which makes it very suitable for low energy FIB applications [31, 73, 74]. For a Lithium extracted ion beam an estimated reduced brightness of  $0.6 \cdot 10^4 \text{ A m}^{-2} \text{ sr}^{-1} \text{ V}^{-1}$  is stated in [74] and for Chromium a value of  $0.9 \cdot 10^4 \text{ A m}^{-2} \text{ sr}^{-1} \text{ V}^{-1}$  is determined in [31]. Many other ion species could be created within the MOTIS from elements as noble gases, alkali metals (Na, K, Rb, Cs), alkaline earths (Mg, Ca, Sr), etc. [75]. The Li MOTIS is already used within a complete Scanning Ion Microscope (SIM) system and at 2 keV it reaches at the best a resolution of 27 nm with 1 pA of ion beam current [74].

## 2.3 Instrumentation

As can be seen in figure 2.1 within a FIB system the ion beam is accelerated by an extraction electrode situated close to the exit of the **ion source**. Within the **ion column** optical elements as lenses and apertures are used to form and guide the ion beam in downstream direction. Typically, a **condenser lens** is used as the probe forming element before the beam size is defined by **different apertures**, which also define the available sample beam current ranging from a few tens of nA down to only a few pA. An **objective lens** is used at the end of the column in order to focus the ion beam onto the **sample stage**. The **ion beam energies** typically used range from **5 keV up to 50 keV** and the ion beam can have an energy spread of a few eV. Very often related chromatic aberration effects represent the limiting factor in the achievable resolution of a FIB device [26]. **Several pumping stages** are present in a standard FIB system. The pressure within the ion column is about  $10^{-8}$  mbar in order to avoid electrical discharges between the different high voltage elements and to avoid a contamination of the ion source. Close to the sample the pressure is typically higher and can be in the range of  $10^{-6}$  mbar. Higher pressures in this region would lead to collisions between ions and residual gas particles and can influence the minimal achievable ion probe size.

As already mentioned in section 2.1 several particle species are generated at the interaction point of the primary ion beam with the sample. Therefore, **different detectors** can be present in the sample region as for example X-ray detectors or detectors to record the signal of secondary charged particles (e. g. multi-channel plates or electron multipliers). The primary FIB system can as well be combined with dedicated **secondary ion optics** for analytical purposes so that a SIMS instrument is obtained, see section 2.4.3 for more details. Very often a **gas injection system** is present within the sample region of a FIB instrument as illustrated in figure 2.1. This allows to perform gas assisted FIB machining processes, some more details can be found in section 2.4.1. The sample stage itself allows typically a 5-axis movement including translation in three directions, rotation and tilt. In a stand alone configuration, also called “**single beam**”, FIB instruments have typically a vertical ion column orientation. Another kind of configuration where the FIB instrument is integrated into another analytical device (e. g. a SEM) is called “**dual beam**” system, in which the FIB column is oriented with a certain angle to the vertical axis [26].

## 2.4 Applications

### 2.4.1 FIB machining

A first application field described in more detail is **FIB milling**. It can in general be understood as a combination of sputtering, redeposition and amorphisation. FIB milling is used for example in **nano fabrication/patterning**, as **TEM sample preparation tool** to cut out small very thin slices of a specimen, but also as **repair tool for photomasks**. Mainly used are  $\text{Ga}^+$  FIB systems with about 10 nm resolution, but also other species such as  $\text{Au}^+$ ,  $\text{As}_2^+$ ,  $\text{He}^+$  or  $\text{Ne}^+$  can be used. The sputter rates of many materials are  $< 1 \mu\text{m}^3/\text{nC}$ , so that with typical ion currents from a few to a few tens of pA the speed of FIB milling processes lies in the range of 0.001 to  $0.1 \mu\text{m}^3/\text{s}$  [3, 5, 15, 76].

As a first example, in figure 2.10a the atomic force microscopy (AFM) image of an array of nano-holes is shown. These tiny holes are produced by a 30 keV/1 pA  $\text{Ga}^+$  FIB (dwell time: 2 s). The ion beam spot has a FWHM of 10 nm and the holes have a quite uniform depth of 20 nm with diameters at the sample surface of 50 nm. The holes are surrounded by uplifted rings, 10 nm to 20 nm high, which are related to amorphisation causing swelling of the material. Amorphisation occurs in areas where the ion dose (ions/unit area) is below the threshold to generate sputtering (for  $\text{Ga}^+$ : amorphisation dose  $\approx 10^{15}$  ions/ $\text{cm}^2$ ) [3]. What can further be seen in the line scan is that no cylindrical holes are obtained, but a V-Shape profile occurs. This is due to redeposition of material from the hole bottom to the side walls. One way to avoid this is to use a series of fast scans with the same total dose as one slow single scan [15].

A second example for FIB milling structures are bow-tie nano-antennas produced and investigated by Kollmann et al. [76] for plasmonic purposes, see figure 2.10b. The production is a combined process of  $\text{Ga}^+$  and  $\text{He}^+$  milling of a gold film (30 nm thick) within a HIM. The first coarser production step creates a fused bow-tie structure (no gap between the two halves) by the use of the  $\text{Ga}^+$  FIB, with low production speed to minimise Ga implantation/contamination. The second step creates a gap  $< 6$  nm in between the two halves to obtain the antenna and edge sharpening is performed. In comparison, gap sizes produce by a single  $\text{Ga}^+$  FIB milling production are  $> 10$  nm with less good edge resolution. A disadvantage of He is the lower milling rate so an increase in the total production time. Within the HIM neon can as well be used to perform nano-fabrication, which has the advantage of a higher direct sputtering yield compared to helium [6, 8, 58].

FIB systems can also be used to perform **ion implantation** in selected areas of specimens. The implantation can be tuned by adjusting the primary ion energy, the dwell time and the dose. One of the first applications is the production and doping of semiconductor devices. The possibility of localising the ion implantation eliminates the need of masks and several lithographic steps, reducing the cost and time for manufacturing. Another FIB implantation example is the creation of microstructures. In figure 2.10c a small cross-cantilever can be seen. The first production step is the implantation of a Si substrate with a 30 keV/100 pA  $\text{Ga}^+$  FIB, which changes the Si etching properties for certain etchants. The second production step is the chemical etching with potassium hydroxide (KOH). While the non-implanted Si is etched away the implanted regions are more or less unaffected and the tiny cross-cantilever is formed [3]. Besides changing etching properties ion implantation can also be used to change the optical, electrical or magnetic properties of samples [65, 77]. An example of **strain doping** by helium implantation within thin films (20 nm thick  $\text{La}_{0.7}\text{Sr}_{0.3}\text{MnO}_3$  films) is given by Guo et al. [77].

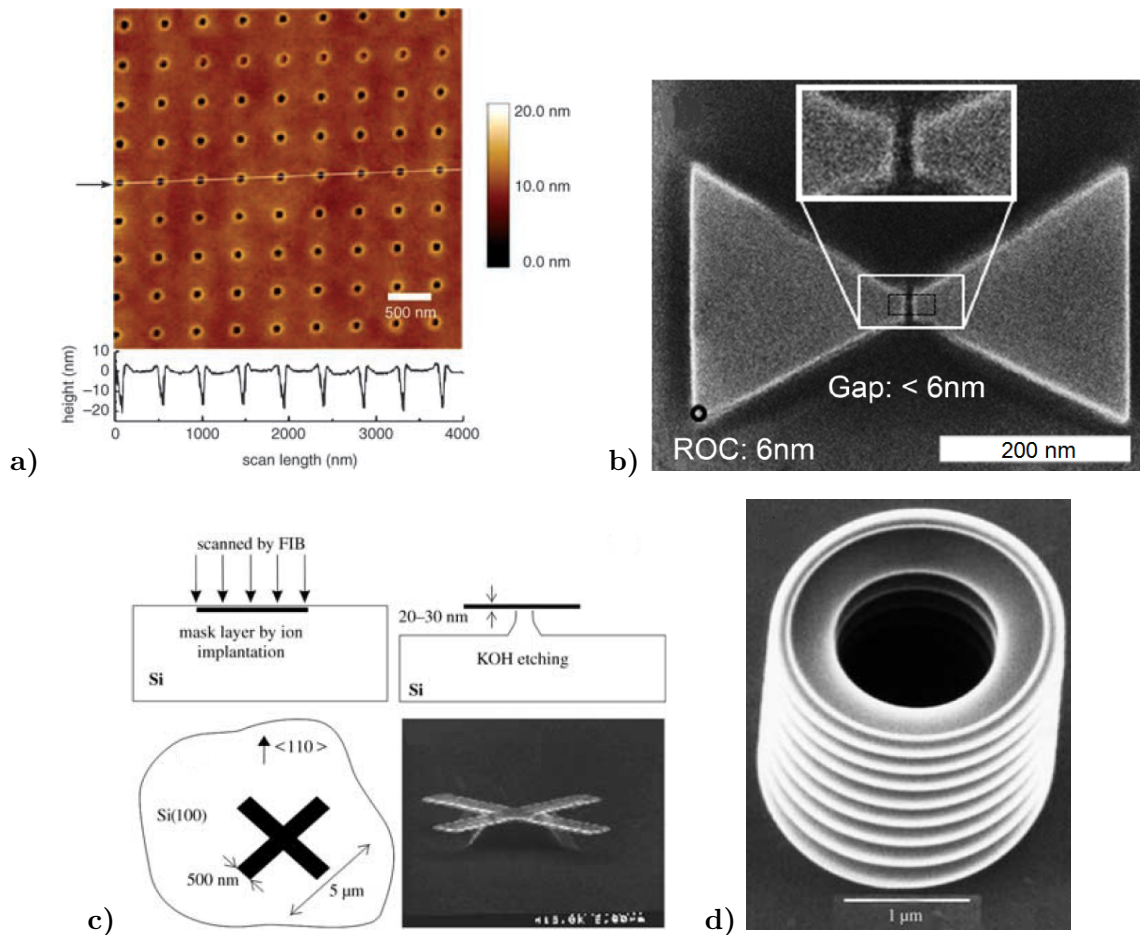


Figure 2.10: a) FIB milled nano-holes in Silicon (30 keV  $\text{Ga}^+$  FIB at 1 pA; taken from [3]).  
 b) HIM image of a bow-tie nano-antenna produced by a combined process of  $\text{Ga}^+$  and  $\text{He}^+$  FIB milling (ROC = Radius Of Curvature; modified from [76]);  
 c) Micro-sized cross-cantilever made by ion implantation in Silicon and subsequent etching with KOH (30 keV  $\text{Ga}^+$  FIB at 100 pA; modified from [3]);  
 d) SIM image of a FIBID produced diamond-like carbon micro-bellow (30 keV  $\text{Ga}^+$  FIB, 7 nm diameter beam, aromatic hydrocarbon precursor gas; modified from [3]).

They state that by He implantation the strain introduced along a single axis of the thin film crystal is precisely controllable and a change of the lattice constant along that axis occurs, resulting in some material property changes. Furthermore, as He is a noble gas it does not introduces any additional damage within the lattice in contrast to hydrogen doping.

When a gas delivery system is available at the sample region, as illustrated in figure 2.1, it is possible to perform **FIB Assisted Etching** (FIBAE) or **FIB Induced Deposition** (FIBID). Very often a capillary is brought close to the sample (about 50 - 300 μm) to inject precursor gases. In FIBAE the ion beam is used to induce chemical reactions between the gas molecules that absorb on the specimen's surface and the surface itself. An enhancement of material removal is the result. Furthermore, redeposition of material on side walls can be reduced to avoid e. g. the creation of V-shaped hole profiles as shown in figure 2.10a [3, 15]. In contrast, in FIBID the ion beam promotes Chemical Vapour Deposition (CVD) at very localised sample areas. An example for FIBID microstructure fabrication can be seen in figure 2.10d. Here a 30 keV  $\text{Ga}^+$  FIB with a 7 nm beam diameter was used to create a diamond-like carbon micro-bellow in presence of an aromatic hydrocarbon precursor gas [3].

Other fields of application using FIB machining are **ion lithography** [15] and **surface func-**

**tionalisation/modification** [1, 13].

Beside the fabrication techniques, where ion implantation is desired, the use of  $\text{Ga}^+$  FIB systems for machining purposes has the drawback that undesired Ga implantation (staining) within the specimens occurs. This can lead e. g. to surface damage, malfunctioning of nano-devices or unwanted effects during sample preparation [78, 79, 80, 81]. Therefore, noble gas ion FIB systems are desired as less damage within machined specimens will occur. Examples for such noble gas FIB systems can be found in [82] and [83]. The authors of [82] report about a SEM equipped with a high current Xenon plasma FIB to speed up the preparation of TEM samples with sizes of several tens of  $\mu\text{m}$ , compared to SEM - Ga FIB preparation. Even if the usable beam size of the Xe FIB is larger than in the case of Ga, a good surface quality is obtained most probably due to a smaller range of  $\text{Xe}^+$  compared  $\text{Ga}^+$  within the samples. A similar system of SEM - Xe Plasma FIB is used in [83] for the speed up of the large volume serial section tomography technique compared to SEM - Ga FIB systems. For example the removal speed for copper by the use of the  $\text{Xe}^+$  beam is determined to be about  $80 \mu\text{m}^3/\text{s}$  compared to about  $20 \mu\text{m}^3/\text{s}$  when using a  $\text{Ga}^+$  beam. The authors report as well about less surface damage and amorphisation by the use of a 60 nA/30 keV  $\text{Xe}^+$  beam.

#### 2.4.2 FIB imaging

A FIB system can also be used as a **Scanning Ion Microscope** (SIM) where mainly two signals are available for imaging purposes, the ejected secondary electrons (SE) or positive/negative secondary ions (SI) from the sample. The SI emission coefficients  $\gamma_{\text{SI}}$  are in the range of  $10^{-2}$  to  $10^{-4}$  which is far lower than the SE emission coefficients  $\gamma_{\text{SE}}$  in the range of 1. A way to enhance  $\gamma_{\text{SI}}$  is to provide oxygen flooding close to the sample stage, improvement factors of about 1000 can be reached. Different image contrast mechanisms can be found in SIM images. Topographic contrast (which is usually stronger for SI mode), channelling contrast (dependence of  $\gamma$  on local crystal orientation in crystalline samples) or material contrast (the specimen chemistry changes  $\gamma$ ). **FIB imaging represents a very surface sensitive technique.** For the SI mode the signal is emerging from 1 to 3 monolayers ( $\approx 1 \text{ nm}$ ) below the sample surface, whereas for the SE mode the signal can emerge from a few tens of nanometres. In many modern instruments a LMIS with a  $\text{Ga}^+$  beam is used with energies between 25 - 50 keV. It is possible to achieve beam diameters below  $1 \mu\text{m}$  containing about 30 nA. When sputtering during imaging is undesired small beam currents have to be used [15, 26]. One of the big advantages of the FIB imaging capability is that FIB fabrication processes can be visualised simultaneously.

Nowadays, one of the high resolution ion microscopes that exist is the **Helium Ion Microscope** (HIM). It uses the GFIS to produce a high brightness helium ion beam. It is possible to get an image resolution of about 0.35 nm (see figure 2.11). The landing energy of the helium ion beam is in the range of 10 - 35 keV with imaging currents between 0.5 and 10 pA. The HIM can also be used to create images with a neon ion beam [6, 8, 58].

In **dual beam systems** FIB imaging can be used as complementary technique to the electron beam imaging capability within such an instrument. Generally the electron beam provides the higher-resolution images but the contrast obtained by ion beam generated images is most often stronger [26]. A recently developed system is a combination of a TEM - Ga FIB - SIMS instrument [84, 85]. Even if the main purpose of this instrument is to obtain high resolution electron beam images ( $1.4 \text{ \AA}$ ) in combination with chemical information from the sample, it is as well possible to generate complementary TEM and SI images.

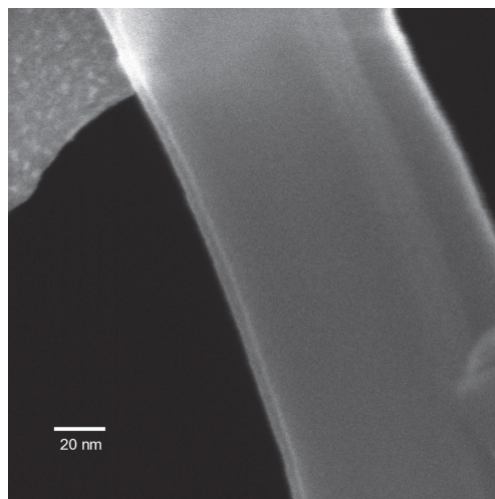


Figure 2.11: HIM image of an asbestos fibre on top of a carbon film (edge resolution of 0.35 nm; taken from [6]).

### 2.4.3 FIB analysis

A last application field is the use of a **FIB to perform SIMS**, where the generated SI signals provide chemical information about the analysed samples. The **sensitivity of SIMS can be in the ppm to ppb range** and it is possible to mass resolve the different isotope contributions of an element within a sample. SIMS can be used in different ways. A mass spectra of the SI signal can be recorded. When the primary ion beam is rastered over the sample surface 2D chemical maps can be generated. Furthermore, 1D depth profiles can be obtained when specific SI signals are recorded while sputtering away the sample. At last, several 2D chemical maps can be taken while sputtering layer by layer in order to create a 3D chemical map. Unfortunately, obtaining quantitative analysis of the sample's elemental composition is very difficult by SIMS. For a given SI species different yields are obtained depending on the local sample matrix from which it is ejected (matrix effect). Furthermore, specific primary ions create different SI yields for a same sputtered element [10, 15, 26, 84]. For example by using  $\text{Ga}^+$  as primary ion beam the useful yield (UY; defined as number of detected SI ions/number of sputtered atoms of the same element) of  $\text{Si}^+$  is determined to be nearly three orders of magnitude higher when it is ejected from a  $\text{SiO}_2$  matrix compared to a pure Si or SiC matrix. Moreover, when using a pure Si or SiC matrix it has been shown that the UY for  $\text{Si}^+$  is nearly two orders of magnitude higher under the primary bombardement with  $\text{O}_2^+$  compared to  $\text{Ga}^+$  [86].

Different SIMS instruments exist: **Time of flight instruments** (mass separation by different flight time), **magnetic sector instruments** (mass/charge dependent spatial position) or **radio frequency (RF) quadrupoles** (SI transmission dependent on the applied RF high voltage signal). A state of the art FIB-SIMS instrument has been developed recently by adding SIMS capability to the HIM, so that now **HIM-SIMS** analyses can be performed, see figure 2.12. A high-performance compact double focusing magnetic sector mass spectrometer has been designed. Specialised SI extraction optics can be placed in close vicinity to the sample stage or fully retracted when the HIM needs to be used in its normal operational mode. The optics are designed in such a way that a sub 10 nm  $\text{He}^+$  or  $\text{Ne}^+$  probe size can still be achieved at the sample surface. The SI extraction optics are coupled to transfer optics mainly consisting of lenses and deflectors to guide the SI towards the energy analyser (Electrostatic Sector Analyser ESA), where SI with different energies have different curvature radii.



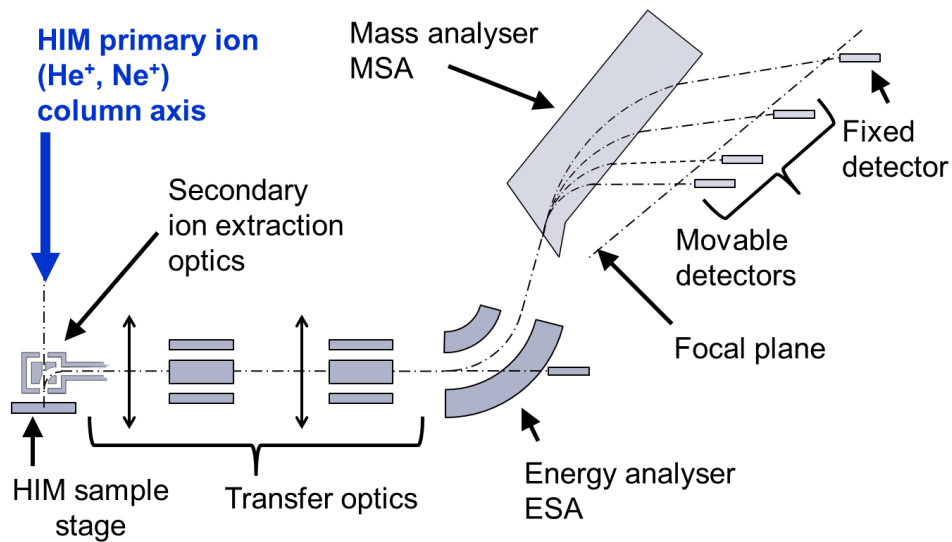


Figure 2.12: Schematic of the recently developed HIM-SIMS instrument.

The ESA is followed by a Magnetic Sector Analyser (MSA) where the SI follow a trajectory depending on their mass over charge ratio. By combining an ESA with a MSA it is possible to achieve achromatic mass filtering (i. e. it is independent of the SI initial energy distribution). At a final stage the transmitted SI signals can be registered by three movable and one fixed detector along the focal plane of the magnet so that currently four masses can be detected in parallel. Sub-20 nm SIMS imaging is possible with the HIM-SIMS instrument, it covers the full mass range from H to U and a high mass resolution ( $m/\Delta m$ ) in the range of 500 to several thousands can be obtained [84, 87, 88].

Primary ion species that are very often used for SIMS are **reactive ion species** as  $\text{Cs}^+$  enhancing the signals of negative SI and  $\text{O}_2^+/\text{O}^-$  enhancing the signals of positive SI compared to other non-reactive species as e. g.  $\text{Ga}^+$ ,  $\text{Au}^+$ ,  $\text{Bi}^+$ ,  $\text{Ar}^+$ ,  $\text{Xe}^+$ ,  $\text{He}^+$  or  $\text{Ne}^+$ . In the case of these non-reactive species the SI signals and therefore the useful yields can be enhanced by simultaneous **reactive gas flooding**. Here again the use of oxygen enhances positive SI-UY and caesium negative SI-UY. For example the use of  $\text{He}^+/\text{Ne}^+$  combined with  $\text{O}_2$  flooding can have enhancement factors up to three orders of magnitude or combined with Cs flooding up to five orders of magnitude [10, 11, 26, 84]. Moreover, negative primary ion species as  $\text{O}^-$  or  $\text{F}^-$  are used for SIMS purposes as presented in [89]. The authors report that the UY of positive SI emitted from semiconductor samples (Si, Ge, InP, GaAs) are higher for the use of  $\text{F}^-$  primary ions, while  $\text{O}^-$  primary ions give better results for positive SI emitted from metals (Cu, Ni).

Not only mono- or diatomic primary ion species are used for SIMS but also **cluster species** as  $\text{Ar}_n^+$ ,  $\text{Au}_n^+$ ,  $\text{Bi}_n^+$  or  $\text{C}_n^+$ . When using mono atomic primary ion species a lot of fragmentation of organic samples occurs and it is difficult to detect large molecular SI. By the use of  $\text{Au}_n^+$  and  $\text{Bi}_n^+$  this effect of fragmentation could already be clearly reduced. The capability of using a  $\text{C}_{60}^+$  primary ion beam even makes it possible to obtain molecular SI information with good sensitivity at quite large primary ion doses. This development makes it possible to perform molecular depth profiling or even 3D molecular imaging [39]. In addition in [90] the combination of  $\text{C}_{60}^+$  and  $\text{Ar}_{4000}^+$  with Cs flooding is investigated. The authors state that the obtained enhancements of negative SI-UY are very similar to results obtained e. g. by  $\text{Ga}^+/\text{He}^+$  with Cs flooding. Furthermore, they report that the use of cluster primary ions promotes the emission of larger SI compounds especially when using the  $\text{Ar}_{4000}^+$  beam.

## 2.5 Summary and conclusions

Section 2 treated FIB systems in general, related ion sources, instrumentation aspects and applications. A summary and conclusions will be given here:

- In general a FIB instrument consists of an ion source, an ion column and a sample region. Various detectors can be used to record the different secondary signals generated during the ion beam sample interaction. The system's performance is closely related to the ion source performance. Characteristic ion beam parameters are: the extracted current, the angular spread, the source size and the current density. Ion beam quality quantities are: the transverse normalised emittances, the reduced brightness and the energy spread  $\Delta E$ .
- FIB applications need high brightness ion sources. This allows one to create small features with good erosion rates. To get high secondary signals combined with a small ion probe size to obtain high resolution images with a good contrast. Furthermore, high lateral resolution 2D/3D chemical maps with good elemental sensitivity or mass spectra of good quality can be obtained by the use of high brightness primary ion beams. Many different kinds of ion species are used for FIB applications, whose performance can be very different depending on the ion species used.
- In table 2.2 an overview is given for comparison of the different ion sources used in FIB systems. Up to now most often a Ga LMIS is used mainly due to its stable/reliable operation and very high brightness. Nevertheless, it has the drawback that staining effects occur in the machined/analysed specimens. In order to avoid these contaminations the ultimate goal is to create a noble gas ion source with a comparable brightness to the LMIS, a very low  $\Delta E$  and a flexible choice in ion species. The laser ionisation source MOTIS for instance provides a versatile ion species choice and a very small  $\Delta E$ . Unfortunately, its brightness is still three orders of magnitude below the LMIS. Nevertheless, it is used for many low energy ion microscopy applications and also FIB machining. A gaseous ion source that has a 100x higher brightness than the LMIS is the ALIS with again a very low  $\Delta E$ . Currently a drawback is that it is limited to Helium/Neon. Combined with a specialised ion column the ALIS builds up the HIM being the highest spatial resolution FIB instrument currently used. A last concept that is expected to have similar brightness values as the LMIS is the NAIS. As this kind of source is based on electron impact ionisation it can virtually provide any gaseous ion species. So far the experimentally determined brightness values do not yet meet the expectation. Furthermore, so far the NAIS is integrated within a SEM and the development of a stand alone ion source has only been started recently.
- In conclusion, by evaluating all the different advantages/disadvantages of the presented ion source concepts it is clear that further development is needed in order to create a versatile high brightness low energy spread gaseous ion source, which can eventually at the end replace the mainly used LMIS. New development attempts are described in more detail in section 4 and 5. The ionisation process of choice is electron impact as this allows one to switch between ion species by simply changing the gas feed to the source and keeps the technical requirements on a quite basic level.

	Electron impact IS	Duoplasmatron	Hyperion plasma source	MOTIS
Ion species	Ar, Xe, O <sub>2</sub> , C <sub>60</sub> , ...	Ar, Xe, O <sub>2</sub> , ...	H, He, O <sub>2</sub> , Ar, Xe, Ne, Kr	Ar, Xe, Ne, Kr, Na, K, Rb, Cs, Mg, Ca, Sr, ...
Source size	100 - 500 $\mu\text{m}$	30 - 500 $\mu\text{m}$	10 - 20 $\mu\text{m}$	10 - 50 $\mu\text{m}$
Extraction current	1 - 1000 $\mu\text{A}$	1 - 500 $\mu\text{A}$	10 - 50 $\mu\text{A}$	1 - 200 pA
Reduced brightness $\text{A}/(\text{m}^2 \text{sr V})$	1	$10^2 - 10^3$	$10^3 - 10^4$	$10^4$
Energy spread	1 - 10 eV	5 - 20 eV	5 - 6 eV	$\lesssim 0.1$ eV

	LMIS	NAIS	GFIS
Ion species	Ga, In, Au <sub>n</sub> , Bi <sub>n</sub>	He, Ne, Ar, Kr, Xe	He, Ne, N <sub>2</sub> , H <sub>2</sub>
Source size	10 - 50 nm	< 100 nm	< 1 nm
Extraction current	1 - 500 $\mu\text{A}$	1 - 400 pA	1 fA - 100 nA
Reduced brightness $\text{A}/(\text{m}^2 \text{sr V})$	$10^6 - 10^7$	$10^7$ * ( $10^2 - 10^4$ **)	$10^{10}$
Energy spread	5 - 50 eV	< 5 eV	$\lesssim 1$ eV

\* estimated range taken from [22], \*\* experimental determined values taken from [25, 54].

Table 2.2: Main characteristics of different ion source types used for FIB applications.

### 3 Theoretical concepts and simulation software

In this chapter the theoretical background of charged particle optics (CPO) is given in section 3.1.1 and the features of the closely related CPO simulation software SIMION are described in section 3.1.2. The development of specialised CPO columns is of importance for our ion source designs described in section 4 and 5. Background about specialised radio frequency ion optics devices, so called ion carpets, is given in section 3.2 as such an ion carpet is incorporated within the ion source prototype described in section 5. Information about the theory of gas conductance calculations and the related simulation software Molflow+ can be found in section 3.3.1 and 3.3.2. During the development of the ion source concepts it is of importance to perform gas conductance calculations, as the pressure gradients across the optical columns influence the performance/operation of the ion source. Finally section 3.4 gives a description of electron stopping ranges in gases and the related simulation software CASINO. This background on stopping an electron beam within a gas region is required for the ion source development in chapter 5.

#### 3.1 Charged particle optics

##### 3.1.1 Theoretical concepts

###### Basic equations

The trajectories of charged particles can be influenced by electric and magnetic fields. The **general relativistic equation of motion** can be expressed as:

$$\frac{d}{dt} \frac{m_0 \cdot \vec{v}}{\sqrt{1 - \left(\frac{v}{c}\right)^2}} = q \cdot (\vec{E} + \vec{v} \wedge \vec{B}) \quad . \quad (3.1)$$

Where  $m_0$ ,  $\vec{v}$  and  $v$  represent the charged particle rest mass, velocity and speed. The speed of light is characterised by  $c$ ,  $q$  is the charge of the particle and the electric and magnetic field vectors are given by  $\vec{E}$  and  $\vec{B}$ . In the case that  $v \ll c$  (non-relativistic case) and that only electric fields are present to influence the particle trajectory the equation 3.1 simplifies to:

$$\frac{d}{dt} m_0 \cdot \vec{v} = q \cdot \vec{E} \quad (3.2)$$

In the material free space and in the electrostatic case the **Gauss theorem** states for  $\vec{E}$  :

$$\vec{\nabla} \cdot \vec{E} = \frac{\rho_C}{\epsilon_0} \quad . \quad (3.3)$$

Where  $\rho_C$  is the charge density and  $\epsilon_0$  the electric constant. In order to calculate  $\vec{E}$  in each point of space  $(x, y, z)$  the **scalar potential**  $\Phi(x, y, z)$  can be used:

$$\vec{E} = -\vec{\nabla} \Phi(x, y, z) \quad . \quad (3.4)$$

By inserting equation 3.4 into equation 3.3 it is possible to obtain the so called **Poisson equation** for the potential which is expressed as:

$$\nabla^2 \Phi(x, y, z) = -\frac{\rho}{\epsilon_0} \quad . \quad (3.5)$$

In the case that no space charge is present (or can be neglected) so that  $\rho = 0$  can be used, the Poisson equation turns into the **Laplace equation** defined as [15, 91, 92]:

$$\nabla^2 \Phi(x, y, z) = 0 \quad . \quad (3.6)$$

In general in order to calculate the trajectory of a charged particle it is mandatory to find a solution to equation 3.6 in order to calculate in each point of space the value of  $\Phi(x, y, z)$ . Then equation 3.4 can be used to determine the related  $\vec{E}$  values, followed by solving the equation of motion 3.2 in the electrostatic case. In the case of **paraxial charged particle beams** it can be written that  $r$  and  $r' = \frac{dr}{dz}$  are small, where  $r'$  corresponds to the slope of the particle trajectories. In this special beam case and for non-relativistic particles only influenced by electrostatic fields, it is possible to write the **trajectory equation** as:

$$\frac{d^2 r}{dz^2} + \frac{\varphi'(z)}{2\varphi(z)} \frac{dr}{dz} + \frac{\varphi''(z)}{4\varphi(z)} r = 0 \quad . \quad (3.7)$$

Where  $\varphi(z) = \Phi(0, z)$  is the axial potential and  $\varphi'(z)$ ,  $\varphi''(z)$  are its derivations with respect to  $z$ . Equation 3.7 is very often referred to as **Gaussian equation** and knowledge about the potential along the axial  $z$ -direction is needed to calculate the particle trajectory. Mathematically speaking equation 3.7 corresponds to a linear homogeneous differential equation of second order and the mass to charge ratio  $m/q$  is not present which means that when considering particles with the same starting energy they will follow identical trajectories in the paraxial approximation case. Electrostatic fields are generated by applying constant voltages (potentials) on metal surfaces (electrodes) that surround the region through which the charged particle is travelling. The homogeneity of equation 3.7 with respect to  $\varphi$  leads to the fact that when scaling all voltages of an electrostatic system by the same factor the particle trajectories remain identical. Furthermore, due to the homogeneity with respect to  $r$  and  $z$ , scaling all the dimensions of the electrode configuration by the same factor has as result a scaling of the particles' trajectories by the identical factor [15, 91, 92, 93].

### Charged particle lenses

If a rotationally symmetric field is created it can have a focussing action on the charged particle beam due to its radial field component  $E_r$ , whereas the axial field component  $E_z$  is responsible for the change of the particle speed in the axial direction. Close to the optical axis of the system  $E_r$  can be calculated by  $E_r = 0.5 \cdot r \cdot \varphi''(z)$ . Very widely used **rotationally symmetric electrostatic lenses** are composed of several coaxial cylinders with identical inner diameter, see figure 3.1. One special lens case is a three electrode cylindrical lens where the two outermost cylinders are kept at the same voltage ( $V_1 = V_3$ ) and the middle electrode voltage  $V_2$  is used to perform the focusing action. This kind of lens is a so called **Einzel lens** and the particle beam energy is identical before and after the lens region. Furthermore, very often the outer electrodes are at ground and by setting a certain value for  $V_2$  with respect to the beam potential  $V_B$  two different operation modes exist: 1st the decel-accel mode ( $V_B - V_2 < V_B$ ) and 2nd the accel-decel mode ( $V_B - V_2 > V_B$ ).

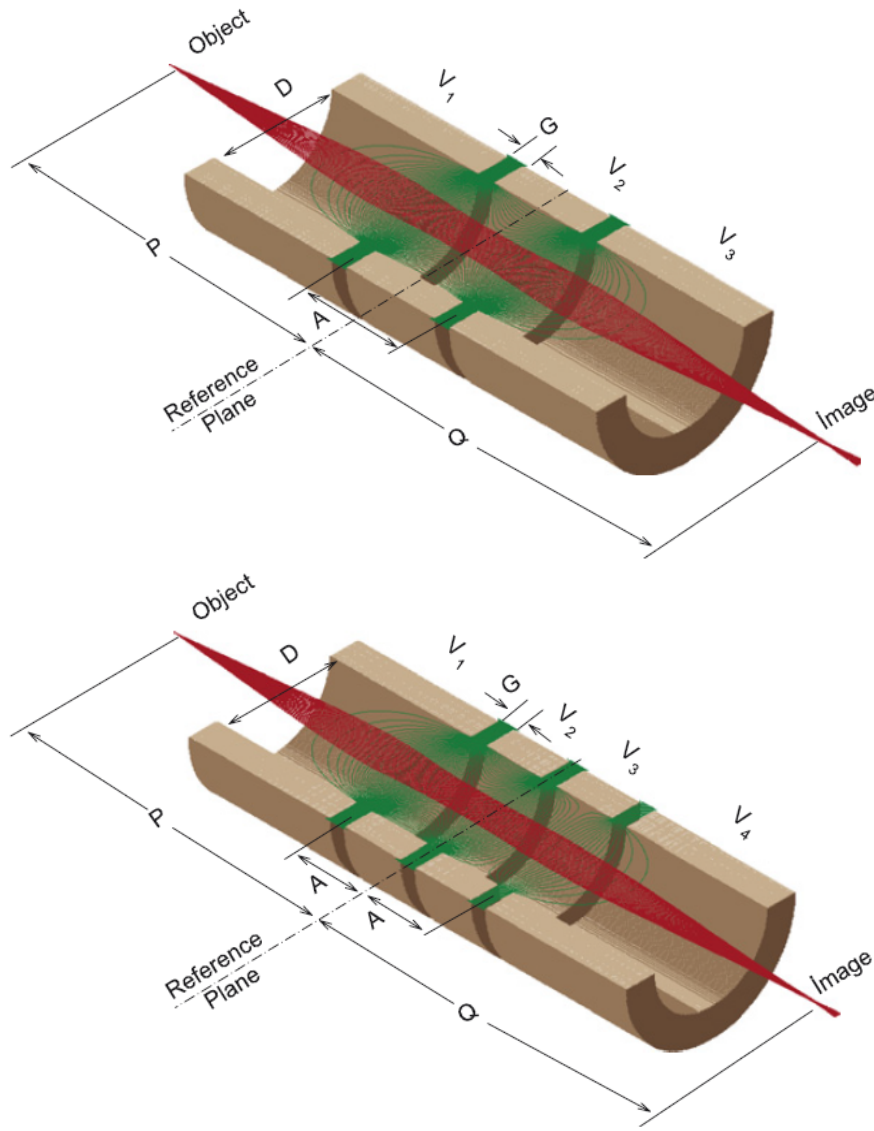


Figure 3.1: Charged particle multiple element cylindrical electrostatic lenses (taken from [94]).

In practice the decel-accel mode is used preferentially as lower absolute voltages are needed to achieve the same focal length compared to the accel-decel mode. When the thickness of the cylindrical electrodes is quite small with respect to their diameters a multi-electrode aperture lens is obtained [15, 93, 95]. Detailed studies of cylindrical electrostatic lenses can for example be found in [94, 96] and [97]. In general not only the applied voltages and number of electrodes but also the geometrical parameters and electrode shapes have an influence on the lens focussing properties. In the publication of Riddle [98] for example many different Einzel lenses have been investigated with a large variation in electrode configuration. These lenses have very often an asymmetric electrode setup with respect to their middle plane and some have electrode shapes that differ from the standard cylindrical (aperture) shape.

### Transfer matrices

In CPO the effect of electrostatic optical elements on the trajectory of a particle can also be evaluated by using the **transfer matrix description**. The effect of a field free drift space on a charged particle trajectory is shown in figure 3.2a and it can be written that:

$$\begin{pmatrix} r_2 \\ r_2' \end{pmatrix} = M_{\text{Drift}} \begin{pmatrix} r_1 \\ r_1' \end{pmatrix} = \begin{pmatrix} 1 & L_{\text{Drift}} \\ 0 & 1 \end{pmatrix} \begin{pmatrix} r_1 \\ r_1' \end{pmatrix} \quad . \quad (3.8)$$

Where  $M_{\text{Drift}}$  represents the drift space transfer matrix and  $L_{\text{Drift}}$  its length. The effect of a uniform electrostatic field (paraxial case), as shown in figure 3.2b, and of an aperture on the particle trajectory can be expressed by the following matrices:

$$M_{\text{UF,para}} = \begin{pmatrix} 1 & \frac{2L_{\text{UF}}}{\sqrt{V_1/V_2+1}} \\ 0 & \sqrt{V_1/V_2} \end{pmatrix} \quad \text{and} \quad M_A = \begin{pmatrix} 1 & 0 \\ -\frac{1}{f_A} & 1 \end{pmatrix} = \begin{pmatrix} 1 & 0 \\ \frac{E_1-E_2}{4V_A} & 1 \end{pmatrix} \quad . \quad (3.9)$$

In equation 3.9,  $V_1$  and  $V_2$  are the potentials generating the uniform electrostatic field,  $V_A$  is the potential applied to the aperture and  $E_1$ ,  $E_2$  are the electric field strengths before and behind the aperture respectively. The focal length of a general aperture can be deduced from equation 3.9 and expressed as follows:  $f_A = 4V_A/(E_2 - E_1)$ . In the case that  $E_1 > E_2$  the aperture has a diverging lens effect and for  $E_1 < E_2$  it has a converging lens effect. For optical elements as for example multi-electrode lenses the complete transfer matrix can be calculated by multiplying several of the afore presented matrices together [15, 93, 95].

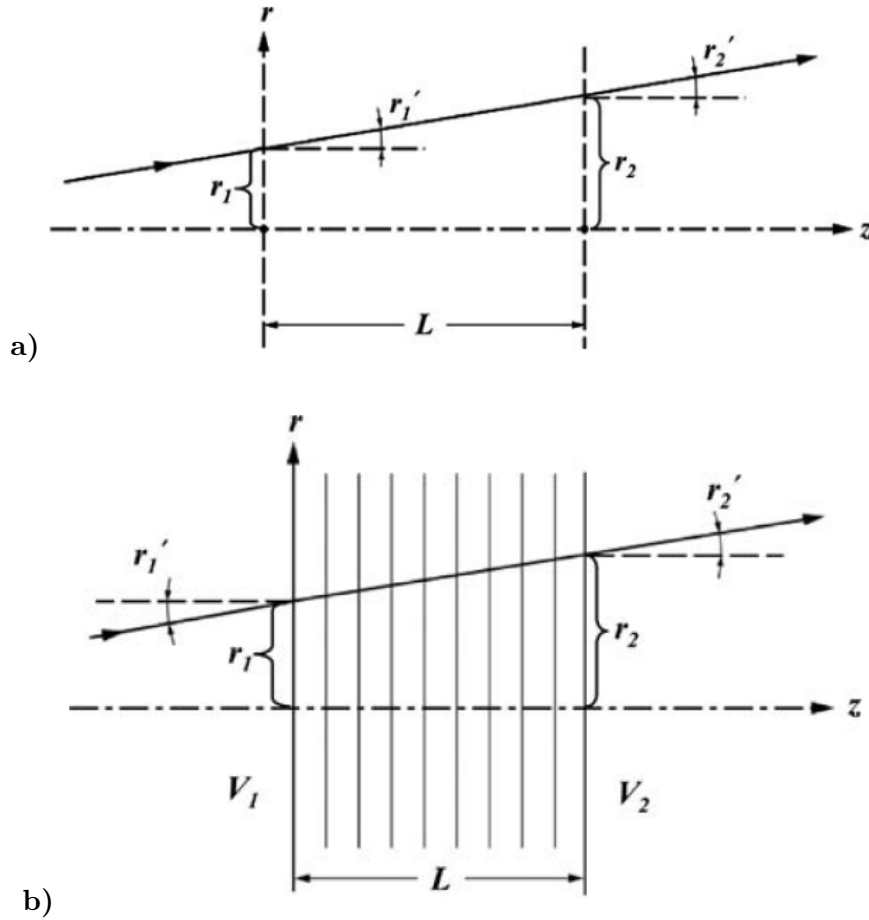


Figure 3.2: a) Field free drift space effect on a charged particle trajectory (taken from [95]);  
b) Electrostatic uniform field effect on a charged particle trajectory (accelerating paraxial case; taken from [95]).

As an example, for an Einzel lens which is preceded and followed by a field free drift space the following can be written for a paraxial particle trajectory:

$$\begin{pmatrix} r_{\text{End}} \\ r'_{\text{End}} \end{pmatrix} = M_{\text{Drift,End}} \cdot M_{A3} \cdot M_{\text{UF,para},23} \cdot M_{A2} \cdot M_{\text{UF,para},12} \cdot M_{A1} \cdot M_{\text{Drift,Start}} \cdot \begin{pmatrix} r_{\text{Start}} \\ r'_{\text{Start}} \end{pmatrix}. \quad (3.10)$$

In order to describe complete CPO systems the matrix multiplication becomes often a very complex task. Nowadays, many computer programmes exist to evaluate complete CPO systems, as for example SIMION which will be described in more detail in the next section 3.1.2.

### Small probe electron beam and ion beam extraction systems

CPO systems that are used for **small probe forming electron beam systems** (e. g. TEMs, SEMs) have very often on the emitter side a **triode extraction electrode setup** which is illustrated in figure 3.3a. It consists of the electron emitter itself, a shielding electrode (often called Wehnelt) and an anode electrode. Important parameters that influence the emission characteristics of such a triode setup are the cathode height  $H$ , the Wehnelt hole diameter  $d_W$  and the potential difference between the Wehnelt and the emitter  $\Delta V_{\text{Bias}}$ . The Wehnelt potential is set more negative than the emitter potential and at a certain negative value of  $\Delta V_{\text{Bias}}$  the emission from the emitter tip is totally suppressed. This suppressing bias value will be called in the following “cut-off bias”. The needed cut-off bias gets more negative when the cathode height  $H$  is decreased at constant distance between Wehnelt and anode. Moreover, at constant  $H$  and  $d_W$  the electron current extracted through the Wehnelt opening  $I_{e,\text{Extr}}$  decreases when  $\Delta V_{\text{Bias}}$  gets more and more negative. This is due to the fact that the effective emission area on the emitter front tip can be controlled by  $\Delta V_{\text{Bias}}$  and decreases when going to more negative values of  $\Delta V_{\text{Bias}}$  [40, 92]. A very detailed study of the characteristics of such a triode extraction system can be found in [99].

Different kinds of emitters are used in small probe forming e-beam systems: **thermionic emitters** as tungsten hairpin filaments or lanthanum hexaboride  $\text{LaB}_6$  emitters, sharp **Schottky emitters** using field assisted thermionic emission and **cold field emitters**. In table 3.1 several properties of the different emitters are listed and are taken from [100]. The thermionic emission current density can be calculated with equation 2.4 already stated in section 2.2.1. Space charge effects can play a role when the emitter is operated at high temperatures but low extraction energies. In order to estimate the influence of space charge effects in the particular case of a triode setup one can use the **Langmuir-Child space-charge equation** [101, 102, 103]:

$$J_{\text{LC}} = \frac{4\epsilon_0}{9} \sqrt{\frac{2e}{m_e}} \frac{\Delta V_{\text{EA}}^{3/2}}{D_{\text{EA}}^2} = 2.335 \cdot 10^{-6} \frac{\Delta V_{\text{EA}}^{3/2}}{D_{\text{EA}}^2}, \quad (3.11)$$

where  $\Delta V_{\text{EA}}$  is the emitter-anode potential difference and  $D_{\text{EA}}$  the emitter-anode distance.

In figure 3.3b a possible setup of an ion source extraction configuration is shown, other configurations have already been seen in the figures of section 2.2.



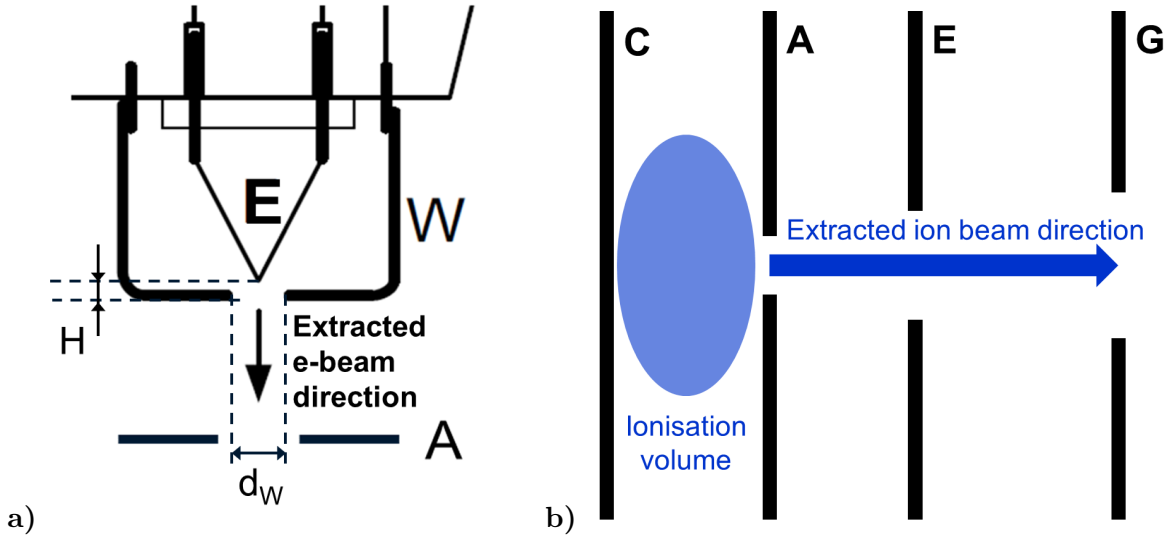


Figure 3.3: a) Schematic of a typical triode extraction setup, E: Emitter, W: Wehnelt, A: Anode (modified from [40]);  
b) Schematic of a general ion source extraction column.

	Thermionic hairpin	Thermionic LaB <sub>6</sub>	Schottky emitter	Cold field emitter
Material	W	LaB <sub>6</sub>	ZrO/W	W
$\phi$ [eV]	4.5	2.4	3.0	4.5
$J_e$ [A/m <sup>2</sup> ] (at 100 kV)	5	$10^2$	$10^5$	$10^6$
T [K]	2700	1700	1700	300
$d_s$ [nm]	$> 10^5$	$10^4$	15	3
B [A/(m <sup>2</sup> sr)] (at 100 kV)	$10^{10}$	$5 \cdot 10^{11}$	$5 \cdot 10^{12}$	$10^{13}$
Vacuum [mbar]	$10^{-4}$	$10^{-6}$	$10^{-8}$	$10^{-11}$
Lifetime [h]	100	1000	$> 5000$	$> 5000$
$\Delta E$ [eV] (at 100 kV)	3	1.5	0.7	0.3

Table 3.1: Small probe electron emitter properties (taken from [100]).

The illustration represents the electrode configuration often used in EI ion sources or plasma sources [29, 30, 34, 36, 38, 104]. The ionisation volume is located in between a cathode C and an anode A. By setting a certain potential difference between those two electrodes  $\Delta V_{CA}$  a first acceleration region is generated for the created ions towards the anode plate and they can leave this region through its opening. For positive or negative ions  $\Delta V_{CA} = V_C - V_A$  needs to be positive or negative respectively. The electrode G represents the ground electrode in the extraction column and the final kinetic energy of the extracted ion beam is closely related to the potential difference of C and G:  $\Delta V_{CG}$ . The ion beam shape, size and spread depends on parameters as the shape and size of the electrode openings, the distances between the different electrodes and the potential setting within the extraction column. In some configurations the electrodes C and A are kept at the same potential and the ion extraction is only done by the leakage of the extraction field generated by the electrode E through the opening of A into the ionisation volume region. The advantage of ending such an ion extraction column with an electrode at ground is that it simplifies the combination of it with other optical elements very often also enclosed by ground electrodes. In this way a field free drift space is created in between the different optical elements (e. g. an ion extraction column followed by an Einzel lens).

### Charge particle deflection

The last optical elements that will be shortly described here are **electrostatic deflectors** to steer charged particle beams. These elements are used to perform beam position adjustments within CPO systems but are also used to scan the charged particle beam over the specimen at the end stage of a probe forming system. One of the simplest ways to deflect a charged particle beam in one direction is to use two parallel plates to generate an electric deflection field as illustrated in figure 3.4a. When the charged particle enters the deflection region it experiences a deflection force (in the presented example in the y-direction) which can be expressed by:

$$F_{\text{Deflection}} = q \cdot E_{\text{Field}} = m_{\text{CP}} \cdot \frac{d^2y}{dt^2} \quad . \quad (3.12)$$

Where  $q$  is the charge of the particle,  $m_{\text{CP}}$  its mass and  $E_{\text{Field}}$  the deflection field strength. Very often in order to be able to deflect the charged particle beam simultaneously in the two transverse directions an electrostatic deflector is composed of 2 pairs of parallel plates (one pair for each direction). More advanced deflector geometries are **cylindrical multiple electrode deflectors** as for example quadrupoles or even octopoles, see figure 3.4b. These kinds of deflectors have the advantage that they generate less aberration effects on the passing charged particle beam compared to the afore mentioned parallel plate deflectors [15, 95].

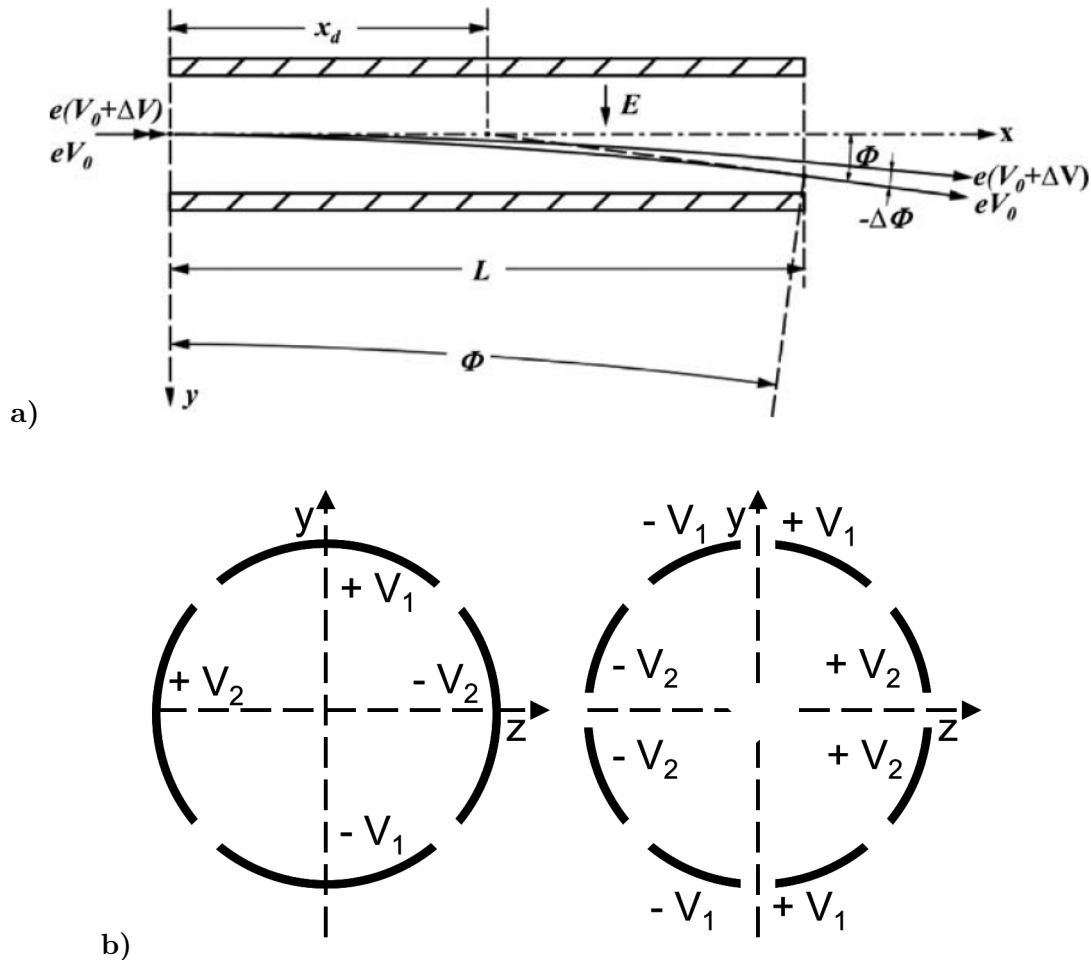


Figure 3.4: a) Schematic of a parallel plate deflector (taken from [95]);  
b) Schematic of a quadrupole (left) and octopole (right) cylindrical deflector.

## Aberrations

As mentioned earlier, aberrations are in reality present in every CPO system. For lenses for example one of the main aberration effects is **spherical aberration** for non-paraxial beams as illustrated in figure 3.5a. A particle that is leaving from an on-axis point in the object plane P with a quite large angle  $\alpha_0$  is focused in a different location along the optical axis compared to the paraxial trajectories. Generally speaking outer trajectories in charged particle beams are focussed in different locations than trajectories in the vicinity of the optical axis and a certain spherical aberration disc with radius  $\Delta r_{\text{sph}}$  is created in the Gaussian image plane Q. The following can be written for  $\Delta r_{\text{sph}}$ :

$$\Delta r_{\text{sph}} = M_L \cdot C_{\text{sph}} \cdot \alpha_0^3 \quad . \quad (3.13)$$

Where  $M_L$  is the linear magnification of the lens (or CPO system in general) and the spherical aberration coefficient is characterised by  $C_{\text{sph}}$ .

Another aberration that occurs is related to the energy spread  $\Delta E$  of the charged particle beam and called **chromatic aberration**. As illustrated in figure 3.5b, particles with the same  $\alpha_0$  but slightly different energies are again focused in different locations along the optical axis. The overall effect  $\Delta r_{\text{chr}}$  of this kind of aberration at the image plane can be expressed by:

$$\Delta r_{\text{chr}} = M_L \cdot C_{\text{chr}} \cdot \alpha_0 \cdot \frac{\Delta E}{E_{\text{Beam}}} \quad . \quad (3.14)$$

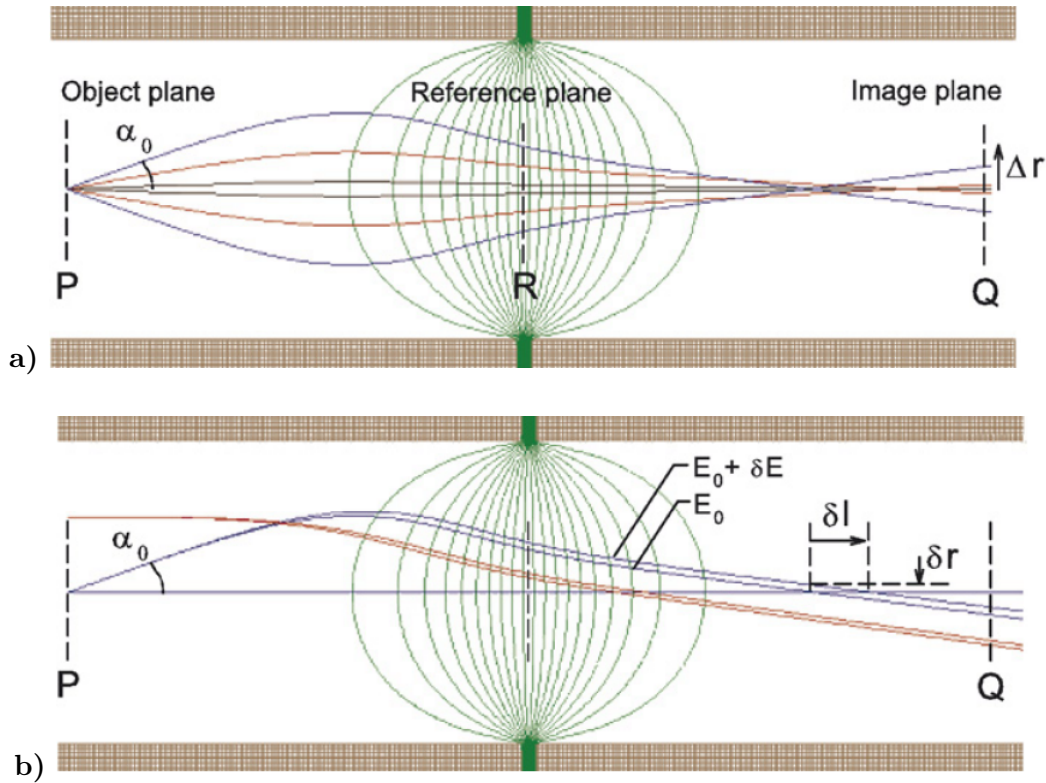


Figure 3.5: a) Illustration of spherical aberration produced by a 2 electrode electrostatic lens (modified from [97]);  
b) Illustration of chromatic aberration produced by a 2 electrode electrostatic lens (modified from [97]).

Similar as before  $C_{\text{chr}}$  represents the chromatic aberration coefficient and  $E_{\text{Beam}}$  the beam energy. By reducing the convergence angle and confining the charged particle beam close to the optical axis it is possible to minimise the spherical and chromatic aberration effects within a CPO system. The calculation of spherical and chromatic aberration coefficients of electrostatic lenses and total CPO systems has been widely treated in the literature, e. g. please refer to [105, 106, 107, 108] or [97] for more detailed information.

It is possible to have on the image side of a charged particle lens two different focal lengths depending on the plane that is considered (e. g. in the XZ- and YZ-plane). This aberration arises when imaging off-axis object points and is called **astigmatism**. As a result an elliptical beam shape can be observed in the image plane. Another kind of aberrations that can be present in real CPO systems are so called **parasitic aberrations** which are related e. g. to a misalignment of different optical elements or imperfections of the electrode shapes. The afore mentioned astigmatism can as well arise for paraxial beams when an elliptically shaped lens electrode aperture is present. This creates an asymmetric field distribution when the beam is passing the lens. A good optical system alignment and a minimisation of geometrical imperfections are therefore mandatory to effectively reduce parasitic aberrations [91, 92].

In charged particle beams of higher currents but low beam energies **Coulomb interactions (CI)** can as well lead to aberration effects. A single particle can for example be deflected due to the average charge of all remaining particles in the beam. This can create a non-uniform charge distribution within the beam and lead to a broadening/defocusing, the effect is known as **space charge effect**. Another CI-effect that can be present is the **Boersch effect** related to the fluctuation of the particle density within the beam due to its stochastic nature. The Boersch effect can raise the total  $\Delta E$  of the charged particle system and manifest itself through the chromatic aberration. A last CI-effect is called **trajectory displacement** and can lead to an axial as well as to a lateral shift of the particle trajectories. In probe forming systems it has as result a direct deterioration of the overall system resolution. The Boersch effect and the trajectory displacement are dominant in narrower beams in the lower density regime and are classified as statistical effects. Due to this statistical nature they can not be corrected within CPO systems. CI-effects are in comparison to e-beam systems more significant in ion beam systems mainly due to the fact that ions travel with a lower speed through the system due to their higher mass and higher beam densities. The evaluation/characterisation of CPO systems by simulations, as with SIMION presented in the next section 3.1.2, are in general performed without taken space charge effects into account but in the cases where it is needed a space charge contribution can be considered [15, 20, 91, 92].

### 3.1.2 Simulation software SIMION

#### Potential arrays and computation method

For the simulation of CPO systems different numerical computation methods can be used as for example first- or second-order finite element methods (FOFEM and SOFEM) for which an overview is given in chapter 1 of [15]. Another computation technique is the **finite difference method** (FDM) on which the simulation software SIMION is based<sup>8</sup>. The optical systems simulated with SIMION are composed of so called **potential arrays (PA)** which can have

---

<sup>8</sup>All simulations presented in this manuscript have been performed with SIMION version 8.0 or 8.1 and related updates.

either a 2D or a 3D structure. These PAs are in general built up of square (2D) or cubic (3D) grid cells, which can if needed be scaled anisotropically. Every grid unit point within a PA can be set to be an electrode or non-electrode grid point, see figure 3.6a. The PA's **symmetry** can be chosen to be planar (2D and 3D PAs) or cylindrical (rotational symmetry about the x-axis, 2D PAs only). Furthermore **mirroring** in the x-, y-, z-direction can be indicated when creating a PA. In order to check if the symmetry and mirroring chosen for a specific PA generates the correct electrode shape and configuration it is possible to view it in a volume view. For example in figure 3.6a the XY-view of the 2D-PA for a simple three electrode lens is shown (cylindrical symmetry) and the volume view indicates clearly that the intended cylindrical Einzel lens is being generated correctly. What should be mentioned here is that when building up optical systems it should be tried to use a maximum of mirroring as possible, especially in 3D-PAs as every supplemental grid point occupies about 10 bytes of random-access-memory (RAM). More occupied RAM means longer calculation times for the potential distributions within the PAs.

Before any simulation with charged particles can be done, SIMION needs to calculate the potential in every grid point of the PA and is doing this by using a specialised form of FDM, the **overrelaxation technique**. In the case of a system where space charge can be neglected FDM is used to approximate the Laplace equation (equation 3.6) by a finite difference equation which establishes a relation between the potential at each grid point with the potentials at its nearest neighbour grid points.

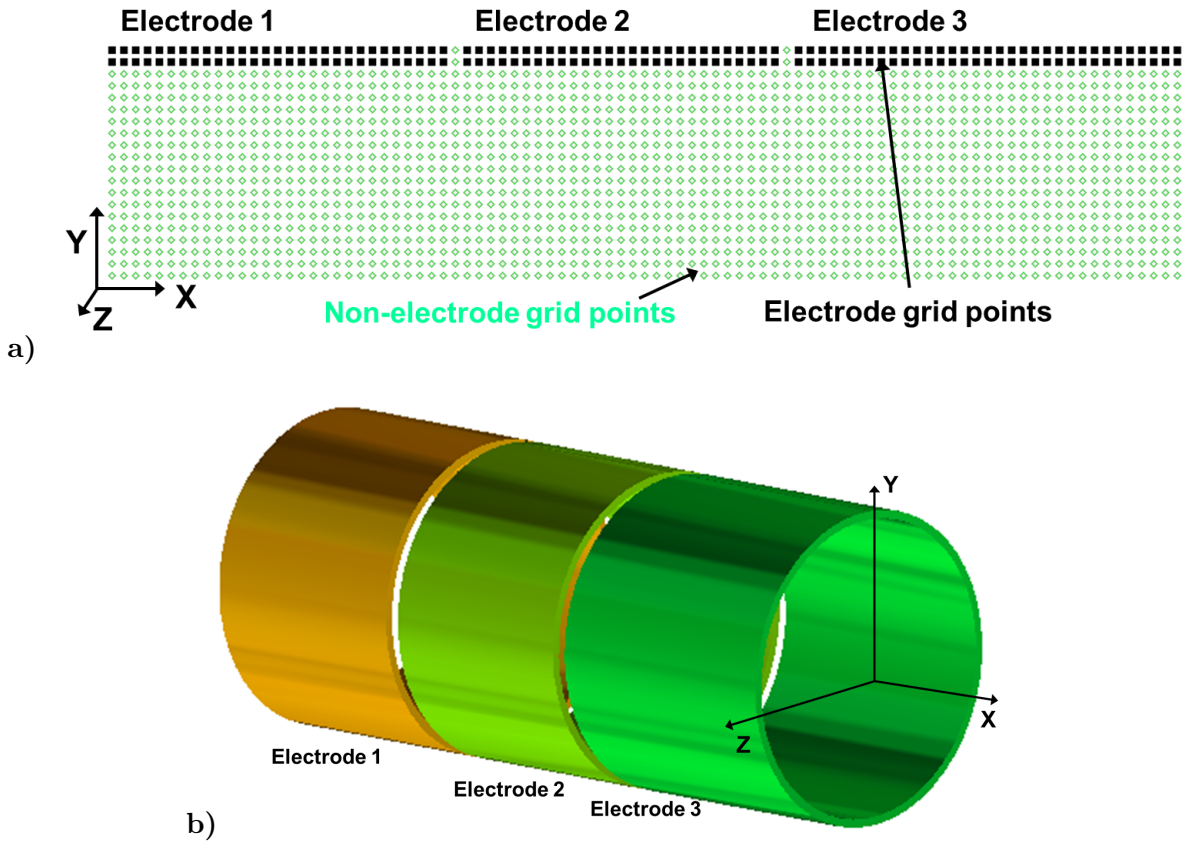


Figure 3.6: a) Illustration of a cylindrical symmetric 2D-PA for a simple three electrode lens;  
b) Corresponding volume view which shows the intended cylindrical Einzel lens.

The following is defined in general for calculating the potential at a specific grid point  $P_0$ , an illustration can be seen in figure 3.7a:

$$\begin{aligned} V_{P_0} &= (V_{P_1} + V_{P_2} + V_{P_3} + V_{P_4}) / 4 \quad \text{in the 2D-PA case;} \\ V_{P_0} &= (V_{P_1} + V_{P_2} + V_{P_3} + V_{P_4} + V_{P_5} + V_{P_6}) / 6 \quad \text{in the 3D-PA case.} \end{aligned} \quad (3.15)$$

In appendix H of [109] many more potential calculation equations are listed which SIMION uses for the interior, corner and boundary grid points of different kinds of PAs. In a normal relaxation technique the calculation of the potential values in each grid point is performed several times (several iterations). At every iteration step potential changes that occurred in the previous iteration step start to propagate more and more through the PA. With increasing number of iterations the potential values at non-electrode grid points start to change less and less in between successive iteration steps and once the potential changes are below a certain threshold the iteration procedure is stopped. The over-relaxation method tries to speed up this calculation procedure by raising each individual potential correction by some factor  $f_{OR}$ . SIMION uses a dynamically self-adjusting procedure to adopt the used value of  $f_{OR}$  during the iterations, see again appendix H of [109] for more details about this and other speeding up calculation capabilities. The complete potential calculation procedure explained here before is referred to as **refining** in SIMION, during which the potential values on the electrode grid points are always kept constant.

As can be seen in figure 3.7b when curved electrode shapes are created their surface has very often a stepwise character related to the grid point system used. The finer the grid mesh of the PA is chosen the smoother the curved electrode surfaces get, but unfortunately as already mentioned before the amount of RAM occupied by the PA increases as well by this manner. Therefore, a compromise between the fineness of the used grid mesh and the occupied computational memory needs to be found. There are **different ways to insert electrode structures into the PAs**. First it is possible to create electrodes by using the **modify panel** where simple shapes as lines, boxes, circles, etc. can be used. The second option is the **use of geometry files** that can be written in any text editor and then converted into a PA.

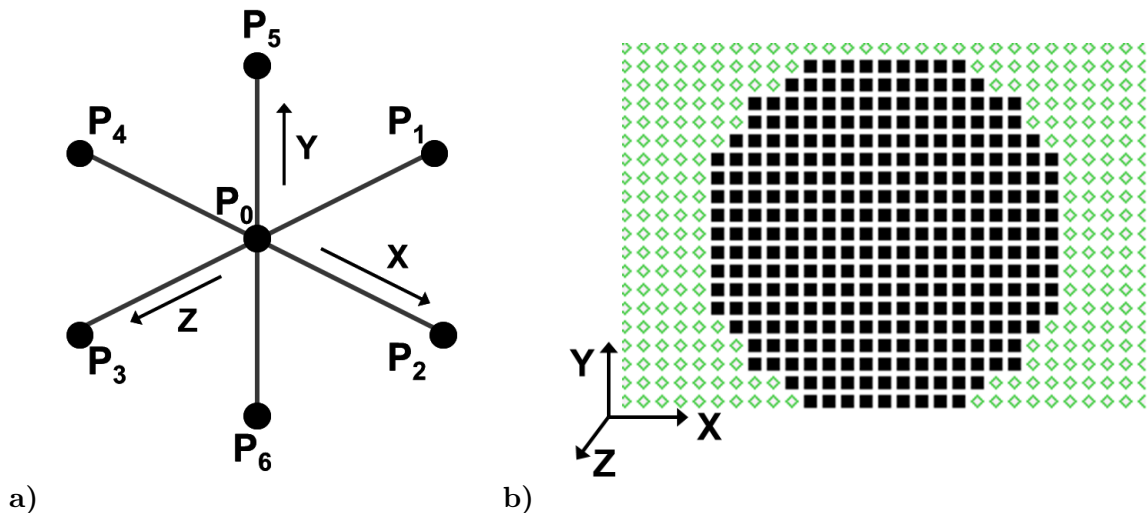


Figure 3.7: a) Illustration of nearest neighbour grid points of point  $P_0$ ;  
b) Illustration of circular electrode surface in 2D-PA.

The specific commands to construct such geometry files can again be found in a lot of detail in [109]. The third and last possibility is to use **STereoLithography-files (STL-files)** generated nowadays by most available computer-aided design (CAD) programmes. SIMION is able to convert these STL-files into PAs.

There are **two classes of PAs** that can be used. In the first class the potential values of the different electrodes need to be set before refining is done for the corresponding PA. In this way the relative potential ratios between the different electrodes are fixed right from the start and all electrode potentials can only be scaled proportionally after refining. This first class of PAs is called **basic potential arrays**. The second class offers a more flexible choice of the individual electrode potentials and is called **fast adjustable potential arrays**. For this kind SIMION makes use of the fact that any linear combination of several solutions of the Laplace equation (equation 3.6) is as well a solution. Therefore, the class of adjustable PAs allows to freely adjust the potential value of each electrode individually after the refining process has been done and no potential scaling between the different electrodes occurs compared to the case of basic PAs. Furthermore, changing potential values on electrodes during the runtime of a simulation can be done which is necessary if time varying potentials need to be considered [109, 110].

### Simulation interface

In order to perform a simulation the user needs to load any type of refined PA into the **SIMION workbench** which represents the actual simulation panel. By using the defined potential distributions within the refined PAs SIMION is able to calculate the electrostatic forces that act on the charged particles and determines the related trajectories, more details can be found in [109]. To be able to perform a simulation the **charged particles need to be initialised** by defining different parameters, e. g. number of particles, charge, mass, initial positions/angles/energies, etc.. For parameters as positions, angles or energy several predefined distributions can be selected. If the user wants to use initial particles' conditions that cannot be generated with the available predefined distributions a **specialised user programme** can be chosen, within which the particles' initial conditions can be programmatically defined. SIMION allows the user to record different particles' parameters at different moments or planes during the simulation (e. g. at the start, when the particle hits an electrode or at a specific plane). If desired all this information can be saved to a file for post-data treatment.

### Ion gas collision simulation

A last feature that is mentioned here is the possibility to include within SIMION **ion-gas particle collisions**. The collision model which is also used during the simulations related to the ion source developments in section 4 and 5 is the predefined collision model HS1. This model follows the general **hard-sphere collision model** illustrated in figure 3.8. When two particle species A and B are involved the collision area can be expressed as  $\pi \cdot (r_A + r_B)^2$ . In the case where the collision occurs between ions and their corresponding neutral gas species it can be written that  $r_A = r_B$  so that the radius of the collision area can be taken as the corresponding gas species molecular diameter, defined by equation 3.21 in section 3.3.1. The corresponding mean free path used within the HS1 model can be expressed by the related equation 3.20. The ion-gas particle collisions are considered to be elastic and no charge is attributed to the background gas.



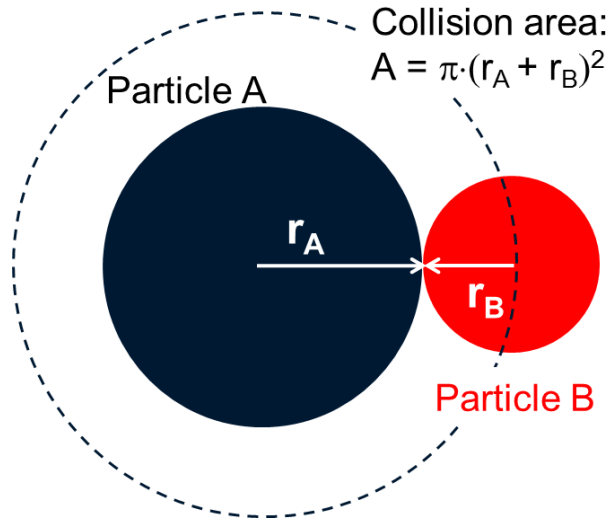


Figure 3.8: Illustration of the hard sphere collision of gas species A and B.

It is possible to define within a PA different regions of uniform gas pressure via the aforementioned user programme. If desired a very detailed pressure distribution can as well be considered and overlaid with the PA during the simulation. Furthermore, the mean velocity of the background gas can be set to be non-zero if desired. By using the HS1 collision model it is possible to simulate with SIMION the effect of collisional heating/cooling. The background gas particle speeds follow the temperature dependent Maxwell-Boltzmann distribution stated in equation 3.22 of section 3.3.1. Important parameters that need to be set for the background gas are its temperature and the gas particle mass [110].

## 3.2 Radio frequency ion guiding and funnelling structures

### General aspects

It is well known that by using specialised electrode structures it is possible to guide/funnel ions in high pressure regions. The so called **ion guides** most often consist of several stacked ring electrodes to surround a cylindrical volume in which the ions can travel. These adjacent ring electrodes can have an identical or progressively decreasing inner diameter to funnel the ion beam towards an extraction aperture for example, see figure 3.9a. By applying **DC-potential gradients** to the ring electrodes it is possible to guide the ions in a specific direction and by superimposing **radio frequency (RF) varying potentials** to prevent the ions of hitting the rings. The simplest case for the RF-signal is to have adjacent rings at potentials that have the same amplitude/frequency but are 180° out of phase. Ion guides have been used for example in different mass spectrometry instruments for the enhancement of the total ion transmission through the devices. Detailed reports and further ion guides/funnels investigations can be found in [111], [112], [113], [114] and [115].

Another kind of RF-structures that are used to manipulate ions and compared to ion guides occupy far less space are **planar structures known as ion carpets**, see figure 3.9b. They consist of many concentric ring electrodes and have most often in their centre an opening. Here again adjacent ring electrodes are set to RF-signals identical in frequency/amplitude but 180° out of phase. In ion carpet applications an attracting DC-field is used to guide/push the ions towards the ion carpet surface where the RF-signals prevent them from hitting the electrodes.



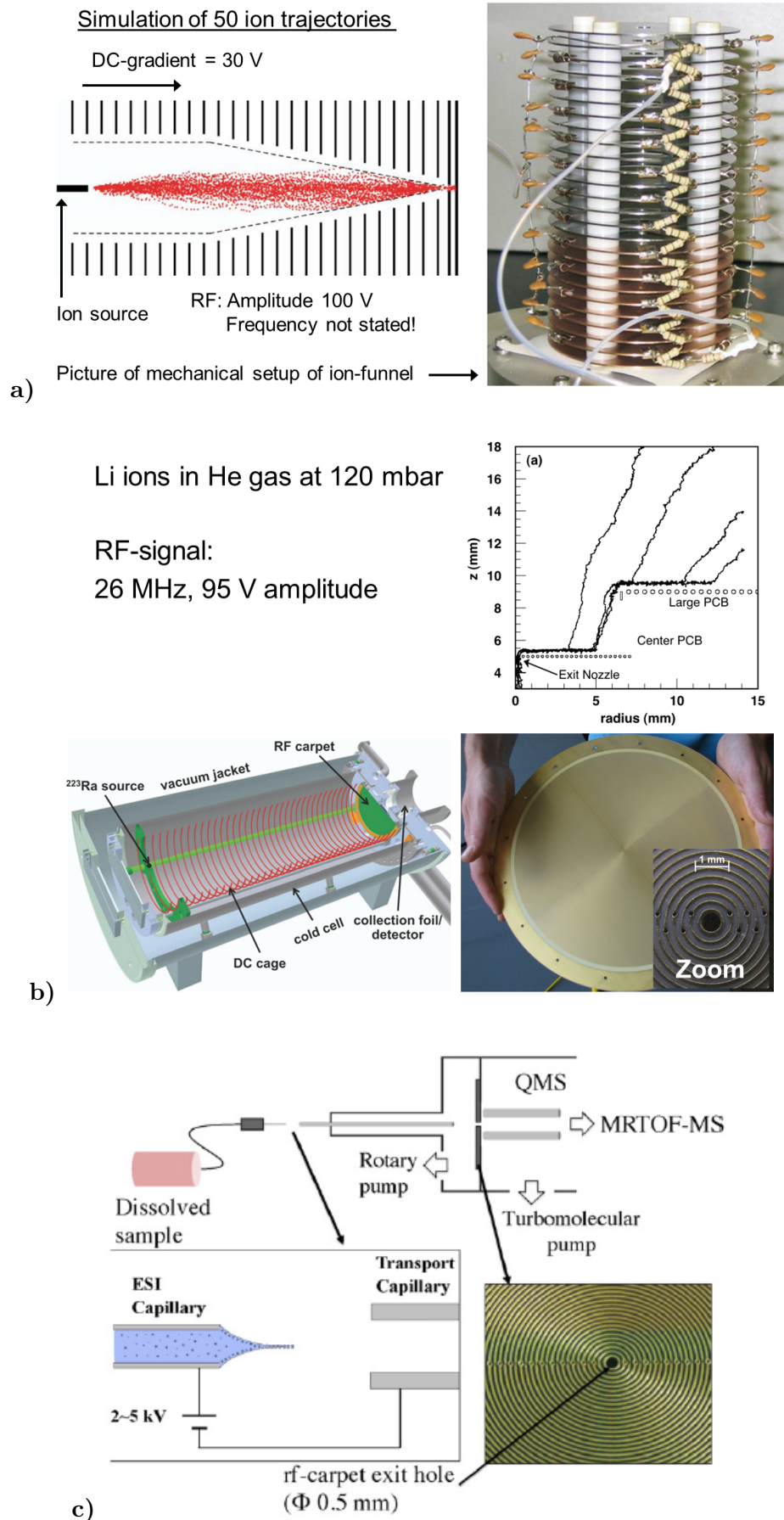


Figure 3.9: a) Schematic and picture of an ion guide/funnel (modified from [111]);  
 b) Ion carpets used in gas stopping cells (taken from: Top [116]; Bottom [117, 118]);  
 c) Ion carpet in an electrospray ion source for mass spectrometry (taken from [119]).

A DC-gradient applied from the outside to the inside (from bigger to smaller rings) creates a DC-field that pulls the ions towards the centre where they can be extracted through the central opening.

Most often these ion carpets are produced by the printed circuit board (PCB) technology as it allows to create inter-ring spacings in the sub-mm range. In figure 3.9b illustrations and pictures of ion carpets used within ion gas stopping cells are shown. In the top typical ion trajectories above such ion carpets are shown. They are pushed towards the carpet surface and hover above it at a certain distance while being pulled towards the centre. The trajectories in figure 3.9b correspond to Lithium ions in 120 mbar He gas with RF-signals of 26 MHz and a 95 V amplitude [116]. Another configuration that uses an ion carpet is described by [117] and [118] and is shown in the bottom of figure 3.9b. The ion carpet is positioned at the end of a cryogenically cooled stopping cell (a combination of an ion guide and carpet). The ion carpet has an outside diameter of 25 cm, 500 rings, 4 rings/mm (inter-ring distance 0.25 mm) and a central small hole of 0.57 mm (see the zoomed picture). In [118] the authors report about the extraction of radon ( $^{219}\text{Rn}$ ) ions when the stopping cell is filled with He gas up to 125 mbar. They applied 5.8 MHz RF-signals with amplitudes up to 40 V. Sharp rising total extraction efficiencies with increasing RF-amplitude followed by plateaus of the curves in the range of 7 to 18 % depending on the applied gas pressure have been measured.

A last application of an ion carpet that will be highlighted here is the use within an electrospray ion source connected to a quadrupole mass separator (QMS) followed by a multi reflection time-of-flight mass spectrometer (MRTOF-MS) described in [119], see figure 3.9c. This carpet has 54 ring electrodes with a width and inter-ring distance of 0.15 mm, the central hole diameter is 0.5 mm. The authors analysed the transport efficiency over a large mass over charge ratio range, while the pressure close to the carpet is in the few mbar range. A conclusion that is drawn is that peaks in the extraction curves appear at different sets of RF-frequency, amplitude and DC-gradients depending on the analysed ion species. Furthermore, for lighter ions the extraction efficiencies decrease when going towards lower frequencies and at a constant frequency the ions with a lower mass need higher RF-amplitudes to be efficiently extracted compared to lower amplitudes for heavier ions. In general what the experiments showed is that **the RF-frequency, amplitude and DC-gradients are critical parameters to obtain a stable ion motion and good extraction efficiency**. Applications with ion carpets where only DC-gradients have been applied can for example be found in [120] and [121].

### Ion motion stability evaluation

The **average repelling force** produced by an ion carpet can be expressed by [116, 118]:

$$F_{\text{rep}} = m_{\text{I}} \cdot \left( K_0 \frac{\rho_0}{\rho} \right)^2 \frac{V_{\text{Amp,RF}}^2}{(0.5 \cdot g)^3} \quad . \quad (3.16)$$

Where  $K_0$  is the reduced ion mobility,  $\rho_0$  the standard gas density,  $\rho$  the gas density and  $m_{\text{I}}$  the ion mass.  $V_{\text{Amp,RF}}$  is the RF-signal amplitude and  $g$  the gap between the ring electrodes. What can be deduced is that a small gap  $g$  between the ring electrodes should generate a strong average repelling force due to the inverse dependence on  $g^3$ . In [122] and [123] different parameters have been defined in order to evaluate if a **stable ion motion** is generated by an ion carpet.

These parameters can be expressed as follows:

$$\begin{aligned}
 Q_d &= \frac{q_n \cdot 8 \cdot V_{\text{Amp,RF}}}{m_I \cdot (2\pi f_{\text{RF}})^2 \cdot \zeta \cdot \Delta^2} \cdot \sin\left(\pi \frac{\zeta}{2}\right) \quad \text{with } \zeta = \frac{g}{\Delta} \\
 Q_{\text{pr}} &= \frac{q_n \cdot \pi \cdot F_{\text{push}}}{m_I \cdot (2\pi f_{\text{RF}})^2 \cdot \Delta} \\
 \kappa &= \frac{f_{\text{Damp}}}{2\pi f_{\text{RF}}} \quad \text{with } f_{\text{Damp}} = \frac{e}{m_I \cdot K} \quad \text{and } K = K_0 \cdot \frac{p_0 \cdot T}{p \cdot T_0} .
 \end{aligned} \tag{3.17}$$

The different quantities are defined as:  $q_n$  is the charge of the ion;  $f_{\text{RF}}$  the RF-signal frequency;  $\Delta$  is the pitch ( $g$  + ring electrode width);  $F_{\text{push}}$  the push field strength towards the ion carpet;  $f_{\text{Damp}}$  the damping factor related to the ion gas particles collisions;  $K$  the ion mobility;  $p$ ,  $T$  are the gas pressure and temperature whereas  $p_0 = 1013.25$  mbar,  $T_0 = 273.15$  K are the standard pressure and temperature [124]. A **stable and unstable region** can be defined in the parameter plot  $Q_d/\kappa$  vs  $Q_{\text{pr}}$  as can be seen in figure 3.10 (data points taken from [122]).

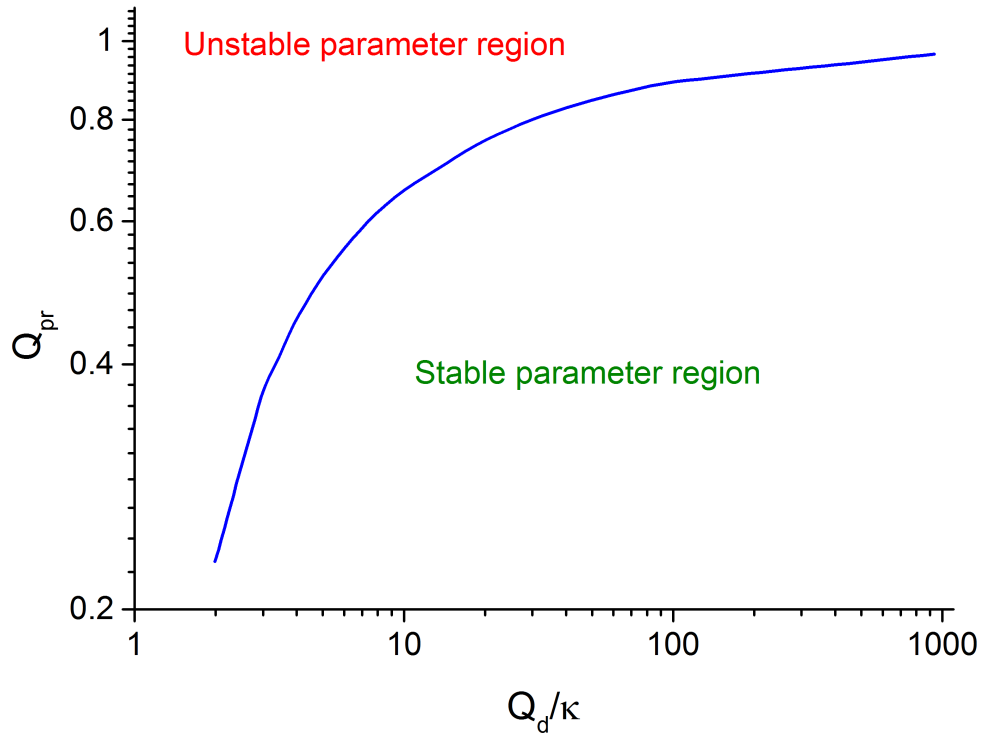


Figure 3.10: Illustration of the parameter plot  $Q_d/\kappa$  vs  $Q_{\text{pr}}$  (data points taken from [122]).

### 3.3 Vacuum technology and gas conductance simulations

#### 3.3.1 Theoretical concepts

##### General equations

In order to correctly evaluate the pressure distributions, gas fluxes, gas conductances, etc., within vacuum chambers and structures it is very important to determine the correct flow regime. An important parameter that indicates which flow regime is reigning within a certain region of a vacuum structure is the **Knudsen number**  $K_n$  defined as:

$$K_n = \frac{\lambda_{\text{free,gas}}}{d_{\text{characteristic}}} \quad . \quad (3.18)$$

In this equation  $\lambda_{\text{free,gas}}$  corresponds to the **mean free path** between two inter-particle collisions and the **characteristic length** of the vacuum structure is represented by  $d_{\text{characteristic}}$  (in a cylindrical pipe for example it is taken as the pipe diameter). The ranges for  $K_n$  which are used to identify the correct **flow regime** are defined as follows [125, 126]:

$$\begin{aligned} K_n > 0.5 &\Rightarrow \text{molecular flow regime} \\ 0.5 > K_n > 0.01 &\Rightarrow \text{transitional flow regime} \\ K_n < 0.01 &\Rightarrow \text{continuum or viscous flow regime} \end{aligned} \quad . \quad (3.19)$$

The **kinetic gas theory of Maxwell and Boltzmann** can be used to obtain a definition for  $\lambda_{\text{free}}$  and related parameters. When the pressure  $p$  and the temperature  $T$  of a gas is known  $\lambda_{\text{free,gas}}$  is defined as:

$$\lambda_{\text{free,gas}} = \frac{k_B \cdot T}{\sqrt{2} \cdot \pi \cdot d_m^2 \cdot p} \quad , \quad (3.20)$$

where  $k_B$  is the Boltzmann constant and  $d_m$  represents the corresponding **molecular diameter** of the gas species [125, 126, 127]. In a model where the gas particles (atoms or molecules) are considered as rigid elastic spheres,  $d_m$  can be calculated by using:

$$d_m = \sqrt{\frac{5}{16 \cdot \eta} \sqrt{\frac{k_B \cdot T \cdot m_{\text{Gas}}}{\pi}}} \quad , \quad (3.21)$$

where  $m_{\text{Gas}}$  represents the particle mass and  $\eta$  the dynamic viscosity of the corresponding gas species [126]. The **Maxwell-Boltzmann distribution** for the speeds  $v$  of the gas particles can be expressed by:

$$f_v = \frac{4}{\sqrt{\pi}} \left( \frac{m_{\text{Gas}}}{2 \cdot k_B \cdot T} \right)^{3/2} v^2 \exp \left[ \frac{-m_{\text{Gas}} \cdot v^2}{2 \cdot k_B \cdot T} \right] \quad . \quad (3.22)$$

An example of such a distribution is shown in figure 3.11 for the case of air ( $m = 28.96$  u) at  $T = 298.15$  K. The vertical lines in the figure represent the values of the **mean speed**  $v_{\text{mean}}$  and the **most probable speed**  $v_{\text{mp}}$  defined as [125, 126, 127]:

$$v_{\text{mean}} = \sqrt{\frac{8 \cdot k_B \cdot T}{\pi \cdot m_{\text{Gas}}}} \quad \text{and} \quad v_{\text{mp}} = \sqrt{\frac{2 \cdot k_B \cdot T}{m_{\text{Gas}}}} \quad . \quad (3.23)$$

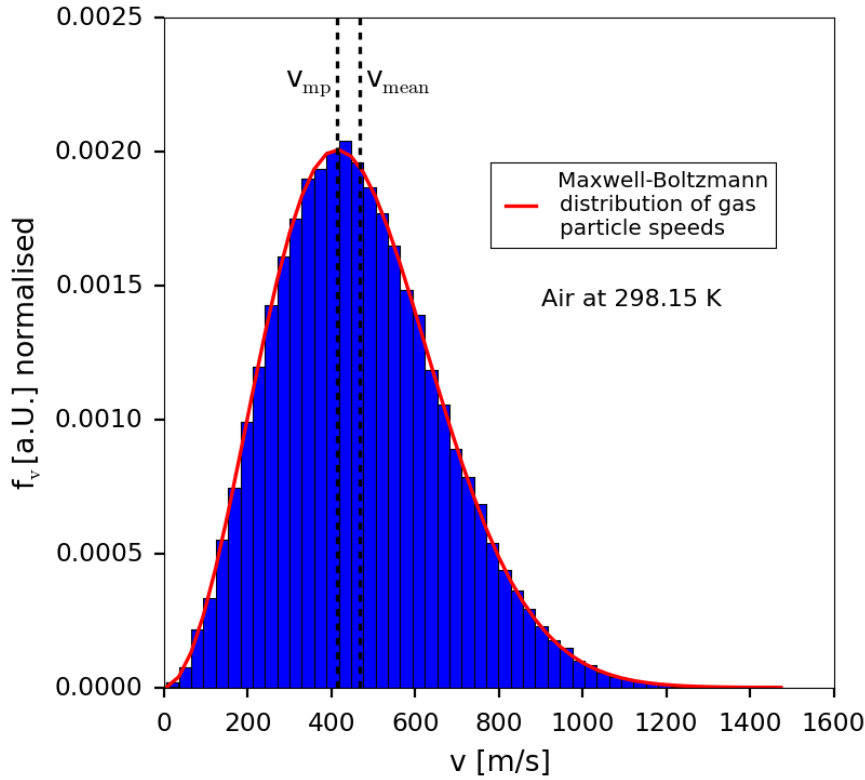


Figure 3.11: Maxwell-Boltzmann distribution of gas particle speeds (Air at  $T = 298.15$  K).

In close related to the speed distribution given by equation 3.22, the Maxwell-Boltzmann energy distribution is defined as:

$$f(E) = 2\sqrt{\frac{E}{\pi}} \left( \frac{1}{k_B T} \right)^{3/2} \exp\left(\frac{-E}{k_B T}\right) \quad . \quad (3.24)$$

Where  $E$  represents the kinetic energy of the gas particle and can be calculated with  $E = \frac{1}{2} m_{\text{Gas}} v^2$ . In the following the molecular flow regime conductance for different elements and related parameters will be discussed in more detail.

### Molecular flow regime

In general the **pV-flow**  $q_{pV}$  from one volume of a vacuum structure to another is defined as:

$$q_{pV} = C \cdot \Delta p = C \cdot (p_1 - p_2) \quad . \quad (3.25)$$

The conductance of the pipe element that connects the two volumes of the vacuum structure, within which the pressures  $p_1$  and  $p_2$  are reigning, is represented by  $C$ . In the case of the molecular flow regime and with the assumption that both volumes are at the same temperature  $T$  it is possible to write  $q_{pV}$  as follows [125, 126]:

$$q_{pV} = \frac{v_{\text{mean}}}{4} \cdot A_E \cdot P \cdot (p_1 - p_2) \quad . \quad (3.26)$$

Where  $P$  represents the **particle pass probability** through the pipe from volume 1 to volume 2 and  $A_E$  the pipe's entrance cross sectional area.

By comparing equation 3.25 with equation 3.26 it is possible to write the expression for the **conductance  $C_{\text{mol}}$  in the molecular flow regime** as:

$$C_{\text{mol}} = \frac{v_{\text{mean}}}{4} \cdot A_E \cdot P \quad (3.27)$$

The molecular flow conductance of an **arbitrary long straight cylindrical tube** can be calculated by [125]:

$$C_{\text{mol,arb,cyl-tube}} = \frac{\pi}{16} \cdot d^2 \cdot v_{\text{mean}} \frac{14+4\frac{l}{d}}{14+18\frac{l}{d}+3(\frac{l}{d})^2} \quad (3.28)$$

Where  $d$  represents the tube diameter and  $l$  is the tube length. For a **circular aperture** the molecular flow conductance can be determined by:

$$C_{\text{mol,cir-aperture}} = \frac{\pi}{16} \cdot d^2 \cdot v_{\text{mean}} \quad (3.29)$$

In the equations 3.28 and 3.29 the needed cross sectional area has been inserted as  $A_E = \pi \cdot \frac{d^2}{4}$ . Another kind of tube that should be mentioned here is a **cylindrical elbow tube with a bending angle of 90°**. The corresponding molecular flow particle pass probability  $P_{\text{mol,elbow90°}}$  can be found in [125] and be inserted into the following equation to obtain the corresponding molecular flow conductance:

$$C_{\text{mol,cyl-elbow90°}} = \frac{\pi}{16} \cdot d^2 \cdot v_{\text{mean}} \cdot P_{\text{mol,elbow90°}} \quad (3.30)$$

When the connection between two volumes of the vacuum structure is composed of several different elements (e. g. several apertures and/or different tube elements) it is mandatory to differentiate between a **series or parallel connection** and the corresponding total conductance can be calculated by:

$$\text{Parallel connection:} \quad C_{\text{Total}} = \sum_{i=1}^N C_i \quad (3.31)$$

$$\text{Series connection:} \quad C_{\text{Total}} = \left( \sum_{i=1}^N \frac{1}{C_i} \right)^{-1} \quad .$$

The individual conductances of the element 1 to  $N$  are represented by  $C_i$ . In the case of a series connection where the cross section of the different elements is varying it is necessary to use the more complex equation of [125]:

$$\frac{1}{C_{\text{Total}}} = \sum_{i=1}^N \left( \frac{1}{C_i} - \frac{4}{v_{\text{mean}} \cdot A_i} \right) + \left[ \frac{4}{v_{\text{mean}}} \sum_{i=1}^N \left( \frac{1}{A_{i+1}} - \frac{1}{A_i} \right) \delta_{i,i+1} \right] + \frac{4}{v_{\text{mean}} \cdot A_1} \quad (3.32)$$

For the parameter  $\delta_{i,i+1}$  in equation 3.32 the following definition is used with  $A_i$  being the individual element cross section areas:

$$\delta_{i,i+1} = 1, \quad \text{if } A_{i+1} < A_i \\ \delta_{i,i+1} = 0, \quad \text{if } A_{i+1} \geq A_i \quad (3.33)$$

In order to evaluate the gas flows present within a vacuum structure, as illustrated in figure 3.12, an individual **gas flow equation** can be written for each chamber of the system. In the stationary state the gas flow through the system is constant and for each chamber the total ingoing and outgoing pV-flows are equal. Therefore, in both cases of figure 3.12 the following equations can be established for the chambers 1 and 2:

$$\begin{aligned} \text{Chamber 1:} \quad q_{1in} &= q_{1out} \iff q_{1in} = (p_1 - p_2) \cdot C_{12} \\ \text{Chamber 2:} \quad q_{2in} &= q_{2out} \iff (p_1 - p_2) \cdot C_{12} = q_{2out} \end{aligned} \quad (3.34)$$

The pV-flow  $q_{1in}$  can for example represent the injection of a certain gas into the system. In general if the outgoing pV-flow is due to a vacuum pump with **pumping speed S** immediately connected to corresponding chamber (see figure 3.12a) it can be written that [125, 126]:

$$q_{i,out} = p_i \cdot S \quad (3.35)$$

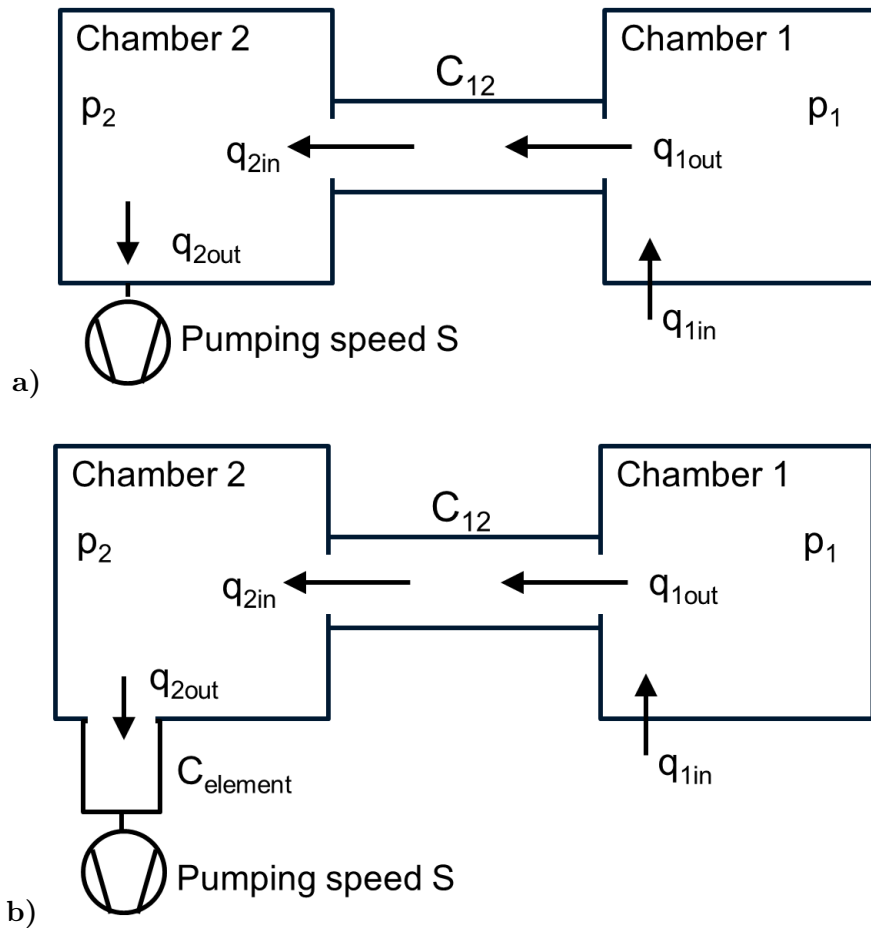


Figure 3.12: Illustration of pV-flows within a connected two chamber system:

- a) Vacuum pump immediately connected to chamber 2;
- b) Vacuum pump indirectly connected to chamber 2 by an intermediate tube.

In contrary to that if a certain element with the conductance  $C_{\text{element}}$  is inserted in between the vacuum pump and the corresponding chamber of the system (see figure 3.12b), it is necessary to take into account the **effective pumping speed**  $S_{\text{eff}}$  that will be present at the exit of the chamber.  $S_{\text{eff}}$  can be determined by [125, 126]:

$$S_{\text{eff}} = \frac{S}{1 + \frac{S}{C_{\text{element}}}} \quad . \quad (3.36)$$

In this case  $S_{\text{eff}}$  needs to be inserted into equation 3.35 in order to determine the corresponding  $q_{i,\text{out}}$ . When the pumping speeds, effective pumping speeds, conductances as well as certain pressures are known for a given system it is possible to rearrange the established pV-flow equations to determine the remaining unknown pressures. In more complex vacuum structures it is more difficult to establish the pV-flow equations and expressions for the different chamber pressures.

### Transitional flow regime

When injecting gas into a system it is possible that at a certain state of pressure distribution the Knudsen numbers within some regions of the vacuum system start to approach the transitional flow regime, as defined by equation 3.19. In such a case the used conductances for the corresponding elements need to be corrected towards the transitional flow regime and cannot any more be taken as molecular flow conductances. More details about different transitional flow regime conductances can be found in [125, 126].

#### **3.3.2 Simulation software Molflow+**

Molflow+ is a computer software with which the molecular flow of gas particles within a vacuum structure can be simulated. It is based on **Monte Carlo (MC) simulations** and it has been developed from 1990 on at CERN (Conseil Européen pour la Recherche Nucléaire). The Molflow+ simulations presented within this manuscript have been done with the version 2.5.6 of the program. By the use of the software the user has the possibility to generate pressure distribution profiles, to obtain knowledge about reigning effective pumping speeds, to evaluate adsorption phenomena, etc., within the simulated vacuum structure. This section is meant to be a summary about different capabilities and for a more detailed description of the complete software capabilities please refer to [128, 129].

### Geometries within Molflow+

**Predefined elements** as for example simple tubes with a certain length to radius ratio (L/R-ratio) can be loaded into the software. Every element that is inserted consists of several facets and those facets again of several vertices. Individual facets as well as complete elements can be moved, scaled, mirrored or rotated within the software. When a structure is set up of several elements it is possible to link those to each other or align individual facets of two different elements to each other. Very often the user's intention is to simulate more complex geometrical vacuum structures and Molflow+ gives the possibility to **import** those by the use of **STereoLithography-files** (STL-files). Nowadays most available computer-aided design (CAD) software allows it to export a developed mechanical structure as an STL file.



### Calculation of pressure

Before a simulation can be started different simulation parameters need to be defined which is explained in more detail in appendix A (section 7.1). Within a MC-simulation only a limited number of “virtual” gas particles can be simulated and traced by the computer. It is therefore mandatory to perform the conversion between the MC-”virtual” particle density and the real particle density. Within the MC-simulations of Molflow+ the **pressure on a surface element** is calculated by [128]:

$$p = 4 \cdot Q_{\text{outgassing}} \cdot \frac{N_{\text{Hits,S}}}{N_{\text{MC}}} \cdot \frac{1}{A_S \cdot v_{\text{mean}}} = 4 \cdot Q_{\text{outgassing}} \cdot \frac{N_{\text{Hits,S}}}{N_{\text{MC}}} \cdot \frac{1}{A_S \sqrt{\frac{8\bar{R}T}{\pi M}}} \quad (3.37)$$

$p$  is the pressure in Pa,  $Q_{\text{outgassing}}$  the total out-gassing of the simulated system,  $A_S$  is the corresponding surface element area,  $N_{\text{Hits,S}}$  represents the total number of hits that have been recorded on that surface element,  $N_{\text{MC}}$  corresponds to the total number of MC-particles used for the simulation. As defined by equation 3.23  $v_{\text{mean}}$  is the mean speed of the gas particles in m/s and by using  $k_B/m_{\text{Gas}} = \bar{R}/M$ , where  $\bar{R}$  is the universal gas constant, it can be deduced that  $v_{\text{mean}} = \sqrt{\frac{8\bar{R}T}{\pi M}}$  [125].

## 3.4 Electron ranges and SREM simulation software

### Electron ranges

The pathways of electrons within matter are related to statistical collision processes. These processes can be due to elastic or inelastic collisions of the incident electrons with the atomic electrons of the penetrated matter as well as to Bremsstrahlung effects that are related to the interaction of the incident electrons with the atomic nucleus of the penetrated matter. In applications such as nuclear physics, solid state physics, radiation technology or semiconductor detector fabrication it is of great importance to have knowledge about the distance that the incident electrons travel within the penetrated medium [130, 131]. Different ranges of the electrons can be determined. The **projected range** is the mean distance travelled by electrons in the incident beam direction [131], the mean electron path length within matter until they come to rest is often determined as **mean range** [131, 132]. Another range that is very often considered as a good measure for the penetration depth of electrons is the so called **extrapolated range  $R_{\text{Ex}}$**  determined by extrapolating the linear part of a **transmission curve** (number of transmitted electrons as function of matter thickness) to the abscissa [132, 133]. Theoretically, transmission curves can be obtained by MC-simulations which represent very often the best functional method [130, 134, 133]. Another approach is based on the Continuous Slowing Down Approximation (CSDA) method where the energy loss along the electron path is considered and a **stopping power**, defined as energy loss per unit path, can be determined [131, 135]. In many range investigations the treated energy range goes up to several MeV but in the case of ionisation chambers for example the interaction of low energy electrons (eV to a few keV range) with gases is of importance. An **empirical expression for  $R_{\text{Ex}}$**  has been established by Iskef et al. [132] for all media in the low energy range and is given by:

$$\begin{aligned}
R_{\text{Ex}} &= 2.37 \cdot 10^{-3} \cdot E \cdot \frac{A}{Z} \quad \text{when} \quad 20 \text{ eV} \leq E \leq 370 \text{ eV} \\
&\text{and} \\
R_{\text{Ex}} &= 1.294 \cdot 10^{-4} \cdot E^{1.492} \cdot \frac{A}{Z} \quad \text{when} \quad 370 \text{ eV} \leq E \leq 10^4 \text{ eV}
\end{aligned} \quad (3.38)$$

Here  $E$  is the incident electron energy in eV,  $Z$  the atomic number and  $A$  the mass number of the given medium.  $R_{\text{Ex}}$  is obtained in  $\mu\text{g}/\text{cm}^2$  and can be expressed as a range in cm by division of the medium density in  $\mu\text{g}/\text{cm}^3$ . For 100 eV electrons the values of  $R_{\text{Ex}}$  within different rare gases as well as oxygen and nitrogen at a gas pressure and temperature of  $p = 0.1$  mbar (10 Pa) and  $T = 298.15$  K are listed in table 3.2 and have been calculated by equation 3.38. The corresponding gas density is calculated for each gas species by:

$$\rho = \frac{M \cdot p}{R \cdot T} \quad (3.39)$$

The **related stopping power**  $P_{\text{Stop}}$  can be calculated by an empirical formula defined in [132] by:

$$P_{\text{Stop}} = \frac{E}{R_{\text{Ex}} \cdot (0.15546 \ln(E) + 0.31104)} \quad (3.40)$$

The stopping powers are obtained in  $\text{eV cm}^2/\mu\text{g}$  and can be transformed to values in  $\text{eV}/\text{cm}$  by multiplication with the corresponding gas density.

### SREM simulation software

**CASINO** is a Stopping and Range of Electrons in Matter (SREM) software designed as **single scattering MC simulation tool** for the interaction of low energy beams with matter [136, 137]. Different e-beam settings can be chosen as e. g. a mono- or multi-energy e-beam, the number of electrons, the beam radius or a tilted specimen surface if desired. A simulated sample can be composed of several layers and for each of these the chemical composition, the thickness and the density can be defined. During the performed MC simulation many different physical models can be selected for the used cross sections, ionisation potentials or stopping power calculation. All CASINO simulations that are presented within this manuscript used the selection of physical models that can be seen in figure 7.3 of appendix A (section 7.1).

General parameters				p [mbar]	T [K]	E [eV]
				0.1	298.15	100

Gas	A	Z	M [ $\frac{\text{g}}{\text{mol}}$ ]	$R_{\text{Ex}}$ [ $\frac{\mu\text{g}}{\text{cm}^2}$ ]	$\rho$ [ $\frac{\mu\text{g}}{\text{cm}^3}$ ]	$R_{\text{Ex}}$ [cm]	$P_{\text{Stop}}$ [ $\frac{\text{eV}}{\text{cm}}$ ]
He	4	2	4.003	0.47	$1.615 \cdot 10^{-2}$	29.36	3.32
Ne	20	10	20.180	0.47	$8.141 \cdot 10^{-2}$	5.82	16.72
Ar	40	18	39.948	0.53	$1.612 \cdot 10^{-1}$	3.27	29.79
Kr	84	36	83.798	0.55	$3.380 \cdot 10^{-1}$	1.64	59.52
Xe	131	54	131.290	0.58	$5.296 \cdot 10^{-1}$	1.09	89.70
O <sub>2</sub>	16	8	31.998	0.47	$1.291 \cdot 10^{-1}$	3.67	26.52
N <sub>2</sub>	14	7	28.014	0.47	$1.130 \cdot 10^{-1}$	4.19	23.22

Table 3.2: Extrapolated range values for 100 eV electrons within different gases (Calculations by using equations 3.38 and 3.40).

An example of displayed trajectories within CASINO can be seen in figure 3.13, where an e-beam of 100 eV with a diameter of 5 mm is entering at normal incidence a region of Argon gas. The corresponding density of Argon is calculated by using equation 3.39 with a temperature set to 298.15 K and a pressure of 0.1 mbar. Electron trajectories where the electron comes to rest within the gas region are shown in blue and backscattered trajectories in red. Identical electron stopping simulations have been done for the gases He, Ne, Kr, Xe, O<sub>2</sub> and N<sub>2</sub>. One result that can be extracted from such simulations is the **transmission probability curve**. Examples of transmission probability curves can be seen for Argon/Neon in figure 3.14a and the presented linear fits are used to determine the corresponding  $R_{Ex,Fit}$  values by:

$$R_{Ex,Fit} = X(Y = 0) = 10^{\frac{-Y_0}{a}} \quad . \quad (3.41)$$

Where  $a$  is the slope and  $Y_0$  the intercept of the corresponding fit having the expression of  $Y(X) = Y_0 + a \cdot \log(X)$ . The obtained  $R_{Ex,Fit}$  results in the different gases are shown in figure 3.14b together with the  $R_{Ex}$  results determined by equation 3.38 and listed in table 3.2. What can be seen is that there is good agreement. Furthermore, very similar trends of range reduction can be seen when going from light to heavier noble gases. For all gases, except Helium, the determined range is below 50 mm for the e-beam of 100 eV entering the gas region at 0.1 mbar. The here presented electron range concepts will be further used in section 5.

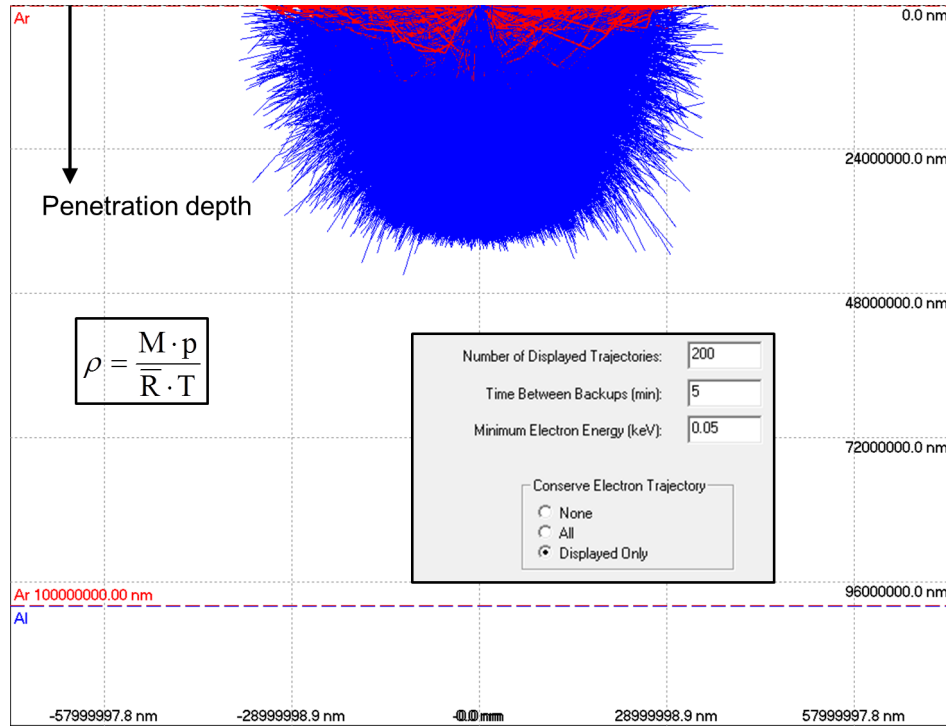


Figure 3.13: CASINO simulation: Incident e-beam 100 eV, 5 mm; Argon gas 298.15 K, 0.1 mbar.

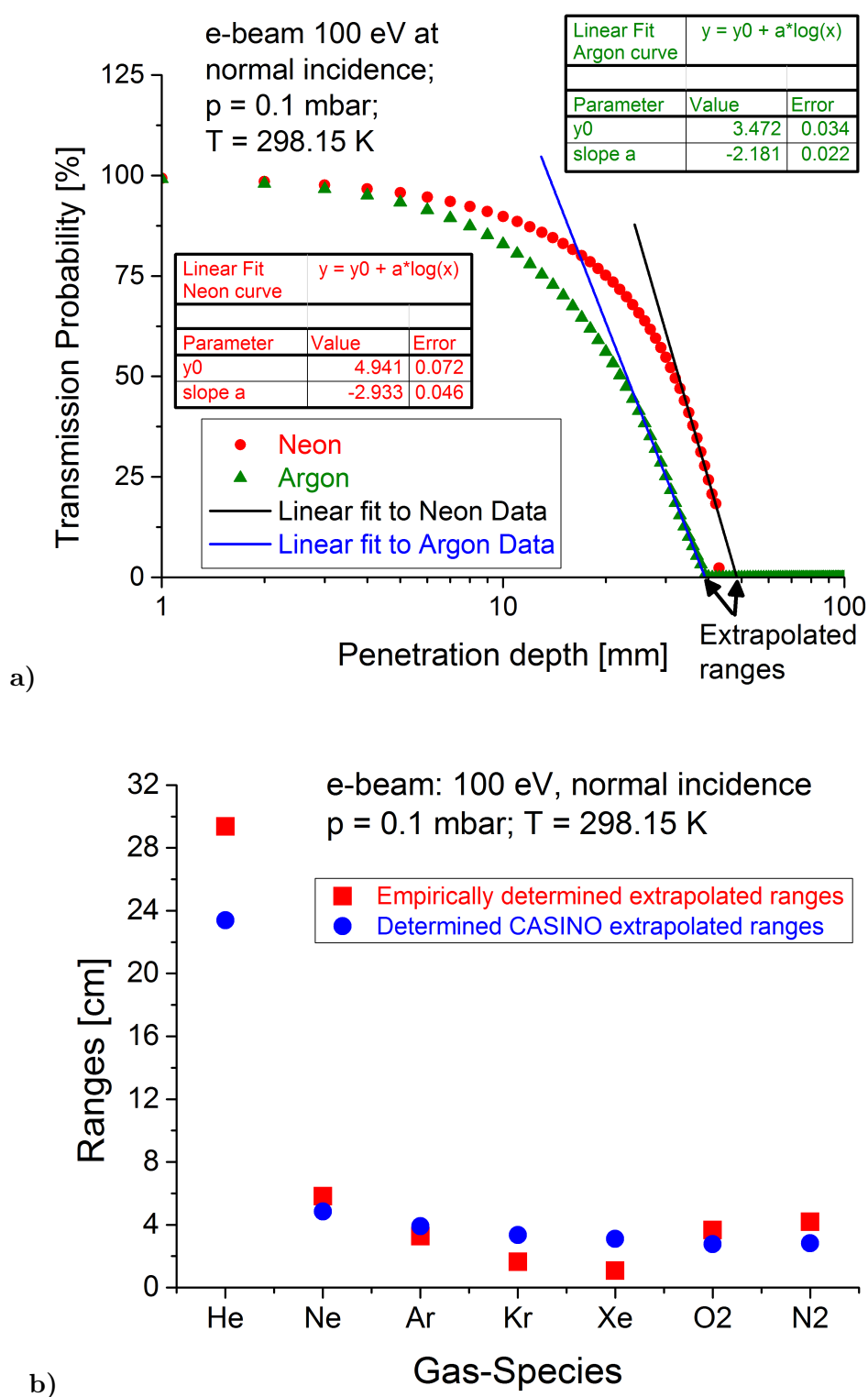


Figure 3.14: a) Examples of CASINO transmission probability curves and related linear fits;  
b) Extrapolated range values for a 100 eV electron beam within different kind of gases at 298.15 K and 0.1 mbar.

### 3.5 Summary and conclusions

- The theoretical concepts of charged particle optics have shown that by applying potentials to different electrode combinations as e. g. cylindrical lenses or deflectors it is possible to guide and focus beams of charged particles. In order to calculate the exact particle trajectories it is mandatory to know the electrical field/potential in every point of space. One method that can be used to determine the influence of optical elements on the particle trajectories is the transfer matrix multiplication method. The evaluation of complete CPO systems by this method represents quite often a very complicated task and therefore nowadays computer simulation programmes such as SIMION can be used to perform this task. The computation method and features of SIMION are explained in more detail in section 3.1.2. A good knowledge of how to use SIMION is mandatory in order to perform and evaluate correctly the simulations related to the ion source developments presented in section 4 and 5.
- Section 3.2 gives some background information about RF ion guides/funnels and carpets. These special electrode arrangements can be used to manipulate ion beams in higher pressure regions. They can for example be used to collect ions from a large ionisation volume and guide them towards a small aperture through which they can be extracted. Parameters for the evaluation of the ion motion stability above a RF ion carpet have been defined. A RF ion carpet is integrated in the ion source design of section 5.
- The ion source developments in section 4 and 5 are based on the electron impact ionisation mechanism, which means that gas injection into the ionisation region is needed. Therefore, it is as well mandatory to evaluate the gas conductance through the source system. The needed theoretical concepts to perform these evaluations are presented in section 3.3.1. Pressure distributions within the optical columns of the new ion source designs can be determined in this way. In close relation the molecular gas flow simulation software Molflow+ is presented in section 3.3.2 and can as well be used to get even more detailed knowledge about the achievable pressure distributions. Precise mechanical models of the optical columns can be incorporated into Molflow+.
- The theory of electron ranges, the related SREM simulation software, as well as performed range calculations within different gases are presented in section 3.4. This theoretical background is of importance for the ion source development described in section 5. The determined extrapolated ranges for a 100 eV electron beam within Ar, Ne, Kr, Xe, O<sub>2</sub> and N<sub>2</sub> gas at  $T = 298.15$  K and  $p = 0.1$  mbar are all below 5 cm. These range results are obtained by the use of empirical formulas as well as SREM simulations.

## 4 Miniature ionisation volume electron impact ion source

### 4.1 Ion source concept

A comparison between conventional EI ion sources, very often based on the design concept of Nier [37, 38, 104], and the here presented new ion source design concept can be seen in figure 4.1. As already mentioned in section 2.2.1 the conventional EI ion source type has large ionisation volume (IV) dimensions, see figure 4.1a, and low reduced brightness values ( $\approx 1 \text{ A m}^{-2} \text{ sr}^{-1} \text{ V}^{-1}$ ). Reducing the **IV-size to the micron scale** results in a considerably reduced virtual ion beam source size and when simultaneously keeping a quite large ionising e-beam current it is possible to increase the EI ion source brightness. In the here proposed design concept the e-beam will be extracted from a small emission area on the front tip of a thermionic emitter. The e-beam will then be guided by an electron column towards the ionisation region within which it will be focused to the  $\mu\text{m}$  range above an **ion extraction aperture having a diameter in the order of  $d_{\text{extr}} \leq 100 \mu\text{m}$**  (see figure 4.1b). The main components of the **ionisation region are two closely spaced parallel plates with a distance  $D_{\text{plates}}$  in the sub-millimetre range**. The ion beam is extracted in orthogonal direction with respect to the e-beam direction.

The **targeted reduced brightness  $B_r$**  of the intended ion source design is in the range of  $10^3 - 10^4 \text{ A m}^{-2} \text{ sr}^{-1} \text{ V}^{-1}$ . Which means that at typical FIB energies up to 50 keV the brightness  $B$  of the ion source is in the range of  $10^6 - 10^8 \text{ A m}^{-2} \text{ sr}^{-1}$ . Virtually any species that can be injected under gas form into the ionisation region can be ionised generating a **versatile choice in provided ion species**.

The **initial energy spread  $\Delta E$  of the ion beam** should be kept in the **low eV range** as this is favourable in order to minimize the broadening effect due to chromatic aberrations on the final achievable spot size in FIB applications. The achievable  $\Delta E$  is strongly related to the potential difference  $\Delta V_{\text{plates}}$  and the spacing  $D_{\text{plates}}$  of the two parallel plates. The part of the IV from which the ions will be extracted, effective IV, can be considered in a simple illustration as a small cylinder with diameter  $d_{\text{IV}}$  above the extraction aperture, see figure 4.2. The magnitude of the electrical field generated between the two parallel plates can be expressed as  $F_E = \frac{\Delta V_{\text{plates}}}{D_{\text{plates}}} = \frac{|V_{\text{Top}} - V_{\text{Bottom}}|}{D_{\text{plates}}}$  and positive generated ions are accelerated towards the bottom plate when  $V_{\text{Top}} > V_{\text{Bottom}}$ . The ions are generated on different equipotential surfaces across the ionisation volume and the energy at which they reach the bottom plate is defined by:

$$E_{\text{Li}} = q_{\text{Li}} \cdot \Delta V_i \quad , \quad (4.1)$$

and

$$\Delta V_i = V_i - V_{\text{Bottom}} = F_E \cdot Y_i = \frac{\Delta V_{\text{plates}}}{D_{\text{plates}}} \cdot Y_i \quad . \quad (4.2)$$

Where  $q_i$  is the charge of the ion and  $\Delta V_i$  is the potential difference between the equipotential on which the ion is created and the bottom plate. The energy difference between two ions of same charge  $q$  created within the ionisation volume at the furthest and closest Y-Position with respect to the bottom plate ( $Y_1$  and  $Y_2$  in figure 4.2) can be expressed by:

$$\Delta E = |E_{\text{L2}} - E_{\text{L1}}| = |q \cdot (\Delta V_2 - \Delta V_1)| \quad . \quad (4.3)$$

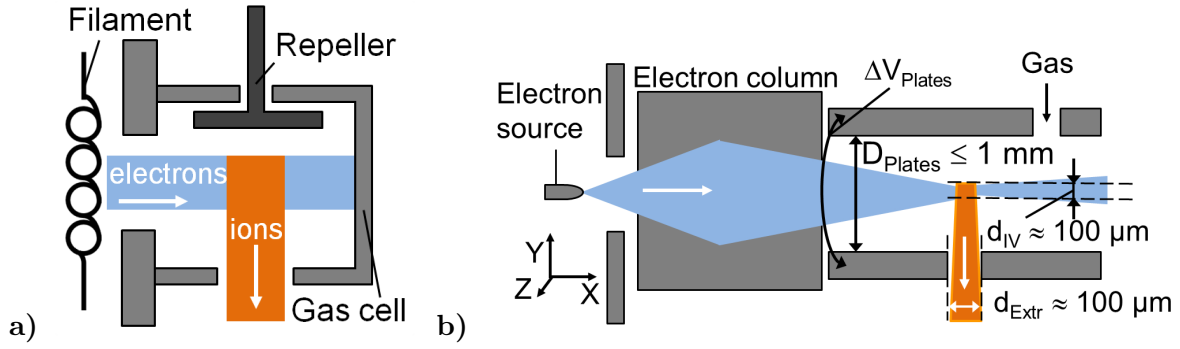


Figure 4.1: a) Schematic of a Nier type EI ion source with ionisation volume of cubic mm size; b) Schematic of the intended design for the new EI ion source with a micron scale ionisation volume size.

When inserting equation 4.2 into equation 4.3 the following is obtained:

$$\Delta E = q \cdot \frac{\Delta V_{\text{Plates}}}{D_{\text{Plates}}} \cdot |Y_2 - Y_1| = q \cdot \frac{\Delta V_{\text{Plates}}}{D_{\text{Plates}}} \cdot d_{\text{IV}} \quad (4.4)$$

By using equation 4.4 for singly charged ions ( $q = 1e$ ) generated within an ionisation volume of  $d_{\text{IV}} = 100 \text{ }\mu\text{m}$  and two parallel plates spaced by 1 mm having a potential difference of 10 V, the initial ion beam energy spread can be determined to be  $\Delta E = 1 \text{ eV}$ . Therefore, as conclusion ion beams with very low energy spreads can be obtained by the design concept presented here.

Moreover, the here evaluated design should have a **mechanical design as compact as possible** and the operation technology should be kept as simple as possible so that the ion source can be used as a handy add-on tool for existing instruments. In the following sections charged particle optics simulations, gas conductance simulations and experimental investigations will be presented in more detail for the **miniature IV EI ion source concept**.

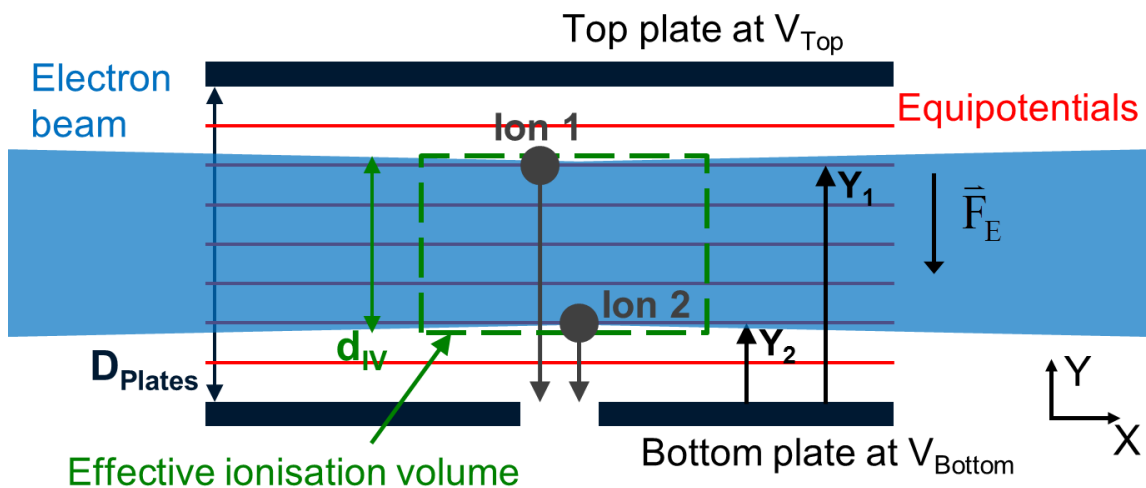


Figure 4.2: Illustration of the positive ion acceleration within the ionisation region when  $V_{\text{Top}} > V_{\text{Bottom}}$ .

## 4.2 Electron column CPO simulations and design

### 4.2.1 Filament and triode extraction setup

The first part of the CPO simulations presented in this section will treat the **evaluation of an electron column (e-Column)** using a thermionic emission cathode. As has already been seen in section 3.1.1 different kinds of electron emitters exist that can be used in small probe forming systems. To start the e-Column design the **emission of a tungsten hairpin filament** (in most cases V-shaped) is simulated. The filament shape that is implemented in the SIMION CPO simulations is very similar to the hairpin shown in the optical microscopy images in figure 4.3. In the simulations the filament is inserted into the triode potential array (PA) with  $\delta = 10^\circ$  and  $\beta = 0^\circ$  slightly differing from the  $13.5^\circ$  determined in figure 4.3. It is assumed that this angle  $\beta$  does not have a very strong influence on the emission of the electrons at the tip end of the filament. Furthermore, as a reason of simplification only the front region of the filament is included in the triode PA and not the complete filament, as can be seen in figure 4.5. The values for H and  $d_W$  are set as 0.6 mm and 1 mm, respectively. This gives a ratio of  $\frac{d_W}{H} = 1.6$  which lies within the range of 1 to 2 stated in [103] as common range for tungsten hairpin electron guns. The filament diameter is set to  $d_F = 125 \mu\text{m}$ .

The **initial energy distribution** of the generated electrons is implemented programmatically within a SIMION workbench user programme. At first the velocity components in x-, y- and z-direction are generated with a normal distribution:

$$f(v_i) = \frac{1}{\sigma\sqrt{2\pi}} \exp\left(\frac{-(v_i - \mu)^2}{2\sigma^2}\right) \quad ; \quad v_i \equiv v_x \text{ or } v_y \text{ or } v_z \quad , \quad (4.5)$$

having as mean value  $\mu = 0$  and as standard deviation  $\sigma = 1$ . These distributions are generated using the **Box-Muller method** explained in more detail in the appendix B (section 7.2) [138]. The generated values for the different velocity components are each then multiplied with  $\sqrt{\frac{k_B T}{m_e}}$  in order to obtain a **Maxwell-Boltzmann distribution** for  $v_x$ ,  $v_y$  and  $v_z$  with the correct standard deviation (T represents the filament temperature). At last, the corresponding kinetic energy is then calculated for each electron and adapted by adding the value of the work function  $\phi$  in order to account for the fact that only electrons having an energy above  $\phi$  can be emitted. T is set to 2700 K as typical operating T for tungsten hairpin filaments and  $\phi$  to 4.5 eV [40, 100].

In the SIMION workbench user programme not only the initial velocity (energy) but also the emission position of the electrons on the filament front tip is generated programmatically. The **filament front tip has the shape of a torus segment**. The surface points P on such a torus segment can be parametrised by using the following expression, see also figure 4.4a for an illustration:

$$\begin{pmatrix} X \\ Y \\ Z \end{pmatrix} = \vec{X}_1 + \vec{X}_2 = R \begin{pmatrix} \cos(\chi) \\ \sin(\chi) \\ 0 \end{pmatrix} + r \begin{pmatrix} \cos(\psi) \cos(\chi) \\ \cos(\psi) \sin(\chi) \\ \sin(\psi) \end{pmatrix} \quad . \quad (4.6)$$

Limits are set to the angles  $\chi$  and  $\psi$  so that the electron generation area  $A_{\text{Gen}}$  covers a certain region on the filament tip surface which is illustrated in figure 4.4b.



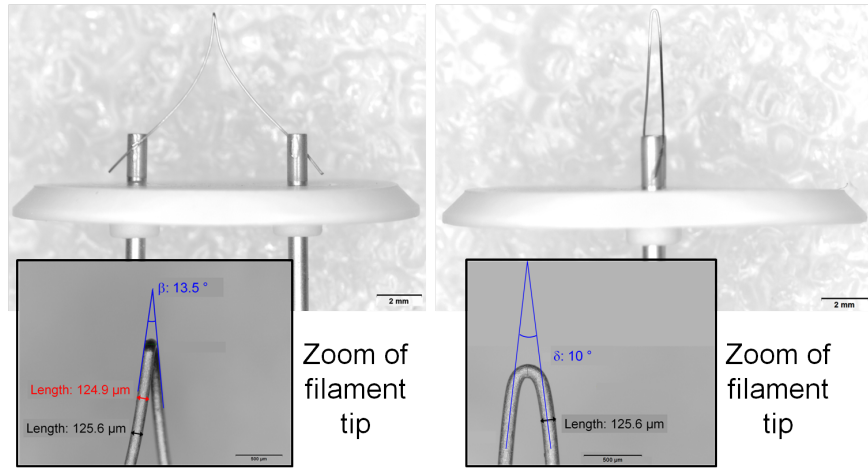


Figure 4.3: Optical images of a hairpin filament, front and side view with additional zoom images of the filament front tip region.

The values for the angles  $\chi$  and  $\psi$  are generated randomly in order to generate random starting positions for the electron emission simulation. A zoom on the filament region within the triode PA can be seen in figure 4.5b. The initial starting locations of the electrons can not be set in SIMION exactly on an electrode surface. The electrons are therefore launched from a torus surface that has a slightly bigger radius  $r$  than the actual modelled filament. This difference in radii can be easily set below 1  $\mu\text{m}$  within the simulations. In the close vicinity of electrodes the shapes of the equipotential surfaces are very similar to the physical electrode surfaces. The filament tip that is modelled within the triode PA has a quite stepwise character, as can be seen in figure 4.5b. This means that the electrons would not be generated on a smooth equipotential surface, which generates an artificial potential energy spread at the start of the simulation. To minimise this artificial effect the **filament electrode surface has to be modelled more precisely**. This could be realised by increasing the amount of grid units per mm (GU/mm) within the triode PA, which is set to a 3D-PA file. By increasing the GU/mm ratio of the triode PA the occupied physical memory increases strongly for the simulation.

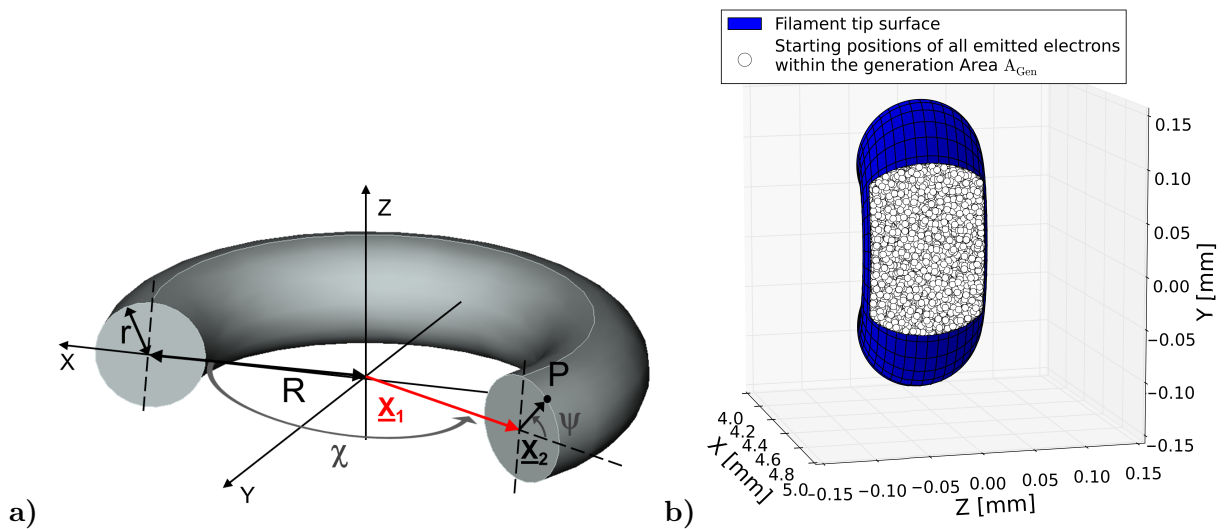


Figure 4.4: a) Schematic of a torus surface point parametrisation;  
b) 3D-Plot of the filament tip surface and the electron starting positions within the generation area  $A_{\text{Gen}}$ , here  $\chi_{\text{Lim}} = 60^\circ$  and  $\psi_{\text{Lim}} = 35^\circ$ .

As the complete workbench for the e-Column simulation incorporates several PAs (the exact

configuration of PAs will be discussed later in this section) a compromise has to be found for the amount of physical memory occupied by each PA-file. Unfortunately, it turned out that increasing the GU/mm ratio of the triode PA does not represent the appropriate option to take. In order to solve this problem of surface modelling precision a smaller and finer meshed 3D-PA-file for the filament tip region ( $2000 \text{ GU/mm} = 0.5 \text{ } \mu\text{m/GU}$ ) is overlapped with the coarser triode PA ( $80 \text{ GU/mm} = 12.5 \text{ } \mu\text{m/GU}$ ), see figure 4.5c. In the top image of figure 4.5c the lines named with VE 1, VE 2, VE 3 and VE 4 represent four of the six side walls of the small 3D filament tip PA. These side walls are one GU thick and represent virtual electrodes, which means that specific potential values can be attributed to the GU-points of these virtual electrodes but they are 100 % transparent for the e-beam. The matching of potentials between the bigger and smaller PA is done programmatically by a **boundary matching technique**, meaning that first the potentials within the triode PA are being calculated with SIMION. Subsequently, the potential values that are obtained within the coarser triode PA at the location of the boundary (side) walls of the finer filament tip PA are stored. Interpolation methods are then used to determine the potential values for each grid point of the boundary walls of the finer PA file. Only after setting the correct potential value to every point on the virtual side wall electrodes the potential distribution within the filament tip PA is being determined by SIMION. In the bottom image of figure 4.5c the shapes of the equipotential lines (in red) are identical in both PAs in front of the filament tip. For more details about the here mentioned boundary matching technique please consult the related paragraph in appendix B (section 7.2).

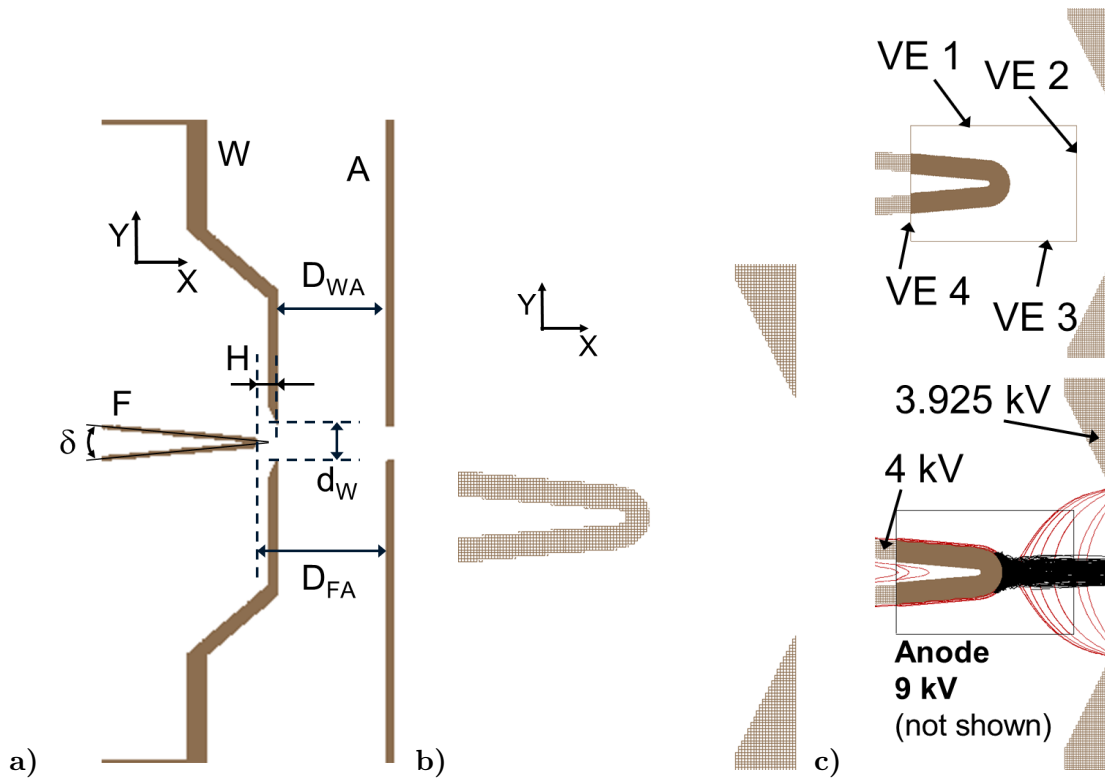


Figure 4.5: a) SIMION PA of the triode PA used in the e-Column CPO-simulations;  
 b) Zoom of the filament tip region within the triode PA;  
 c) Top: Triode PA (80 GU/mm) overlapped with filament tip PA (2000 GU/mm; VE 1, 2, 3 and 4 are side wall virtual electrodes); Bottom: Extraction of the e-beam, F: 4 kV, W: 3.925 kV, A: 9 kV (not shown). The equipotential lines are shown in red.

#### 4.2.2 Estimation of the extracted electron beam current

The initial positions of all extracted electrons are shown in figure 4.6a. In a good approximation the **extraction area**  $A_{\text{Extr}}$  can be represented as half of the surface area of an ellipsoid with the semi-axes  $a$ ,  $b$  and  $c$ , schematically shown in figure 4.6b. For a tungsten hairpin filament ( $\phi = 4.5$  eV) the thermionic current density at  $T = 2700$  K can be determined to  $J_{\text{thermionic}} = 3.5 \cdot 10^4 \frac{\text{A}}{\text{m}^2}$  with equation 2.4. In the e-Column simulations the distance between Wehnelt and Anode is chosen as  $D_{\text{WA}} = 3$  mm and the cathode height is set to  $H = 0.6$  mm which gives a value of  $D_{\text{FA}} = D_{\text{WA}} + H = 3.6$  mm. Furthermore, a filament-anode potential difference  $\Delta V_{\text{FA}}$  of 5 kV is set within the simulations which leads to a space-charge limited current density of  $J_{\text{LC}} = 6.4 \cdot 10^4 \frac{\text{A}}{\text{m}^2}$  calculated with equation 3.11. This value is clearly bigger than the afore determined value for  $J_{\text{thermionic}}$  so that the current density at the cathode is not limited by space charge effects and  $J_{\text{thermionic}}$  is used within the **estimation of the extracted e-beam current**  $I_{\text{e,Extr}}$ . The following equation is used for  $I_{\text{e,Extr}}$ :

$$I_{\text{e,Extr}} = A_{\text{Extr}} \cdot J_{\text{thermionic}} \cdot f_{\text{Extr}} = \frac{A_{\text{Surface-Ellipsoid}}}{2} \cdot J_{\text{thermionic}} \cdot f_{\text{Extr}} \quad , \quad (4.7)$$

where  $A_{\text{Surface-Ellipsoid}} = 4\pi \left( \frac{a^k b^k + a^k c^k + b^k c^k}{3} \right)^{1/k}$  and  $k \approx 1.6075$  [139].  $f_{\text{Extr}}$  represents an extraction factor due to the fact that more electrons are generated within the ellipsoidal area  $A_{\text{Extr}}$  than the total number of electrons actually extracted through the Wehnelt hole. Moreover, a value for  $\Delta V_{\text{Bias}}$  has to be set within the e-Column simulations. In [99] the optimum e-beam brightness for a setup having a  $\frac{dw}{H}$  ratio of 1.8 was obtained when the bias voltage was set to about 85 % of the cut-off bias. As  $\frac{dw}{H} = 1.8$  is very similar to the here simulated triode setup with  $\frac{dw}{H} = 1.6$ , a bias voltage  $\Delta V_{\text{Bias}}$  of - 75 V is chosen during the simulations, being close to 85 % of - 90 V which represents the here determined value for the cut-off bias. With  $\Delta V_{\text{Bias}} = - 75$  V,  $\frac{dw}{H} = 1.6$ ,  $D_{\text{WA}} = 3$  mm and  $\Delta V_{\text{FA}} = 5$  kV the extraction factor  $f_{\text{Extr}}$  in equation 4.7 has a value of about 13 % for all e-Column simulations presented in this section.

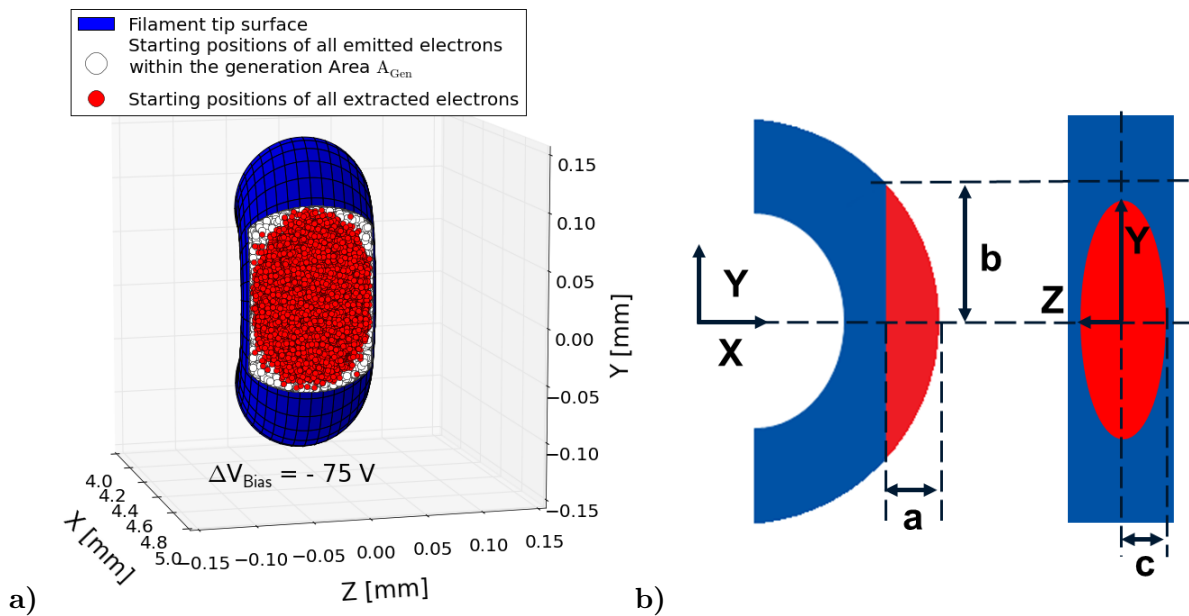


Figure 4.6: a) Initial starting positions of the extracted electrons on the filament tip surface ( $\Delta V_{\text{Bias}} = -75$  V,  $\frac{dw}{H} = 1.6$ ,  $D_{\text{WA}} = 3$  mm and  $\Delta V_{\text{FA}} = 5$  kV);  
b) Schematic of the ellipsoidal extraction area  $A_{\text{Extr}}$ .

The extraction area  $A_{\text{Extr}}$  is about  $1.9 \cdot 10^4 \mu\text{m}^2$  with  $a \approx 30 \mu\text{m}$ ,  $b \approx 80 \mu\text{m}$  and  $c \approx 55 \mu\text{m}$ . The e-beam current extracted through the Wehnelt is determined to  $I_{e,\text{Extr}} \approx 80 \mu\text{A}$ , which is comparable to the typical emission current of  $50 \mu\text{A}$  stated in [140] for tungsten hairpin filaments.

#### 4.2.3 Beam collimation

The **complete e-Column** consists of the **triode extraction region**, a **first beam collimating lens**, a **second lens to focus** the e-beam into the ionisation region, a **quadrupole deflector between both lenses** and the **ionisation region** itself. As already mentioned before, the e-Column SIMION workbench is composed of several overlapping PA-files. In figure 4.7 the optical system for example consists of three overlapping PA files. The two first PAs are the triode PA and the filament tip PA already shown in figure 4.5. The third one contains all electrodes from the filament until the electrode  $L_{2\text{Start}}$  and has a GU-ratio of 40 GU/mm (25  $\mu\text{m}$ /GU). The images shown in figure 4.7 represent XY-middle plane cut views of the e-Column setup. The electrodes W, A,  $L_{1\text{Mid}}$ ,  $L_{1\text{End}}$ , and  $L_{2\text{Start}}$  are cylindrical symmetric electrodes with respect to the X-axis. The filament F and the quadrupole deflector electrodes  $A_{\text{Defl.}}$  and  $B_{\text{Defl.}}$  have no cylindrical symmetry (only two of the four deflector elements can be seen in the XY-middle plane cut views).

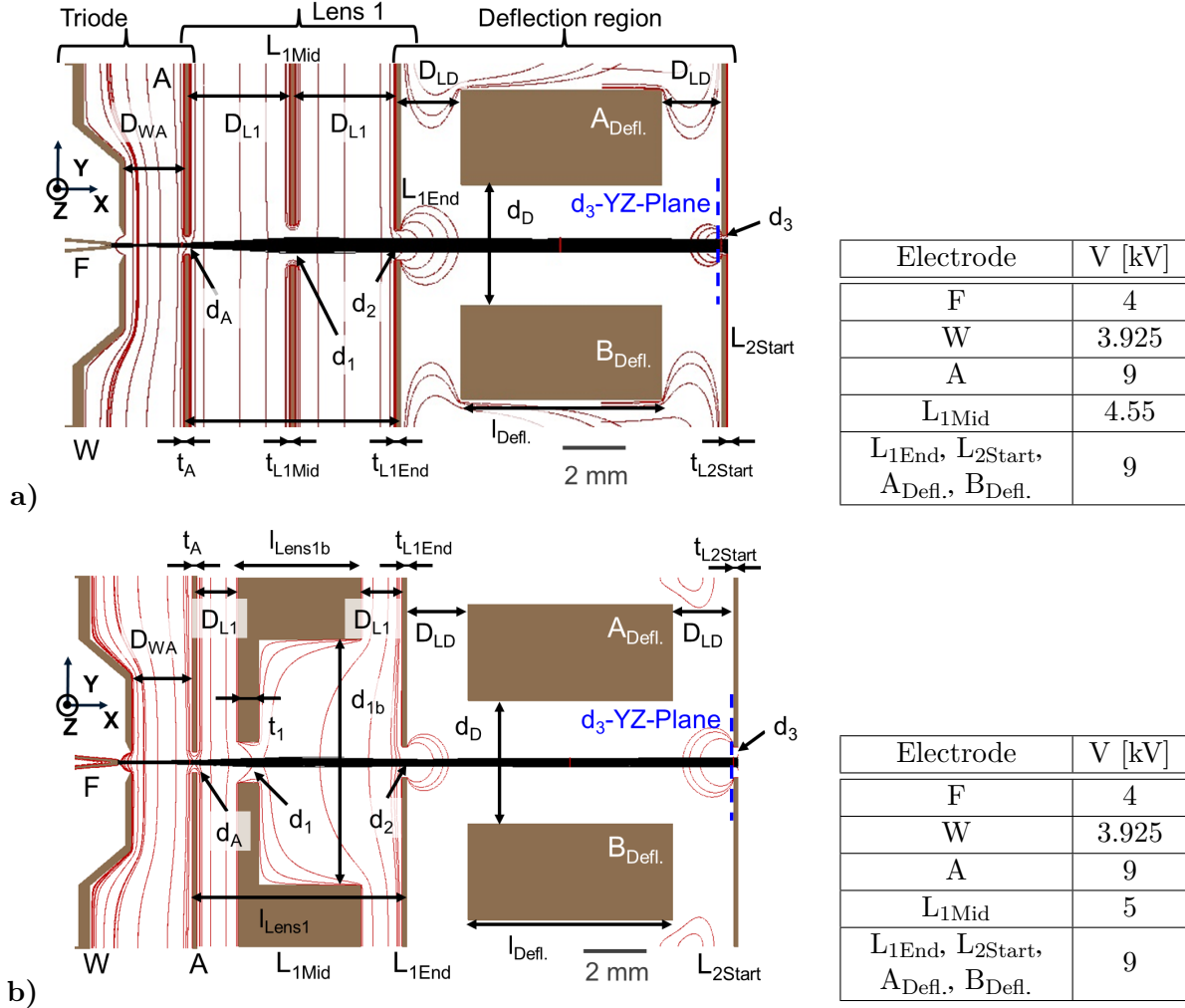


Figure 4.7: a) XY-middle plane cut view: Lens 1 as symmetric Einzel lens;

b) XY-middle plane cut view: Lens 1 as asymmetric Einzel lens.

For more detailed 2D and 3D figures of the individual PAs with all electrodes that they contain please consult the appendix B (section 7.2).

The first investigation that is performed here is the **comparison of the performance of two different lenses used for the collimation of the e-beam** that is extracted from the triode setup. In both cases the anode acts simultaneously as first lens element for the collimating lens (Lens 1), as can be seen in figure 4.7. The base potential of the quadrupole deflector ( $V_{\text{Defl,Base}}$ )<sup>9</sup> is kept at the same value as the potentials for the end electrode of Lens 1 ( $V_{\text{L1End}}$ ) and the start electrode of Lens 2 ( $V_{\text{L2Start}}$ ). The comparison of the collimation performance is done between a **symmetric Einzel lens** (figure 4.7a) and an **asymmetric Einzel lens** (figure 4.7b). In the paper of Riddle [98] many different three element Einzel lenses have been investigated in order to be used in combination with field-emission cathodes. The results of this paper show that an asymmetric three element Einzel lens similar to Lens 1 of figure 4.7b has very low spherical and chromatic aberration coefficients. The geometrical parameters of the asymmetric Einzel lens investigated here are similar to those used in the paper of Orloff and Swanson [107] which refer themselves to the paper of Riddle [98] for their choice of the lens electrode shapes, hole diameters and electrode distances. The exact geometrical values for the two optical systems compared in figure 4.7 can be found in table 4.1. What should be mentioned here as well is that a thick anode would tend to increase the spherical aberration coefficient of the lens [98]. Therefore the anode (element A) is chosen to be only 0.25 mm thick within the simulations presented here. The same thickness is used for other lens electrodes namely  $L_{1\text{Mid}}$ ,  $L_{1\text{End}}$  and  $L_{2\text{Start}}$ , which can be seen in figure 4.7.

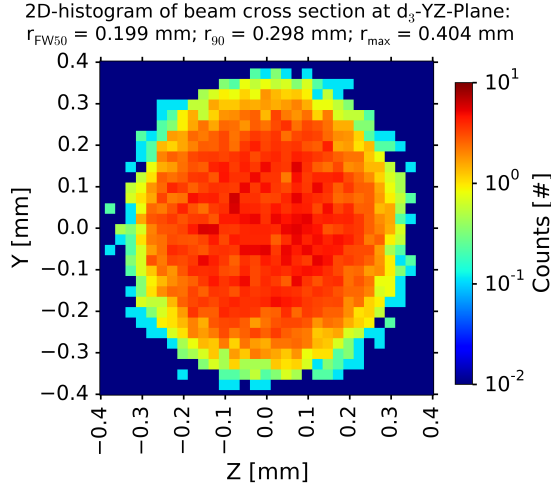
Two dimensional histograms of the e-beam YZ-cross sections that are obtained at the end of the quadrupole deflector region ( $d_3$ -YZ-Plane in figure 4.7) can be seen in figure 4.8 for the symmetric and asymmetric Lens 1 case. In both cases the Y- and Z-coordinates of each electron in the  $d_3$ -YZ-Plane are used to calculate a radius value by  $r_i = \sqrt{Y_i^2 + Z_i^2}$ . The circle that contains 90 % of all particles is defined by the radius  $r_{90}$  and the circle that contains 50 % of all particles is defined by  $r_{\text{FW50}}$ , where FW50 stands for Full Width 50. Beside  $r_{90}$  and  $r_{\text{FW50}}$  the maximum radius  $r_{\text{max}}$  is also shown in figure 4.8 but as it represents in most of the cases an outlier trajectory in the statistical distribution of the particle positions it is not very useful for the performance comparison of the two lens geometries. The different obtained radii values for each geometrical setup of Lens 1 can be found in table 4.2. What can be clearly seen is that for the asymmetric Lens 1 case the values of  $r_{90}$  and  $r_{\text{FW50}}$  are smaller than compared to the values of the symmetric case.

	Lens 1 sym.	Lens 1 asym.		Lens 1 sym.	Lens 1 asym.
$D_{\text{WA}}$	3	3	$d_{1b}$	/	12
$D_{\text{L1}}$	5	2	$d_2$	1.5	1.5
$D_{\text{LD}}$	3	3	$d_{\text{D}}$	6	6
$t_1$	/	1	$d_3$	1	1.5
$l_{\text{Lens1}}$	10.75	10.5	$t_{\text{A}}$	0.25	0.25
$l_{\text{Lens1b}}$	/	6	$t_{\text{L1Mid}}$	0.25	/
$l_{\text{Defl.}}$	10	10	$t_{\text{L1End}}$	0.25	0.25
$d_{\text{A}}$	1	1	$t_{\text{L2Start}}$	0.25	0.25
$d_1$	2	2	<b>All dimensions listed here are in mm!</b>		

Table 4.1: Geometrical parameters of the two optical systems presented in figure 4.7.

<sup>9</sup>In the case where a deflection is desired the deflector electrodes are set to:  $V_{\text{Defl,Base}} \pm \Delta V$ .

a) Symmetric Lens 1 case



b) Asymmetric Lens 1 case

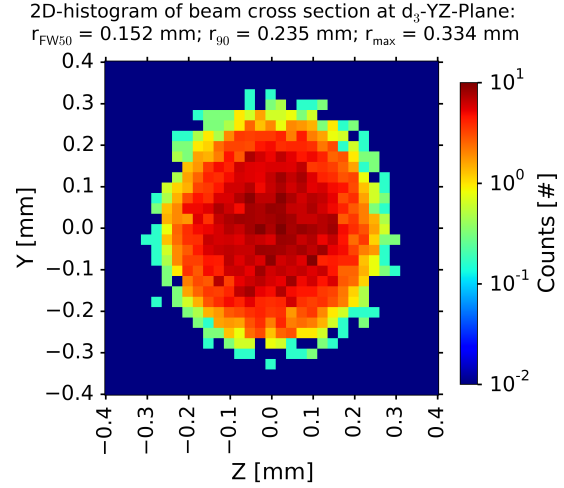


Figure 4.8: 2D-histogram of the e-beam cross section at  $d_3$  YZ-plane: a) Symmetric Lens 1 case; b) Asymmetric Lens 1 case.

	d <sub>3</sub> YZ-plane	
	Lens 1 sym.	Lens 1 asym.
$r_{max}$ [ $\mu$ m]	404	334
$r_{90}$ [ $\mu$ m]	298	235
$r_{FW50}$ [ $\mu$ m]	200	152

Table 4.2: Obtained statistical radii values for the e-beam at  $d_3$ -YZ-Plane.

A value below 200  $\mu$ m is obtained for  $r_{FW50}$  in the asymmetric Lens 1 case. It can be expected that an overall smaller e-beam size at the  $d_3$ -YZ-Plane will be focussed into an ionisation volume of a smaller diameter above the ion extraction aperture within the ionisation region. For this reason the **asymmetric Lens 1 is chosen as the first lens of the designed e-Column setup** and is used in the simulations presented in the following.

#### 4.2.4 Beam focalisation within the ionisation region

After that the extracted e-beam is collimated with Lens 1 a second lens needs to be used to focus the electrons within the ionisation region in between two closely spaced parallel plates. As can be seen in figure 4.9 also for this **second lens (Lens 2) a comparison between a symmetric and asymmetric shape** is done. A last PA-file is added to the e-Column SIMION workbench and it contains the deflector electrodes, the Lens 2 electrodes  $L_{2Start}$  and  $L_{2Mid}$  and all elements of the ionisation region ( $IR_1$ ,  $IR_2$ ,  $Extr_1$  and  $Extr_2$ ). The images in figure 4.9 represent again XY-middle plane cut views, this time of the complete simulated e-Column. The middle electrode of Lens 2 ( $L_{2Mid}$ ) has cylindrical symmetry with respect to the X-Axis. The element  $IR_1$  has a 3D box shape and its left side plane is parallel to  $L_{2Mid}$ . This left side plane is used as the third and last electrode of the second Einzel lens Lens 2. A 3D representation of the ionisation region PA can be found in the figure 4.10 which can help to make clearer its exact geometry. The electrodes  $Extr_1$  and  $Extr_2$  have a cylindrical symmetry with respect to the ionisation region Y-axis ( $Y_{Axis,IR}$ ) and represent electrodes of the ion extraction column that will be discussed in more detail at a later point of this section.

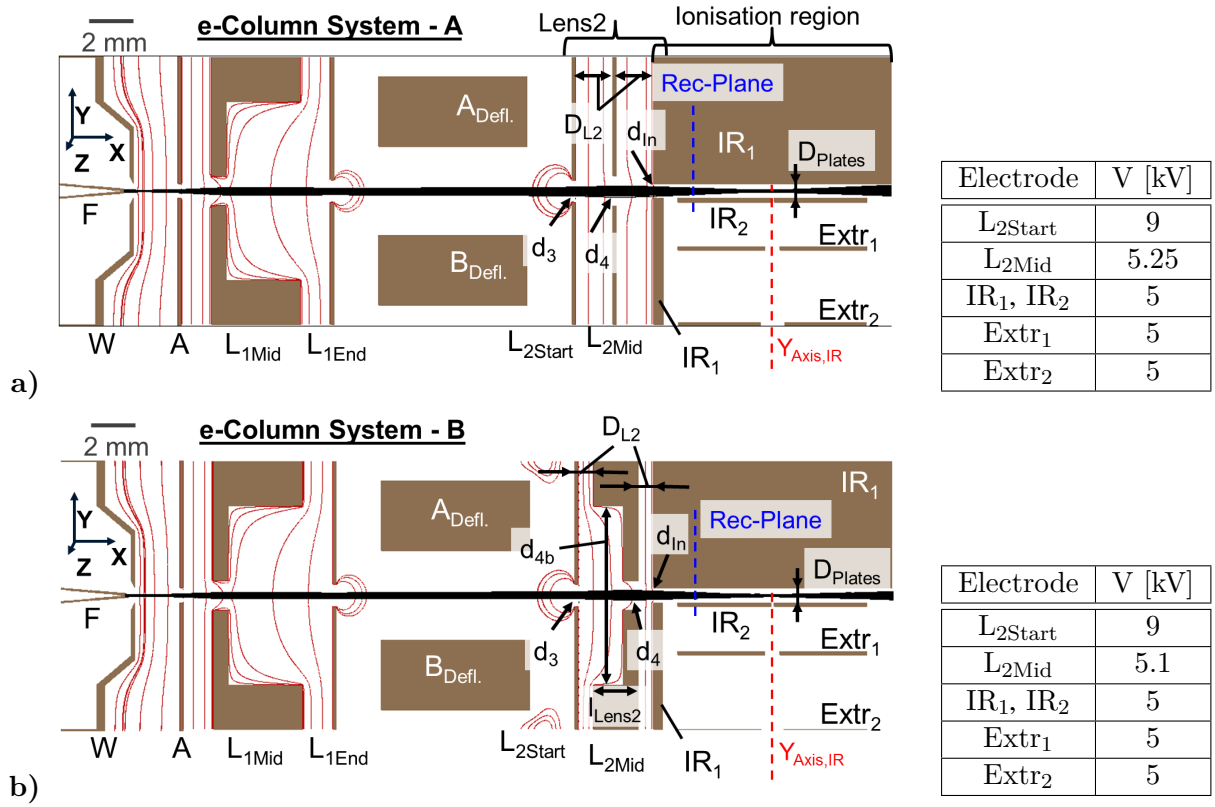


Figure 4.9: a) XY-middle plane cut view: Lens 2 as symmetric Einzel lens (For all potentials not listed here please see figure 4.7);  
b) XY-middle plane cut view: Lens 2 as asymmetric Einzel lens (For all potentials not listed here please see figure 4.7).

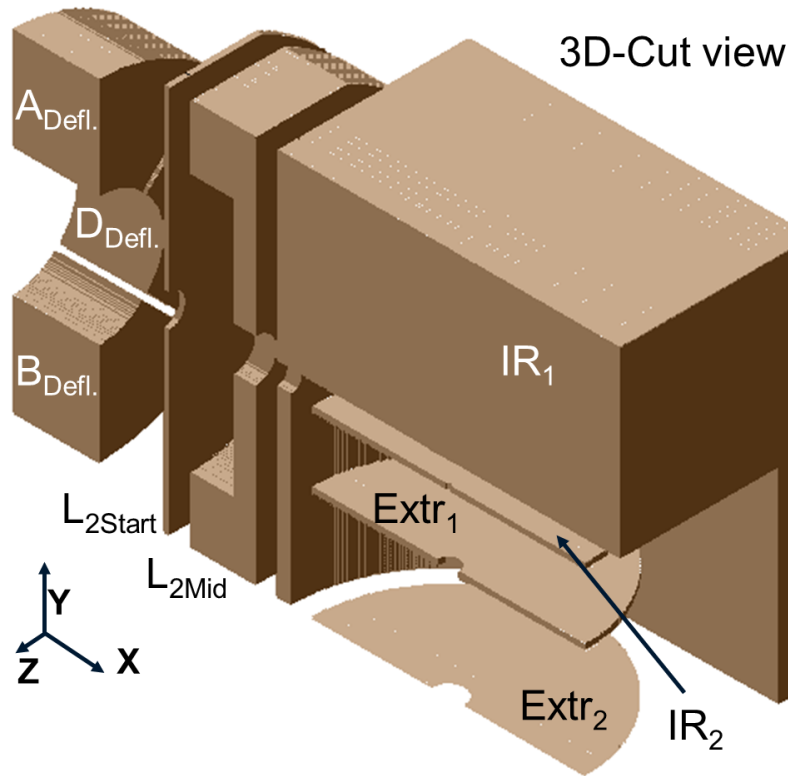


Figure 4.10: 3D-Cut view of the ionisation region PA used for the complete e-Column CPO simulations.



	Lens 2 sym.	Lens 2 asym.		Lens 2 sym.	Lens 2 asym.
$D_{L2}$	2.5	1	$d_{4b}$	/	12
$l_{Lens2}$	/	3	$d_{In}$	1	1
$d_3$	1.5	1.5	$D_{Plates}$	1	1
$d_4$	2	2	<b>All dimensions listed here are in mm!</b>		

Table 4.3: Additional geometrical parameters for the two optical systems presented in figure 4.9.

All additional geometrical parameters that are used for the complete e-Column CPO simulations (shown in figure 4.9) can be found in table 4.3. The remaining e-Column parameters are unchanged and can be found in table 4.1.

For the focussing evaluation of the e-beam all electrodes of the ionisation region ( $IR_1$ ,  $IR_2$ ,  $Extr_1$  and  $Extr_2$ ) are kept at a constant potential of 5 kV. The potential of the middle element of Lens 2  $V_{L2Mid}$  is the tuning voltage for the position of the e-beam focus within the ionisation region.  $V_{L2Mid}$  is tuned in order to find the minimal beam focus, defined as minimal FW50, at the centre of the ionisation region  $X_{IR,Mid}$  (X-position where the e-beam crosses  $Y_{Axis,IR}$ ), see figure 4.9. The potential difference between the ionisation region potential  $V_{IR1}$  and the filament potential  $V_F$  defines the end e-beam energy  $E_{e,End}$  which is simultaneously the energy at which the EI ionisation will take place within the gas cell. In figure 4.9 for example the e-beam has an  $E_{e,End}$  value of 1 keV in both cases.

In order to determine the e-beam size at  $X_{IR,Mid}$ , the electron velocities and YZ-positions at the recording plane (Rec-Plane) are stored. This Rec-Plane in the here presented simulations is situated within a field free region and an **electron trajectory extrapolation method** can be used to track the change of the e-beam size along the beam axis towards  $X_{IR,Mid}$ . In a field free region the electron trajectories can be represented as straight paths and in figure 4.11 an illustration is shown for a better understanding of this method. The new YZ-cross-plane in which the new particle coordinates ( $X_2$ ,  $Y_2$ ,  $Z_2$ ) need to be determined is at a distance of  $\Delta X$  from the Rec-Plane at which the particle has the starting coordinates ( $X_1$ ,  $Y_1$ ,  $Z_1$ ).

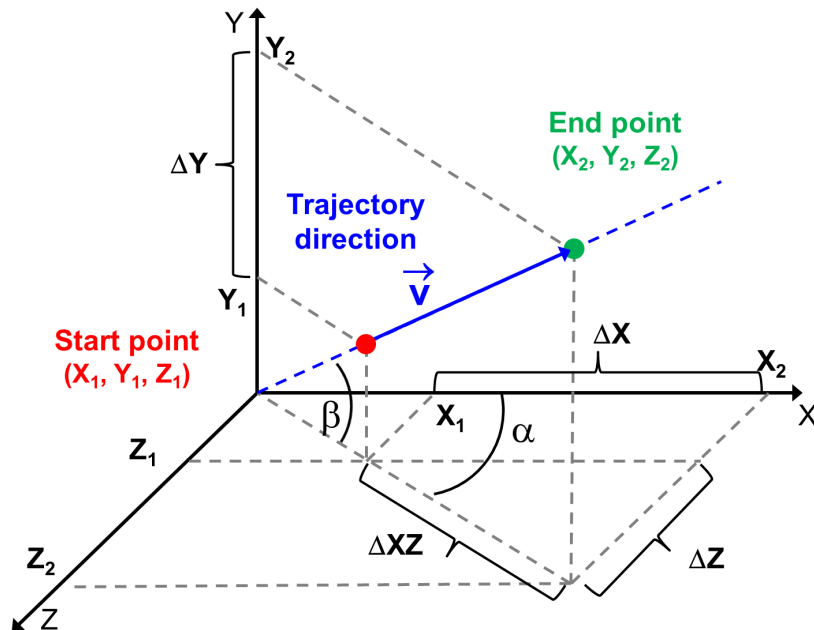


Figure 4.11: Illustration for the trajectory extrapolation in a field free region.



In the following the equations that are used to perform the trajectory extrapolation will be shown in detail. The new coordinates can be expressed as:

$$\begin{aligned} X_2 &= X_1 + \Delta X \\ Y_2 &= Y_1 + \Delta Y = Y_1 + \Delta X Z \cdot \tan(\beta) = \frac{\Delta X}{\cos(\alpha)} \cdot \tan(\beta) \\ Z_2 &= Z_1 + \Delta Z = Z_1 + \Delta X \cdot \tan(\alpha) \end{aligned} \quad (4.8)$$

As in the field free region the velocity of the particle is unchanged, equation 4.8 can also be expressed by using the different velocity components:

$$\begin{aligned} X_2 &= X_1 + \Delta X \\ Y_2 &= Y_1 + \Delta Y = Y_1 + \Delta X \cdot \frac{v_y}{v_x} \\ Z_2 &= Z_1 + \Delta Z = Z_1 + \Delta X \cdot \frac{v_z}{v_x} \end{aligned} \quad (4.9)$$

This trajectory extrapolation is done for many different YZ-cross-planes along the beam propagation towards the centre of the ionisation region by using for each cross-plane an individual value for  $\Delta X$  expressed by  $\Delta X_j = j \cdot dX$ , where  $dX$  represents a very small step size in X-direction (can be as small as 1  $\mu\text{m}$ ) and  $j$  starts at 1 and ends at  $N_{\text{Plane,End}}$ . In each individual YZ-cross-plane and for each particle the new determined coordinates  $(X_2, Y_2, Z_2)$  are used to calculate the corresponding radius value by  $r_{2i} = \sqrt{Z_{2i}^2 + Y_{2i}^2}$ . In this manner the change of the statistical beam sizes  $r_{\text{max}}$ ,  $r_{90}$  and  $r_{\text{FW50}}$  can be tracked along the e-beam axis. In figure 4.12 an example is shown for such a variation starting at the Rec-Plane and propagating towards the centre of the ionisation region in positive X-direction. The curves shown correspond to the simulation of e-Column System B shown in figure 4.9b with an end beam energy of  $E_{\text{e,End}} = 1 \text{ keV}$ . What can be seen is that the choice of the potential of the electrode  $L_{2\text{Mid}}$  is chosen so that the **minimal FW50 (the beam focus)** is found at the ionisation region centre. The curves for  $r_{90}$  and  $r_{\text{FW50}}$  show a smooth variation along the X-axis and for the  $r_{90}$  curve the minimum is as well located around the  $X_{\text{IR,Mid}}$  position. The 2D-histogram and the corresponding 1D-projections of the YZ-cross-plane at  $X_{\text{IR,Mid}}$  can be seen in figure 4.12b. It is clearly visible that the e-beam shows a 2D-Gaussian distribution behaviour at the position of the beam focus.

**The trajectory extrapolation and the beam focus determination are done for different electron end beam energies  $E_{\text{e,End}}$**  by varying the potential difference between the filament and the ionisation region. In order to obtain a collimated e-beam at the different  $E_{\text{e,End}}$  situations and then focus the beam at the ionisation region centre (at  $X_{\text{IR,Mid}}$ ) the potentials on the different e-Column electrodes have to be adjusted. All potential values used can be found in table 7.1 of appendix B (section 7.2). For every  $E_{\text{e,End}}$  simulation and for both e-Column Systems A and B the beam focus size  $d_{\text{Focus}}$  corresponding to the diameter of the minimal FW50 circle is determined. Furthermore, the FW50 ellipse is determined within the YZ-cross section at  $X_{\text{IR,Mid}}$  in order to compare its axes values  $w_{Z,\text{Focus}}$  and  $w_{Y,\text{Focus}}$  to the size of  $d_{\text{Focus}}$ . As the beam cross section profile has a distribution very similar to a 2D-Gaussian distribution, the start point for the procedure to find the FW50 ellipse uses two axis values defined by:

$$\begin{aligned} w_{Z,\text{FW50,Start}} &= 2 \cdot \sigma_Z \cdot \sqrt{K_{2\text{DGauss},50}} \\ w_{Y,\text{FW50,Start}} &= 2 \cdot \sigma_Y \cdot \sqrt{K_{2\text{DGauss},50}} \end{aligned} \quad , \quad (4.10)$$

where  $\sigma_Z$  and  $\sigma_Y$  represent the standard deviations in Z- and Y-direction.

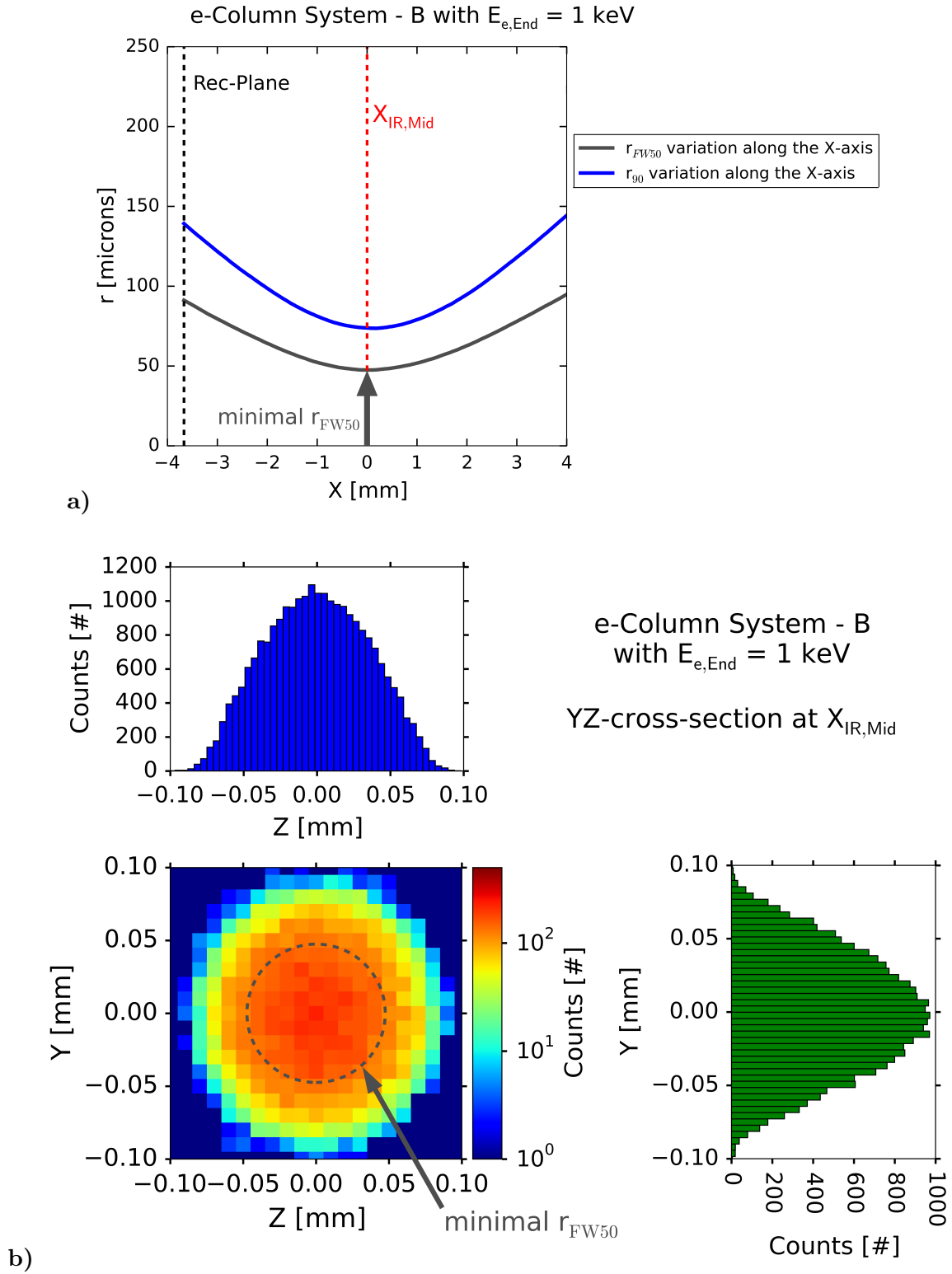


Figure 4.12: a) Statistical radii variations along the X-axis related to the simulation case shown in figure 4.9b;  
b) Corresponding 2D-histogram and 1D-projections of the YZ-cross-plane at the X-position of the e-beam focus (minimal  $r_{FW50}$  position).

$K_{2DGauss,50}$  is equal to 1.386 and when inserted into equation 4.10 it gives the axis sizes of the ellipse that contains 50% of all particles in the case of a perfect 2D-Gaussian distribution [141]. As the e-beam focus 2D-distribution does not correspond exactly to a 2D-Gaussian the axis values for the ellipse are varied step by step until it contains 50 % of the electrons. With this procedure the values for  $w_{Z,Focus}$  and  $w_{Y,Focus}$  are determined for each  $E_{e,End}$  case. During the

performed axis variation the axis size ratio  $f_{\text{ellipse,axis}}$  is kept constant so that:

$$f_{\text{ellipse,axis}} = \frac{W_{Z,\text{FW50,Start}}}{W_{Y,\text{FW50,Start}}} = \frac{W_{Z,\text{Focus}}}{W_{Y,\text{Focus}}} . \quad (4.11)$$

In figure 4.13 the **focus size** values are plotted in dependence of  $E_{e,\text{End}}$  for both e-Column Systems A and B. In both cases the size of  $d_{\text{Focus}}$  is **clearly decreasing with an increase in e-beam end energy  $E_{e,\text{End}}$** . The e-Column System B shows a slightly smaller beam focus than System A, but when going towards 1 keV for  $E_{e,\text{End}}$  the difference of both e-Column systems is below 2 % for the size of  $d_{\text{Focus}}$  being close to 95  $\mu\text{m}$ . As expected the results of the elliptical focus evaluation show axis size values in the same order of magnitude as the  $d_{\text{Focus}}$  results. Here again the sizes of the ellipse axes decrease with increasing  $E_{e,\text{End}}$  and are very similar for both e-Column systems when approaching 1 keV. In both systems the Z-axis is determined to be smaller than the Y-axis of the focus ellipse, which can be explained by the fact that the ellipsoidal surface emission area at the filament has a longer axis in Y-direction ( $b \approx 80 \mu\text{m}$ ) than in Z-direction ( $c \approx 55 \mu\text{m}$ ) within the simulation, see figure 4.6. When going from 1 keV towards 100 eV for  $E_{e,\text{End}}$  the EI cross section increases (e. g. for  $\text{Ar}^+$  by a factor  $\approx 3$  [45, 47], see also figure 4.14 for an illustration). This is beneficial for the generated ion current within the ionisation region as the ionisation efficiency increases when approaching 100 eV. On the other hand the e-beam focus size increases by about a factor of 2 when reducing  $E_{e,\text{End}}$  from 1 keV to 100 eV. This results in an increase of the ionisation volume size and therefore in a bigger ion beam source size  $d_{\text{IS}}$  having a decreasing effect on the ion beam brightness as indicated by equation 4.12. The increase in  $d_{\text{IS}}$  is expected to have a more deteriorating influence on the ion beam brightness ( $1/d_{\text{IS}}^2$  dependence) than the ameliorating influence related to the increase in ion beam current (linear dependence, equation 4.12). It is therefore assumed that the **e-beam focus results at  $E_{e,\text{End}} = 1 \text{ keV}$  represent a good compromise in terms of e-beam focus size and EI ionisation efficiency**. The results obtained here will be used in the following within the ion beam generation and brightness estimation simulations.

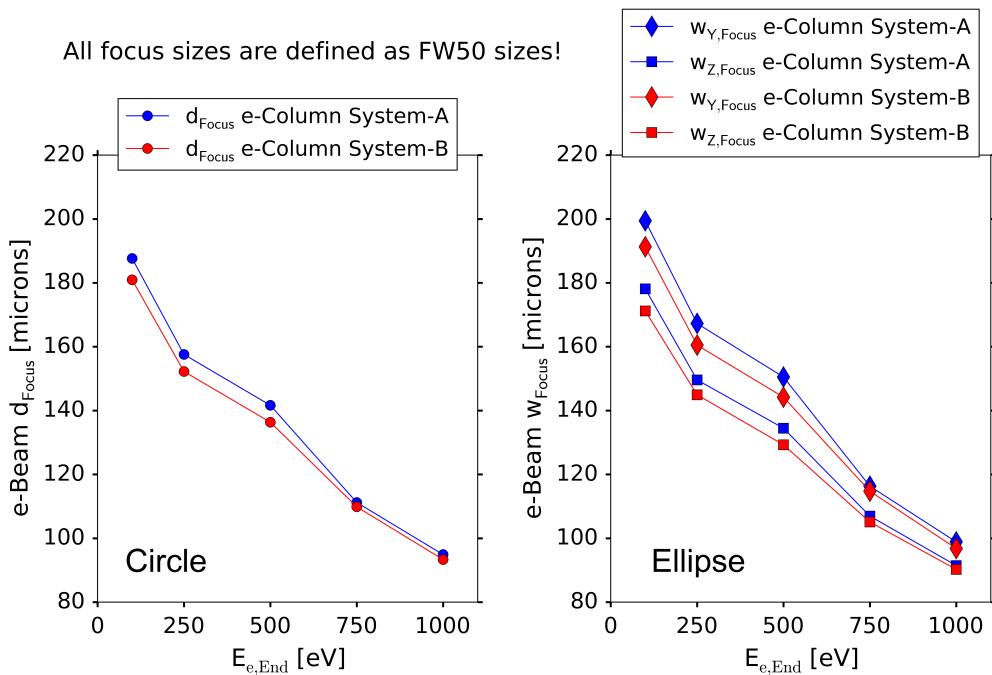


Figure 4.13: Focussing results for e-Column System A and B. FW50 circle and ellipse results.

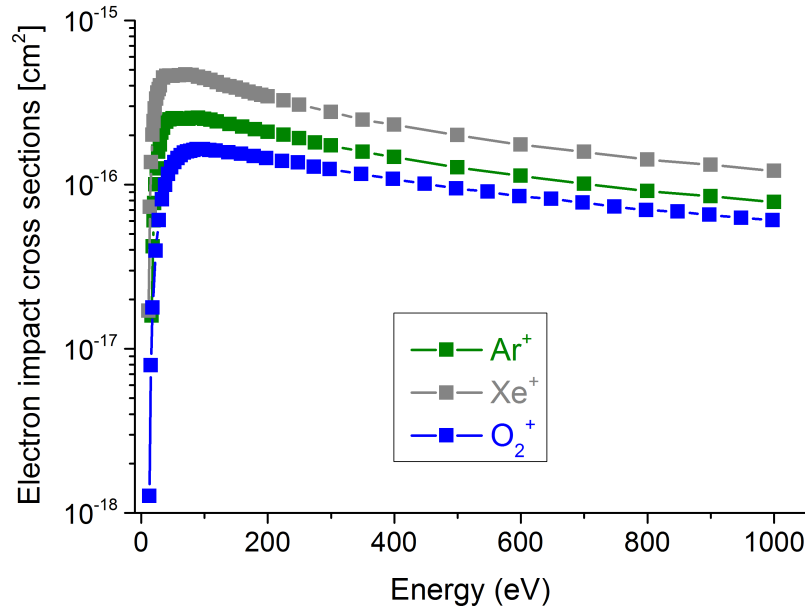


Figure 4.14: Energy dependent EI ionisation cross sections for  $\text{Ar}^+$ ,  $\text{Xe}^+$  and  $\text{O}_2^+$  (values taken from [45, 48]).

### 4.3 Brightness of the ion source

#### 4.3.1 Ion beam generation and current estimation

The variation of the e-beam  $r_{\text{FW50}}$  within the ionisation region that can be seen in figure 4.12a shows that the value of  $r_{\text{FW50}}$  only varies by about 10 % within a X-distance of  $\pm 1$  mm away from  $X_{\text{IR,Mid}}$  which represents as well the central X-position of the ion extraction aperture. This small variation in the e-beam  $r_{\text{FW50}}$  supports the decision to simulate the ionisation volume in which the ions are generated as cylindrical volume above the ion extraction aperture, see figure 4.15 and 4.16a. The **starting positions that are generated for the ions** are uniformly distributed in the X-direction and have a Gaussian distribution for the Y- and Z-direction, see figure 4.16b. The FW50 of the Gaussian distribution is set to 100  $\mu\text{m}$  (**IV-hairpin filament**) being slightly above the hairpin focussing result of the e-Column at  $E_{\text{e,End}} = 1$  keV shown in figure 4.13. The e-beam simulation represents an optimal condition, but in reality small misalignments or non-ideal shapes of the electrodes can alter the field distribution and lead to a broader e-beam focus size than simulated. Therefore, choosing a slightly bigger FW50 size for the Gaussian distribution of the initial ion starting positions in Y- and Z-direction is justified. **The initial ion kinetic energy distribution is set to a Maxwell-Boltzmann distribution**, again programmatically generated within the SIMION workbench user programme by using the Box-Muller Method explained in appendix B (section 7.2). The temperature of the ionisation region is chosen as  $T_{\text{IR}} = 298.15$  K (25 °C) and the initial velocity vector is randomly generated in any XYZ-direction.

In the **ion column setup** the cylindrical ionisation volume is located above an ion extraction aperture of diameter  $d_{\text{Extr}} = 100$   $\mu\text{m}$  and the plate spacing is set to  $D_{\text{Plates}} = 1$  mm, see figure 4.15. In a first configuration, the bottom plate of the ionisation region (electrode  $\text{IR}_2$ ) is followed in downstream direction by an extraction electrode  $\text{Extr}_1$  and the ground electrode G, see figure 4.15. In figure 4.15 only the central part of the simulated ionisation region is shown, the complete corresponding SIMION PA file can be found in appendix B (section 7.2).

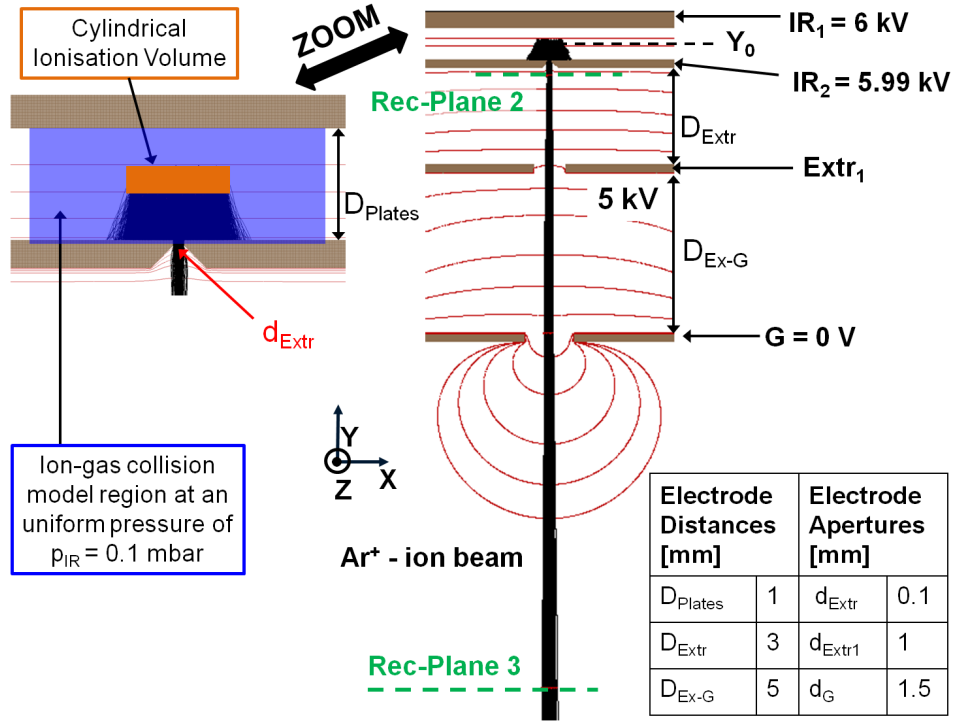


Figure 4.15: Illustration of the  $\text{Ar}^+$  - ion beam extraction within the ion column (XY-cut view).

The SIMION **hard sphere collision model HS1** is used to account for collisions between the created ions and the gas atoms/molecules present **in the ionisation region** between the closely spaced parallel plates IR<sub>1</sub> and IR<sub>2</sub>. The model assumes the background gas to be neutrally charged with a Maxwell-Boltzmann gas particle speed distribution. The background gas mean speed  $v_{\text{mean,BG}}$  is always set to 0 m/s during the simulations. While the model simulates collisional cooling/heating of the ions, the assumption is made that over many collisions the cooling/heating of the background gas is negligible. The collision diameters needed for the application of the HS1 model are calculated as molecular diameters with equation 3.21 by using the viscosity values from [142] for the noble gases (e. g. for Argon at 298.15 K  $d_{\text{m}} = 0.36$  nm).

In the simulations presented here **ion gas particle collisions within the ion column** in the downstream direction (beyond IR<sub>2</sub>) **are not taken into account**. The precise ion column pressure gradient is depending on the applied vacuum pumping configuration. For a first estimation of the ion source brightness the development of the actual mechanical design and the choice of the vacuum pumps is not the main interest and therefore no ion column pressure gradient is used during the following simulations.

**The extraction of  $\text{Ar}^+$  ions is investigated in dependence of the pressure  $p_{\text{IR}}$  applied within the ionisation region.** The potential difference between the top and the bottom plate ( $\Delta V_{\text{Plates}}$ ) of the ionisation region is set to only 10 V and the potential of the extraction electrode Extr<sub>1</sub> is kept constant at 5 kV. Only a fraction of all generated ions is extracted through the bottom plate aperture  $d_{\text{Extr}}$ , see figure 4.16a right picture. As can be seen in the X-position distribution in figure 4.16c, the majority of the extracted ions originate from X-Positions close to the centre of the extraction aperture and only a small part from the X-limits of the ionisation volume can leave the extraction aperture. After that some test simulations have been performed, the length of the cylindrical ionisation volume is set to  $L_{\text{Gen}} = 0.8$  mm ( $\pm 0.4$  mm from the ionisation region centre  $X_{\text{IR,Mid}}$ ).

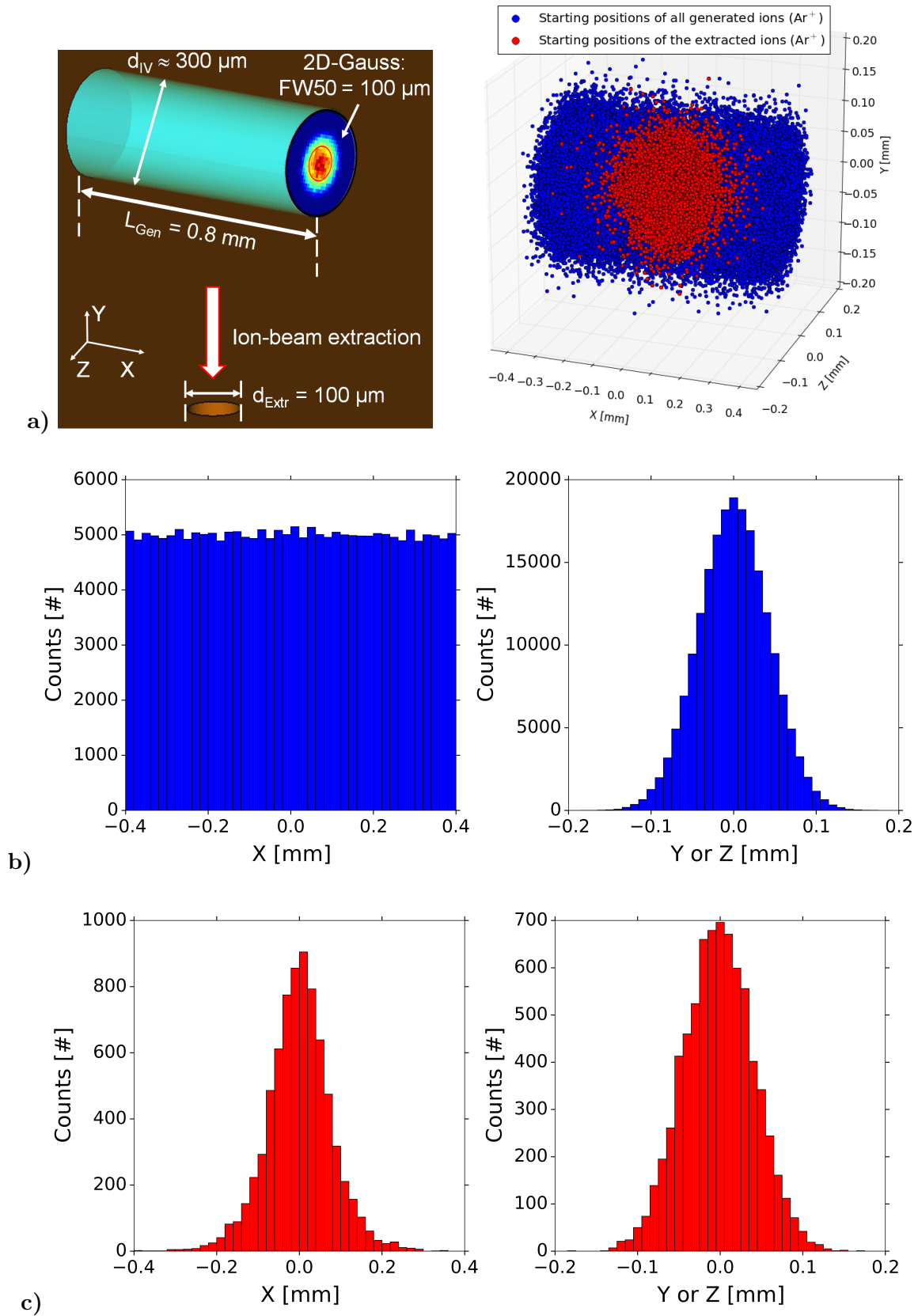


Figure 4.16: a) Cylindrical ionisation volume illustration. Starting positions of all generated and extracted  $\text{Ar}^+$  ions;  
 b) Starting position distributions of all generated  $\text{Ar}^+$  within the ionisation volume;  
 c) Starting position distributions of all extracted  $\text{Ar}^+$  within the ionisation volume.

This represents the minimal needed length of the ionisation volume in order to cover the complete region from which extracted ions can originate. Moreover, in this manner the needed simulation time to obtain a sufficient number of extracted ions to ensure good statistics for the further ion beam evaluations is minimised.

Before a more precise calculation of the ion source brightness is performed a simple **estimation of the extractable ion current** is done. For this purpose the ion extraction ratio  $f_{\text{Extr,Ion}} = \frac{N_{\text{Extr,Ion}}}{N_{\text{Gen,Ion}}}$  is determined at Rec-Plane 2 of figure 4.15 in dependence of the applied pressure  $p_{\text{IR}}$ , where  $N_{\text{Gen,Ion}}$  is the total number of generated and  $N_{\text{Extr,Ion}}$  the total number of extracted ions. The total ion current within the ionisation volume  $I_{\text{Ion,IV}}$  is calculated by using equation 2.7 with  $L_{\text{Gen}} = 0.8 \text{ mm}$ ,  $\sigma_{\text{EI,Ar}^+} = 0.783 \cdot 10^{-20} \text{ m}^2$  at 1 keV [45] and an ionising e-beam current  $I_e$  of 50  $\mu\text{A}$ . This value is below the afore determined electron extraction current  $I_{e,\text{Extr}}$  of 80  $\mu\text{A}$  for the hairpin filament simulation. Reducing  $I_e$  that enters the small cylindrical ionisation volume of figure 4.16a accounts for the fact that in reality transmission losses and e-beam current losses due to residual gas ionisation will occur along the e-beam column before the beam reaches the central region of the ionisation cell at  $X_{\text{IR,Mid}}$ . The extracted ion current  $I_{\text{Ion,Extr}}$  can be calculated by multiplying  $I_{\text{Ion,IV}}$  with  $f_{\text{Extr,Ion}}$ . The results for the  $\text{Ar}^+$  extraction are shown in figure 4.17. The extraction ratio drops with increasing  $p_{\text{IR}}$  as more collisions occur between the generated ions and the gas particles. **The total ion current  $I_{\text{Ion,IV}}$  and also the extracted ion current  $I_{\text{Ion,Extr}}$  increases with increasing  $p_{\text{IR}}$ .** The greyed out area that can be seen in figure 4.17 marks the pressure region from which on the single collision condition (SCC) loses its validity and calculating  $I_{\text{Ion,IV}}$  with equation 2.7 starts to be inaccurate. At a pressure of  $p_{\text{IR}} = 0.1 \text{ mbar}$  the SCC is still valid and the estimation of the generated total ion current is appropriate.

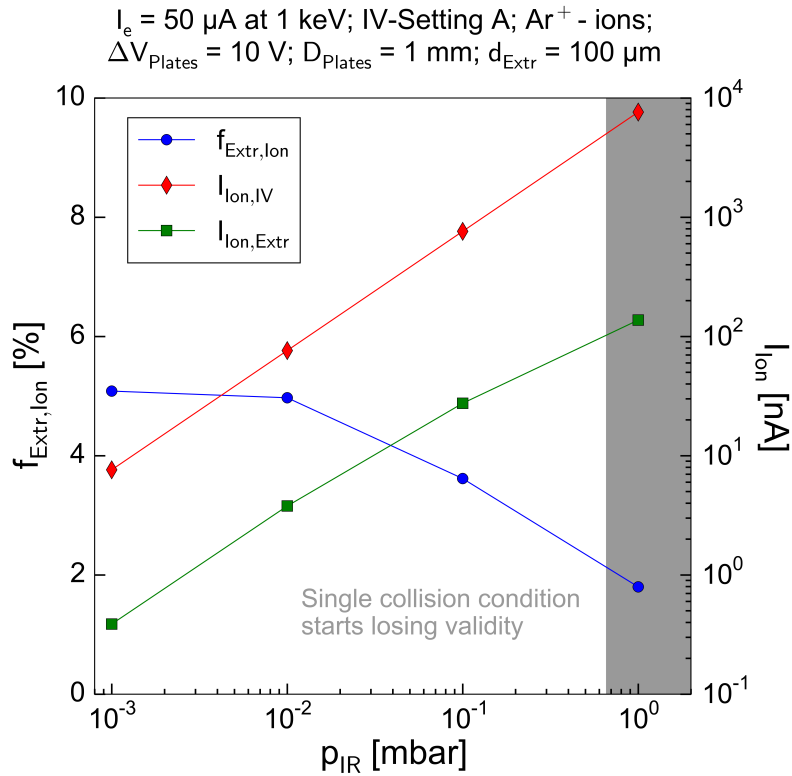


Figure 4.17: IV-hairpin filament with  $\text{Ar}^+$ :  $f_{\text{Extr,Ion}}$ ,  $I_{\text{Ion,IV}}$  and  $I_{\text{Ion,Extr}}$  in dependence of  $p_{\text{IR}}$ .

### 4.3.2 Ion beam reduced brightness calculation

In order to determine the **reduced brightness of the ion beam**  $B_{r,\text{Ion-beam}}$ , the quantities that need to be obtained are  $d_{\text{IS}}$  and  $\alpha_{\text{Ion-beam}}$ , where  $d_{\text{IS}}$  is the ion beam source size defined as the minimal FW50 value along the ion beam axis and  $\alpha_{\text{Ion-beam}}$  is the corresponding half-beam opening angle. The value of  $B_{r,\text{Ion-beam}}$  is calculated by using:

$$B_{r,\text{Ion-beam}} = \frac{0.5 \cdot I_{\text{Ion,Extr}}}{\pi \cdot \left(\frac{d_{\text{IS}}}{2}\right)^2 \pi \cdot \alpha_{\text{Ion-beam}}^2 \cdot V_{\text{Ion,Accel}}} , \quad (4.12)$$

where the factor 0.5 accounts for the fact that  $d_{\text{IS}}$  is defined as FW50 size and therefore only half of the extracted ion beam current is contained within that source size. The solid angle of the ion beam is approximated to  $\Omega_{\text{Ion-beam}} \approx \pi \cdot \alpha_{\text{Ion-beam}}^2$  for small half-opening beam angles. The ion beam acceleration potential is represented by  $V_{\text{Ion,Accel}}$  and has a value of 6 kV for the simulations presented in this section.

The ion XZ-positions and velocities are stored in the recording plane 3 (Rec-Plane 3) which is situated within a field free region behind the ground electrode G in downstream direction, see figure 4.15. As already explained for the determination of the focus size of the e-beam within the ionisation region, the **trajectory extrapolation method** is used here to determine the **ion beam FW50 variation** (this time along the Y-direction) and find in this way the needed  $d_{\text{IS}}$ , see figure 4.18a for an illustration obtained with the parameters defined in figure 4.15. Once that the Y-Position of the ion beam source size  $Y_{\text{IS}}$  is found, the **variation of the half-beam opening angle**  $\alpha_{\text{half}}$  along the Y-direction can be calculated at each  $Y_i$  - plane with:

$$\alpha_{i,\text{half}} = \arctan\left(\frac{d_{i,\text{FW50,Ion-beam}} - d_{\text{IS}}}{2 \Delta Y_i}\right) , \quad (4.13)$$

where  $d_{i,\text{FW50,Ion-beam}}$  represents the ion beam FW50 size at the variable plane  $Y_i$  and the distance in Y-direction  $\Delta Y_i = Y_i - Y_{\text{IS}}$ .

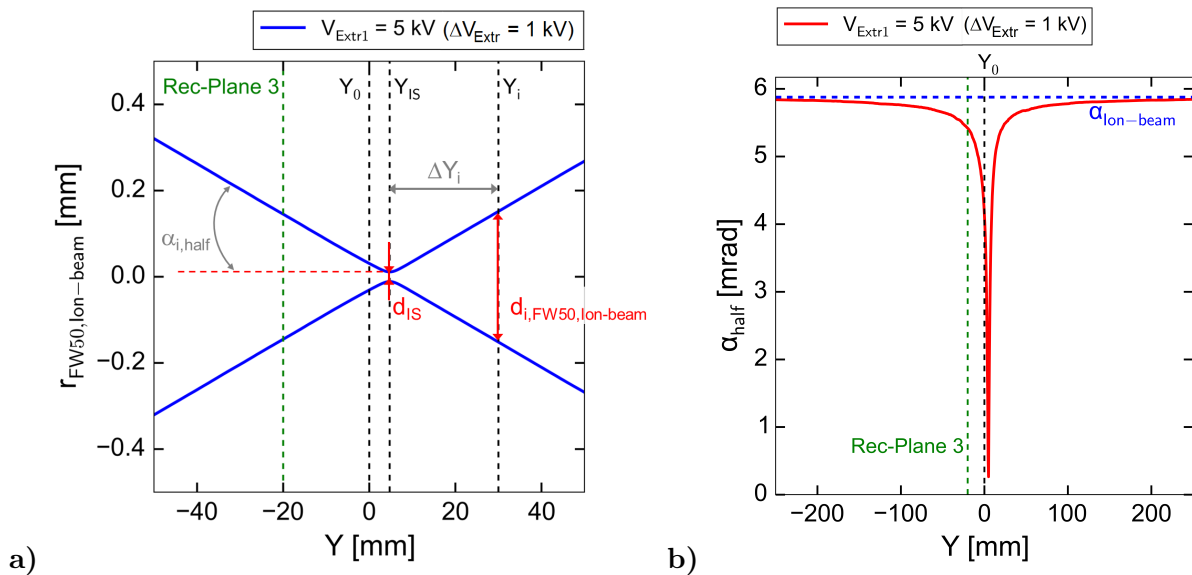


Figure 4.18: Trajectory extrapolation results for the simulation of figure 4.15:

- a)  $\text{Ar}^+$  ion beam FW50 variation;
- b)  $\text{Ar}^+$  ion beam half-opening angle variation.



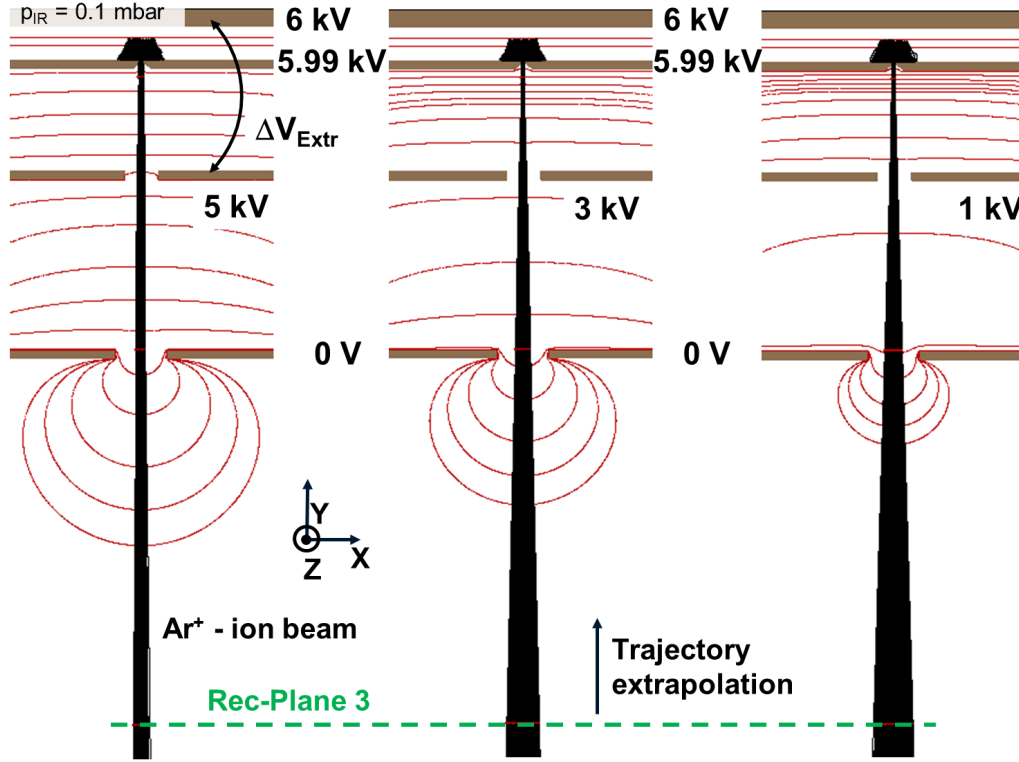


Figure 4.19: Illustration of the  $Ar^+$  ion beam simulation with a variation of  $V_{Extr1}$  (IV-hairpin filament,  $p_{IR} = 0.1 \text{ mbar}$ ,  $d_{Extr} = 100 \text{ }\mu\text{m}$ ).

In figure 4.18b the variation of  $\alpha_{half}$  along the Y-direction can be seen, it shows as well the result for the simulation case of figure 4.15. It is clearly visible that it approaches in positive and negative Y-direction an asymptotic value at about  $5.9 \text{ mrad}$  which is defined as the ion beam half-opening angle  $\alpha_{Ion-beam}$  that will be used for the calculation of  $B_{r,Ion-beam}$ .

Several ion column simulations are done for an  $Ar^+$  ion beam with  $d_{Extr} = 100 \text{ }\mu\text{m}$  and a variation of the extraction potential  $V_{Extr1}$ . In figure 4.19 it can be clearly seen that when the potential difference  $\Delta V_{Extr}$  between the ionisation region top plate and the extraction electrode is raised, the ion beam has a larger divergence at Rec-Plane 3 which should have an influence on  $d_{IS}$  and  $\alpha_{Ion-beam}$ . Not only  $Ar^+$  ions but also  $Xe^+$  and  $O_2^+$  ions are simulated. The determination of the total ion current  $I_{Ion,IV}$  is again done for an e-beam of  $50 \text{ }\mu\text{A}$  at  $1 \text{ keV}$  and the used EI-cross sections are:  $\sigma_{EI,Ar^+} = 0.783 \cdot 10^{-20} \text{ m}^2$ ,  $\sigma_{EI,Xe^+} = 1.210 \cdot 10^{-20} \text{ m}^2$  and  $\sigma_{EI,O_2^+} = 0.607 \cdot 10^{-20} \text{ m}^2$  [45, 48].

The reduced brightness calculation results and the related parameters are shown in figure 4.20. For all simulated ion species the ion beam source size decreases with increasing  $\Delta V_{Extr}$  and falls at  $\Delta V_{Extr} = 3 \text{ kV}$  below  $10 \text{ }\mu\text{m}$ . In contrast to that  $\alpha_{Ion-beam}$  increases with increasing  $\Delta V_{Extr}$  and reaches for the considered ion species a maximal value close to  $20 \text{ mrad}$  ( $\approx 1.2^\circ$ ) at  $\Delta V_{Extr} = 5 \text{ kV}$ . The differences that can be seen for the transmitted ion beam currents  $I_{Ion,transmitted}$  are mainly due to the change in the EI-cross sections for the different ion species. **The overall calculation results for the reduced ion beam brightness are within  $50 - 65 \text{ A}/(\text{m}^2 \text{ sr V})$ .** This result is still quite far away from the targeted range of  $10^3 - 10^4 \text{ A m}^{-2} \text{ sr}^{-1} \text{ V}^{-1}$ , nevertheless it represents already a clear improvement compared to the  $B_r \approx 1 \text{ A}/(\text{m}^2 \text{ sr V})$  that can be obtained with conventional EI ion sources. The simulations with  $V_{Extr1} = 4 \text{ kV}$  or  $2 \text{ kV}$  that are not shown in figure 4.19 can be found in appendix B (section 7.2) as completion of the results.

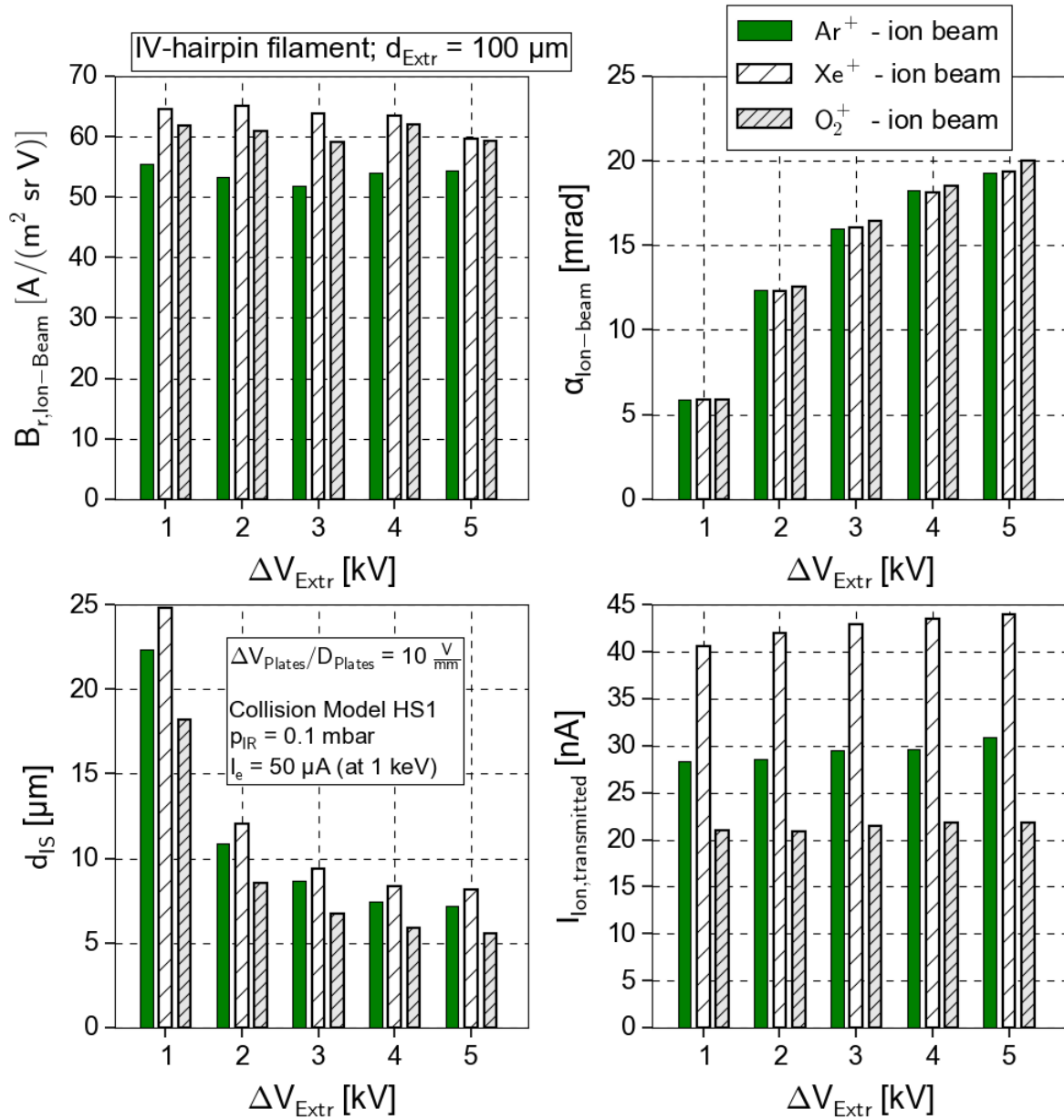


Figure 4.20: Results of the reduced brightness  $B_{r,\text{Ion-beam}}$  determination and related parameters (IV-hairpin filament,  $p_{\text{IR}} = 0.1$  mbar,  $d_{\text{Extr}} = 100$   $\mu\text{m}$ ).

**A possible means for increasing the EI ion source reduced brightness would be to decrease the diameter of the cylindrical ionisation volume** and by this manner reduce the ion beam source size while keeping a similar ionising electron current to generate a similar ion beam current as in the hairpin filament case. Single crystal Lanthanum hexaboride ( $\text{LaB}_6$ ) cathodes represent one kind of thermionic emitter (see figure 4.21) that have similar characteristics as hairpin filaments in terms of emission currents while having a few tens times smaller emission areas [140, 143]. The typical operating temperature for these  $\text{LaB}_6$  emitters lies in the range of 1400-2000 K being below 2700 K, which is typical for hairpin filaments. One disadvantage that  $\text{LaB}_6$  emitters have is that they need a vacuum level of  $< 10^{-6}$  mbar for their operation which is hundred times lower than the vacuum needed for the hairpin filaments [40, 100].

A standard  $\text{LaB}_6$  front tip area (Zoom in figure 4.21) has a diameter of 15  $\mu\text{m}$ . Such an emitter tip is incorporated in the e-Column System A (see figure 4.9) and replaces the hairpin filament, while the triode setup parameters are unchanged with  $d_{\text{W}}/H = 1.6$  and  $D_{\text{WA}} = 3$  mm.

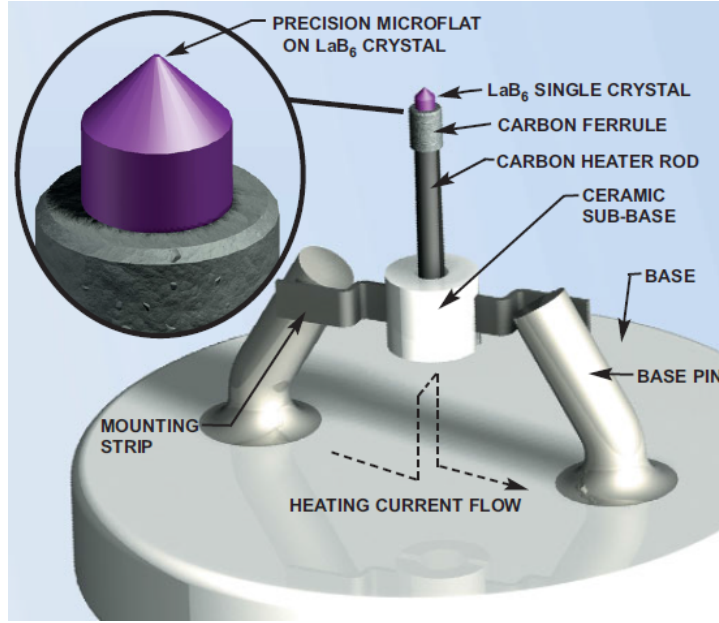


Figure 4.21: Illustration of a  $\text{LaB}_6$  thermionic emitter (taken from [143]).

It is determined that at an end e-beam energy of  $E_{e,\text{End}} = 1 \text{ keV}$  the **e-beam focus  $d_{\text{Focus}}$**  (defined as minimal FW50 along the e-beam axis) **above the ion extraction aperture reduces to  $d_{\text{Focus}} \approx 40 \text{ }\mu\text{m}$** . This is a reduction factor of 2.5 compared to the hairpin filament case where  $d_{\text{Focus}} \approx 100 \text{ }\mu\text{m}$ . Ion column simulations were performed with this reduced ionisation volume situation, which will be referred to as IV- $\text{LaB}_6$  setting in the following, for an  $\text{Ar}^+$  ion beam and again a variation of  $\Delta V_{\text{Extr}}$  was applied. The ions are generated identically to the explanations given at the beginning of section 4.3.1, except that this time the FW50 of the Gaussian distribution in Y- and Z-direction is set equal to  $40 \text{ }\mu\text{m}$ .

An illustration is given in figure 4.22a about how the different ionisation volume settings can be interpreted when looking from below the bottom plate (IR2) into the ionisation region through the up to now used extraction aperture of  $d_{\text{Extr}} = 100 \text{ }\mu\text{m}$ . In the IV-hairpin filament setting  $d_{\text{Extr}}$  is completely filled by the ionisation volume so that the virtual source shape for the extracted ion beam will be circular. In contrast to this the IV- $\text{LaB}_6$  setting does not completely fill  $d_{\text{Extr}}$  but in this case the ionisation volume looks actually like as cylinder from below the IR2 electrode. This has as an effect that the virtual source size will be reduced only in one dimension (Z-direction) and be unaffected in the other dimension (X-direction). Nevertheless, ion column simulations have been done by combining the IV- $\text{LaB}_6$  setting with  $d_{\text{Extr}} = 100 \text{ }\mu\text{m}$  to evaluated which effect this has on the ion source performance. In figure 4.22b it is illustrated that when **adapting as well  $d_{\text{Extr}}$  to the size of the reduced ionisation volume** the virtual source size will be reduced this time in both dimensions. Therefore, ion column simulations are performed as well for this combination case of IV- $\text{LaB}_6$  setting with  $d_{\text{Extr}} = 40 \text{ }\mu\text{m}$ .

The obtained ion source performance in the different situations can be seen in figure 4.23. The following conclusions can be drawn by comparing the combinations of IV-hairpin filament setting/ $d_{\text{Extr}} = 100 \text{ }\mu\text{m}$  and IV- $\text{LaB}_6$  setting/ $d_{\text{Extr}} = 100 \text{ }\mu\text{m}$ : The reduction of the ionisation volume size has a positive effect on the transmitted ion current  $I_{\text{Ion,transmitted}}$  as the ion generation is more concentrated above  $d_{\text{Extr}}$ . The half-opening beam angle  $\alpha_{\text{Ion-beam}}$  is unaffected but as expected the determined  $d_{\text{IS}}$  size is decreased in the IV- $\text{LaB}_6$  setting compared to the IV-hairpin filament setting over the complete  $\Delta V_{\text{Extr}}$  range.

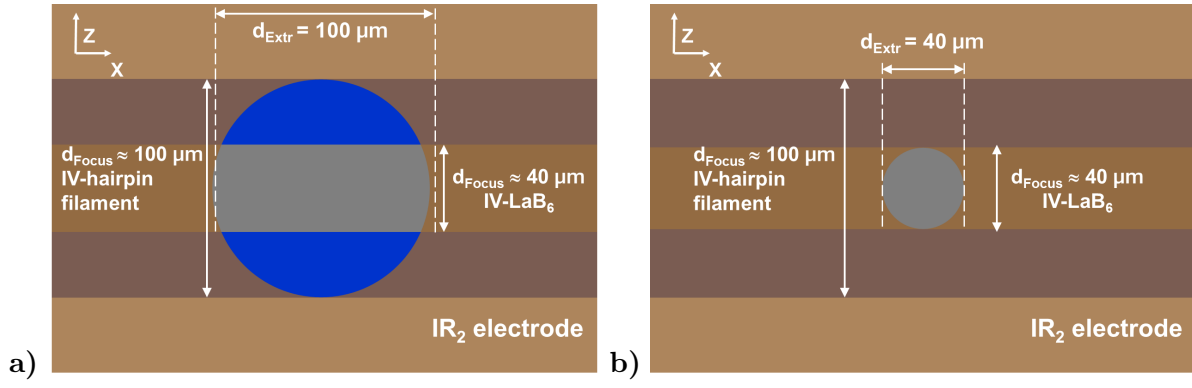


Figure 4.22: a) Bottom view into the ionisation region: Different IV-settings;  $d_{\text{Extr}} = 100 \mu\text{m}$ ;  
 b) Bottom view into the ionisation region: Different IV-settings;  $d_{\text{Extr}} = 40 \mu\text{m}$ .

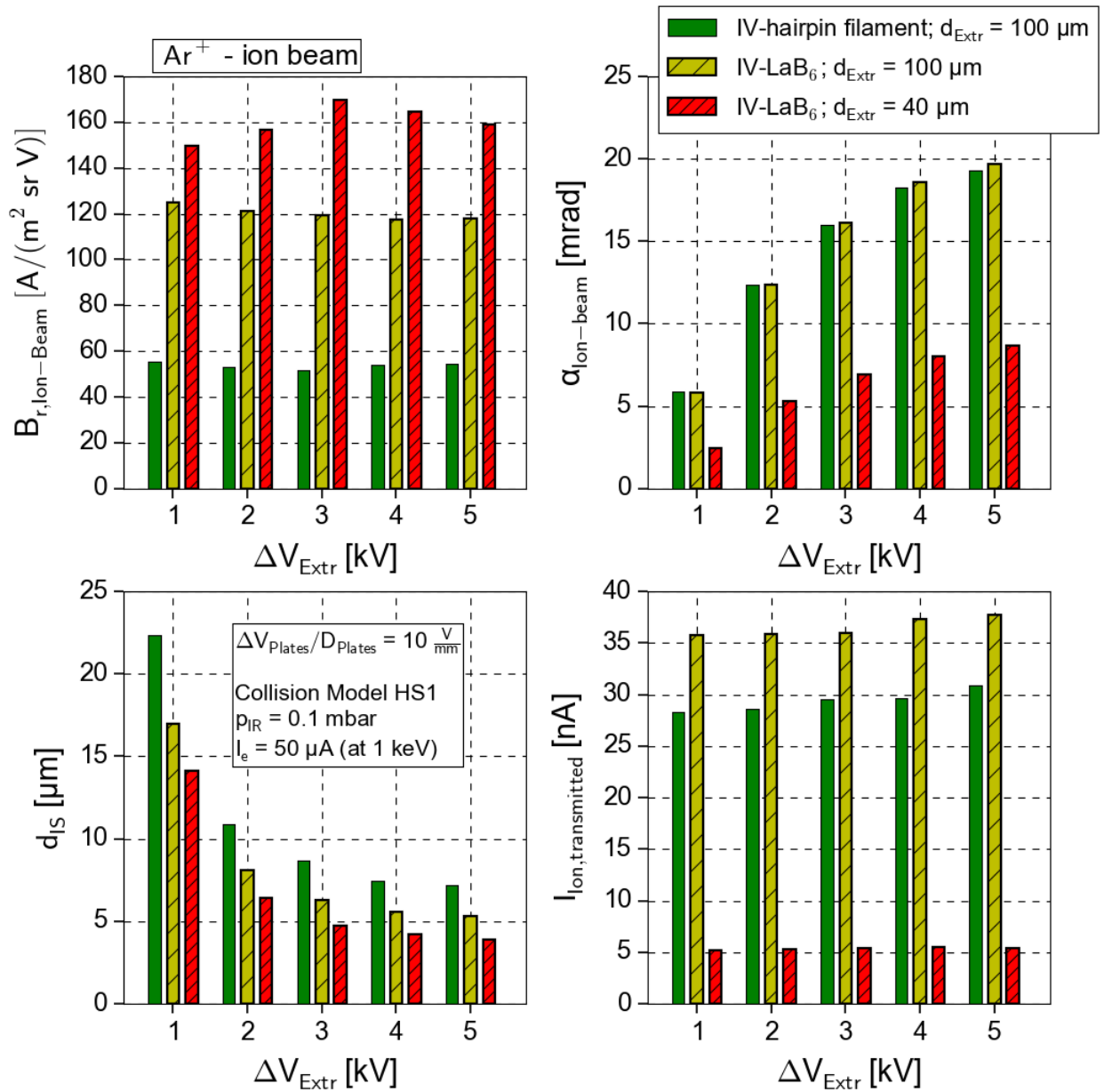


Figure 4.23: IV-Setting/ $d_{\text{Extr}}$  combination comparison: Results of the determination of  $B_{r,\text{Ion-beam}}$  and related parameters (Ar<sup>+</sup> ion beam,  $p_{\text{IR}} = 0.1 \text{ mbar}$ ).

**The reduced brightness is increased by the use of an LaB<sub>6</sub> emitter by about a factor of 2 reaching an average value of  $B_{r, \text{Ion-beam}} = 1.2 \cdot 10^2 \text{ A}/(\text{m}^2 \text{ sr V})$  for Ar<sup>+</sup> ions.**

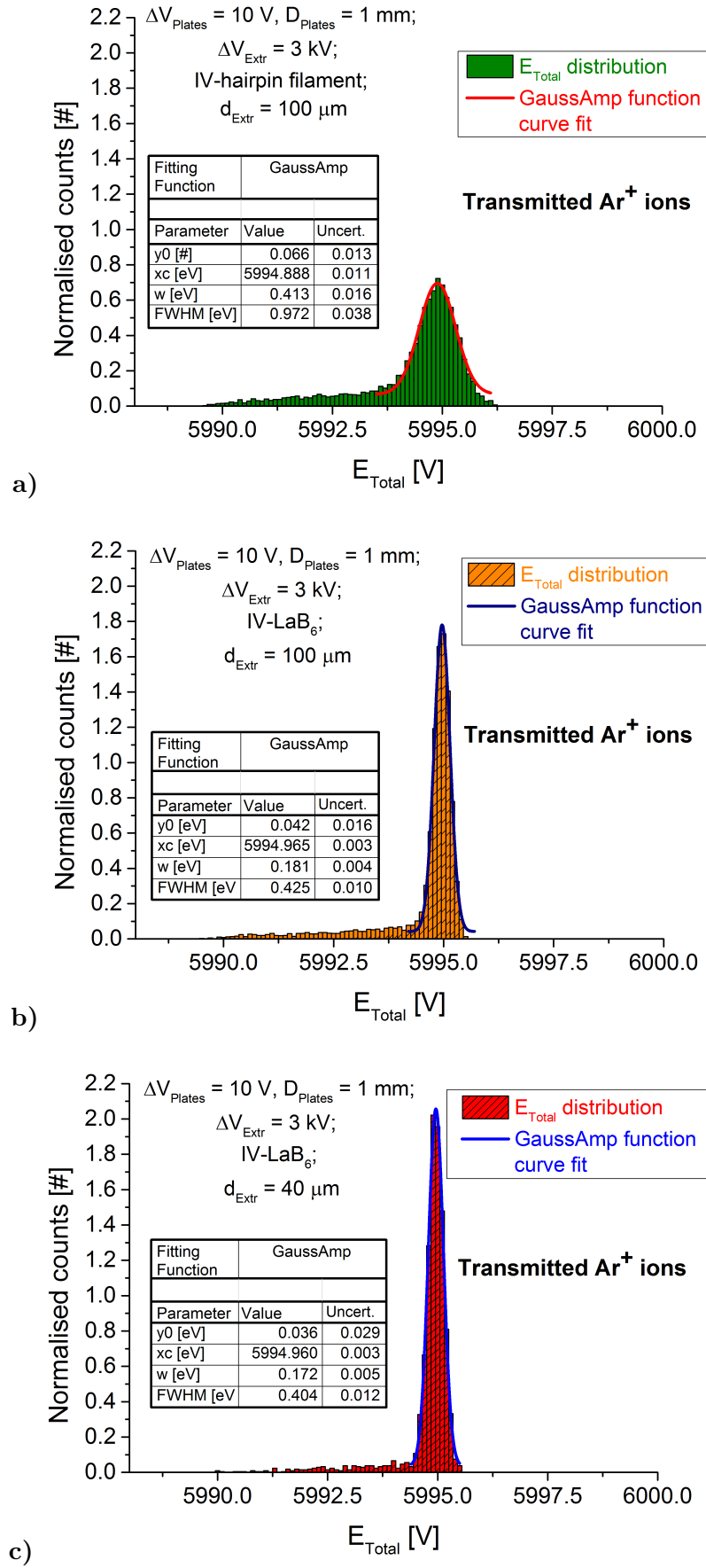
A further comparison can be done for the IV-LaB<sub>6</sub> setting between both cases of  $d_{\text{Extr}}$  size. The determined values of  $I_{\text{Ion,transmitted}}$  drop towards 5 nA due to the reduction of  $d_{\text{Extr}}$  to 40  $\mu\text{m}$ . The spread of the transmitted Ar<sup>+</sup> ion beam is clearly reduced and an average value of  $\alpha_{\text{Ion-beam}} \approx 6 \text{ mrad}$  can be determined. A further reduction is also seen for the  $d_{\text{IS}}$  size when going from  $d_{\text{Extr}} = 100 \text{ }\mu\text{m}$  to 40  $\mu\text{m}$ . Over the complete evaluated  $\Delta V_{\text{Extr}}$  range the determined  $d_{\text{IS}}$  size is below 15  $\mu\text{m}$ . Overall, the fact that less ion current is extracted by the reduction of  $d_{\text{Extr}}$  is compensated by a decrease in  $d_{\text{IS}}$  and  $\alpha_{\text{Ion-beam}}$  so that **the reduced brightness is even further increased to  $1.6 \cdot 10^2 \text{ A}/(\text{m}^2 \text{ sr V})$  on average for the Ar<sup>+</sup> ion beam.**

### 4.3.3 Energy distributions

As can be seen in figure 4.2 and equation 4.4 a reduction of the ionisation volume diameter is expected to have a positive effect on the obtained energy spread of the generated ions. Therefore, a last performed evaluation is **the determination of the energy spread for the transmitted ion beam** in the different combination cases of IV-setting and  $d_{\text{Extr}}$ . The evaluation is done for the Ar<sup>+</sup> ion beam in the potential setting case of  $\Delta V_{\text{Extr}} = 3 \text{ kV}$  (see figure 4.19 for remaining potentials). The total energy is calculated by  $E_{\text{Total}} = E_{\text{kinetic}} + q_{\text{Ion}} \cdot \text{Pot}_{\text{Ion}}$  where  $q_{\text{Ion}}$  represents the ion charge and  $\text{Pot}_{\text{Ion}}$  the potential value at the corresponding ion position. For the IV-hairpin filament case and  $d_{\text{Extr}} = 100 \text{ }\mu\text{m}$  in figure 4.24a, the  $E_{\text{Total}}$  distribution has a clearly pronounced peak around 5995 eV and a low intensity tail towards lower energies. This tail can most probably be explained by outlier trajectories within the ion column caused by some ions that underwent a gas collision within the ionisation region just before they are extracted through  $d_{\text{Extr}}$  and therefore have larger off-axis beam angles. A GaussAmp function fit (defined in appendix B (section 7.2)) is used to determine the FWHM of the high intensity peak. **A value of 1 eV is determined and defines the  $\Delta E$  of the transmitted ion beam.**

In figure 4.24b the total energy distribution of the transmitted ions can be seen for the IV-LaB<sub>6</sub> setting,  $d_{\text{Extr}} = 100 \text{ }\mu\text{m}$  combination case. In comparison to 4.24a a narrower and more pronounced peak is found around the same value of 5995 eV. Again a GaussAmp function fit is performed at the peak location and as expected **a smaller FWHM value of 0.43 eV is determined** which is related to the smaller ionisation volume size in Y-direction. The energy tail at lower energies is quite similar to the case in figure 4.24a.

The last energy distribution is shown in figure 4.24c corresponding to the IV-LaB<sub>6</sub> setting with the reduced  $d_{\text{Extr}}$  of 40  $\mu\text{m}$ . Compared to the first two mentioned distributions the maximum intensity of the energy peak is further increased. In contrast to that, the tail of the energy distribution is less pronounced and is most probably related to the fact that a clearly smaller half-opening beam angle is obtained in this case (see figure 4.24) which results in a more confined ion beam around the optical axis and less outlier trajectories. **The determined FWHM by the GaussAmp function fit is very similar to the case of figure 4.24b and is equal to 0.40 eV.** This is not surprising as the main influence on the energy distribution comes from the ionisation volume size in Y-direction which is equal for the cases of figure 4.24b and 4.24c. The energy distribution is only slightly affected by the reduction of the effective ionisation volume size in X-/Z-direction from which the ions are extracted when going to a smaller extraction aperture. **The final conclusion that can be drawn is that the miniature IV EI ion source concept produces ion beams with a  $\Delta E \lesssim 1 \text{ eV}$  which corresponds to the objective.**

Figure 4.24: Total energy distribution of all transmitted  $\text{Ar}^+$  ions:

- a) IV-hairpin filament setting,  $d_{\text{Extr}} = 100 \text{ }\mu\text{m}$  and  $\Delta V_{\text{Extr}} = 3 \text{ kV}$ ;  
 b) IV-LaB<sub>6</sub> setting,  $d_{\text{Extr}} = 100 \text{ }\mu\text{m}$  and  $\Delta V_{\text{Extr}} = 3 \text{ kV}$ ;  
 c) IV-LaB<sub>6</sub> setting,  $d_{\text{Extr}} = 40 \text{ }\mu\text{m}$  and  $\Delta V_{\text{Extr}} = 3 \text{ kV}$ .

## 4.4 Technical considerations

### 4.4.1 Gas conductance simulations

A certain pressure gradient has to be achieved within the e-Column as on one end the thermionic electron emitters need a low vacuum level (see table 3.1) in order to be operated and at the other end the ionisation region needs to be kept at quite high pressure of about 0.1 mbar. **Gas conductance simulations are used to estimate the achievable pressure gradient along the e-Column.** For this purpose a mechanical setup related to the e-Column Setup A of figure 4.9 is developed as illustrated in figure 4.25 and it will be referred to as **the e-Column Model A** in the following. The electrodes are separated by insulating spacers so that the needed potentials can be applied.

The volume in which the gas particles can freely move within the mechanical e-Column Model A is loaded into the simulation software Molflow+, see figure 4.26a. During the simulations the complete geometry is set to a constant temperature of 298.15 K. The gas injection flow  $q_{IN}$  is adjusted so that the pressure within the ionisation chamber is very close to 0.1 mbar for each simulation case. The particles are injected uniformly from the surface shown in figure 4.26b in direction of the indicated arrow. The e-Column Model A has the advantage that many pumping channels are present all along the e-Column, as illustrated in figure 4.26c. For each pumping channel (opening) the conductance value  $C_{Opening}$  needed for the Molflow+ simulation is calculated by equation 3.27, using  $P = 1$  and the open area  $A_{Opening}$  of the channel. Different cases for the pumping speed  $S$  at the outside of the e-Column Model A and the injection of different gases is investigated. For each pumping channel the related effective pumping speed is calculated by equation 3.36 with  $S$  and  $C_{Opening}$ . In each simulation case the 2D-pressure distribution along the middle plane of the e-Column Model A is recorded.

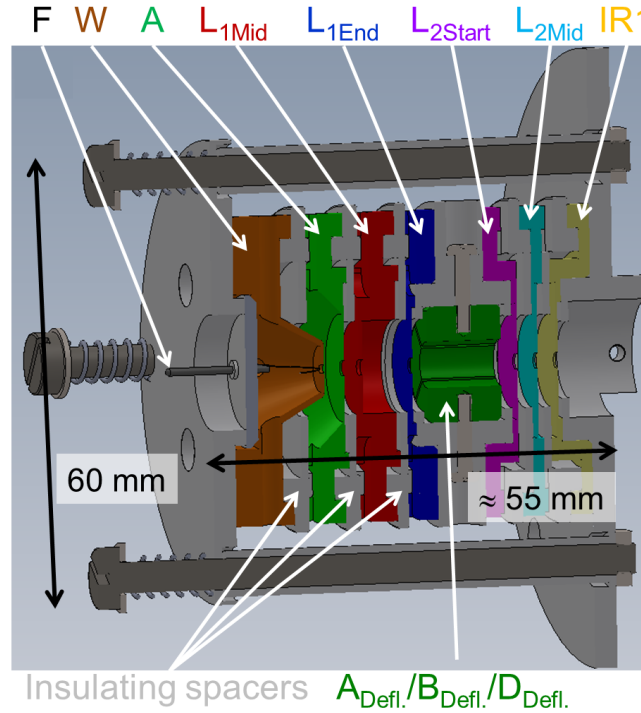


Figure 4.25: Illustration of the designed mechanical setup for e-Column model A.



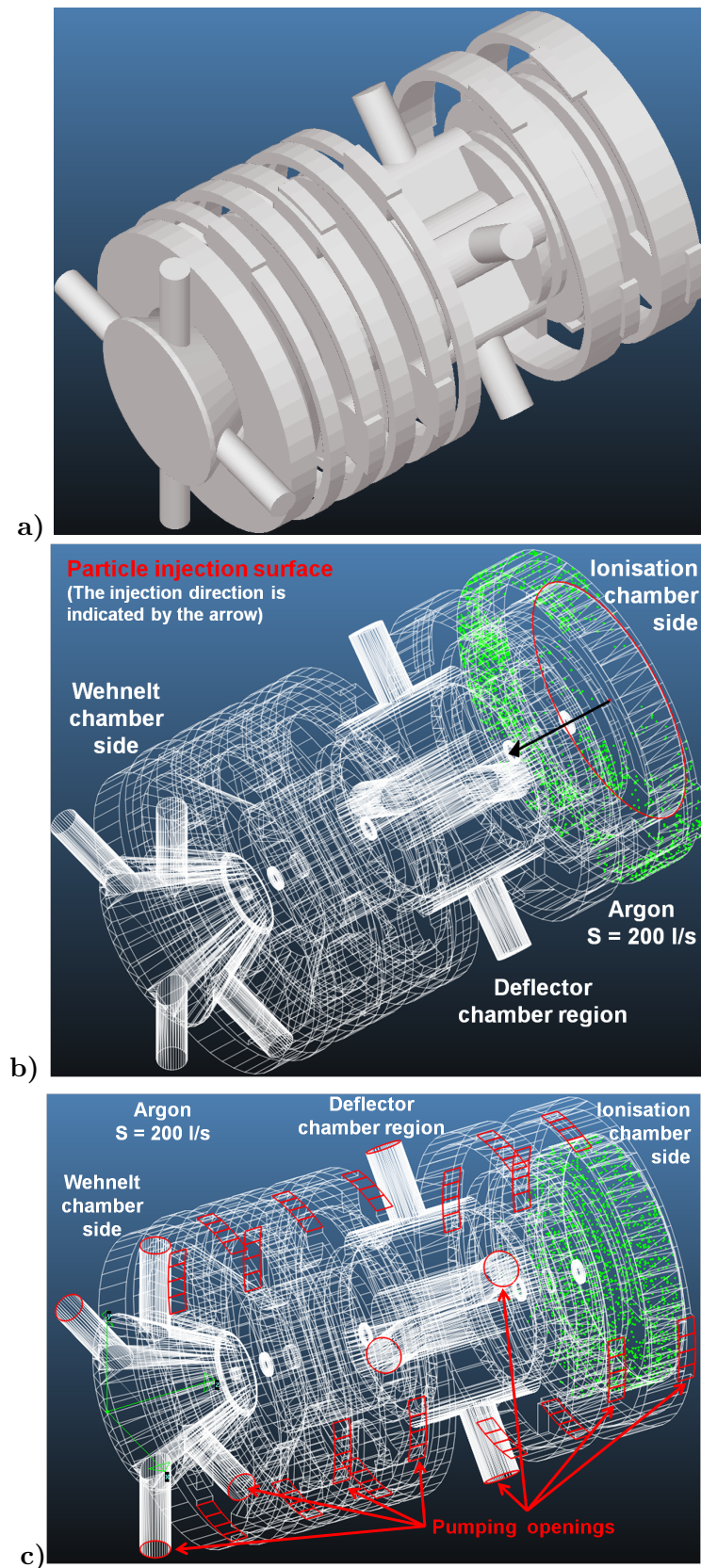


Figure 4.26: a) Free space volume of the mechanical e-Column Model A loaded into Molflow+; b) Injection of gas particles (Facet-view; particles represented as green points) c) Pumping channels available along the e-Column Model A.

The obtained simulation results are listed in table 4.4 for two gas species, **Argon and Nitrogen**. What should be mentioned is that during the simulations it is very difficult to obtain in each case exactly the same pressure within the ionisation chamber. Therefore, for



means of comparison the ratio of the ionisation chamber pressure  $p_I$  to the Wehnelt chamber pressure  $p_W$  is listed as well in table 4.4. The determined pressure values can be understood as average for each region of the obtained 2D-pressure distributions, as illustrated in figure 4.27. In the case of  $S = 200$  l/s the obtained  $p_I/p_W$  values for Argon and Nitrogen are very similar and indicate that slightly more than four orders of magnitude for the pressure drop across the e-Column Model A are achieved. In both cases  $p_W$  falls below  $1 \cdot 10^{-5}$  mbar so that **the operation of a thermionic hairpin filament** ( $p_W \leq 1 \cdot 10^{-4}$  mbar needed) **is possible** within the Wehnelt chamber of e-Column Model A. Unfortunately, this simulation result indicates that **the possibility to operate a LaB<sub>6</sub> emitter is very unlikely** and further pumping optimisation efforts would be needed to achieve the necessary  $p_W$  below  $1 \cdot 10^{-6}$  mbar.

As can be seen in table 4.4 the effect of an increase of  $S$  to 1000 l/s is evaluated for Argon. By comparing the  $p_I/p_W$  value for the case of  $S = 200$  l/s to the one of  $S = 1000$  l/s, it is clear that no further decrease of  $p_W$  is obtained when raising  $S$  to 1000 l/s. Furthermore, the simulated case of  $S = 100$  l/s with Argon injection gives very similar results compared to the  $S = 200$  l/s situation, which indicates that already at a quite low outside pumping speed the needed Wehnelt pressure for a hairpin filament operation can be achieved. A conclusion that can be drawn is that **the pressure distribution within the e-Column Model is only marginally influenced by a change in  $S$** . It is expected that **additional pumping channels can have a far stronger effect** in order to obtain even higher  $p_I/p_W$  values to finally reach  $p_W < 1 \cdot 10^{-6}$  mbar. In appendix B (section 7.2) the obtained 2D-pressure distributions are illustrated for all those simulation cases listed in table 4.4 but not shown in figure 4.27.

Gas	$S$ [l/s]	$q_{IN}$ [mbar l/s]	$p_I$ [mbar]	$p_D$ [mbar]	$p_W$ [mbar]	$p_I/p_W$
Ar	100	$5.0 \cdot 10^{-3}$	$9.46 \cdot 10^{-2}$	$1.82 \cdot 10^{-3}$	$7.11 \cdot 10^{-6}$	$1.3 \cdot 10^4$
	200	$5.5 \cdot 10^{-3}$	$1.04 \cdot 10^{-1}$	$2.00 \cdot 10^{-3}$	$8.96 \cdot 10^{-6}$	$1.2 \cdot 10^4$
	1000	$5.0 \cdot 10^{-3}$	$9.47 \cdot 10^{-2}$	$1.81 \cdot 10^{-3}$	$7.75 \cdot 10^{-6}$	$1.2 \cdot 10^4$
N <sub>2</sub>	200	$6.0 \cdot 10^{-3}$	$9.51 \cdot 10^{-2}$	$1.82 \cdot 10^{-3}$	$7.05 \cdot 10^{-6}$	$1.3 \cdot 10^4$

Table 4.4: Molflow+ simulation results related to the e-Column Model A ( $T = 298.15$  K).

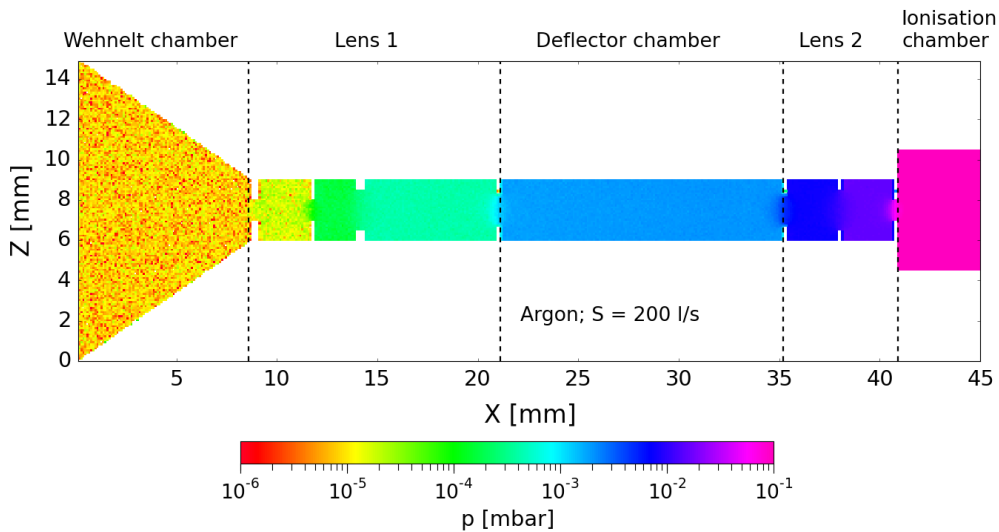


Figure 4.27: 2D pressure distribution along the e-Column Model A (Argon,  $S = 200$  l/s).

#### 4.4.2 Experimental gas conductance and electron beam transmission tests

##### Electron column dummy model for gas conductance tests

In the previous sections it has been shown that it is important to know what pressure within the Wehnelt chamber can be obtained when the ionisation chamber of e-Column Model A is kept at a quite high pressure of 0.1 mbar. **In order to perform experimental gas conductance measurements a simplified dummy model of e-Column Model A was designed and built**, see schematic shown in figure 4.28. The dummy model consists of cylindrical apertures and spacers that are inserted into a small cylindrical e-Column tube in a specific configuration in order to represent the e-Column Model A as precisely as possible, see figure 4.29. Some of the spacers have a special U-shape in order to create additional pumping channels all along the e-Column tube. An illustration of such an additional pumping channel can as well be found in figure 4.29. By the use of small screws that can be inserted into the holes of the e-Column tube it is possible to suppress or allow the additional pumping of the e-Column dummy model during the gas conductance tests.

Figure 4.30a schematically shows the **experimental setup configuration** that is used to perform the gas conductance tests by injection of Nitrogen into the ionisation volume side of the dummy model. The e-Column tube is inserted into a slightly bigger vacuum tube to which pressure gauges and a small turbo pump can be connected. The Wehnelt volume side of the test structure is attached to a vacuum chamber which is pumped by a turbo-molecular pump with a pumping speed of  $S_{V1001} = 950$  l/s for Nitrogen (Turbo-V 1001 Navigator [144]). The main part of this vacuum chamber is an elbow tube and the test structure is connected to it via a small cylindrical port.

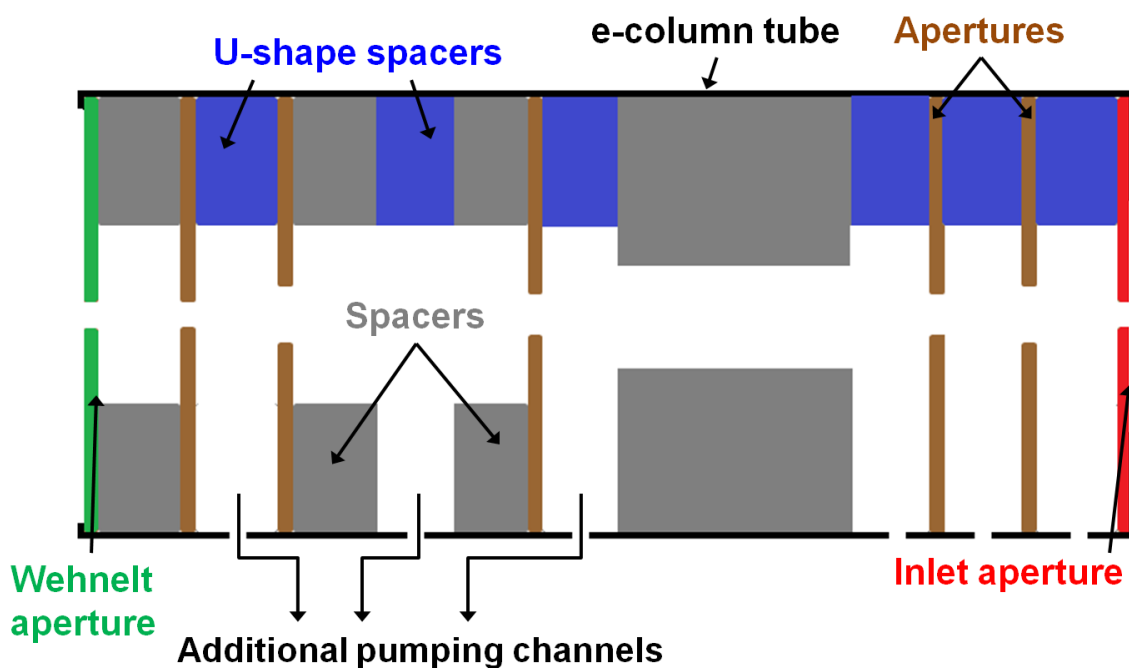


Figure 4.28: Schematic of the e-Column dummy model for the gas conductance measurements related to e-Column Model A.

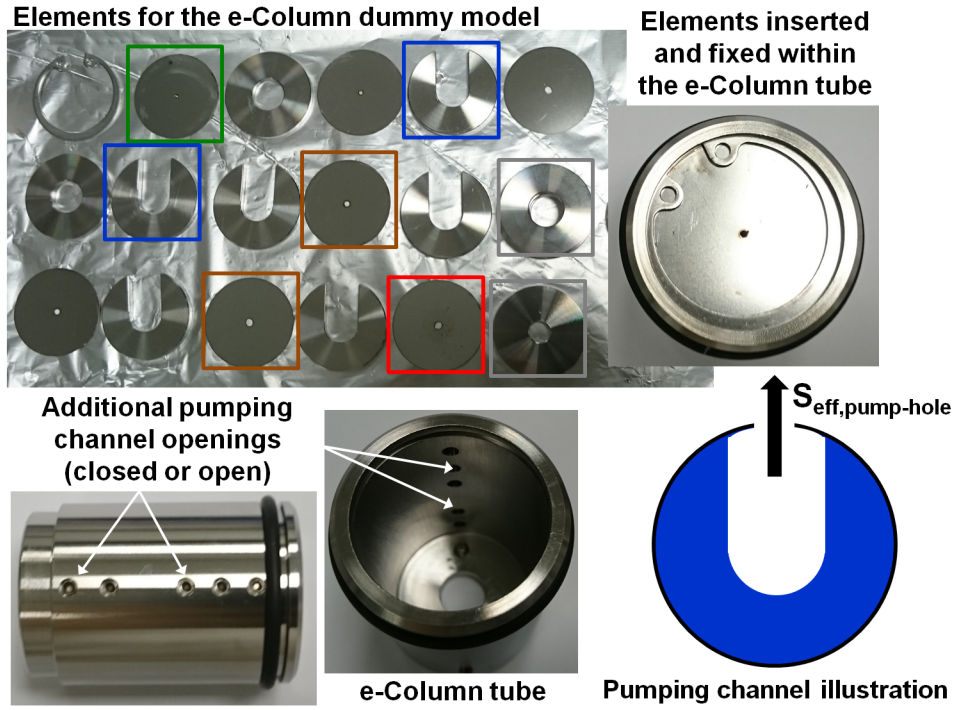


Figure 4.29: Elements of the e-Column dummy model used to perform the experimental gas conductance measurements.

Therefore, in order to get an estimation of the effective pumping speed of the Wehnelt volume side  $S_{\text{eff},W}$  a series connection of an elbow tube and a straight cylindrical tube is taken into account and the following equation is used:

$$S_{\text{eff},W} = \frac{S_{V1001}}{1 + \frac{S_{V1001}}{C_{\text{VacChamber}}}} \quad . \quad (4.14)$$

The vacuum chamber conductance  $C_{\text{VacChamber}}$  is calculated by using equation 3.32 for a series connection of several elements with varying cross section and equations 3.28 and 3.30 are used to obtain the individual conductances of the straight and the elbow tube in the molecular flow regime. For all conductance and pumping speed estimations performed in this section the temperature is taken as  $T = 298 \text{ K}$ . Three pressure gauges are installed to measure the ionisation volume pressure  $p_I$ , the Wehnelt volume pressure  $p_W$  and the external e-Column pressure  $p_{eC}$ . A small turbo-molecular pump having a pumping speed of  $S_{V81} = 50 \text{ l/s}$  for Nitrogen (Turbo-V 81-M [144]) is connected to the e-Column region of the test structure. The conductance  $C_{V81,eC}$  for the V81 connection to the e-Column region is again determined by using equation 3.28 for a straight cylindrical tube in the molecular flow regime and the effective pumping speed  $S_{\text{eff},\text{outside},eC}$  at the outside of the e-Column tube is estimated by:

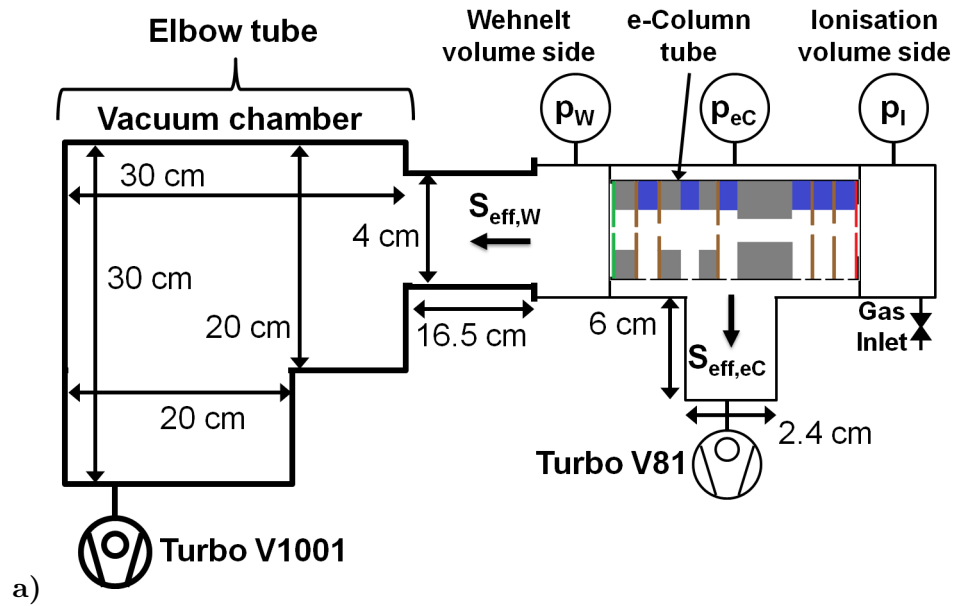
$$S_{\text{eff},\text{outside},eC} = \frac{S_{V81}}{1 + \frac{S_{V81}}{C_{V81,eC}}} \quad . \quad (4.15)$$

Furthermore, when taking into account the conductance  $C_{\text{pump-hole},eC}$  of the small pumping holes (2.5 mm in diameter) present in the e-Column tube by equation 3.29 for a circular aperture in the molecular flow regime, the effective pumping speed  $S_{\text{eff},\text{pump-hole}}$  at the end of each additional pumping channel of the e-Column tube (illustrated in figure 4.29) can be estimated by:

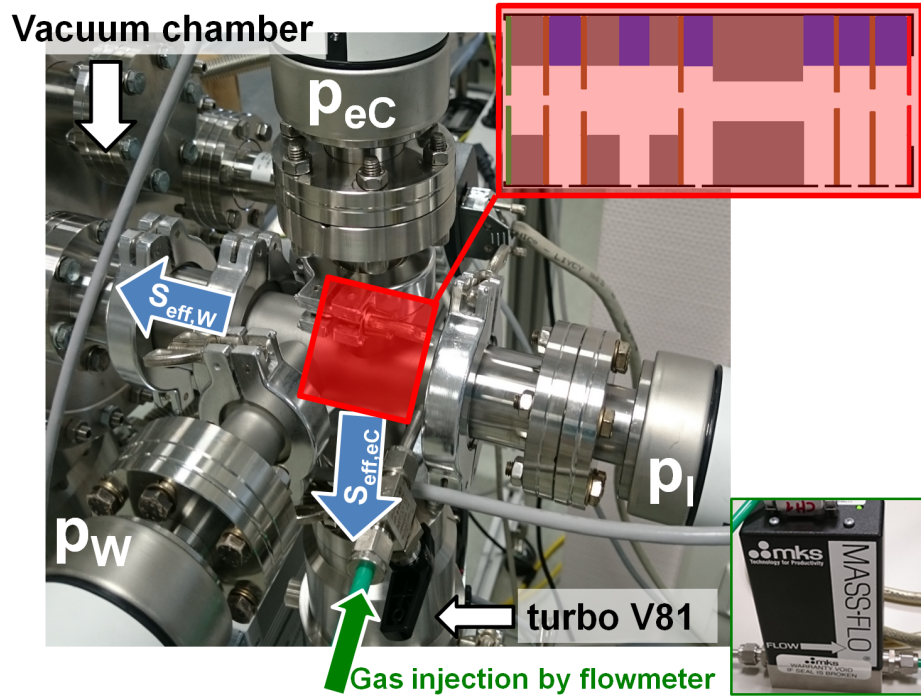
$$S_{\text{eff,pump-hole}} = \frac{S_{\text{eff,outside,eC}}}{1 + \frac{S_{\text{eff,outside,eC}}}{C_{\text{pump-hole,eC}}}} \quad (4.16)$$

In figure 4.30b a picture of the experimental gas conductance measurement setup is shown when mounted on the afore mentioned vacuum chamber. In order to obtain a stable pressure in the ionisation volume side a 10 sccm flowmetre [145] is connected to the gas injection port.

The obtained pressure results for the dummy model configuration with an inlet aperture and a Wehnelt aperture of 1 mm are listed in table 4.5.



a)



b)

Figure 4.30: a) Schematic of the experimental gas conductance measurement setup;  
b) Experimental gas conductance measurement setup for the tests with Nitrogen.

Experimental gas conductance tests							
Gas	Additional pumping channels	$S_{\text{eff,W}}$ [l/s]	$S_{\text{eff,outside,eC}}$ [l/s]	$S_{\text{eff,pump-hole}}$ [l/s]	$p_I$ [mbar]	$p_{eC}$ [mbar]	$p_W$ [mbar]
N <sub>2</sub>	closed	29.12	12.45	0	$1.0 \cdot 10^{-1}$	$5.60 \cdot 10^{-2}$	$1.75 \cdot 10^{-4}$
N <sub>2</sub>	open	29.12	12.45	0.56	$1.0 \cdot 10^{-1}$	$4.45 \cdot 10^{-3}$	$3.35 \cdot 10^{-5}$

Table 4.5: Experimental gas conductance tests with Nitrogen injection: dummy model of e-Column Model A and the experimental setup configuration shown in figure 4.30a.

What can be seen is that by opening the additional pumping channels along the e-Column tube the pressure at the Wehnelt chamber side  $p_W$  is lowered by a factor 5 compared to the case where the additional pumping channels are closed. A pressure of  $p_W = 3.35 \cdot 10^{-5}$  mbar is reached when the ionisation volume side is kept at a Nitrogen pressure of  $p_I = 1.0 \cdot 10^{-1}$  mbar. What should be mentioned here is that the dummy model e-Column tube has only seven pumping holes to allow additional pumping whereas the designed mechanical setup of e-Column Model A shown in figure 4.25 has in total 22 openings for the additional pumping purpose. It is estimated that the e-Column Model A will give a 2.5 lower  $p_W$  compared to the dummy model if it is integrated in the afore explained experimental setup, so that  $p_W$  drops to  $1.34 \cdot 10^{-5}$  mbar.

Therefore, it is possible at this stage to draw the intermediate conclusion that **the designed mechanical e-Column Model A allows the operation of a tungsten hairpin filament** ( $p_{W,\text{needed}} < 1.0 \cdot 10^{-4}$  mbar) when the ionisation volume side is set to a Nitrogen pressure of  $p_I = 1.0 \cdot 10^{-1}$  mbar. Unfortunately, the obtained experimental results highlight again that **the operation of a LaB<sub>6</sub> emitter seems to be not feasible with the designed e-Column Model A** ( $p_{W,\text{needed}} < 1.0 \cdot 10^{-6}$  mbar). The injection of Argon should give very similar results as the gas conductance simulations have already shown, see table 4.4.

#### Additional flight tube to decrease the gas conductance

**In order to achieve an even lower Wehnelt chamber pressure within the e-Column** than the afore determined value of  $p_W = 1.34 \cdot 10^{-5}$  mbar (Nitrogen injection) different options can be considered. **A first option is to introduce into the e-Column an additional cylindrical tube** in between the element  $L_{2\text{Start}}$  and the deflector (see figure 4.7) to decrease the conductance between these parts. When this additional tube is kept at the same potential as the element  $L_{2\text{Start}}$  the e-beam passes at the inside of the tube through a field free region and its path will not be influenced by the presence of the additional tube. Therefore, when having a look at the CPO-simulation results shown in table 4.2 for the size of the collimated e-beam at the end of the deflector region it is possible to deduce that an additional tube with an inner diameter of 1 mm will have no or very small impact on the transmission of the e-beam from the emitter region towards the lens 2 region.

In table 4.6 it is shown that by increasing the length of such an additional tube the optimised Wehnelt chamber pressure  $p_{W,\text{optimised}}$  can be gradually lowered until it reaches a value of  $1 \cdot 10^{-6}$  mbar or below at a length of approximately 500 mm, allowing for the operation of a LaB<sub>6</sub> emitter.

Gas	Additional tube			
	$d_{\text{tube}}$ [mm]	$l_{\text{tube}}$ [mm]	$p_I$ [mbar]	$p_{W,\text{optimised}}$ [mbar]
N <sub>2</sub>	1	100	$1.0 \cdot 10^{-1}$	$3.74 \cdot 10^{-6}$
N <sub>2</sub>	1	200	$1.0 \cdot 10^{-1}$	$2.19 \cdot 10^{-6}$
N <sub>2</sub>	1	300	$1.0 \cdot 10^{-1}$	$1.55 \cdot 10^{-6}$
N <sub>2</sub>	1	400	$1.0 \cdot 10^{-1}$	$1.20 \cdot 10^{-6}$
N <sub>2</sub>	1	500	$1.0 \cdot 10^{-1}$	$9.80 \cdot 10^{-7}$

Table 4.6: Estimated optimised gas conductance results when adding an additional cylindrical tube into the already designed e-Column setup.

As has already be shown by the CPO simulations in section 4.2 the use of a LaB<sub>6</sub> emitter is advantageous for the achievable ion source brightness. Unfortunately, the additional tube length increases the total e-Column length which is in contradiction to the intended compact design of the ion source. Even if it is possible to say that an electron column length of a few tens of centimetres still offers a quite practical size of the total design, it should be mentioned that the intention is to create an electron column which has similar dimensions as the ionisation region. Dimensions up to a few tens of millimetres are targeted and realised with the mechanical design shown in figure 4.25.

### Graphene grids as gas barrier

**A second option** in order to further decrease the Wehnelt chamber pressure as well as the pressure within the lens 1 and deflector region **is to introduce an electron transparent gas impermeable graphene grid** into the opening  $d_{I_n}$  of the lens 2 region of the e-Column.

Such graphene grids have already be used in SEM or TEM applications in order to be able to analyse objects that are embedded in a liquid or gaseous environment [146]. Researchers had to find a way to be able to enclose their samples within small cells and still be able to access them with the e-beam. Therefore, a perfect candidate material for such **e-beam transparent “windows”** is graphene an its derivates, for example graphene oxide (GO) [147, 146]. Those materials have a good electron transparency [148, 149], are highly gas or liquid impermeable [150] and have an extremely high mechanical stiffness [151, 152]. In [146] it has been reported that pure graphene films with thicknesses up to a few monolayers (one monolayer (ML) is about 0.34 nm thick) are even more e-beam transparent than the afore mentioned GO-films with thicknesses ranging from a few to a few hundred nanometres. The **graphene films** are estimated to withstand a  $\Delta p$  up to several bars and the covered holes had diameters up to 10  $\mu\text{m}$ . In [148] and [153] SEM and scanning transmission electron microscopy (STEM) investigations have been done with commercially available **graphene grids** having many holes and serving as sample or sample holder. The base of these structures is a copper grid on top of which a holey carbon film is deposited which serves as support film for the graphene layers. Similar graphene grids have been used here and are illustrated in figure 4.31a.

The advantage of using such graphene grids is that there is no need of increasing the length of the e-Column and a compact mechanical setup can still be realised. In figure 4.31a it can be seen that the initial grid state can be very different when received from the manufacturer. A well covered grid with as few as possible open holes needs to be chosen to perform the pressure tests, e. g. Grid B in figure 4.31a.



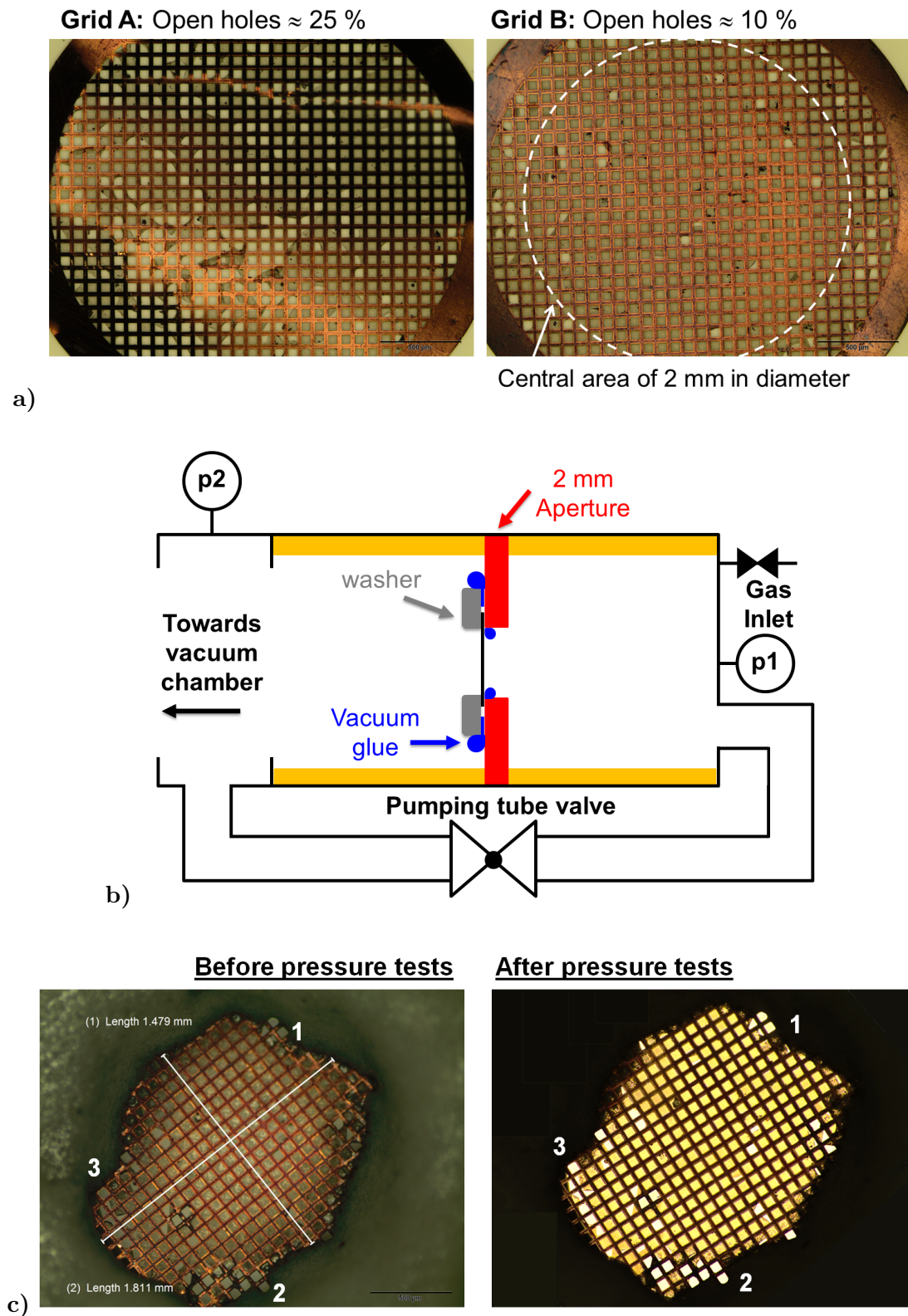


Figure 4.31: a) Optical microscopy images of two graphene grids in their initial state;  
 b) Illustration of the pressure test setup with Grid B;  
 c) Optical microscopy images of Grid B glued to the 2 mm aperture before and after the pressure tests (Numbers 1, 2 and 3 are shown for orientation purposes).

The experimental test configuration is shown in figure 4.31b. The 3 mm diameter grid is positioned concentrically on top of a disc so that it covers the 2 mm central hole. A small washer and vacuum glue is then carefully used to achieve gas tightness on the outer diameter of the graphene grid.

Gas	Graphene grid inserted	$p_1$ [mbar]	$p_2$ [mbar]	$p_1/p_2$
N <sub>2</sub>	NO	$1 \cdot 10^{-1}$	$1.40 \cdot 10^{-3}$	71.4
N <sub>2</sub>	NO	1	$2.00 \cdot 10^{-2}$	50.0
N <sub>2</sub>	YES	$1 \cdot 10^{-1}$	$2.50 \cdot 10^{-4}$	400.0
N <sub>2</sub>	YES	1	$2.10 \cdot 10^{-3}$	476.2

Table 4.7: Pressure test results for graphene Grid B glued to a 2 mm aperture.

Unfortunately, the central well covered area of Grid B could not be preserved during the glueing process, compare the central grid area in the right picture of figure 4.31a with the uncovered grid area in the left picture of figure 4.31c. The glueing process introduce at the border of the remaining free standing grid area additional open holes especially close to marker point 2 and 3. Nevertheless, pressure tests are performed to get an idea about the benefit for the pressure difference of  $p_1$  and  $p_2$  by the use of such a graphene grid.

As can be seen in figure 4.31b a tube is installed to connect the gas injection side to the pumping side. This allows that at the beginning of the gas injection tests the pressures  $p_1$  and  $p_2$  are in the same order of magnitude when the residual air is pumped out of the test setup. In this way any damaging of the grid due to bending related to a too high pressure difference of  $p_1$  and  $p_2$  should be avoided. After that the residual air was evacuated, the pumping tube valve is closed to isolate the injection from the pumping side and Nitrogen is again injected by the use of flowmetres [145]. The first measurements were done with an uncovered aperture of 2 mm in diameter, followed by measurements where the aperture was covered by the graphene Grid B. In both cases the pressure  $p_1$  is set to 0.1 mbar and 1 mbar.

The results for  $p_2$  can be found in table 4.7. What can be seen is that for each  $p_1$  - case the pressure on the pumping side  $p_2$  is clearly reduced when the graphene grid is inserted compared to the situation without grid. In the case of  $p_1 = 1 \cdot 10^{-1}$  mbar the benefit for the ratio  $\frac{p_1}{p_2}$  in the situation with the graphene grid is about a factor 6 compared to the situation without grid. Taking into account the fact that the afore mentioned glueing process is a non ideal fixation method, as it introduces additional open grid holes, leads to the conclusion that a better fixed grid with less open holes can very likely give a 10 times smaller pressure  $p_2$  compared to the open aperture structure. The pumping side of the here presented test setup can be interpreted as the lens 2 region within the real e-Column setup. **Therefore, by the use of a graphene grid it is possible to further lower the pressure** within this region which has as well a direct impact on the Wehnelt chamber, the deflection region and lens 1 region pressure. The afore determined Wehnelt chamber pressure of  $p_W = 1.34 \cdot 10^{-5}$  mbar can be further reduced by a factor in the range of 5 - 10, which would then allow the operation of a LaB<sub>6</sub> emitter within the e-Column ( $p_{W,needed} < 1 \cdot 10^{-6}$  mbar). When comparing the two pictures of figure 4.31c and considering the applied pressure values listed in table 4.7 it can in addition be concluded that **the graphene grids are able to withstand a pressure difference of nearly three orders of magnitude without that any additional open grid holes appear.**

#### Electron beam transmission tests

In order to assess the viability of using such graphene grids in the e-Column setup, experimental e-beam transmission tests were performed. These tests are carried out with an electron gun (e-Gun) EMG - 4212 from Kimball Physics [103], which covers the energy range up to 30 keV and



depending on the emitter kind used it produces spot sizes ranging from 25 mm down to small spots of 100  $\mu\text{m}$ . The e-Gun is mounted onto a vacuum chamber and is situated above a special measuring rod into which two small metal cylinders (inner diameter 6 mm and length 7 mm) can be placed below two 1.8 mm holes, see figure 4.32a and b. During the e-beam transmission tests one of these holes is covered by a graphene grid (Grid C) and the other hole is uncovered. As can be seen in figure 4.32c only a few open holes are present in the area of Grid C that is exposed to the e-beam so that the transmission results can be considered as the results for a well covered graphene grid.

The measuring rod is fixed to a XYZ - positioner in order to be able to move the rod below the e-beam. Furthermore, a view port is mounted on the opposite side of the XYZ - positioner so that the Caesium-Bromide (CsBr) screen, which is fixed to the inclined side face of the measuring rod, can be used to do a first coarse positioning below the electron gun (the e-beam generates a bluish spot on the CsBr - screen). During the measurements the working distance (distance from the end of the e-Gun to the measuring rod) is about 125 mm and the pressure within the vacuum chamber is in the range of  $1 \cdot 10^{-8}$  mbar to  $3 \cdot 10^{-8}$  mbar. After measuring the e-beam current without ( $I_0$ ) and with the grid ( $I_T$ ), **the experimental transmission of the graphene grid  $\text{Tr}_{\text{exp}}$**  is calculated by using the following equation:

$$\text{Tr}_{\text{exp}} = \frac{I_T}{I_0} \quad . \quad (4.17)$$

The transmission results for the analysed graphene Grid C can be found in table 4.8. **What can be seen is that the transmission goes up as expected with the increase in e-beam energy.** A theoretical estimation is done in order to compare those values to the experimental results. For this estimation the transmission  $\text{Tr}_{\text{Grid}}$  of the copper grid is determined and is defined as the open area of the grid holes divided by the total area of diameter  $d_{\text{Grid}} = 2.4$  mm, see figure 4.33. A value of  $\text{Tr}_{\text{Grid}} = 48.9$  % is determined. This value needs to be multiplied by the energy dependent transmission  $\text{Tr}_{2\text{ML-graphene}}$  of the 2 monolayer graphene film deposited on top of the copper grid. More information about the theoretically determined energy dependent graphene film transmission can be found in appendix B (section 7.2), where  $\text{Tr}_{2\text{ML-graphene}}$  is determined to be equal to 80.7 % for 2 keV and 68.9 % for 1 keV. **The final theoretical estimated transmission  $\text{Tr}_{\text{theo}}$**  is defined as  $\text{Tr}_{\text{theo}} = \text{Tr}_{\text{Grid}} \cdot \text{Tr}_{2\text{ML-graphene}}$  and the obtained results are listed in table 4.8.

**The determined experimental transmission values are in both energy cases lower than the theoretical estimation.** This can be mainly explained by the fact that in reality between copper grid and graphene film there is in addition a carbon support film with a cobweb like structure which additionally blocks part of the e-beam that hits the grid. Due to this cobweb structure it is very difficult to give an estimation of its contribution to the total grid transmission and was therefore not included in the theoretical estimation.

$p_{\text{Chamber}}$ [mbar]	e-beam E [keV]	$\text{Tr}_{\text{exp}}$ [%]	$\text{Tr}_{\text{theo}}$ [%]
$1.73 \cdot 10^{-8}$	1	24.1	33.7
$1.73 \cdot 10^{-8}$	2	32.4	39.5

Table 4.8: e-beam transmission test results for graphene Grid C.

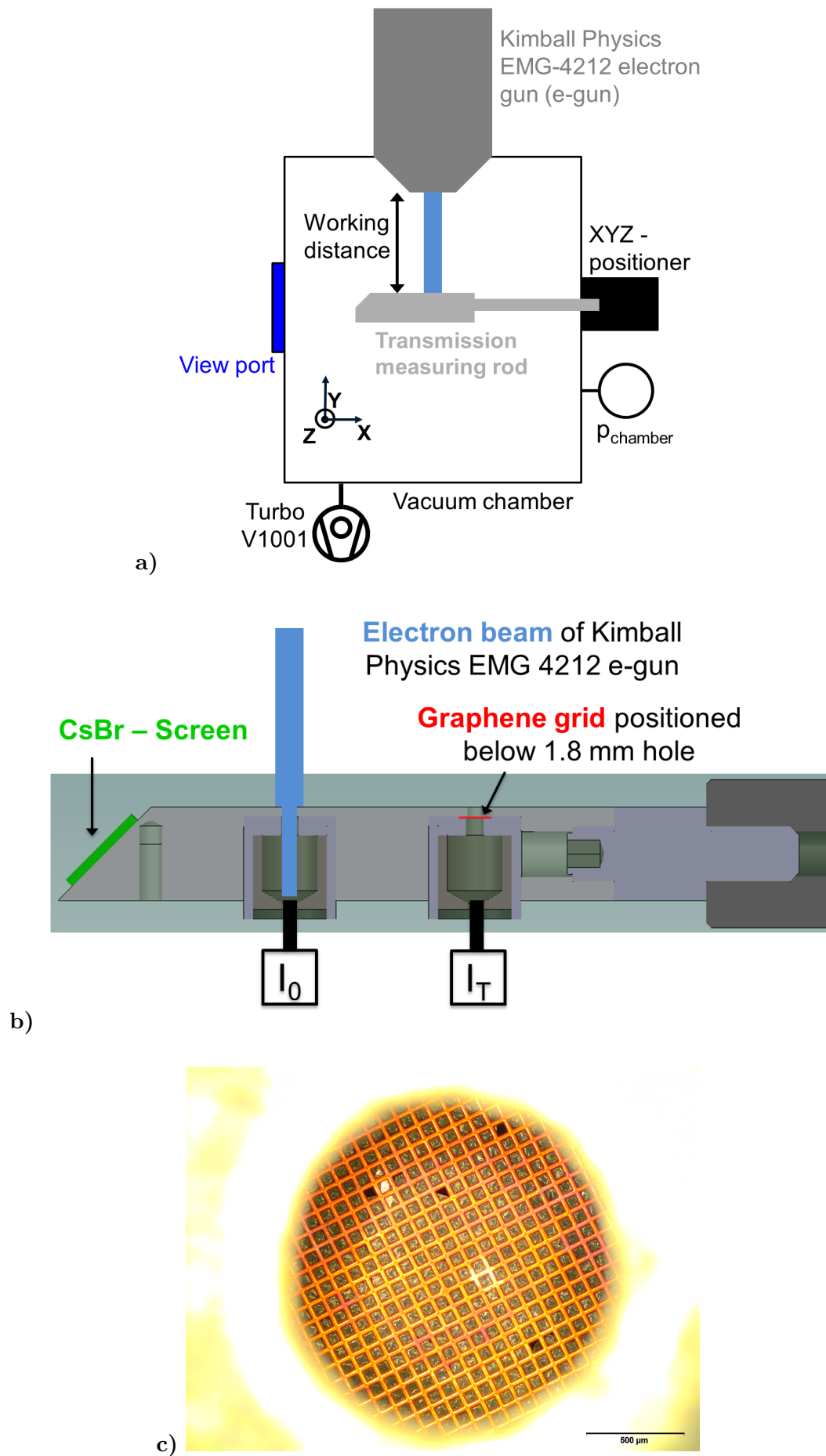


Figure 4.32: a) Illustration of the e-beam transmission measurement setup;  
 b) More precise illustration of the transmission measuring rod;  
 c) Optical microscopy image of the graphene grid (Grid C) inserted below the 1.8 mm hole of the measuring rod.

Furthermore, as mentioned as well in appendix B (section 7.2)  $\text{Tr}_{2\text{ML-graphene}}$  does not include the attenuation contribution of elastic scattering events within the graphene film which are of course present in reality and have an influence on the total graphene grid transmission. In section 4.2 the **e-beam energy of 1 keV** has been chosen as good compromise between ionisation volume size and EI-ionisation efficiency. **At this energy the transmission is determined to be only 24.1 %**. This means that if the graphene grid were incorporated immediately before the ionisation region (e-beam energy  $\approx 1$  keV) the e-beam current that can be used for the ionisation process is drastically reduced. This current reduction has a direct impact on the produced ion beam current and therefore on the achievable brightness of the ion source. One could consider positioning the graphene grid at a location of the electron column where the e-beam energy is higher than 1 or 2 keV and increase in this way the grid transmission. Nevertheless, in this way a decrease of the gas pressure within the complete e-Column is not any more achieved and the benefit of decreasing the gas ionisation losses disappears.

An aspect that currently has not been investigated in more detail is the time that the graphene grids could withstand the quite intense electron beam until irreversible changes in their morphological structure appear or until disruption of the thin graphene film occurs. In [146] the authors state that disruption of the graphene film occurs at a dose above  $1.6 \cdot 10^{-9} \text{ C}/\mu\text{m}^2$ . This dose value has been determined at electron beam energies larger than 10 keV. Therefore, for the purpose of using the graphene grids within the ion source concept presented here, more precise tests would be needed in order to find the maximal dose that the grids can withstand in the energy range of about 1 keV.

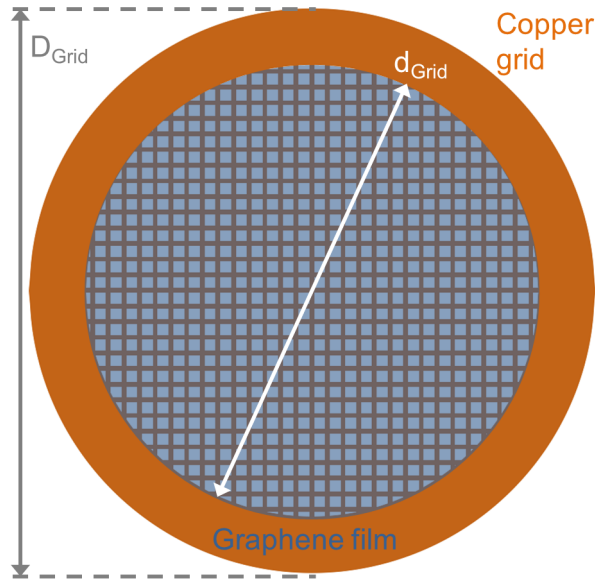


Figure 4.33: Illustration of the copper grids covered by the graphene film.

## 4.5 Summary and conclusions

- During the design development of the miniature IV EI ion source the e-Column CPO-simulations using thermionic emission from a tungsten hairpin filament show that at 1 keV of e-beam energy within the ionisation region a cylindrical IV diameter of about 100  $\mu\text{m}$  can be achieved. The e-beam energy case of 1 keV is determined to be the best compromise between the IV size and the ionisation efficiency for the further ion source development [154].
- The related ion beam CPO-simulations used for the ionisation region a parallel plate spacing of 1 mm and a plate potential difference of only 10 V. With an ionisation region pressure of 0.1 mbar and a circular ion extraction aperture of 100  $\mu\text{m}$  in diameter the extracted ion beam current is determined to be in the range of 20 - 45 nA depending on the simulated ion species ( $\text{Ar}^+$ ,  $\text{Xe}^+$  and  $\text{O}_2^+$ ) and the ion column extraction potential setting. The achieved ion beam source sizes, defined as FW50 value, lie in the range of 5 - 25  $\mu\text{m}$  and the corresponding half-opening angle range is 5 - 20 mrad. The determined  $B_r$  values are within 50 - 65  $\text{A}/(\text{m}^2 \text{sr V})$ .
- The change towards a  $\text{LaB}_6$  thermionic electron emitter is considered for the ion source design. It has a similar electron emission current but a smaller effective emission area compared to the hairpin filament. The benefit for the IV size is determined to be a reduction by a factor of about 2.5. Performed CPO-simulations show that when matching the extraction aperture size to the reduced IV dimension a decrease in ion beam source size and half-opening beam angle is obtained. As an outcome the reduced brightness  $B_r$  increases towards the range of 150 - 180  $\text{A}/(\text{m}^2 \text{sr V})$  for the case of an  $\text{Ar}^+$  ion beam containing about 5 nA of ion current and having sources sizes below 15  $\mu\text{m}$ , the extraction aperture diameter used is 40  $\mu\text{m}$ . This result is a clear improvement compared to conventional EI-ion sources with  $B_r$  of about 1  $\text{A}/(\text{m}^2 \text{sr V})$  but unfortunately the target of  $10^3 - 10^4 \text{ A}/(\text{m}^2 \text{sr V})$  could not be reached. The evaluation of the ion beam energy spread shows FWHM values  $\leq 1 \text{ eV}$  for the  $\text{Ar}^+$  ion beam case and reveal that the miniature IV EI ion source concept can produce very low energy spread ion beams.
- One challenge for the use of a  $\text{LaB}_6$  emitter is the needed operation pressure  $p_{\text{Em,Oper}}$  below  $1 \cdot 10^{-6}$  mbar. With the ionisation region at 0.1 mbar a pressure drop of more than five orders of magnitudes is needed across the compact e-Column. A mechanical e-Column design is used to perform related gas conductance simulations. In addition, experimental measurements are performed. The results further show that the low  $1 \cdot 10^{-5}$  mbar regime can be reached for the Wehnelt region. A first evaluated optimisation option consists in introducing an additional cylindrical flight tube of 1 mm in diameter within the e-Column which does not modify the e-beam path but is favourable for lowering the pressure. The needed length to get  $< 1 \cdot 10^{-6}$  mbar is about 500 mm which will considerably increase the length of the e-Column. This is in contradiction with the target of creating an e-Column with similar dimensions as the ionisation region, namely a few tens of millimetres, in order to create an overall compact ion source design. The second option is the use of electron transparent gas impermeable graphene grids within the e-Column. Related pressure tests show that the additional pressure difference benefit is about a factor of 10 which would allow the operation of the  $\text{LaB}_6$  emitter in a compact ion source design.

- However, the experimental e-beam transmission measurements through these graphene grids reveal that at 1 keV of e-beam energy the total grid transmission is about 24 %. This low value will result in a strongly reduced ionising e-beam current and therefore in a far lower ion beam current. The afore mentioned benefit for the reduced brightness by using the LaB<sub>6</sub> emitter would therefore be partially counteracted by the graphene grid implementation. Furthermore, the grids are in overall very fragile during handling and would therefore introduce further challenges to the mechanical design.
- At this point of the ion source development it is decided to not proceed to a prototype construction. The main fact that leads to this decision is that the maximal achievable  $B_r$  value determined by CPO-simulations is still quite far away from the initial target and in reality the achievable reduced brightness is most probably even below this theoretical estimation. By the use of extraction apertures below 100  $\mu\text{m}$  the gas conductance towards the ion column is low and the effect of ion beam broadening due to ion gas collisions will only be marginal. Nevertheless, the simulations do not take into account any space charge effects, misalignments of electrodes or imperfections of the electrode aperture shapes which in reality can have a degrading effect on the ion source performance. Furthermore, the revealed difficulty of achieving across the compact e-Column the needed pressure drop for the use of a low operating pressure electron emitter as the LaB<sub>6</sub> emitter substantiates even more the decision against a prototype construction.
- Another EI ion source concept idea that is expected to reach a higher reduced brightness and to be less restrictive in terms of electron emitter operation pressure is evaluated and described in more detail in section 5.

## 5 Electron impact radio frequency ion source

### 5.1 Ion source concept

In the ion beam CPO simulation part of section 4.2 it has already been mentioned that the reduced brightness of an ion source can be raised by going towards smaller ion beam source sizes or to achieved a very small angular ion beam spread. In addition it is evident that an increase in ion beam current also increases the ion beam reduced brightness. The ion source concept that is investigated in more detail in the following is based on the idea to **achieve a high ion beam current while keeping an ion beam source size of a few to a few tens of  $\mu\text{m}$  and a half-opening angle of a few to a few tens of mrad**. These values were determined for the afore investigated miniature ionisation volume ion source concept of section 4.

As can be seen in figure 4.14 the electron impact ionisation cross section for argon, xenon or oxygen reach their maximum for electron beam energies of 50 eV to 100 eV so that a high ionisation efficiency can be achieved. Furthermore, due to the fact that a high electron current can produce a high total ion beam current (equation 2.7) the thermionic emitter used for the ion source concept presented here is a **yttria-coated iridium ( $\text{Y}_2\text{O}_3 - \text{Ir}$ ) disc cathode** as shown in figure 5.1. These cathodes have a typical emission current density of  $0.5 \text{ A/cm}^2$ , a typical operation temperature of about 1800 K, a work-function of  $\phi = 2.6 \text{ eV}$  and emission areas of  $5.5 \cdot 10^{-3} \text{ cm}^2$  to  $1.95 \cdot 10^{-2} \text{ cm}^2$  depending on the cathode disc diameter. The emitted electron current can be several mA and a very big advantage of this kind of emitter is that they can be operated in quite pore vacuum conditions as their recommended operation pressure is  $p \leq 10^{-4} \text{ mbar}$  [155]. A complete illustration of the ion source concept idea can be seen in figure 5.2a. The extraction of the e-beam is performed by a triode electrode setup consisting of the disc cathode, the Wehnelt electrode to control the electron emission area and the anode to apply the extraction voltage. The e-beam is then collimated by a lens before it reaches the inlet electrode of the ionisation region at an energy of 100 eV.

Within the ionisation region the e-beam will be slowed down due to electron gas collisions and a retarding field  $F_{\text{e,retard}}$  which is shown in figure 5.2b. The energy loss of the e-beam within the ionisation region can be expressed by:

$$E(\Delta X) = E(X_0) - P_{\text{Stop}} \cdot \Delta X - e \cdot F_{\text{e,retard}} \cdot \Delta X \quad . \quad (5.1)$$



Figure 5.1: Illustration of the yttria-coated iridium disc cathode (modified from [156]).

$X_0$  represents the inlet electrode's X-position and  $\Delta X$  the distance from  $X_0$  in the direction of the e-beam.  $P_{\text{Stop}}$  is the stopping power due to the electron gas collisions defined by equation 3.40.  $E(X_0) = E_{e,0}$  is the electron beam energy when it is entering the ionisation region. **The range within the ionisation region at which the e-beam will be stopped** can be calculated by using  $E(\Delta X) = 0$  eV and reorganising equation 5.1 to:

$$R_{\text{Stop}} = \frac{E_{e,0}}{P_{\text{Stop}} + e \cdot F_{e,\text{retard}}} \quad (5.2)$$

In table 5.1 the electron gas collision stopping power  $P_{\text{Stop}}$  for different gases is listed together with the product of  $e \cdot F_{e,\text{retard}}$  which can be considered as the electric field stopping power. The pressure used is  $p_{\text{IR}} = 0.1$  mbar, the temperature is taken as  $T_{\text{IR}} = 298.15$  K and the field strength is chosen to be  $F_{e,\text{retard}} = 10$  V/cm. Furthermore, the extrapolated ranges  $R_{\text{Ex}}$ , already calculated in section 3.4, together with the total stopping ranges  $R_{\text{Stop}}$  are listed for comparison. See figure 5.3 for a graphical representation of the determined range results.

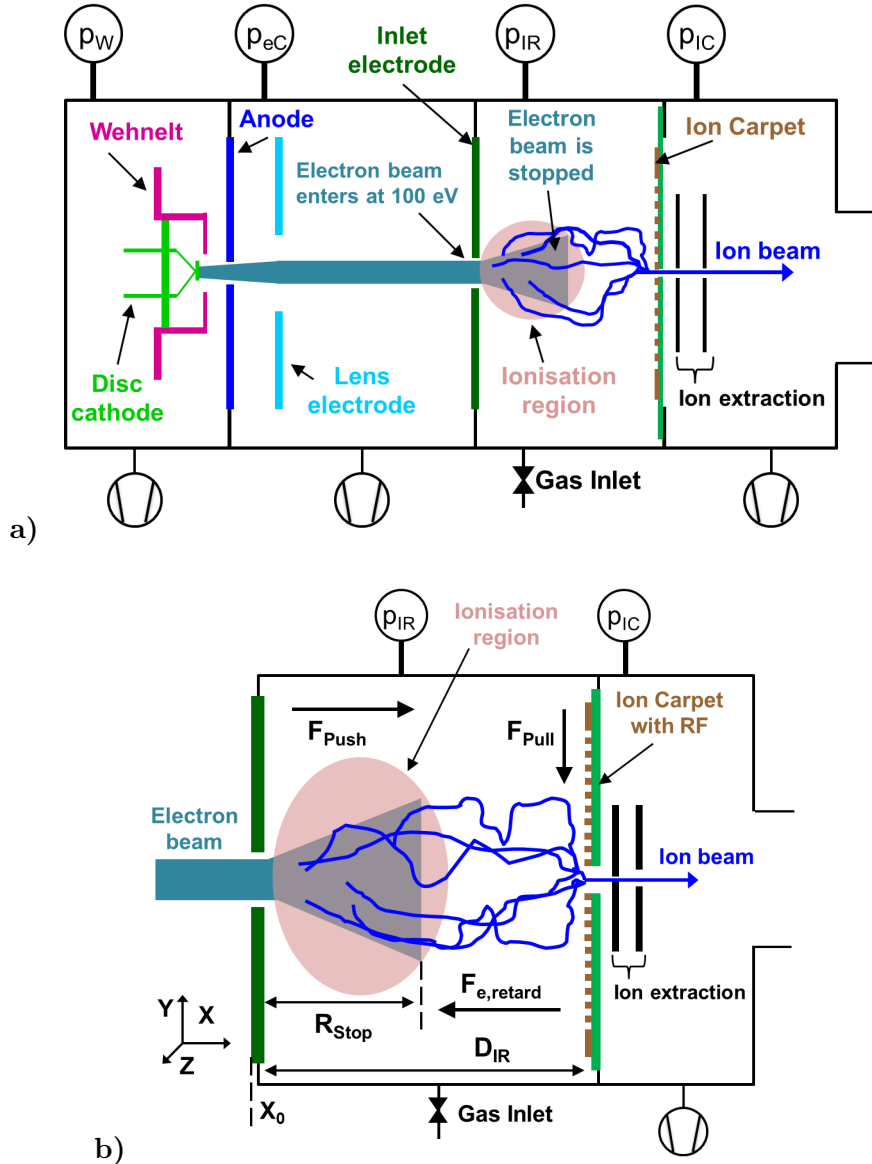


Figure 5.2: a) Illustration of the electron impact radio frequency ion source (EIRFIS) concept; b) More detailed representation of the electric fields within the ionisation region.

General parameters	$p_{\text{IR}}$ [mbar]	$T_{\text{IR}}$ [K]	$E_{e,0}$ [eV]	$F_{e,\text{retard}}$ [V/cm]
	0.1	298.15	100	10

Gas	$P_{\text{Stop}}$ [ $\frac{\text{eV}}{\text{cm}}$ ]	$e \cdot F_{e,\text{retard}}$ [ $\frac{\text{eV}}{\text{cm}}$ ]	$R_{\text{Ex}}$ [cm]	$R_{\text{Stop}}$ [cm]
He	3.32	10	29.36	7.51
Ne	16.72	10	5.82	3.74
Ar	29.79	10	3.27	2.51
Kr	59.52	10	1.64	1.44
Xe	89.70	10	1.09	1.00
O <sub>2</sub>	26.52	10	3.67	2.74
N <sub>2</sub>	23.22	10	4.19	3.01

Table 5.1: Comparison:  $P_{\text{Stop}}$  vs  $e \cdot F_{e,\text{retard}}$  and  $R_{\text{Ex}}$  vs  $R_{\text{Stop}}$  ( $P_{\text{Stop}}$  and  $R_{\text{Ex}}$  as in table 3.2).

What can be seen is that for helium the additional contribution of  $F_{e,\text{retard}}$  decreases strongly the stopping range for the 100 eV e-beam. For neon, argon, oxygen and nitrogen the reduction of the stopping range due to the additional contribution of  $F_{e,\text{retard}}$  is still visible but not as strong as for helium. For the heavier noble gases krypton and xenon it can be seen that the electron gas collisions represent the main contribution to the stopping range and  $F_{e,\text{retard}}$  only has a very small effect. A general conclusion that can be drawn here is that for all evaluated gases, except helium, the 100 eV e-beam is stopped within a range below 4 cm ( $p_{\text{IR}} = 0.1$  mbar,  $T_{\text{IR}} = 298.15$  K and  $F_{e,\text{retard}} = 10$  V/cm) so that the ionisation region size  $D_{\text{IR}}$  is set to 5 cm.

The SREM simulations of section 3.4 have already shown that due to the electron gas collisions the stopped e-beam covers a quite large volume which can as well be identified as the ionisation volume (IV). **In order to efficiently extract the produced ions from the large IV through an aperture at the end of the ionisation region a radio-frequency (RF) ion carpet will be used as illustrated in figure 5.2.**

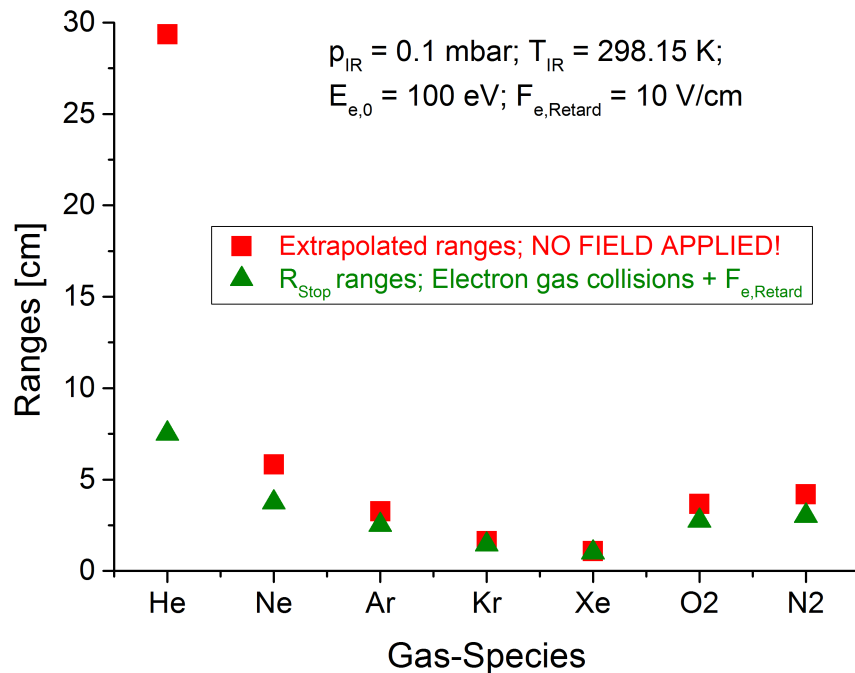


Figure 5.3: Electron extrapolated ranges  $R_{\text{Ex}}$  and total stopping ranges  $R_{\text{Stop}}$  for different gases ( $p_{\text{IR}} = 0.1$  mbar,  $T_{\text{IR}} = 298.15$ ,  $F_{e,\text{retard}} = 10$  V/cm and  $E_{e,0} = 100$  eV).



Closely behind the ion carpet central a small aperture in the range of 100  $\mu\text{m}$  will be positioned. In this way a quite large part of the extracted ion beam is cut off. This extraction aperture is needed to reach for the transmitted ion beam<sup>10</sup> a source size and half-opening beam angle comparable to the results of the miniature ionisation volume ion source concept (chapter 4).

The use of an ion carpet within an electron impact ionisation source has already been reported by Chaudhary et al. [121, 157]. A first difference between their ion source concept and the here investigated concept idea is that they use as electron beam emitter a deep ultraviolet range light-emitting diode (DUV LED) in combination with two micro channel plates (MCP). The light beam of the DUV LED is shining on the active MCP area in order to create a broad beam of electrons at the exit of the MCPs with 60 eV to 70 eV for ionisation. A second difference is that in their case the ionisation chamber is separated from the chamber where the ion carpet is located while in the concept idea presented here the ionisation region is located right above the ion carpet. The last major difference is that in [121] the ion carpet is used in direct current mode (DC-mode) so that only a DC-potential gradient is applied across the ring electrodes to efficiently extract the ions through the central carpet hole and no RF-potentials are applied.

As the ion source concept presented here combines electron impact ionisation with the use of a RF ion carpet, the concept will in the following be referred to as **Electron Impact Radio Frequency Ion Source**, short EIRFIS.

## 5.2 CPO simulations

### 5.2.1 Electron column investigations

Some preliminary SIMION test simulations are used to obtain an idea about how to set up the EIRFIS e-Column in order to be able to guide an electron current of a few hundreds of  $\mu\text{A}$  into the ionisation region. These test simulations will not be discussed in detail here but they are the basis for the **design of the mechanical setup of the EIRFIS prototype**. The e-Column and ionisation region are shown in figure 5.4a, the ion extraction is not yet included. Furthermore, a total 3D representation can be seen in figure 5.4b for a better illustration. The ceramic support structure can be introduced into the vacuum tube from the ionisation region side and 2 O-rings are used to achieve gas tightness on its outside diameter between the ionisation region and the e-Column as well as between the e-Column and the Wehnelt region. Four pumping channels (2 in y- and 2 in z-direction) within the support structure guarantee that the e-Column can be efficiently pumped via a connected turbo pump during the ion source operation. Ceramic spacers are used to electrically isolate the different e-Column electrodes from each other and two potential connector rings are used to apply the anode and lens potential onto the much thinner disc electrodes. The inlet electrode is fixed from the right side onto the support structure.

As can be seen in figure 5.5a all e-Column electrodes, the potential connectors, the inlet electrode, the ion carpet (simplified here as solid disc electrode) and the vacuum tube are introduced into a SIMION PA file (the electrodes' colour within the PA is meant to ease the comparison with the mechanical model). None of the insulating parts are taken into account within the shown PA file which has a cylindrical symmetry with respect to the X-axis. In parallel to the CPO simulations gas conductance calculations are performed. It is determined that an anode aperture of  $d_A = 0.8 \text{ mm}$  combined with an inlet electrode aperture of  $d_W = 1.5 \text{ mm}$  is a good compromise between a quite high e-beam transmission into the ionisation region and a

<sup>10</sup>With transmitted ion beam is meant the ion beam that leaves the ion extraction column of the ion source.

good enough pressure gradient across the e-Column to be able to operate the disc cathode when  $p_{IR} = 0.1$  mbar. Further details about the performed gas conductance calculations can be found in section 5.4.1. The different geometrical parameters of the EIRFIS e-Column are illustrated in figure 5.5 and listed in table 5.2.

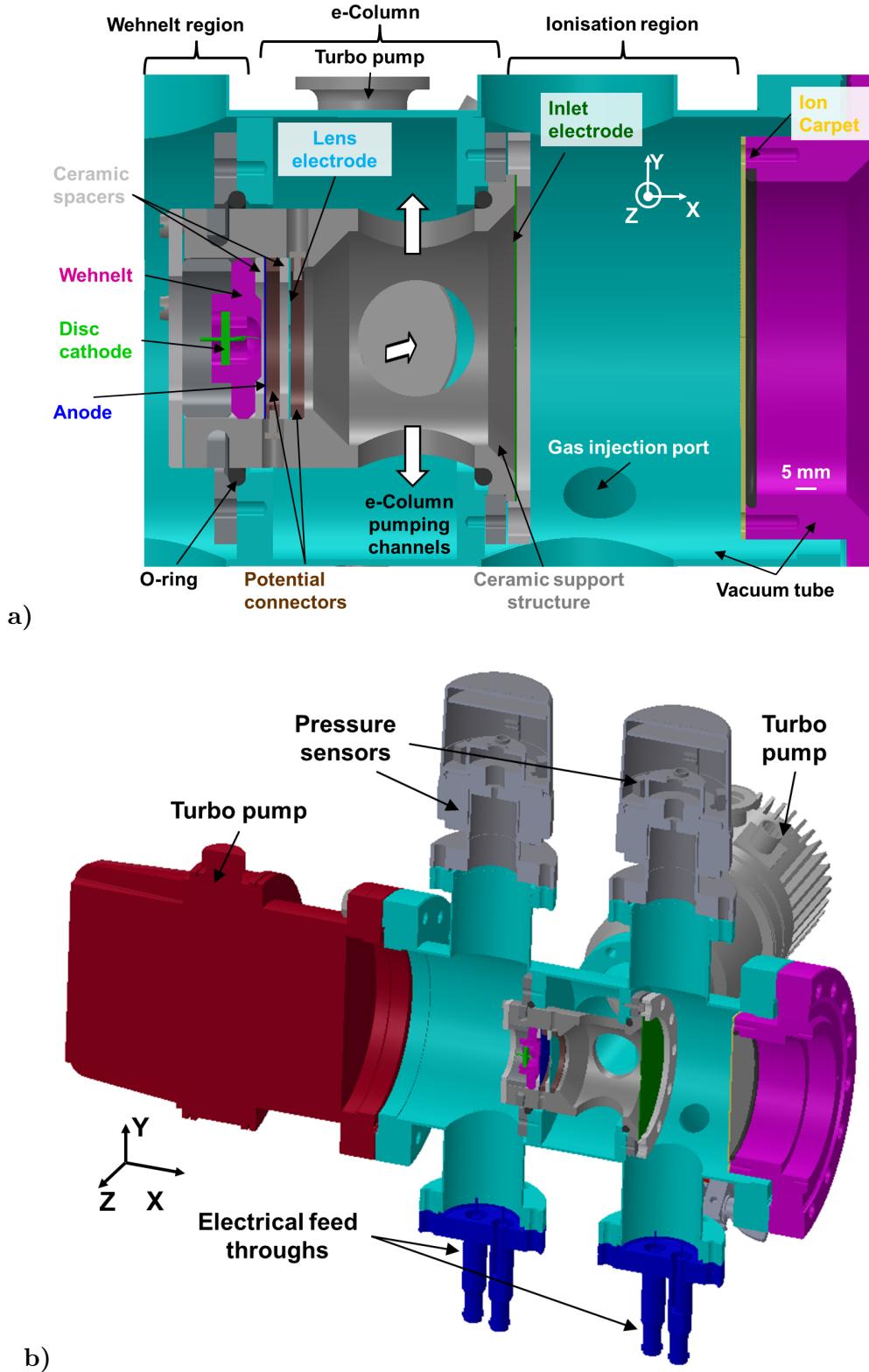


Figure 5.4: EIRFIS mechanical model schematic:

- a) e-Column and ionisation region (XY-cut view);
- b) e-Column and ionisation region (3D view).

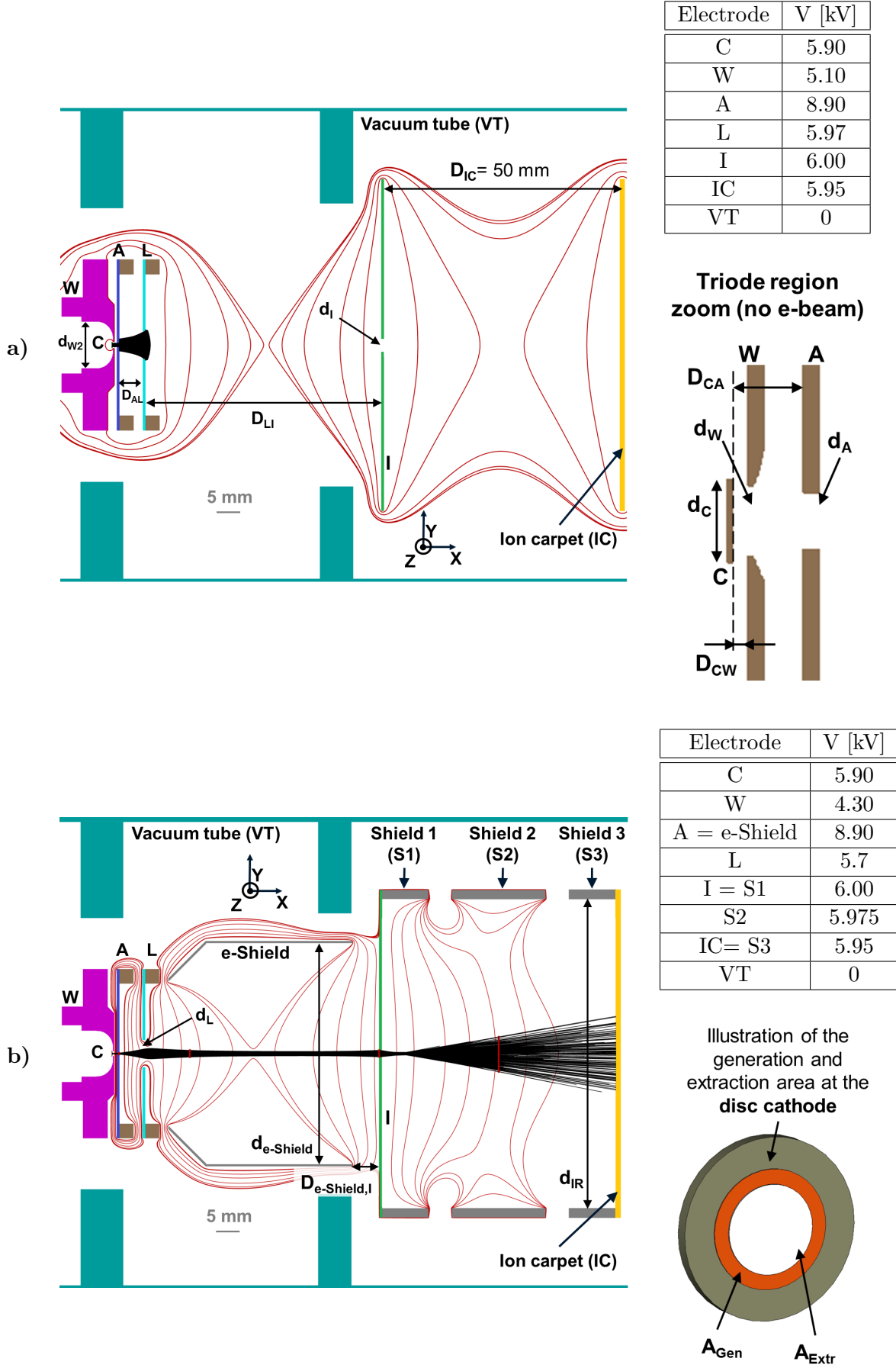


Figure 5.5: a) EIRFIS e-Column simulation with vacuum tube included;  
b) EIRFIS e-Column simulation with vacuum tube and shielding included  
(The geometrical parameters can be found in table 5.2).

	size [mm]		size [mm]		size [mm]
$d_{W2}$	13	$d_I$	1.5	$D_{AL}$	5
$d_W$	1	$d_{e-Shield}$	47	$D_{LI}$	50
$d_C$	1.22	$d_{IR}$	66	$D_{e-Shield,I}$	6
$d_A$	0.8	$D_{CW}$	0.2		
$d_L$	6	$D_{CA}$	1		

Table 5.2: Geometrical parameters for the designed EIRFIS e-Column and ionisation region.

The inlet electrode during the **EIRFIS e-Column simulations** is set to 6 kV as this potential defines the energy of the ion beam leaving the ion extraction column, which is not included in the here presented e-Column simulations. The extraction potential  $\Delta V_{\text{Extr}}$  is fixed to 3 kV and the cathode inlet electrode potential difference to  $\Delta V_{C-I} = -100$  V, which produces the desired energy of 100 eV when the e-beam is passing electrode I into the ionisation region.

What can be clearly seen in figure 5.5a is that the e-beam is reflected very close behind electrode L. This is due to the fact that the vacuum tube potential kept at 0 V influences the potential distribution in between electrodes L and I so much that the e-beam can not any more pass this region. Therefore in order to keep the e-Column at potentials of a few kV it is **mandatory to introduce an additional shielding electrode** in the space between electrode L and I as shown in figure 5.5b. As this region needs to be pumped through the pumping channels within the ceramic support structure it is mandatory to use a shielding electrode allowing pumping. For this reason it is simulated within SIMION as a mesh following the inner shape of the ceramic support structure with a hole size of 0.7 mm as this corresponds to the smallest mesh size available for protection grids of turbo pumps [144]. The idea is to create the shielding electrode with such a turbo pump grid in order to still have good pumping capabilities through the four pumping channels. Furthermore, as can be seen in figure 5.5b the e-Column shield (e-Shield) is disconnected from the lens and the inlet electrode and is kept at the same potential as the anode. In this manner the anode, the lens electrode and the e-Shield form an Einzel lens and the e-beam is kept at a high energy until the end of the e-Shield region and is only slowed down towards 100 eV immediately before the ionisation region. In this way the e-beam current losses due to residual gas ionisation within the e-Column are kept small.

Shielding electrodes are as well included in a very simple configuration within the ionisation region, see figure 5.5b. Shield 1 is always kept at  $V_I$ , Shield 3 at  $V_{IC}$  and Shield 2 at  $(V_I + V_{IC})/2$ . During the e-beam simulations the ionisation region potentials create a retarding field of 1 V/mm for the e-beam<sup>11</sup>. The PA file used for these e-beam simulations with included shielding electrodes is a 3D-PA with Y- and Z-direction symmetry. In figure 5.5b the XY-cut view of a performed simulation is shown. The corresponding 3D-view can be seen in figure 5.6.

An evaluation of the effective extraction area  $A_{\text{Extr}}$ , the extraction factor  $f_{e,\text{Extr}}$ , the size of the collimated e-beam and the e-Column transmission factor  $f_{e,\text{Tr}}$ <sup>12</sup> is done by varying the potential difference between Wehnelt and cathode:  $\Delta V_{WC} = \Delta V_{\text{bias}}$ . As illustrated in figure 5.5b the electrons are generated uniformly within a certain generation area  $A_{\text{Gen}}$  very close to the cathode surface (always  $A_{\text{Gen}} > A_{\text{Extr}}$ ). As already explained in section 4.2 the Box-Muller method is used within the SIMION workbench programme to generate a Maxwell-Boltzmann velocity/energy distribution for the created electrons.

<sup>11</sup>The e-beam is not stopped within the ionisation region as no electron gas collisions are simulated but only the retarding field effect is present during the e-Column simulations.

<sup>12</sup>Defined as ratio between the number of electrons passing electrode I and the number of extracted electrons.

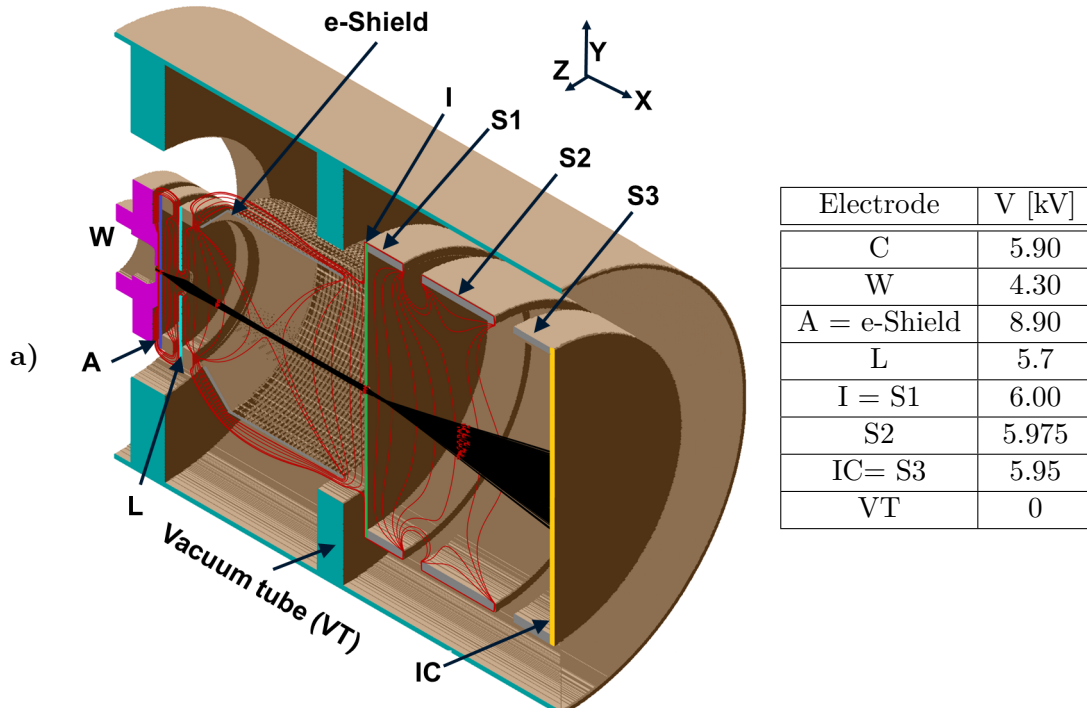


Figure 5.6: EIRFIS e-Column simulation with vacuum tube and shielding:  
3D-cut view of the 3D-PA file with Y- and Z-symmetry.

The emission angles are chosen randomly with an initial velocity vector always pointing into the positive half space in X-direction. The cathode temperature is set to 1800 K and the work function  $\phi$  to 2.6 eV. In each  $\Delta V_{\text{bias}}$  case the lens electrode potential is tuned in order to find the smallest e-beam radius  $r_{\text{e-beam},90\%,\text{Inlet}}$  containing 90 % of the beam current in front of the inlet electrode.

As already mentioned the electrode combination chosen for the e-Column in figure 5.5b has the effect that the e-beam is retarded at the end of the e-Shield region so that the collimated e-beam increases in size just before the inlet electrode. Moreover, it forms a crossover in close vicinity to the inlet electrode within the ionisation region. **In figure 5.7 the results for the EIRFIS e-Column simulations can be seen.** In the evaluated  $\Delta V_{\text{bias}}$  range the effective extraction area radius  $r_{\text{eff,Extr}}$  is clearly below the disc cathode radius. The value of  $r_{\text{e-beam},90\%,\text{Inlet}}$  becomes at  $\Delta V_{\text{bias}} \geq -1500$  V bigger than the inlet electrode aperture radius which is immediately visible in a quite fast drop of the transmission factor  $f_{\text{e,Tr}}$ . The extracted e-beam current  $I_{\text{e,Extr}}$  is calculated by equation 4.7 using as  $J_{\text{thermionic}}$  a value of  $0.5 \text{ A/cm}^2$  as typical value for the  $\text{Y}_2\text{O}_3 - \text{Ir}$  disc cathodes<sup>13</sup> and the transmitted e-beam current is calculated by the product of  $I_{\text{e,Extr}}$  and  $f_{\text{e,Tr}}$ . The curve for  $I_{\text{e,Extr}}$  is continuously increasing with less and less  $\Delta V_{\text{bias}}$  applied which is related to the continuously increasing size of the extraction area and extraction factor  $f_{\text{e,Extr}}$  reaching at  $\Delta V_{\text{bias}} = -1300$  V a value of about 75 %. For the transmitted e-beam current  $I_{\text{e,Tr}}$  it can be seen that at the beginning it closely follows the increase of  $I_{\text{e,Extr}}$  and at the end for  $\Delta V_{\text{bias}} \geq -1500$  V it reaches a plateau at about 430 to 500  $\mu\text{A}$ . As the chosen EIRFIS prototype e-Column setup (figure 5.5b) will be favourable to efficiently reduce e-beam losses due to less residual gas ionisation within the e-Column, **it is estimated that in reality the maximum e-beam current that enters the ionisation region is about 400  $\mu\text{A}$ .**

<sup>13</sup>By using  $\Delta V_{\text{Extr}} = 3 \text{ kV}$ ,  $D_{\text{CA}} = 1 \text{ mm}$  and equation 3.11 it can be calculated that  $J_{\text{LC}} \approx 38 \text{ A/cm}^2$  so that no space charge limitation is expected.

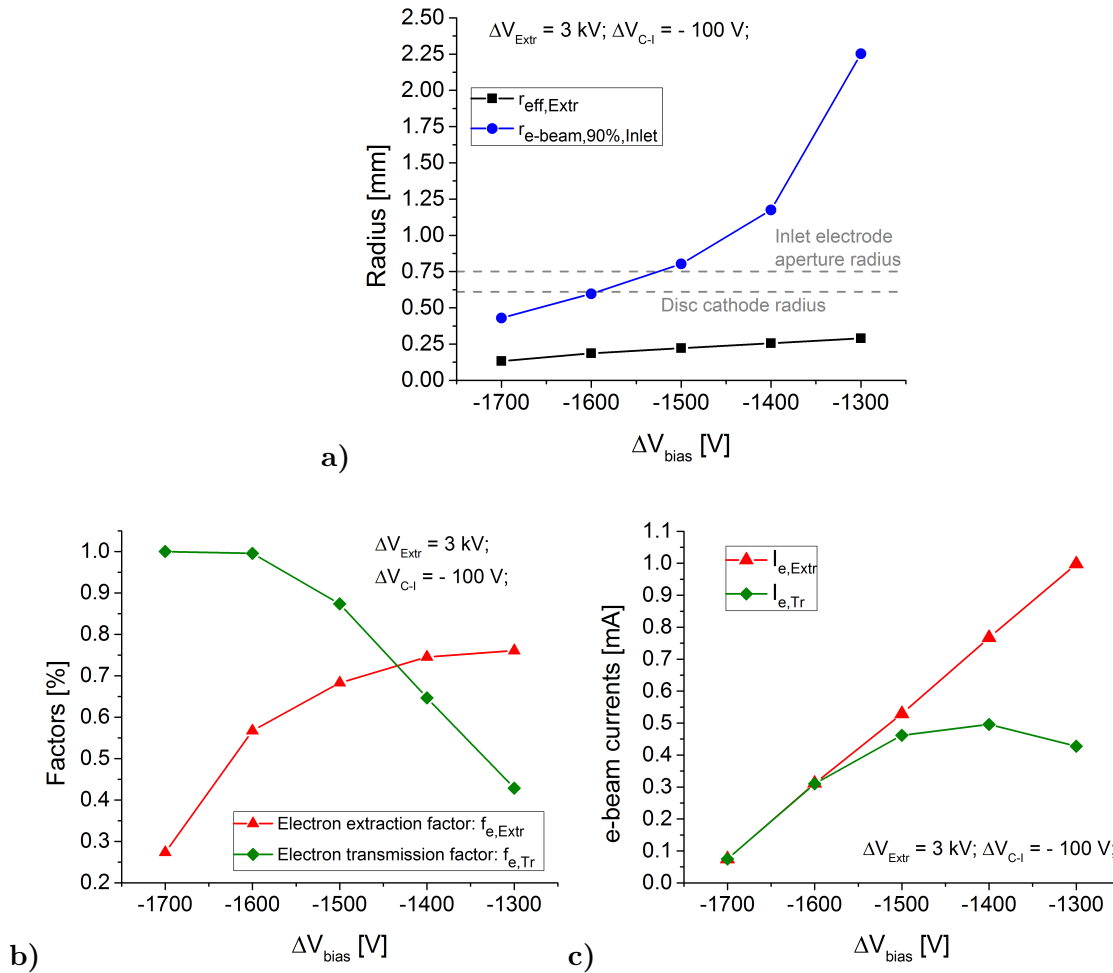


Figure 5.7: Results of the EIRFIS e-Column simulations:

- a) Extraction area radius and 90 % e-beam radius at the inlet electrode;
- b) Extraction and transmission factor;
- c) Estimated extraction and transmission e-beam current.

In order to complete this first CPO simulation section the total potential settings that are used to obtain the results shown in figure 5.7 are listed in table 7.2 of appendix C (section 7.3). Furthermore, a more detailed representation of the e-beam YZ-cross sections within the ionisation region can be found in the appendix C.

### 5.2.2 Ion generation and ion carpet extraction

The second kind of CPO simulations that is performed is related to the generation of ions within the ionisation region, the extraction by the ion carpet and the characterisation of the complete ion extraction column. In figure 5.8 a schematic of the mechanical setup of the ionisation region with shielding and the ion extraction column can be seen. For a further illustration a 3D-view can be found in figure 7.21 of appendix C (section 7.3). This electrode configuration is implemented into a SIMION PA-file being cylindrical symmetric about the X-axis as shown in figure 5.9a, where the different geometrical parameters can also be found. The shielding of the ionisation region is done by the three electrodes S1, S2 and S3 which have a special shape in order to guarantee at the same time an effective shielding of the vacuum tube at 0 V and a good gas flow through the channels in between those electrodes. The ion extraction column is composed of three electrodes Ex1, Ex2 with a top hat shape and the flat ground plate G. The potential difference between the inlet electrode I and the electrode G

$\Delta V_{IC}$  defines the end energy range of the ion beam leaving the extraction column.

Results of some test CPO simulations with  $Ar^+$  ions in 0.1 mbar argon gas (not treated in detail here) are combined with information given by PCB design manufacturers (e. g. from [158]) to find a good and in reality feasible electrode structure for the ion carpet. In figure 5.9b more details are shown related to the exact configuration of the ion carpet. The gap  $g$  between the ring electrodes is equal to 0.25 mm, the pitch  $\Delta$  is equal to 0.75 mm so that the width  $w$  of the rings is equal to 0.5 mm. The thickness (height)  $h$  of the carpet electrodes is 0.1 mm corresponding to a standard thickness of the copper film that can be deposited by PCB technology. Two slightly different **Ion Carpets A and B** are investigated during the CPO simulations presented here. Both have a central hole of  $d_0 = 1$  mm and 26 ring electrodes ( $E_1$  to  $E_{26}$ ) covering an area of  $d_{RF-rings} = 39.5$  mm. In both cases a **linear DC-potential gradient** is applied to the ring electrodes and the DC-potential of each ring  $V_{DC,E_i}$  can be calculated by:

$$V_{DC,E_i} = V_{IC} + (i - 1) \cdot \frac{\Delta V_{DC}}{(N_{rings} - 1)} \quad . \quad (5.3)$$

Where  $V_{IC}$  is the ion carpet DC-base potential,  $\Delta V_{DC}$  the potential difference applied to ring  $E_{26}$  in order to create the linear potential gradient,  $i$  the ring index and  $N_{rings}$  the total number of rings. To each ring electrode a **RF varying potential with frequency  $f_{RF}$  and amplitude  $V_{Amp,RF}$  is added to the DC-potential** so that the final potential can be expressed as:

$$V_{E_i} = V_{IC} + (i - 1) \cdot \frac{\Delta V_{DC}}{(N_{rings} - 1)} + V_{RF_i} \quad . \quad (5.4)$$

The RF-potentials applied to adjacent rings have the same  $V_{Amp,RF}$  but are out of phase by  $180^\circ$  as illustrated in figure 5.9b. This means that for odd numbered rings the RF-potential can be expressed by  $V_{RF_i} (i = \text{odd}) = V_{Amp,RF} \cdot \sin(2\pi f_{RF} \cdot t)$  and for the even numbered rings very similar by  $V_{RF_i} (i = \text{even}) = -V_{RF_i} (i = \text{odd})$ .

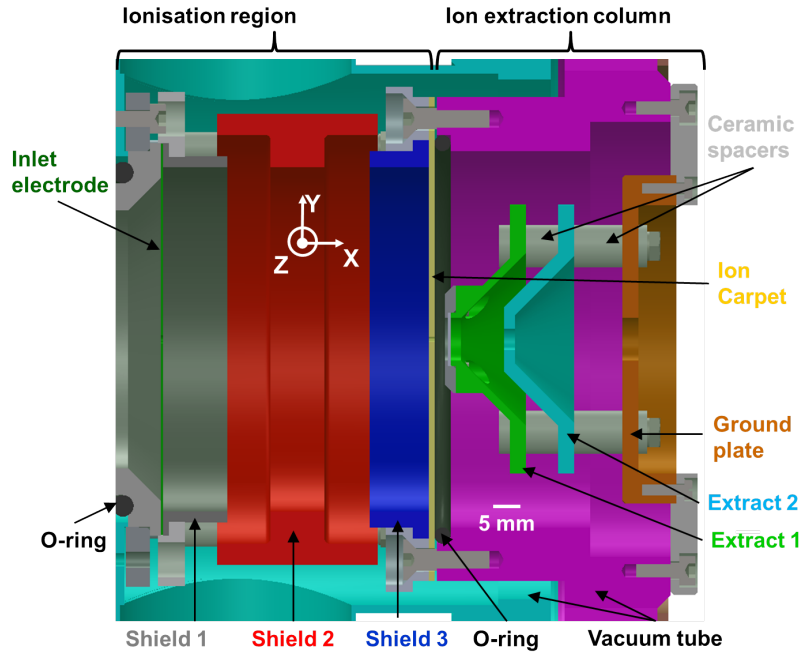


Figure 5.8: EIRFIS mechanical model schematic: Ionisation region (with shielding) and ion extraction column (XY-cut view).

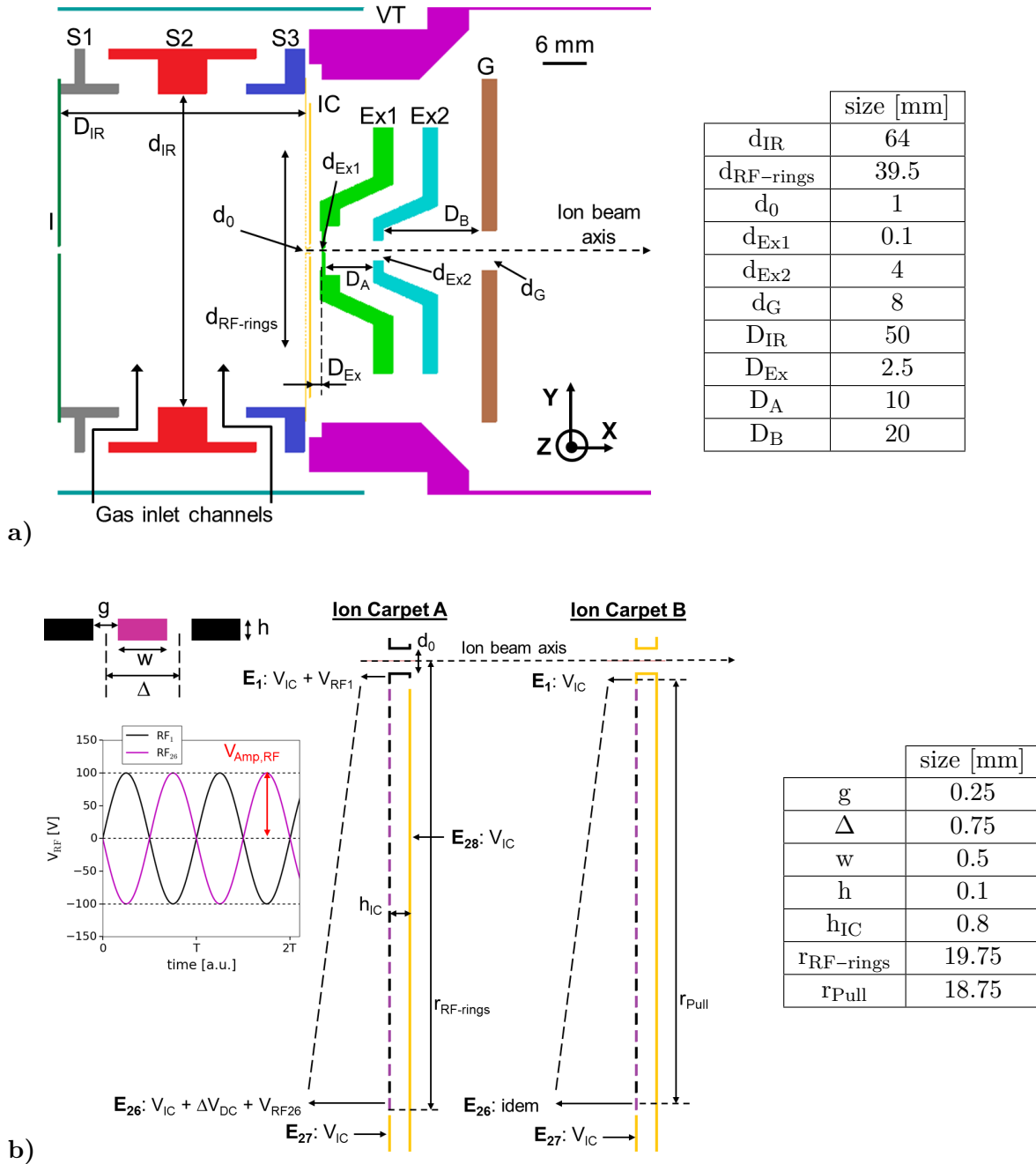


Figure 5.9: a) PA-file of the EIRFIS ionisation region and ion extraction column (XY-cut view);  
b) Illustration of the Ion Carpet A and B setups, dimensions and applied potentials.

In the case of Ion Carpet A the RF-potential is as well applied to the central hole electrode  $E_1$  which is isolated from the carpet back side electrode  $E_{28}$  kept at the DC-base potential  $V_{IC}$ . By applying the RF-signal to  $E_1$  it is expected that high ion extraction efficiencies can be obtained as the majority of the ions is prevented from hitting any carpet electrode until they are extracted through the central hole. Nevertheless, it can be expected that a large energy spread of the extracted ion beam is obtained as the ions pass through a region of varying potential in between the backside of the ion carpet and the extraction electrode  $Ex1$ . In contrast to this, in the case of Ion Carpet B the central hole electrode  $E_1$  is connected to the back side electrode and no RF-potential is applied to it (fixed at  $V_{IC}$ ). This second configuration will most probably result in lower ion extraction efficiencies as more ions hit the central ring but it is expected that Ion Carpet B is favourable to obtain a lower energy spread compared to Ion Carpet A.



Both ion carpets have on their front side a large annular electrode  $E_{27}$  surrounding the RF ring electrodes which is as well kept at the constant potential  $V_{IC}$ . In figure 5.2b the electrical fields  $F_{Push}$  and  $F_{Pull}$  are illustrated and in the following these fields are defined as:

$$F_{Push} = \frac{V_I - V_{IC}}{D_{IR}} \quad \text{and} \quad F_{Pull} = \frac{\Delta V_{DC}}{r_{Pull}} \quad . \quad (5.5)$$

For both ion carpets the parameter  $h_{IC}$  between the front side and back side electrodes is set to 0.8 mm corresponding to a standard thickness of the insulating layer for structures produced by PCB-technology. This insulating layer is not taken into account by the CPO simulations. In appendix C (section 7.3) 3D views of the ion carpets can be seen in figure 7.22.

**A first evaluation** is performed by using equation 3.17 in order to see **if a stable ion motion can be realised** by using the afore mentioned Ion Carpets A and B. The strength of the push field  $F_{Push}$  is taken as 1 V/mm and the ionisation region pressure as 0.1 mbar. These are the conditions for which the electron stopping ranges have been determined in section 5.1 and which led to the decision of fixing  $D_{IR}$  to 50 mm. The temperature of the ionisation region is taken as 298.15 K and the ion mobility of  $Ar^+$  ions in 0.1 mbar argon gas is determined to  $K = 1.69 \text{ m}^2 \cdot \text{s}^{-1} \cdot \text{V}^{-1}$  (defined in equation 3.17) for which a reduced mobility of  $K_0 = 1.53 \cdot 10^{-4} \text{ m}^2 \cdot \text{s}^{-1} \cdot \text{V}^{-1}$  is used [159]. The frequency range for which the parameters  $Q_d/\kappa$  and  $Q_{pr}$  (as well defined by equation 3.17) are evaluated spans from 1 MHz to 12 MHz and the RF-amplitude  $V_{Amp,RF}$  goes up to 150 V. In figure 5.10 it can be seen that the corresponding parameter range is clearly situated in the region defined as the stable parameter region. It can be concluded that the Ion Carpets A and B will have a positive effect on the extraction of  $Ar^+$  ions at the conditions evaluated here.

The ion column CPO simulations are started by **determining the extraction efficiency of both Ion Carpets A and B for  $Ar^+$  ions by varying the RF frequency and amplitude** in the same ranges as stated here before for the evaluation of the ion motion stability.

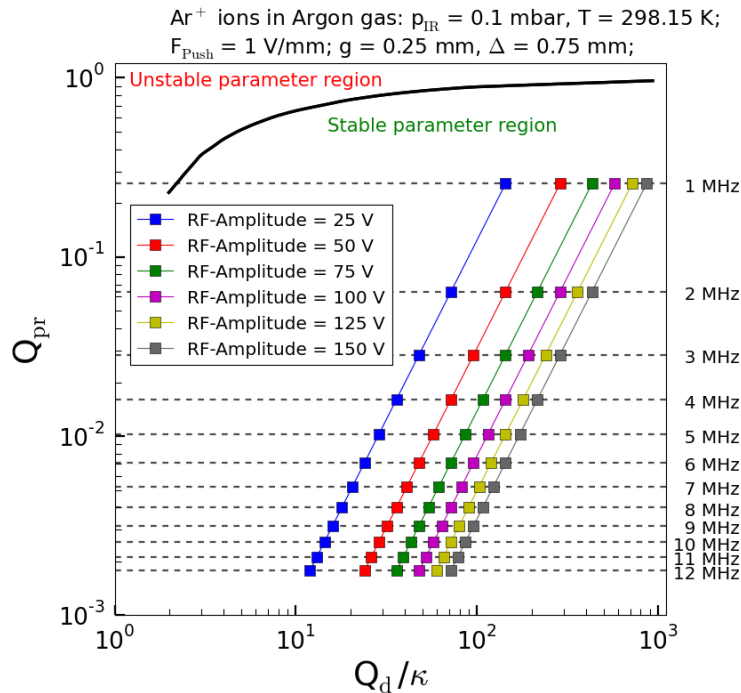
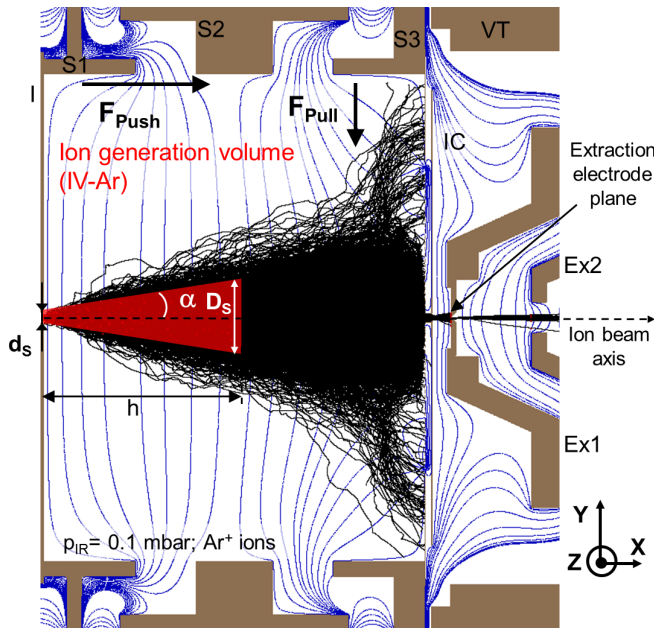


Figure 5.10: Evaluation of the  $Ar^+$  motion above Ion Carpet A/B (parameters shown in figure).

The push field  $F_{\text{Push}}$  is fixed to 1 V/mm and the pull field  $F_{\text{Pull}}$  is set to about 1 V/mm by using  $\Delta V_{\text{DC}} = 19$  V ( $r_{\text{Pull}} = 18.75$  mm). The potential difference between the DC-base potential  $V_{\text{IC}}$  and the first extraction electrode (Ex1) is fixed to  $\Delta V_{\text{IC-Ex1}} = V_{\text{IC}} - V_{\text{Ex1}} = 500$  V. During the extraction simulations the SIMION hard sphere ion gas collision model HS1 is taken into account within the ionisation region with  $p_{\text{IR}} = 0.1$  mbar, as well as inside the central carpet hole with  $p_{\text{IC-d}_0} = 0.01$  mbar and in between the ion carpet IC and Ex1 with  $p_{\text{IC-Ex1}} = 0.001$  mbar. This pressure gradient is used as a first approximation (Test-pressure-gradient).

In figure 5.11 the  $\text{Ar}^+$  trajectories are shown for the case of Ion Carpet B with  $f_{\text{RF}} = 8$  MHz and  $V_{\text{Amp,RF}} = 100$  V, the remaining potentials are listed within the figure. **The ionisation volume (IV) is a truncated cone volume** and its height  $h$  is fixed to 25.1 mm corresponding to the e-beam stopping range listed in table 5.1 for a 100 eV e-beam in 0.1 mbar argon gas and  $F_{\text{e,Retard}} = 1$  V/mm. The smaller diameter of the IV is set to  $d_s = 1.5$  mm corresponding to the inlet electrode aperture size  $d_i$ . The end diameter of IV is fixed at  $D_s = 10$  mm leading to an angle  $\alpha$  close to  $10^\circ$  (in the following this IV case will be referred to as IV-Ar). To use a truncated cone is an approximation of the obtained e-beam trajectories within the ionisation region shown in figure 5.5b where the e-beam first focusses and then widely spreads up. During the e-Column simulations the e-beam spread angle is below  $10^\circ$ . Taking  $\alpha$  here as  $10^\circ$  within the IV-Ar setting accounts for the fact that in reality the e-beam spread is enhanced due to electron gas collisions which are not taken into account during the EIRFIS e-Column CPO simulations. More details about the ion starting position generation can be found in appendix C (section 7.3). The initial ion kinetic energy distribution is set to a Maxwell-Boltzmann distribution, again programmatically generated within the SIMION workbench user programme by using the Box-Muller Method explained in appendix B (section 7.2). The temperature of the ionisation region is chosen as  $T_{\text{IR}} = 298.15$  K (25 °C) and the initial velocity vector is randomly generated in any XYZ-direction.



$d_s$ [mm]	1.5
$D_s$ [mm]	10
$h$ [mm]	25.1
$d_0$ [mm]	1
$d_{\text{Ex1}}$ [mm]	0.1
$\alpha$ [°]	9.6

Electrode	V [kV]
I = S1	6
S2	5.975
S3 = IC ( $V_{\text{IC}}$ )	5.95
IC ( $\Delta V_{\text{DC}}$ )	0.019
Ex1	5.45
Ex2	2.45
VT	0

$f_{\text{RF}} = 8$  MHz and  $V_{\text{Amp,RF}} = 100$  V  
 $F_{\text{Push}} = 1$  V/mm;  $F_{\text{Pull}} \approx 1$  V/mm

Figure 5.11: Illustration of the  $\text{Ar}^+$  ion generation volume and the extraction towards Ex1 (Ion Carpet B;  $p_{\text{IR}} = 0.1$  mbar and the Test-pressure-gradient is applied).

**The results for the extraction efficiency of  $\text{Ar}^+$  ions  $f_{\text{Extr},\text{Ar}^+}$** , defined as ratio between the number of ions reaching the extraction electrode plane and the total number of generated ions ( $N_{\text{Ions,Ex1}}/N_{\text{Ions,gen}}$ ), can be seen in figure 5.12. Not all evaluated frequency cases are shown in order to keep a clearer graphical representation. In the case of **Ion Carpet A** the curve of 2 MHz falls below the horizontal line which indicates the only-DC situation. This means that the application of the RF-signal at 2 MHz does not increase  $f_{\text{Extr},\text{Ar}^+}$  but in contrary deteriorates the ion extraction compared to the situation without RF-signal. An enhancement of  $f_{\text{Extr},\text{Ar}^+}$  compared to the only-DC situation can be seen for frequencies  $\geq 4$  MHz depending on the applied  $V_{\text{Amp,RF}}$ . The curves in between 4 and 10 MHz go through a maximum within the covered  $V_{\text{Amp,RF}}$  range. The 11 MHz curve most probably reaches its maximum beyond a value of  $V_{\text{Amp,RF}} = 150$  V. It is assumed that for the use of the ion carpet within the prototype, the cases with  $V_{\text{Amp,RF}} = 100$  V and  $f_{\text{RF}} \geq 8$  MHz will be a good compromise between a good extraction efficiency (70 - 80 %) and a not too high voltage difference between neighbouring carpet rings ( $\Delta V_{\text{rings}} = 2 \cdot V_{\text{Amp,RF}}$ ) in order to avoid electrical breakdowns. **A good choice for further simulations is 9 MHz and  $V_{\text{Amp,RF}} = 100$  V.**

The shape of the extraction curves clearly changes for **Ion Carpet B** compared to Ion Carpet A and overall lower extraction efficiencies are obtained. At 1 MHz the  $f_{\text{Extr},\text{Ar}^+}$  curve corresponds to the only-DC situation and a clearer increase starts to be seen at 3 and 4 MHz. The best extraction efficiencies are obtained at 6 to 8 MHz for which the curves are very similar and a continuous increase can be seen from below 10 % to about 45 % when increasing from  $V_{\text{Amp,RF}} = 25$  V to 150 V. Going to frequencies  $> 8$  MHz reduces again the efficiency of the  $\text{Ar}^+$  extraction with Ion Carpet B. As already mentioned before for Ion Carpet A it is assumed that the case with a  $V_{\text{Amp,RF}} = 100$  V is a good choice to avoid in reality electrical breakdown problems and still get a satisfactory extraction efficiency. **For Ion Carpet B a good choice for further simulations is 7 MHz and  $V_{\text{Amp,RF}} = 100$  V** where about 35 % of extraction efficiency can be reached. For completion of the data all evaluated frequency cases for Ion Carpet A and B can be seen in figure 7.24 of appendix C (section 7.3) and identical conclusions can be drawn as here before when considering all of the data sets.

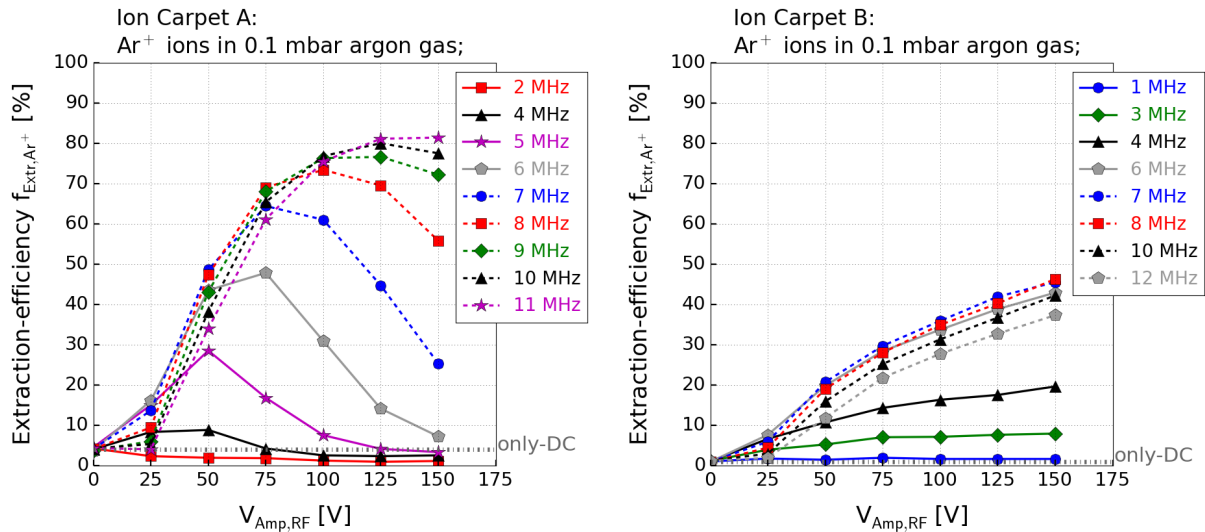


Figure 5.12: Extraction efficiency Ion Carpet A/B:  $\text{Ar}^+$  in argon (IV-Ar;  $p_{\text{IR}} = 0.1$  mbar,  $T_{\text{IR}} = 298.15$  K;  $d_0 = 1$  mm;  $d_{\text{Ex1}} = 0.1$  mm;  $\Delta V_{\text{IC-Ex1}} = 500$  V; Use of the Test-pressure-gradient).

### 5.3 Brightness of the ion source

#### 5.3.1 Ion current calculation

In order to be able to perform the reduced brightness calculation by using equation 4.12 an estimation of the ion beam current is needed. For this purpose first of all a calculation needs to be done for **the total ion current that is produced within the ionisation region**. Equation 2.7 can be used to calculate the produced ion current along a certain generation length  $L_{\text{Gen}}$  if the ionising e-beam is parallel, mono-energetic and if the single collision condition (SCC)  $n_{\text{Gas}} \cdot \sigma \cdot L_{\text{Gen}} \leq 0.01$  is fulfilled. In the case of the EIRFIS ionisation region the e-beam is progressively slowed down so that the beam energy changes. As the IV is taken as a truncated cone the e-beam cross section changes as well and a non-parallel situation is obtained. Furthermore, the ionising e-beam has an energy of 100 eV when entering into the ionisation region so that  $\sigma_{\text{Ar}^+} = 2.51 \cdot 10^{20} \text{ m}^2$  (taken from [45]). At the conditions of  $p_{\text{IR}} = 0.1 \text{ mbar}$ ,  $T_{\text{IR}} = 298.15 \text{ K}$  and  $L_{\text{Gen}} = 1 \text{ mm}$  it can be calculated that  $n_{\text{Gas}} \cdot \sigma_t \cdot L_{\text{Gen}} = 0.061$  which indicates a non fulfilled SCC ( $n_{\text{Ar}} = 2.43 \cdot 10^{21} \text{ m}^{-3}$ ). In order to be able to use equation 2.7 the following approach is used and is also illustrated in figure 5.13.

**The truncated cone volume is subdivided into several slices of width  $dX$ .** The e-beam is passing the inlet aperture at an energy of  $E_{e,0} = 100 \text{ eV}$  with a current of  $I_{e,0}$ . The e-beam energy at the exit of each single slice  $E_{\text{slice-}i,\text{Out}}$  is determined by using equation 5.1 to:

$$E_{\text{slice-}i,\text{Out}} = E_{\text{slice-}i,\text{In}} - dX \cdot (P_{\text{Stop}} + e \cdot F_{\text{retard}}) \quad . \quad (5.6)$$

It can be deduced that  $E_{\text{slice-}i,\text{Out}} = E_{\text{slice-}(i+1),\text{In}}$  and for each slice a mean e-beam energy is calculated with  $E_{\text{slice-}i,\text{mean}} = 0.5 \cdot (E_{\text{slice-}i,\text{In}} + E_{\text{slice-}i,\text{Out}})$ . The EI ionisation cross section results from [45] are used to find for each slice the values of  $\sigma_t$  and  $\sigma_{\text{Individual}}$  at  $E_{\text{slice-}i,\text{mean}}$ . As the cross section results in [45] are only stated for particular values of energy, for each slice  $\sigma_t$  and  $\sigma_{\text{Individual}}$  are taken at the stated energy being closest to  $E_{\text{slice-}i,\text{mean}}$ .

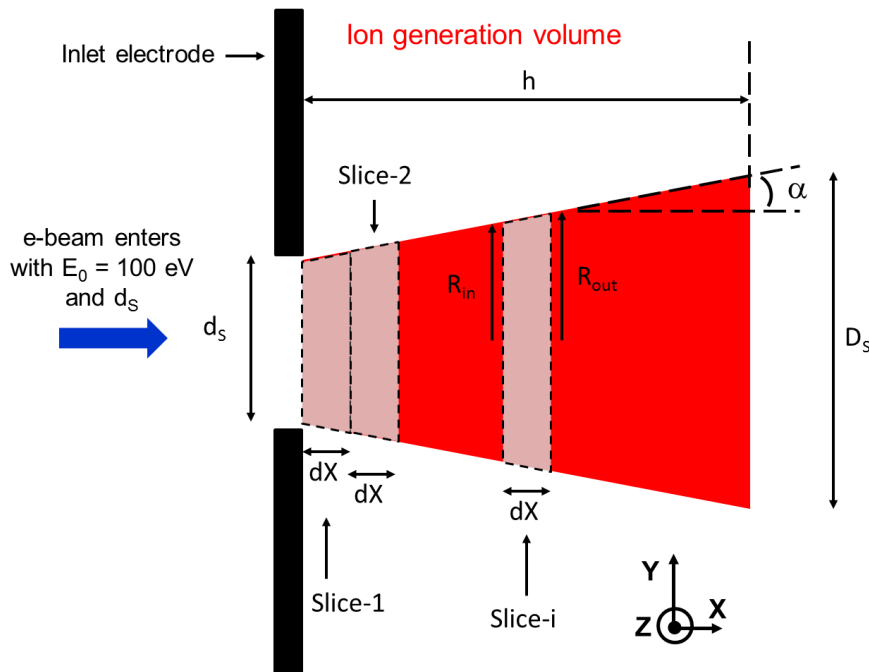


Figure 5.13: Illustration of the IV slice approach for the total ion current calculation.

The electron current at the exit of each slice is determined by:

$$I_{e,slice-i,Out} = I_{e,slice-i,In} \cdot \exp(-n_{Gas} \cdot \sigma_{t,slice-i} \cdot dX) \quad . \quad (5.7)$$

Here again it can be written that  $I_{e,slice-i,Out} = I_{e,slice-(i+1),In}$  and for each slice a mean e-beam current is calculated with  $I_{e,slice-i,mean} = 0.5 \cdot (I_{e,slice-i,In} + I_{e,slice-i,Out})$ . When properly choosing  $dX$ , the SCC will be fulfilled within each slice. Furthermore, combining a small  $dX$  with  $\alpha \approx 10^\circ$  (IV-Ar) leads to a minor change of the IV cross section along  $dX$  so that the e-beam is in good approximation parallel within each slice and equation 2.7 can be used. **The total generated current within the truncated cone IV** for a certain ion species is determined by:

$$I_{Ion,total} = \sum_{i=1}^N n_{Gas} \cdot \sigma_{Individual,slice-i} \cdot dX \cdot I_{e,slice-i,mean} \quad . \quad (5.8)$$

What is further done is that for each slice the extraction efficiency within that slice is determined  $f_{Extr,slice-i} = N_{Ions,Ex1,slice-i} / N_{Ions,gen,slice-i}$ , where  $N_{Ions,gen,slice-i}$  is the total number of generated ions within slice-i and  $N_{Ions,Ex1,slice-i}$  is the total number of ions that are extracted from slice-i towards the extraction electrode Ex1. Therefore, by taking  $f_{Extr,slice-i}$  into account **the total extracted current for a certain ion species** is determined by:

$$I_{Ion,Ex1} = \sum_{i=1}^N n_{Gas} \cdot \sigma_{Individual,slice-i} \cdot dX \cdot I_{e,slice-i,mean} \cdot f_{Extr,slice-i} \quad . \quad (5.9)$$

As an example the case of Ion Carpet B with  $f_{RF} = 8$  MHz and  $V_{Amp,RF} = 100$  V is used to determine the different ion currents for  $Ar^+$  ions. As already stated within the paragraph of the EIRFIS e-Column simulations the maximal estimated e-beam current that will enter the ionisation region through the inlet electrode aperture of 1.5 mm in the real prototype is about 400  $\mu A$ , used here as  $I_{e,0}$ . The ionisation region parameters are used as  $p_{IR} = 0.1$  mbar,  $T_{IR} = 298.15$  K and  $dX$  is set to 0.1 mm so that  $n_{Gas} \cdot \sigma_{Ar^+} \cdot dX \leq 0.01$  is fulfilled for all slices. The change of the IV YZ-cross sections is below 5 % across  $dX$  so that the approximation of a parallel e-beam within each slice is justified. The total generated  $Ar^+$  current  $I_{Ar^+,total}$  is determined to about 260  $\mu A$  and the total extracted current through the central ion carpet hole is  $I_{Ar^+,Ex1} \approx 90$   $\mu A$ . In figure 7.25 of appendix C (section 7.3) the variation of different parameters related to the ion current calculation can be seen. What should be mentioned here is that the current values determined by the slice approach are estimations as only the ionisation by the primary e-beam along its forward stopping path is taken into account. No further ionisation related to the electrons ejected from the gas atoms by EI, no ion recombination or ion gas atom ionisation is taken into account. These processes can in reality be present within the ionisation region.

### 5.3.2 Brightness calculation

**The parameters that are still needed** in order to be able to get an estimation about the achievable reduced brightness **are the ion beam source size and the half-opening beam angle**. The simulations that will be presented in the following include a pressure gradient within the ion column that is determined by molecular flow simulations performed with the Molflow+ software described in more detail in section 5.4.2. In order to be as close as possible to the real EIRFIS prototype performance it is important to include this pressure gradient as the angular

spread as well as the source size of the ion beam is increased due to ion gas collisions within the ion column. In this way a lower ion source brightness is determined compared to a situation where no ion gas collisions are taken into account, which would result in a wrong estimation of the ion source performance. When comparing the values of the afore used Test-pressure-gradient ( $p_{\text{IC-d}_0} = 0.01$  mbar;  $p_{\text{IC-Ex1}} = 0.001$  mbar) with the more precisely evaluated gradient for Argon (Ar-pressure-gradient) listed in table 5.4 ( $p_{\text{IC-d}_0} = 0.0078$  mbar;  $p_{\text{IC-Ex1}} = 0.00155$  mbar) it is clear that the Test-pressure-gradient already provides a good approximation.

Some preliminary test simulations are used to evaluate the change in ion beam size at the location of the extraction electrode Ex1 by **varying the potential of Ex1 while keeping the remaining DC-potentials fixed** at the values listed in figure 5.11. In this way a variation of  $\Delta V_{\text{IC-Ex1}} = V_{\text{IC}} - V_{\text{Ex1}}$  is achieved. The  $d_{\text{FW50}}$  of the  $\text{Ar}^+$  ion beam at Ex1 is only marginally affected by this change in  $\Delta V_{\text{IC-Ex1}}$  and is about 380  $\mu\text{m}$  or 480  $\mu\text{m}$  for the Ion Carpet A and B case, respectively. This clearly indicates that only a small part of the ion beam will pass the extraction aperture with  $d_{\text{Ex1}} = 100$   $\mu\text{m}$ . It is expected that a lens effect should occur at the exit of the ion carpet so that a clear minimal  $d_{\text{FW50}}$  ion beam size at Ex1 can be found at a certain  $\Delta V_{\text{IC-Ex1}}$  value. Most probably this effect does not show up due to the ion gas collisions that spread up the beam size as the pressure in between the ion carpet and Ex1 is still quite high. Nevertheless, a parameter that does vary with  $\Delta V_{\text{IC-Ex1}}$  is the extraction factor  $f_{\text{Extr}, \text{Ar}^+}$ , which increases with increasing  $\Delta V_{\text{IC-Ex1}}$ . Therefore, for both ion carpets the potential settings of  $\Delta V_{\text{IC-Ex1}} = 300$  V, 500 V and 1000 V are chosen to perform in the following a more detailed evaluation of the remaining ion beam parameters by combining them with a variation of the potential difference of the Ex1 and Ex2 electrode  $\Delta V_{\text{Ex1-Ex2}}$ .

In figure 5.14 a complete EIRFIS ion column simulation is shown for the case of Ion Carpet B with  $f_{\text{RF}} = 7$  MHz,  $V_{\text{Amp, RF}} = 100$  V and  $\Delta V_{\text{IC-Ex1}} = 300$  V. The ion beam positions are for each simulation case stored at a recording plane in the field free region behind the electrode G in downstream direction (Rec-Plane in figure 5.14).

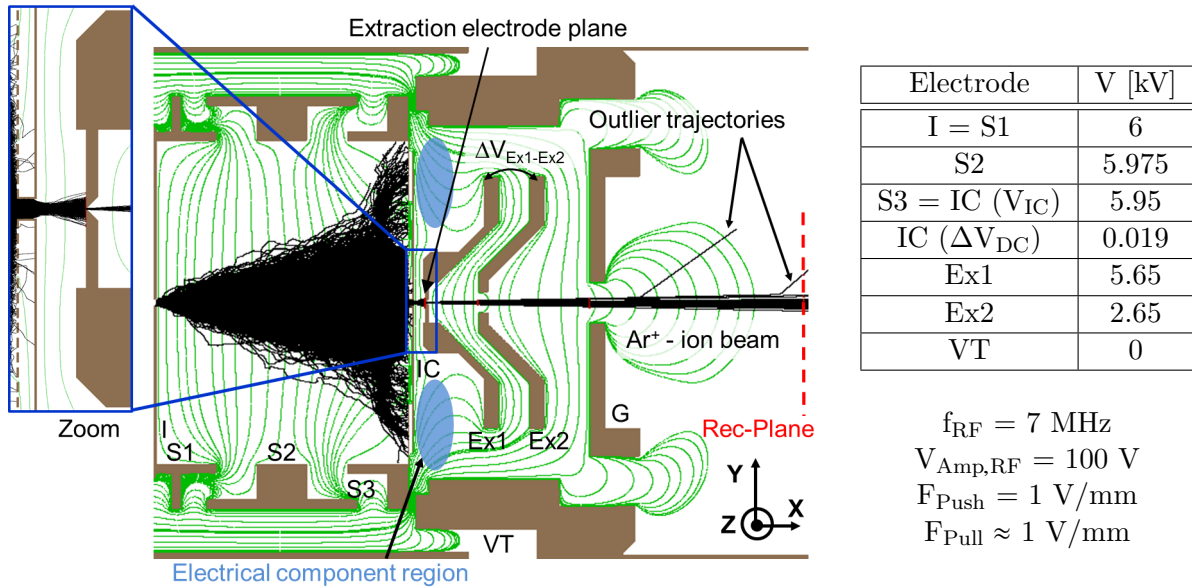


Figure 5.14: Illustration of a complete EIRFIS ion column simulation for  $\text{Ar}^+$  ions (Ion Carpet B; IV-Ar;  $p_{\text{IR}} = 0.1$  mbar,  $T_{\text{IR}} = 298.15$  K; Ar-pressure-gradient used).

At this Rec-Plane the **trajectory extrapolation method (in X-direction)** is used to find the **ion beam source size and half-opening angle**, as already explained in more detail in section 4.2. As can be seen in figure 5.14 the PA file used for the simulations incorporates the detailed shape of the ion column electrodes shown in figure 5.8 for the mechanical setup of the EIRFIS prototype to be as close as possible to the real situation. In the zoomed area the special shape of Ex1 close to the ion carpet can be seen in detail. The shape is related to the idea to use standard apertures available for SEMs, TEMs or FIB systems [160] and fix those to the top hat shaped electrode Ex1. This allows an easy exchange of the standard aperture with hole size  $d_{\text{Ex1}}$ . Furthermore, the top hat shape of electrode Ex1 is used to be able to get the distance of  $D_{\text{Ex}} = 2.5$  mm close to the ion beam axis while keeping a bigger distance further away from the ion beam axis, where electrical components (resistors, capacitors) will be present on the backside of the PCB ion carpet. The electrode Ex2 has as well a top hat structure which is needed to achieve the desired distance  $D_A$  of 10 mm. A further illustration of the ion column electrodes can be seen within pictures in section 5.5. What can be further seen in figure 5.14 are outlier trajectories due to the ion gas collisions considered within the ion column, but those outliers are not taken into account when performing the ion beam trajectory extrapolation. A complete ion column simulation illustration for the case of Ion Carpet A can be seen in figure 7.26 of appendix C (section 7.3) as well as in figure 7.27 and 7.28 some illustrations of the ion beam profile at different planes along the ion column are shown. This is meant to give an idea about the profiles that are obtained by the performed CPO simulations and the related trajectory extrapolation method.

The **reduced brightness calculation results for  $\text{Ar}^+$  ions** and related parameters are shown for the **Ion Carpet A case** on the left side and for the **Ion Carpet B case** on the right side of figure 5.15. The ion beam current that reaches the end of the ion column is described by the parameter  $I_{\text{Ion,transmitted}}$ . First, the total generated ion current  $I_{\text{Ar}^+, \text{total}}$  is taken as 260  $\mu\text{A}$  for the case of an ionising electron beam current of  $I_{e,0} = 400$   $\mu\text{A}$ , see the afore section 5.3.1. The extracted current  $I_{\text{Ar}^+, \text{Ex1}}$  in the case of Ion Carpet A increases from about 180 to 210  $\mu\text{A}$  when going from 300 V to 1000 V in  $\Delta V_{\text{IC-Ex1}}$ . This highlights once again that a higher extracted current is obtained at a higher value of  $\Delta V_{\text{IC-Ex1}}$ . In the case of Ion Carpet B overall lower values for  $I_{\text{Ar}^+, \text{Ex1}}$  are obtained, namely from 80 up to 110  $\mu\text{A}$ , which is related to the lower extraction efficiency compared to the Ion Carpet A case as already discussed in section 5.2.2. For each simulation case shown in figure 5.15 the corresponding  $I_{\text{Ar}^+, \text{Ex1}}$  value is then multiplied with the determined transmission factor  $f_{\text{Tr,Ar}^+}$ , defined as number of ions at the Rec-Plane divided by number of ions at the extraction plane, in order to obtain a value for  $I_{\text{Ion,transmitted}}$ . In both cases  $I_{\text{Ion,transmitted}}$  increases with increasing  $\Delta V_{\text{IC-Ex1}}$  and is in the range of 7 to 10  $\mu\text{A}$  in the Ion Carpet A case and 1 to 3  $\mu\text{A}$  in the Ion Carpet B case.

In both ion carpet cases the curves for  $\alpha_{\text{Ion-beam}}$  show very similar trends over the covered  $\Delta V_{\text{Ex1-Ex2}}$  range for all investigated  $\Delta V_{\text{IC-Ex1}}$  situations. When comparing the  $\alpha_{\text{Ion-beam}}$  curves obtained at the same  $\Delta V_{\text{IC-Ex1}}$  setting in both ion carpet cases it can be seen that the curves in the Ion Carpet B case are slightly shifted to higher values. In general a higher value of  $\Delta V_{\text{IC-Ex1}}$  leads to larger beam angles and  $\alpha_{\text{Ion-beam}}$  is in the range of 9 mrad to 19 mrad. The ion beam source size  $d_{\text{IS}}$  curves are nearly identical for the same  $\Delta V_{\text{IC-Ex1}}$  setting when comparing both ion carpet cases to each other. All curves go through their minimum in the  $\Delta V_{\text{Ex1-Ex2}}$  range of 2 kV to 3 kV and the global minimum or maximum value for  $d_{\text{IS}}$  can be determined to about 50  $\mu\text{m}$  and 76  $\mu\text{m}$ , respectively.



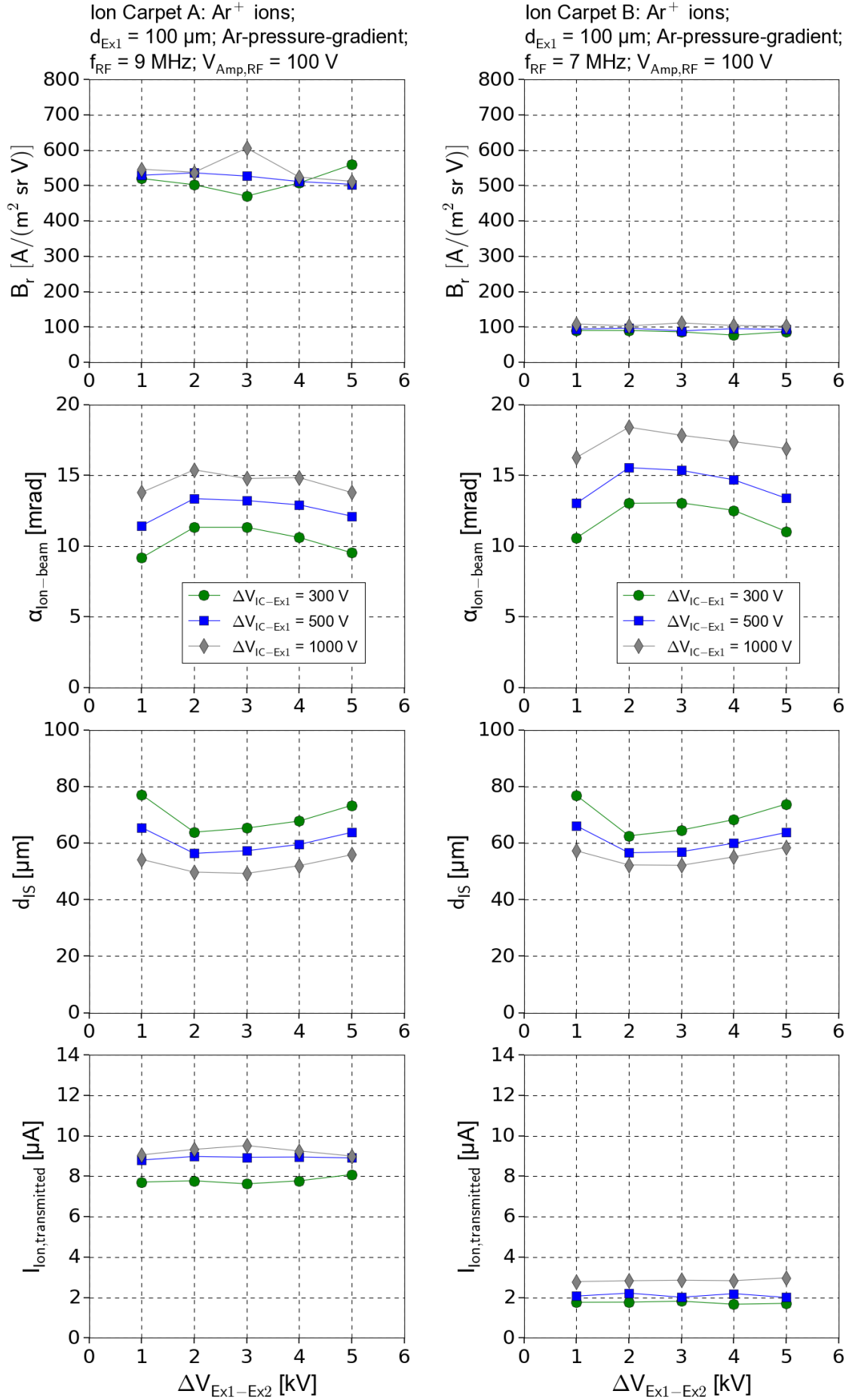


Figure 5.15: Brightness calculation for  $\text{Ar}^+$  ions: Left Ion Carpet A; Right Ion Carpet B; (IV-Ar;  $p_{\text{IR}} = 0.1 \text{ mbar}$ ,  $T_{\text{IR}} = 298.15 \text{ K}$ ; Ar-pressure-gradient used).



As expected the resulting curves for the reduced brightness  $B_r$  show some variation over the covered ion column voltage setting range but in a global conclusion the mean  $B_r$  value for the Ion Carpet A case can be determined to  $526 \text{ A}/(\text{m}^2 \text{ sr V})$ . Mainly due to the fact that a lower ion current is extracted from the ionisation region and therefore a lower transmitted ion beam current is obtain, the mean  $B_r$  value for the Ion Carpet B case drops to  $95 \text{ A}/(\text{m}^2 \text{ sr V})$ . A slight degrading contribution comes as well from the overall larger  $\alpha_{\text{Ion-beam}}$  values in the Ion Carpet B compared to the Ion Carpet A case.

**These estimated reduced brightness values of the EIRFIS concept are within the  $10^2 \text{ A}/(\text{m}^2 \text{ sr V})$  range** and are still below the target of  $10^3 - 10^4 \text{ A}/(\text{m}^2 \text{ sr V})$ , although Ion Carpet A is just a factor 2 below the lower limit of this range. Most probably with an optimised electron column that results in a smaller collimated e-beam cross section more ionising e-beam current can be guided into the ionisation region which will raise the amount of generated ion current. In this way the reachable  $B_r$  can be further raised if the evaluated performance in terms of ion beam source size and half-opening angle is unchanged. Nevertheless, the currently determined ion source performance in terms of  $B_r$  clearly represent an improvement compared to standard EI ionisation sources with about  $B_r \approx 1 \text{ A}/(\text{m}^2 \text{ sr V})$ .

### 5.3.3 Energy distributions

To finish this section **the energy distributions and the energy spread  $\Delta E$  will be evaluated for the  $\text{Ar}^+$  ion beam obtained at the end of the ion column.** The total energy is calculated by  $E_{\text{Total}} = E_{\text{kinetic}} + q_{\text{Ion}} \cdot \text{Pot}_{\text{Ion}}$ , where  $q_{\text{Ion}}$  represents the ion charge and  $\text{Pot}_{\text{Ion}}$  the potential value at the corresponding ion position. In figure 5.16a the  $E_{\text{Total}}$  distribution is shown for the **Ion Carpet A case** related to the simulation shown in figure 7.26 of appendix C (section 7.3). The distribution shows a broad energy peak within the range of 5935 eV to 5975 eV. Two pronounced peaks can as well be seen within the mentioned broad peak, the first one at about 5940 eV and the second at about 5970 eV. These peaks are related to the fact that in the Ion Carpet A case the central hole electrode (electrode E1 in figure 5.9b) is kept at the varying RF signal which produces a broad energy distribution for the extracted ions and therefore as well for the transmitted ion beam. The FWHM of the distribution is determined graphically to 30 eV (no fitting is performed here) and can be interpreted as the ion beam  $\Delta E$  at the end of the extraction ion column, see figure 5.16a. This very large value is way out of the targeted range of  $\Delta E \lesssim 1 \text{ eV}$  and will lead to a quite strong ion beam broadening related to chromatic aberrations, especially if the EIRFIS concept is used for low energy applications.

What can be seen in figure 5.16b for the **Ion Carpet B case** is a clearly narrower  $E_{\text{Total}}$  distribution compared to the Ion Carpet A case and a single pronounced peak is obtained. A curve fit by using the GaussAmp function (see appendix C (section 7.3) for its definition) is performed and a FWHM value of 2.6 eV is determined. The broad distribution with two pronounced peaks as in the Ion Carpet A case does not appear any more because in the Ion Carpet B case the central carpet hole electrode is kept at the fixed DC-base potential  $V_{\text{IC}}$  of the ion carpet. **In general it can be concluded that the Ion Carpet B case produces a 10 times smaller ion beam  $\Delta E$  compared to the Ion Carpet A case.** Nevertheless, the determined FWHM value is still above the targeted range but at least in the same order of magnitude. The energy distributions that are shown in figure 5.16b are related to the simulation case illustrated in figure 5.14.

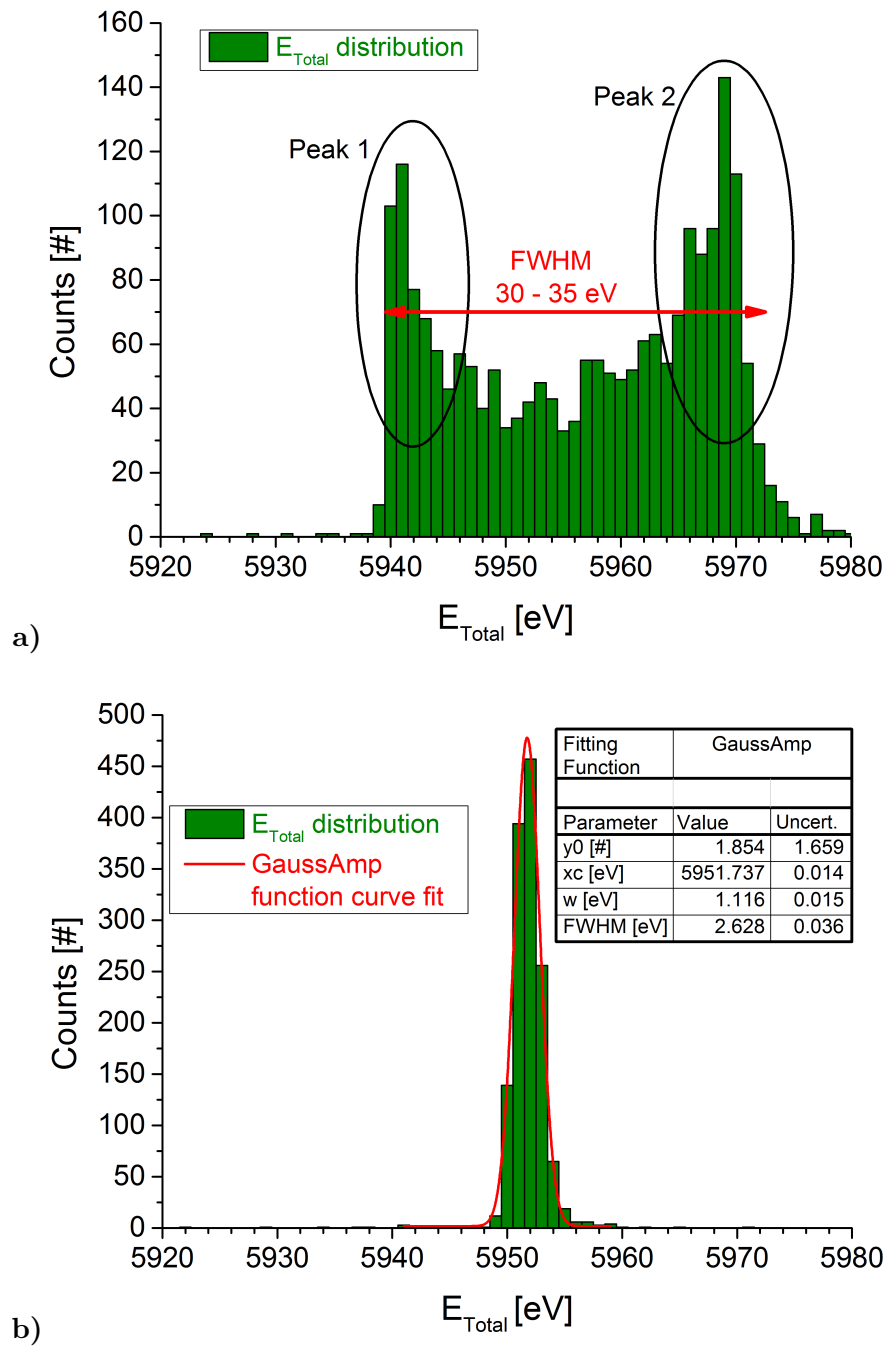


Figure 5.16: Total energy distributions at the Rec-Plane for  $\text{Ar}^+$  ions:

a) Ion Carpet A case; b) Ion Carpet B case; (related to the simulation cases shown in figure 5.14 and figure 7.26 of appendix C (section 7.3)).

## 5.4 Technical considerations

### 5.4.1 Gas conductance calculations for the e-Column

Before the construction of the EIRFIS prototype is launched, **gas conductance calculations for the e-Column are done in order to get an idea about the achievable pressures within the different parts of the e-Column.** The **simplified model** that is used to perform these calculations is shown in figure 5.17a. Different pressure regions are considered: the ionisation region ( $p_{IR}$ ), the inner region of the e-Column ceramic support structure ( $p_{eC,In}$ ), the outside region around the ceramic ( $p_{eC,Out}$ ), the Wehnelt volume in which the disc cathode is located ( $p_W$ ) and the chamber to which the bigger turbo pump is connected ( $p_P$ ). A detailed description of the established pV-flow equations can be found in appendix C (section 7.3). After some reorganisation and recombination of these equations the final obtained expressions for the different region pressures are:

$$\begin{aligned}
 p_P &= p_W \cdot \frac{C_4}{S_{eff,P+C_4}} \quad ; \\
 p_{eC,Out} &= p_{eC,In} \cdot \frac{C_2}{S_{eff,eC+C_2}} \quad ; \\
 p_W &= p_{eC,In} \cdot \frac{C_3}{K_A} \quad \text{with} \quad K_A = \left(1 - \frac{C_4}{S_{eff,P+C_4}}\right) \cdot C_4 + C_3; \\
 p_{eC,In} &= p_{IR} \cdot \frac{C_1}{K_B} \quad \text{with} \quad K_B = \left(1 - \frac{C_2}{S_{eff,eC+C_2}}\right) \cdot C_2 + \left(1 - \frac{C_3}{K_A}\right) \cdot C_3 + C_1;
 \end{aligned} \tag{5.10}$$

**The gas conductance calculations are performed in the molecular flow regime.**  $C_1$  represents the molecular flow conductance of the inlet electrode aperture and is determined by equation 3.29. The inner region of the e-Column ceramic is pumped in parallel by four holes each of which has a diameter of 26 mm and a width of 5 mm. The total pumping hole conductance is determined by  $C_{eC,total} = 4 \cdot C_{eC,pump-hole}$  and each individual  $C_{eC,pump-hole}$  is calculated by using equation 3.28 for a cylindrical tube of arbitrary length in the molecular flow regime. What needs to be further taken into account is that the pumping holes will be in addition covered by the e-Shield mesh made of a turbo pump grid for which the manufacturer states a conductance reduction of about 10 % [144]. Therefore, the final value of  $C_2$  is calculated by  $C_2 = 0.9 \cdot C_{eC,total}$ . The inner ceramic region is connected to the Wehnelt volume by a series connection of the lens, anode and Wehnelt electrode apertures as well as two spacers in between the electrodes ( $S_{PLA}$ ,  $S_{PAW}$ ). The conductance values for the three apertures are again determined by equation 3.29 and equation 3.28 is used for the spacers. The total conductance  $C_3$  is calculated by using equation 3.32 for a series connection of several elements with varying sections. More details about the exact expression for  $C_3$  can be found in appendix C (section 7.3). It is intended to pump the e-Column of the EIRFIS prototype by a small turbo pump having a pumping speed of  $S_{V81} = 50$  l/s for Nitrogen/Argon (Turbo-V 81-M [144])). This turbo pump is connected to the vacuum tube via a cylindrical port (diameter = 45 mm, length = 150 mm) for which the conductance  $C_{V81,eC}$  is determined by equation 3.28 and the related effective pumping speed is expressed as:

$$S_{eff,eC} = \frac{S_{V81}}{1 + \frac{S_{V81}}{C_{V81,eC}}} \quad . \tag{5.11}$$

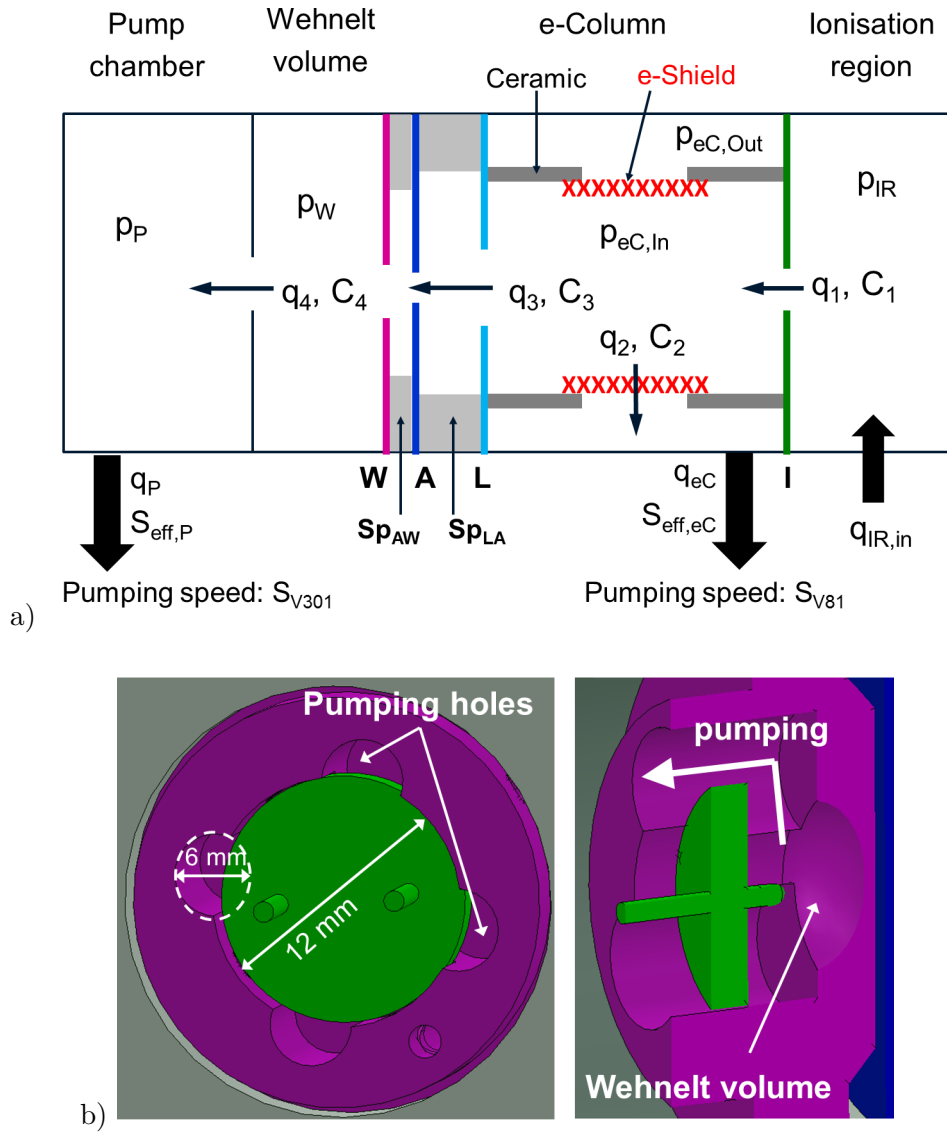


Figure 5.17: a) Simplified EIRFIS e-Column model used for the gas conductance calculations; b) Illustration of the Wehnelt volume pumping holes.

As can be seen in figure 5.17b the Wehnelt volume is pumped in parallel via four pumping holes (diameter = 6 mm) which are partially covered by the disc cathode base. These four pump holes are virtually replaced by one single aperture having the same area as the total open area of the pump holes  $A_{open,W,pump-holes}$ . The diameter of this virtual aperture is therefore determined by  $d_{Virtual,Aperture} = \sqrt{4 \cdot A_{open,W,pump-holes} / \pi}$  and the related conductance  $C_4$  again by equation 3.29. The pump that is intended to be connected to the vacuum tube in order to efficiently pump the Wehnelt volume is a bigger turbo pump having a pumping speed of  $S_{V301} = 250$  l/s for Nitrogen/Argon (Turbo-V 301 [144, 161]). This pump is as well connected to the vacuum tube via a cylindrical port (diameter = 97 mm, length = 20 mm) for which the conductance  $C_{V301,P}$  is determined by equation 3.28 and the related effective pumping speed is expressed as:

$$S_{eff,P} = \frac{S_{V301}}{1 + \frac{S_{V301}}{C_{V301,P}}} \quad . \quad (5.12)$$

**The pressure distribution is evaluated for the injection of Argon and Xenon.** The inlet electrode aperture size  $d_I$  and the anode aperture size  $d_A$  are varied in order to see the effect on the different pressures in the molecular flow regime. The used geometrical parameters and pressure results can be seen in table 5.3. During the performed calculations the e-Column is considered as isothermal at a temperature of 298.15 K reflecting the case where the disc cathode emitter is not yet heated, which can be considered as a first good estimation for the reachable pressures. The corresponding dynamic viscosity values are taken for Argon from [162] and for Xenon from [142]. What can be seen in table 5.3 is that with a large inlet electrode aperture of  $d_I = 5$  mm, an already quite small anode aperture of  $d_A = 1.5$  mm and an ionisation region at  $p_{IR} = 0.1$  mbar the pressure at the inside of the e-Column ceramic  $p_{eC,In}$  lies for both gases in the upper  $10^{-3}$  mbar range. Furthermore, the pressure within the Wehnelt volume  $p_W$  is still above  $10^{-4}$  mbar so that the recommended pressure level below  $10^{-4}$  mbar is not reached for the operation of the  $Y_2O_3 - Ir$  disc cathode.

By reducing  $d_I$  to 1.5 mm  $p_{eC,In}$  is decreased by one order of magnitude towards the upper  $10^{-4}$  mbar range for both gases which means that, as already mentioned in the CPO-simulation section 5.2.1, the e-beam losses due to residual gas ionisation can be clearly reduced. Moreover, the pressure  $p_W$  close to the disc cathode drops clearly below  $10^{-4}$  mbar so that a stable operation of it will be possible in this case. A last combination of apertures is  $d_I = 1.5$  mm and  $d_A = 0.8$  mm, this further decrease of the anode aperture size reduces  $p_W$  by a factor of about 2 compared to the case of  $d_I = 1.5$  mm and  $d_A = 1.5$  mm, so that  $p_W$  is for both gases in the mid  $10^{-6}$  mbar range. In the real EIRFIS prototype the disc cathode will be heated and so the temperature of the Wehnelt volume will be higher than the here assumed 298.15 K which will also lead to an increased value of  $p_W$ . Therefore, in order to be on the safe side for the operation of the disc cathode in the real situation and to efficiently reduce e-beam losses due to residual gas ionisation within the e-Column when the ionisation region pressure is set to  $p_{IR} = 0.1$  mbar, the aperture combination of  $d_I = 1.5$  mm and  $d_A = 0.8$  mm is retained for the final prototype construction. These sizes are used as well for the e-Column CPO-simulations already described in more detail in section 5.2.1.

$d_L$ [mm]	6
$d_W$ [mm]	1.5

Spacer	$d$ [mm]	thickness [mm]
$Sp_{PLA}$	27.5	5
$Sp_{AW}$	25	0.6

$S_{V81}$ [l/s]	50
$S_{V301}$ [l/s]	250

Argon:		Xenon	
$S_{eff,eC}$ [l/s]	22.3	$S_{eff,eC}$ [l/s]	15.4
$S_{eff,P}$ [l/s]	177.4	$S_{eff,P}$ [l/s]	143.5

Gas	$d_I$ [mm]	$d_A$ [mm]	$p_{IR}$ [mbar]	$p_{eC,In}$ [mbar]	$p_{eC,Out}$ [mbar]	$p_W$ [mbar]	$p_P$ [mbar]
Ar	5	1.5	0.1	$9.0 \cdot 10^{-3}$	$7.9 \cdot 10^{-3}$	$1.2 \cdot 10^{-4}$	$4.3 \cdot 10^{-6}$
	1.5	1.5	0.1	$8.9 \cdot 10^{-4}$	$7.8 \cdot 10^{-4}$	$1.2 \cdot 10^{-5}$	$4.2 \cdot 10^{-7}$
	1.5	0.8	0.1	$8.9 \cdot 10^{-4}$	$7.8 \cdot 10^{-4}$	$5.4 \cdot 10^{-6}$	$1.9 \cdot 10^{-7}$
Xe	5	1.5	0.1	$7.6 \cdot 10^{-3}$	$6.4 \cdot 10^{-3}$	$1.0 \cdot 10^{-4}$	$2.4 \cdot 10^{-6}$
	1.5	1.5	0.1	$7.3 \cdot 10^{-4}$	$6.2 \cdot 10^{-4}$	$9.6 \cdot 10^{-6}$	$2.4 \cdot 10^{-7}$
	1.5	0.8	0.1	$7.3 \cdot 10^{-4}$	$6.2 \cdot 10^{-4}$	$4.4 \cdot 10^{-6}$	$1.1 \cdot 10^{-7}$

**The molecular flow regime has been used here!** ( $T = 298.15$  K)

Table 5.3: Gas conductance calculation results for the EIRFIS e-Column.

### 5.4.2 Molecular flow simulations for the ion column

In figure 5.18a it can be seen that the ceramic holder plate to which the ion column electrodes are attached possesses additional pumping holes (8 in total) to efficiently pump the ion column when the EIRFIS prototype is mounted onto a vacuum chamber for test purposes or in a later stage to vacuum chambers of instruments. **In order to get an estimation of the pressure gradient within the ion column Molflow+ simulations are performed.** For these simulations the ionisation region is simplified as cylindrical volume (the electrodes S1, S2 and S3 are not taken into account) and the ion carpet as simple disc with a central hole of the size  $d_0 = 1$  mm listed already in figure 5.9. Furthermore, the electrodes Ex1, Ex2, G, the ion column vacuum tube as well as the ceramic holder plate are included in the Molflow+ model. In close relation to the test bench setup, described in more detail in the experimental investigation section 5.5, an additional vacuum tube element is added to the ion column side.

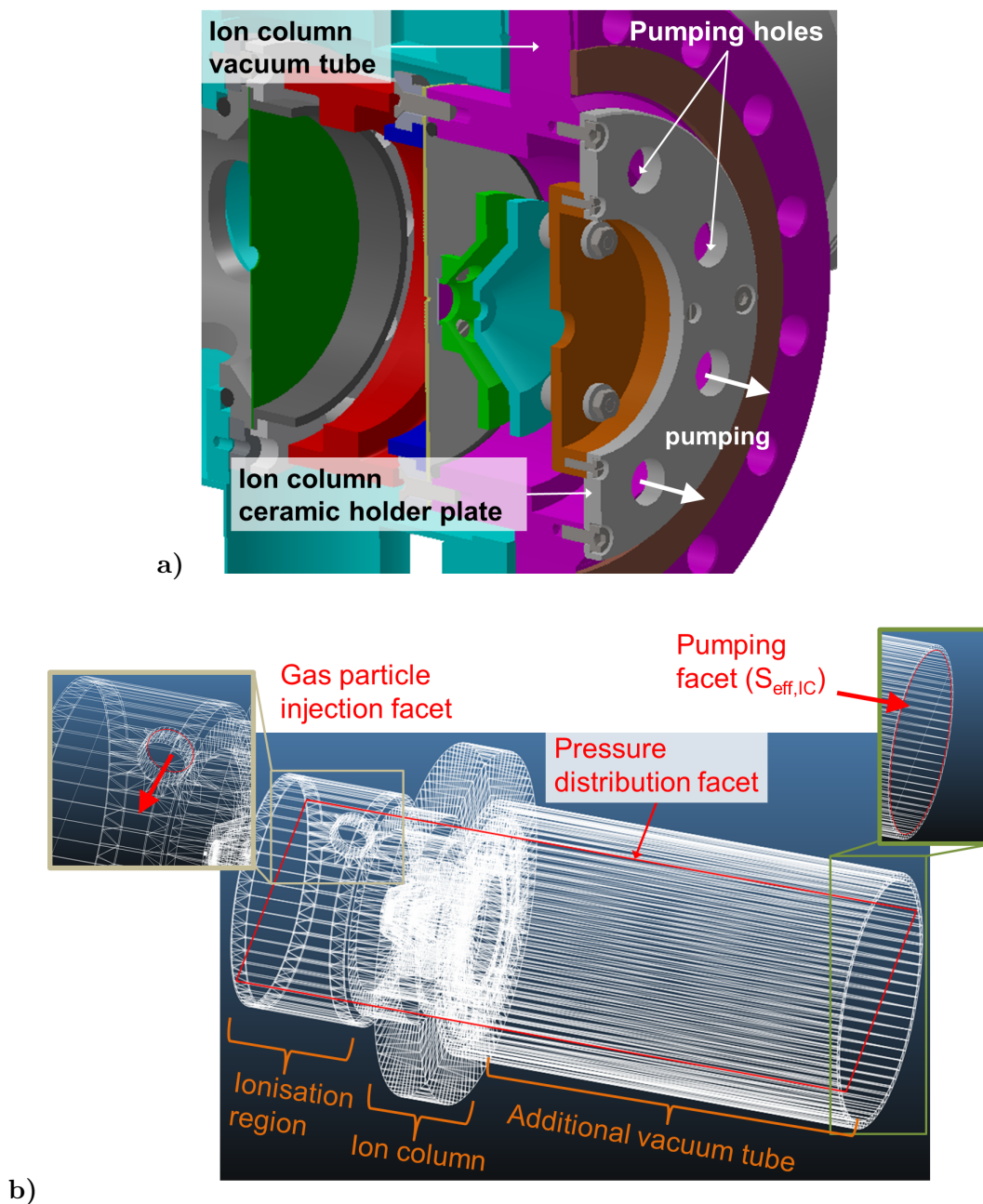


Figure 5.18: a) Illustration of the ion column pumping within the EIRFIS prototype;  
b) Molflow+ setup illustration for the EIRFIS ion column simulation.

Its end surface is used as pumping facet as can be seen in figure 5.18b. On the test bench setup the ion column is pumped by a turbo pump whose pumping speed  $S_{V361}$  can be taken as 350 l/s for argon and xenon (TURBOVAC 361 [163]). The vacuum structure connection from this turbo pump towards the pumping facet used in the Molflow+ simulation can be considered as an elbow tube and its molecular flow conductance (equation 3.30) is determined to  $C = 173$  l/s for argon and  $C = 96$  l/s for xenon at a temperature of 298.15 K. By using equation 3.36 an effective pumping speed at the pumping facet is determined to  $S_{\text{eff,IC}} = 116$  l/s for argon and  $S_{\text{eff,IC}} = 75$  l/s for xenon, which are introduced into the Molflow+ software. The injection of gas particles into the ionisation region is done uniformly from a circular facet as illustrated in figure 5.18b. The gas injection flow  $q_{\text{in}}$  is adjusted during the Molflow+ simulations so that the ionisation region pressure  $p_{\text{IR}}$  is close to 0.1 mbar. The complete ion column system is treated as isothermal and its temperature is fixed to 298.15 K.

In order to evaluate in more detail the pressure gradient along the ion column a transparent facet is added in each simulation to **record the 2D pressure distribution**. The extraction electrode Ex1 hole size is set to  $d_{\text{Ex1}} = 100$   $\mu\text{m}$  and the distance between the ion carpet and Ex1 to  $D_{\text{Ex}} = 2.5$  mm. The 2D pressure distribution for the case of argon injection can be seen in figure 5.19. The white areas correspond to the location of the vacuum tube and of the ion column electrodes. What can be seen is that the pressure drops already within the central ion carpet hole compared to the ionisation region. In the volume between the electrodes Ex1, Ex2 and G the achieved pressures are about three orders of magnitude below  $p_{\text{IR}}$  mainly due to the low gas conductance through the small extraction aperture  $d_{\text{Ex1}}$ . The pressure within the additional vacuum tube used for the Molflow+ simulation drops below  $10^{-4}$  mbar. As additional illustration the corresponding **pressure gradient along the ion beam axis** is represented in more detail in figure 5.20, the different electrode positions are marked as orientation help.

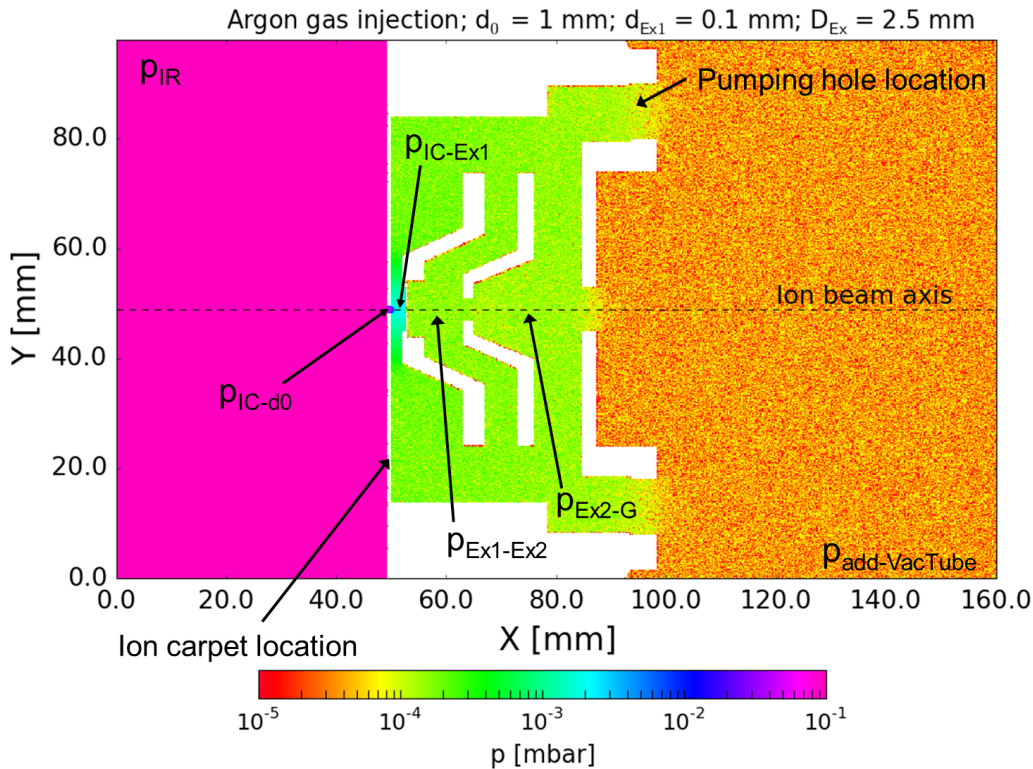


Figure 5.19: Molflow+ EIRFIS ion column simulation ( $d_0 = 1$  mm,  $d_{\text{Ex1}} = 100$   $\mu\text{m}$ ): 2D pressure distribution (Ar,  $S_{\text{eff,IC}} = 116$  l/s,  $T = 298.15$  K).



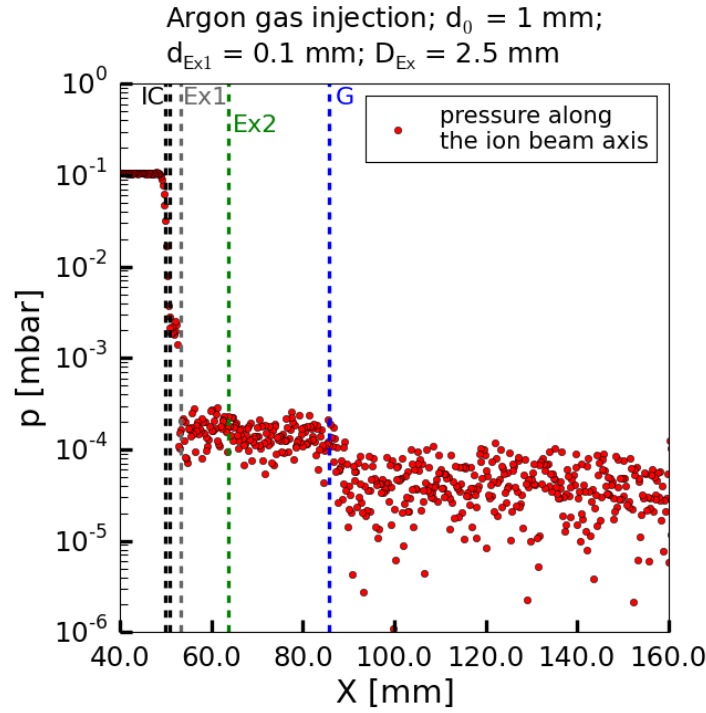


Figure 5.20: Molflow+ EIRFIS ion column simulation ( $d_0 = 1$  mm,  $d_{\text{Ex1}} = 100$   $\mu\text{m}$ ): Pressure gradient along the ion beam axis (Ar,  $S_{\text{eff,IC}} = 116$  l/s,  $T = 298.15$  K).

In table 5.4 the corresponding mean pressures within the different ion column regions are listed for the gas injection case of argon and xenon. The results for both gas species are very similar and as already mentioned in section 5.2.1 the obtained pressure gradient for argon has been used during the ion column CPO simulations to incorporate ion gas collision effects. **The gradients listed in table 5.4 do represent a good approximation for the in reality reigning gradients within the EIRFIS prototype ion column.** The only region where most probably it is needed to consider a non-molecular flow regime situation is the ionisation region with the quite high pressure close to 0.1 mbar. What should be further mentioned here is that the pressure within the additional vacuum tube is determined in the  $10^{-5}$  mbar range. In order to be able to use the EIRFIS prototype as an add-on tool for FIB instruments an additional differential pumping stage needs to be integrated between the source and the remaining ion column of the FIB instrument. The pressure within the analysis chamber is most often desired to be in the range of  $10^{-6} - 10^{-7}$  mbar. The 2D pressure distribution and the pressure gradient along the ion beam axis in the Xenon case can be found in figure 7.29 of appendix C (section 7.3).

Gas	Ar-pressure-gradient	Xe-pressure-gradient
$S_{\text{eff,IC}}$ [l/s]	116	75
$p_{\text{IR}}$ [mbar]	$1.04 \cdot 10^{-1}$	$1.06 \cdot 10^{-1}$
$p_{\text{IC-d}_0}$ [mbar]	$7.80 \cdot 10^{-3}$	$7.93 \cdot 10^{-3}$
$p_{\text{IC-Ex1}}$ [mbar]	$1.55 \cdot 10^{-3}$	$1.59 \cdot 10^{-3}$
$p_{\text{Ex1-Ex2}}$ [mbar]	$1.70 \cdot 10^{-4}$	$1.65 \cdot 10^{-4}$
$p_{\text{Ex2-G}}$ [mbar]	$1.41 \cdot 10^{-4}$	$1.29 \cdot 10^{-4}$
$p_{\text{add-VacTube}}$ [mbar]	$3.95 \cdot 10^{-5}$	$3.48 \cdot 10^{-5}$

Table 5.4: Results of the Molflow+ pressure gradient simulations for the EIRFIS ion column.



## 5.5 Experimental investigations

### 5.5.1 Mechanical assembly

Figure 5.21 shows the main e-Column components of the EIRFIS prototype. In the schematic of the mechanical setup (centre of the figure) the e-Shield is added as a simple x-mesh into the more complex 3D-model. As can be seen in the corresponding picture the e-Shield is inserted into the ceramic support structure and attached by capton tape to fix its position and electrically isolate it from the inlet electrode. The ceramic spacer, the potential connectors, the lens and anode electrode are inserted from the Wehnelt side into the ceramic support structure, shown in the two top pictures. The  $Y_2O_3 - Ir$  disc cathode is inserted into the Wehnelt electrode. Four small screws within the sides of the Wehnelt are used to move the cathode base and to centre in this way the disc within the Wehnelt hole. This centring procedure is monitored by using an optical microscope as can be seen in the image in the bottom right corner. After this the Wehnelt, containing the cathode, is inserted into the ceramic support structure and by the means of a press ring, a ceramic end cap disc and metal screw holders all elements are tightly fixed, see the left side pictures of figure 5.21. The complete ceramic support structure is then inserted into the vacuum tube from the ionisation region side and O-rings together with further fixation pieces are used to get a gas tight separation of the different regions at the outside diameter of the ceramic.

Within the ionisation region the inlet and the Shield 1 electrode are fixed on the ceramic support structure by using a PEEK (polyetheretherketon) fixation ring and a metal screw thread ring. In this manner the e-Column is closed from the ionisation region side, see figure 5.22.

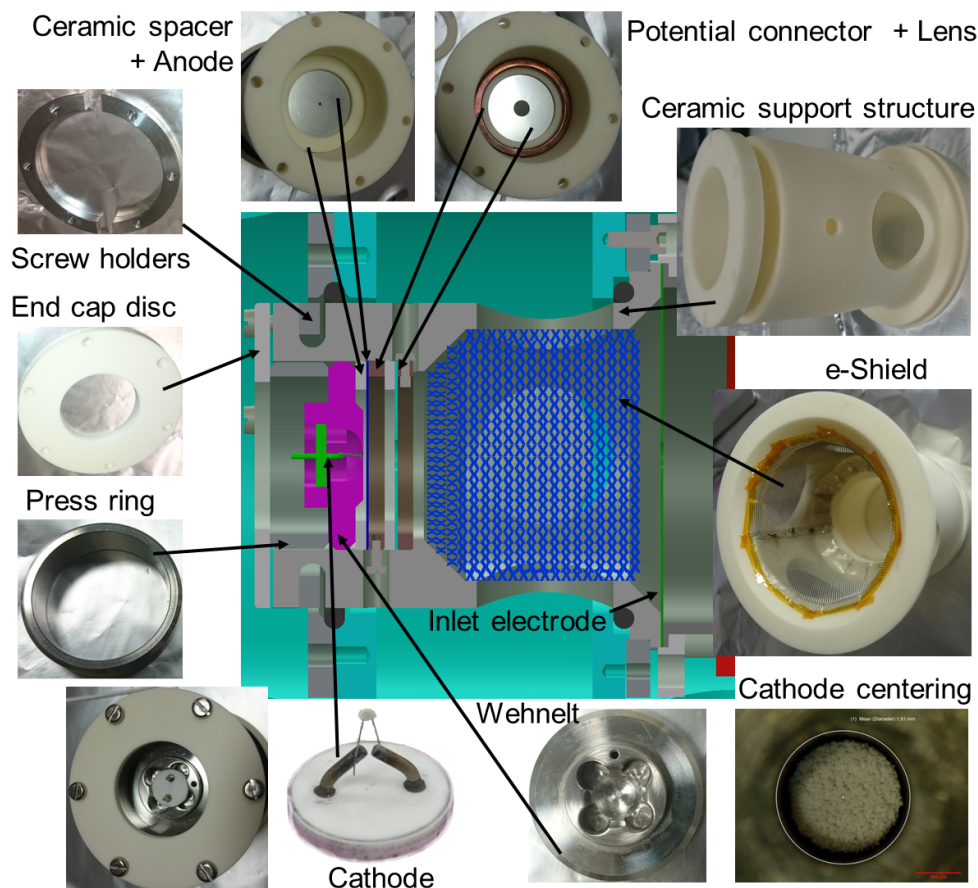


Figure 5.21: Illustration/pictures of the EIRFIS prototype e-Column and its assemblage.

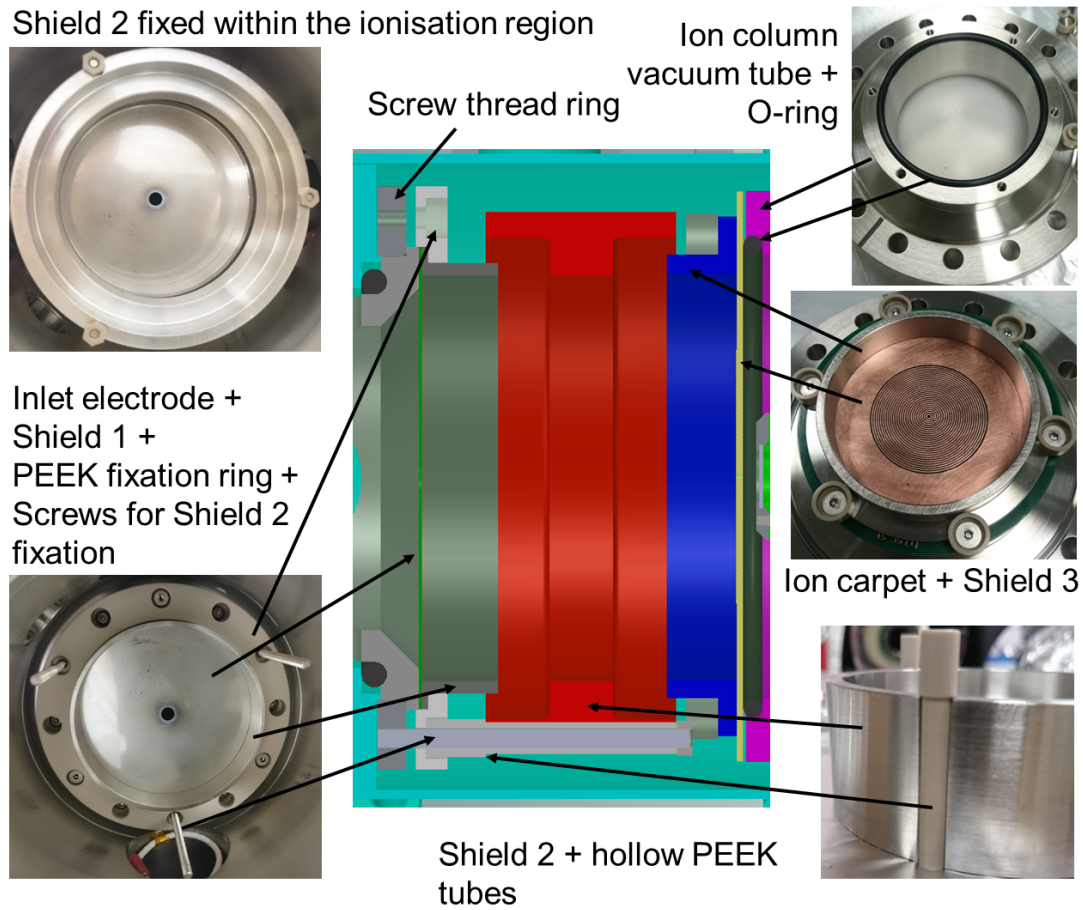


Figure 5.22: Illustration/pictures of the EIRFIS prototype ionisation region and its assemblage.

Longer screws are then mounted into the thread ring and used as holders for the hollow PEEK rods that can be clipped into the protrusions of the Shield 2 electrode and in this way keep it in place, bottom right and left side pictures. The PCB ion carpet together with the Shield 3 electrode is fixed onto the vacuum tube by using screws that are surrounded by special PEEK pieces in order to electrically insulate the ion carpet and the Shield 3 electrode from the vacuum tube. At the backside of the ion carpet an O-ring guarantees that the only way for gas to pass between the ionisation region to the ion column is the central hole of the ion carpet. As already mentioned in section 5.3.2, a standard aperture (10 mm in outer diameter) is fixed onto the extraction electrode Ex1 for the ease of replacement/exchange of the extraction aperture. In the top left of figure 5.23 it can be seen that the Ex1 electrode consists of two pieces. The standard aperture is introduced into the smaller disc shaped piece which is fixed onto the second bigger top hat shaped piece. The Ex2 electrode is a single top hat shaped metal part. The electrodes Ex1 and Ex2 are fixed together with the ground electrode onto the ceramic holder plate before the complete assembly is fixed onto the ion column vacuum tube. The complete EIRFIS prototype vacuum tube consists of two separate parts. The shorter vacuum tube part of the ion column is attached to the larger vacuum tube of the e-Column/ionisation region. In this way the correct distance of  $D_{IR} = 50$  mm is achieved, see figure 7.21 of appendix C (section 7.3).

In order to get a better idea about how the PCB ion carpet looks like see figure 5.24. The outer diameter is 90 mm and the RF-ring electrodes cover an area of 40 mm in diameter as already stated during the CPO-simulation section 5.2.2.

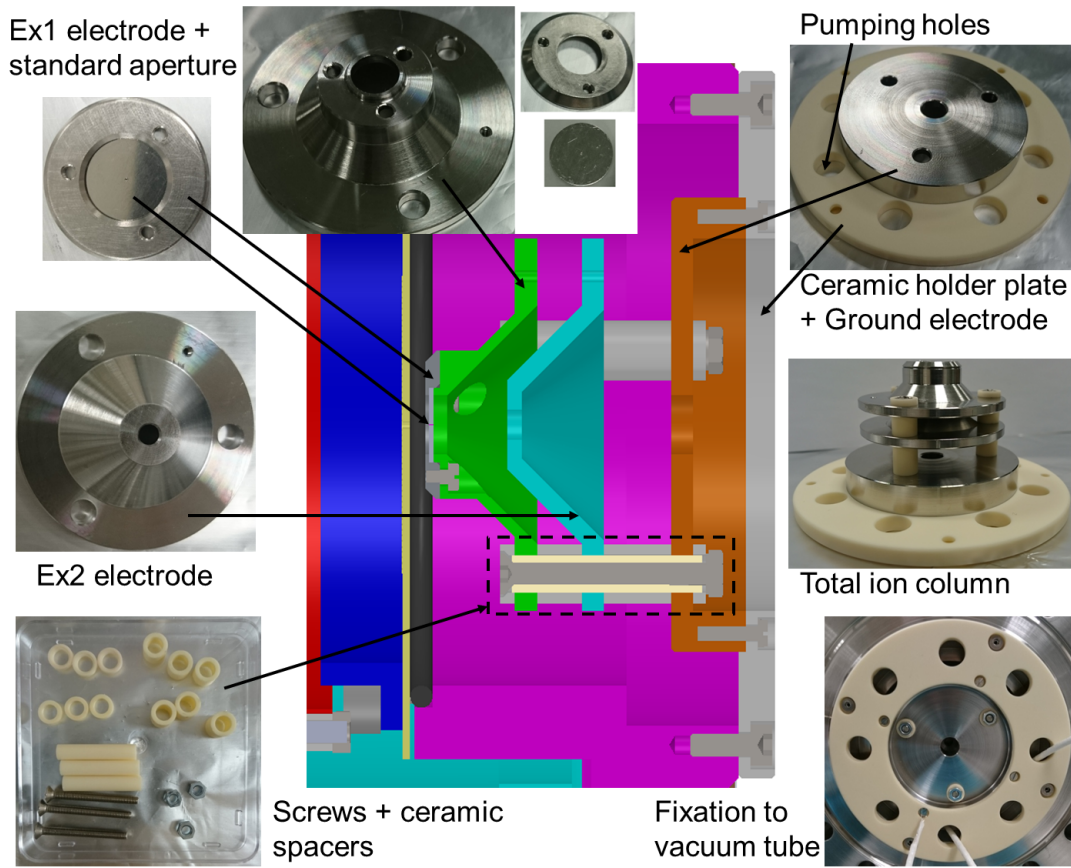


Figure 5.23: Illustration/pictures of the EIRFIS prototype ion column and its assemblage.

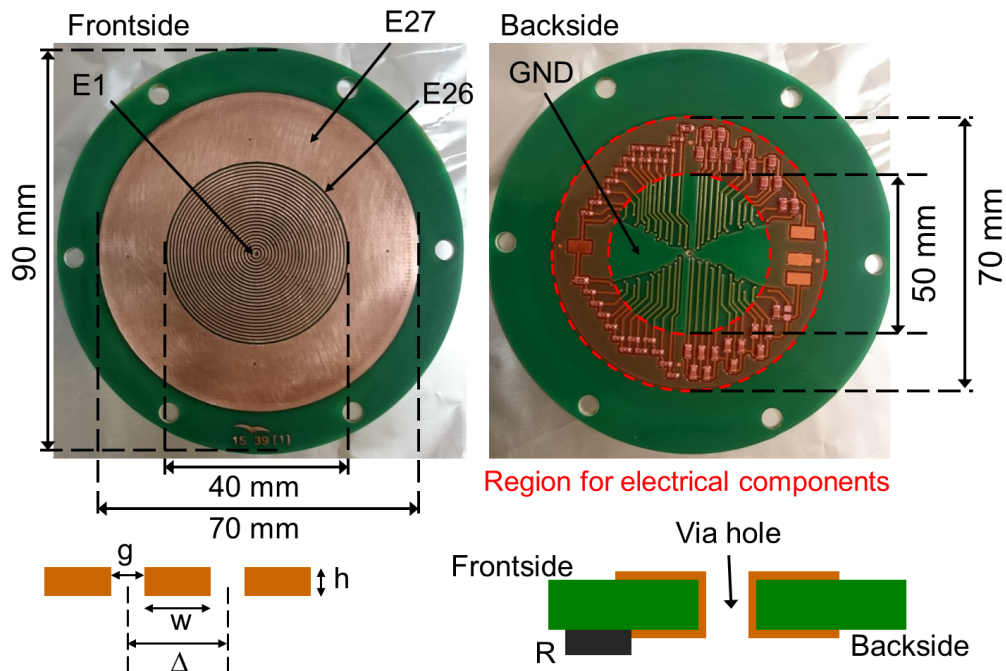


Figure 5.24: Illustration/pictures of the PCB ion carpet (front- and backside).

On the backside it is shown that the area where the electrical components can be mounted is an annulus in order to mount the ion carpet onto the ion column vacuum tube and to be able to position the electrode Ex1 closely to the ion carpet backside in the central region.

### PCB ion carpet : Electrical circuit layout

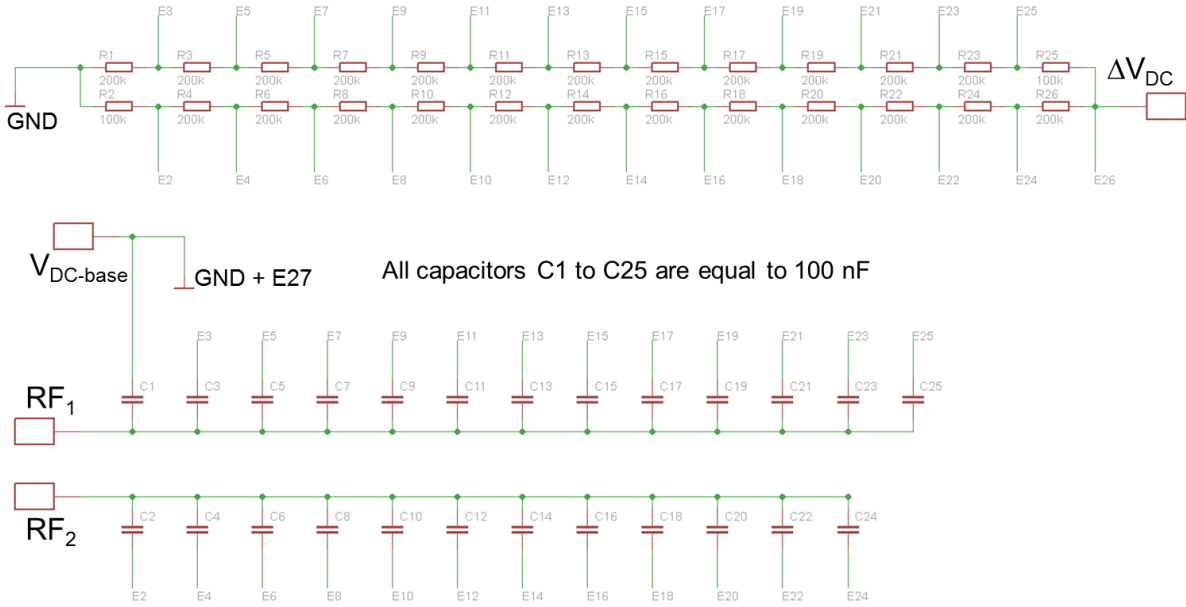


Figure 5.25: Electrical circuit layout of the PCB ion carpet.

The PCB technology uses tiny so called via holes to connect the frontside ring electrodes to the copper tracks on the backside leading towards the electrical components as illustrated in figure 5.24. In addition to the positioned O-ring, these open via holes are carefully closed with vacuum glue. In this way the only channel for gas conductance from the ionisation region towards the ion column is the ion carpet central hole. This central metallised hole (E1) has a diameter of  $d_0 = 1$  mm and is connected to the ground (GND) plane of the ion carpet. Moreover, the parameters of the ring electrodes are set to  $g = 0.25$  mm,  $w = 0.5$  mm,  $\Delta = 0.75$  mm and  $h = 0.1$  mm, see figure 5.24 for their definition. In this configuration the PCB ion carpet is in terms of geometrical parameters identical to the Ion Carpet B case evaluated in section 5.3.2, which represents a good compromise between a determined  $B_r \approx 10^2$  A/(m<sup>2</sup>sr V) and a low energy spread of  $\Delta E \leq 3$  eV. An illustration of the exact electrical circuit layout and the used electrical components can be found in figure 5.25.

#### 5.5.2 Electron column characterisation

**The experimental tests with the EIRFIS prototype are started by a characterisation of the e-Column functioning.** The  $Y_2O_3 - Ir$  disc cathode heating procedure is always carried out in relation to the advices given in [164]. The heating current for the disc cathodes should not be raised higher than 4.2 A as otherwise cathode failure occurs rapidly. For the initial tests, **the ion carpet is replaced by a solid copper plate** in order to be able to measure the e-beam current that enters the ionisation region, see figure 5.26. This copper plate has at its centre a 1 mm hole so that the ionisation region can be pumped from the ion column side exactly as it will be the case when the ion carpet is in place.

In a first configuration the e-Column parameters are set to  $d_C = 1.2$  mm,  $D_{CW} = 0.9$  mm,  $d_W = 2$  mm,  $D_{CA} = 1.7$  mm,  $d_A = 1.5$  mm,  $D_{AL} = 5$  mm,  $d_L = 6$  mm,  $D_{LI} = 50$  mm and  $d_I = 1.5$  mm. This e-Column configuration will be referred to in the following as **e-Column Setup 1**. As a reminder the different parameters of the disc cathode region are illustrated in figure 5.27.



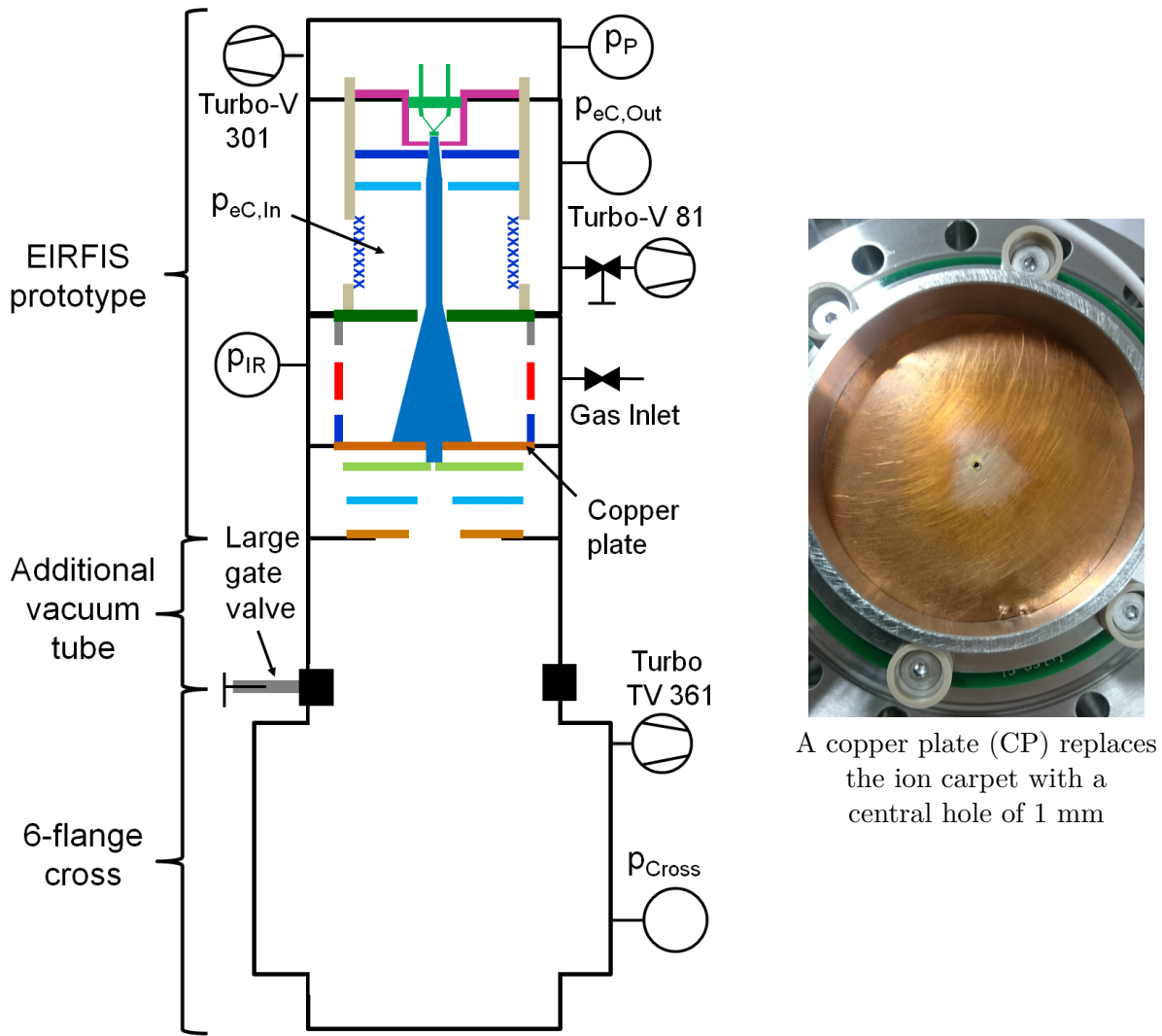


Figure 5.26: Illustration of the EIRFIS prototype test bench setup for the first e-Column/ionisation region tests.

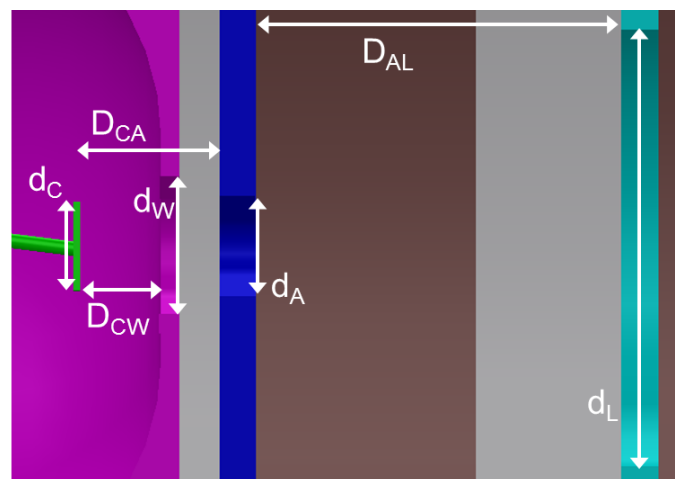


Figure 5.27: Illustration of the different parameters of the EIRFIS prototype e-Column disc cathode region.

Furthermore, the used e-Shield electrode is shown in figure 5.21 and has a mesh hole size of about 0.7 mm. It is always kept at the same potential as the anode in order to form an Einzel lens with the anode and the lens electrode. Some of the afore listed parameters are different to

those used for the CPO simulations listed in table 5.2 of section 5.2.1. The distance between the cathode disc and the Wehnelt electrode is increased to  $D_{CW} = 0.9$  mm and the Wehnelt hole diameter is opened up to  $d_W = 2$  mm (CPO simulations:  $D_{CW} = 0.2$  mm and  $d_W = 1.5$  mm). This adapted configuration makes it possible to get a stable operation of the  $Y_2O_3 - Ir$  disc cathode without any potential dependency or charging problems within the triode extraction region. Furthermore, the anode aperture is increased to  $d_A = 1.5$  mm compared to 0.8 mm for the CPO simulations. This is due to the fact that preliminary experimental e-beam extraction tests showed that even at extraction potentials<sup>14</sup>  $\Delta V_{Extr}$  of 3 to 4 kV quite a lot of the total emitted e-beam current hits the anode when a  $d_A$  of 0.8 mm is used. Increasing  $d_A$  to 1.5 mm has as effect that at the same  $\Delta V_{Extr}$  more e-beam current is transmitted towards the ionisation region. Nevertheless, the pressure will be still below the needed cathode operation pressure of  $1 \cdot 10^{-4}$  mbar as can be seen in table 5.3 of section 5.4.1 listing the gas conductance calculation results for different values of  $d_A$ .

During the corresponding **e-beam transmission tests** the inlet electrode is grounded and the potential difference between the installed copper plate (CP) and the inlet electrode is always kept at  $\Delta V_{CP-I} = 100$  V. In this way the secondary electron (sec-e) emission from the copper plate is suppressed and the transmitted primary e-beam current  $|I_{e,Tr}| = |I_{CP}|$  is measured accurately. The Shield 2 electrode within the ionisation region is kept at the mid-potential of the inlet electrode and the copper plate  $V_{Shield2} = (V_I + \Delta V_{CP-I}/2)$ . The potential of the disc cathode with respect to the inlet electrode is fixed to  $\Delta V_{C-I} = V_C - V_I = -100$  V in order to get an e-beam energy of 100 eV when it is entering into the ionisation region. A variation of the potential difference between Wehnelt and disc cathode  $\Delta V_{Bias} = V_W - V_C$  is performed. The pressures that are measured just before the e-beam transmission tests are listed in table 5.5, no gas injection is done so far. What should be mentioned is that the pressure within the e-Column ceramic support structure  $p_{eC,In}$  can not be measured directly but it will only be slightly higher than  $p_{eC,Out}$  as the gas conductance calculations have already shown in section 5.4.1 (see table 5.3). The cathode heating current is set to 3.9 A ( $T_{Cathode} \approx 1440$  K [165]) which is below the recommended maximum of 4.2 A.

The **results of the e-beam transmission tests with e-Column Setup 1** can be seen in figure 5.28. A variation of the measured copper plate current  $|I_{CP}| = |I_{e,Tr}|$  and of the Shield 2 electrode current  $|I_{Shield2}|$  in dependence of the applied  $\Delta V_{CP-I}$  can be seen in figure 5.28a. During this measurement the values of  $\Delta V_{Bias}$  and  $\Delta V_{Extr}$  are kept fixed at - 480 V and 3 kV, respectively. The curve of  $|I_{e,Tr}|$  continuously increases as  $\Delta V_{CP-I}$  gets more positive which is related to the fact that the emission of secondary electrons is more and more suppressed.

Gas injection	Gas species	$p_p$ [mbar]	$p_{eC,Out}$ [mbar]	$p_{IR}$ [mbar]	$p_{Cross}$ [mbar]
NO	Air	$1.0 \cdot 10^{-8}$	$9.0 \cdot 10^{-7}$	$7.1 \cdot 10^{-5}$	$1.3 \cdot 10^{-7}$

e-Column Setup 1 (no e-beam).

Table 5.5: EIRFIS prototype: Pressures measured just before the e-beam transmission tests.

<sup>14</sup>With extraction potential is meant the potential difference between anode and cathode  $\Delta V_{AC} = \Delta V_{Extr}$ .

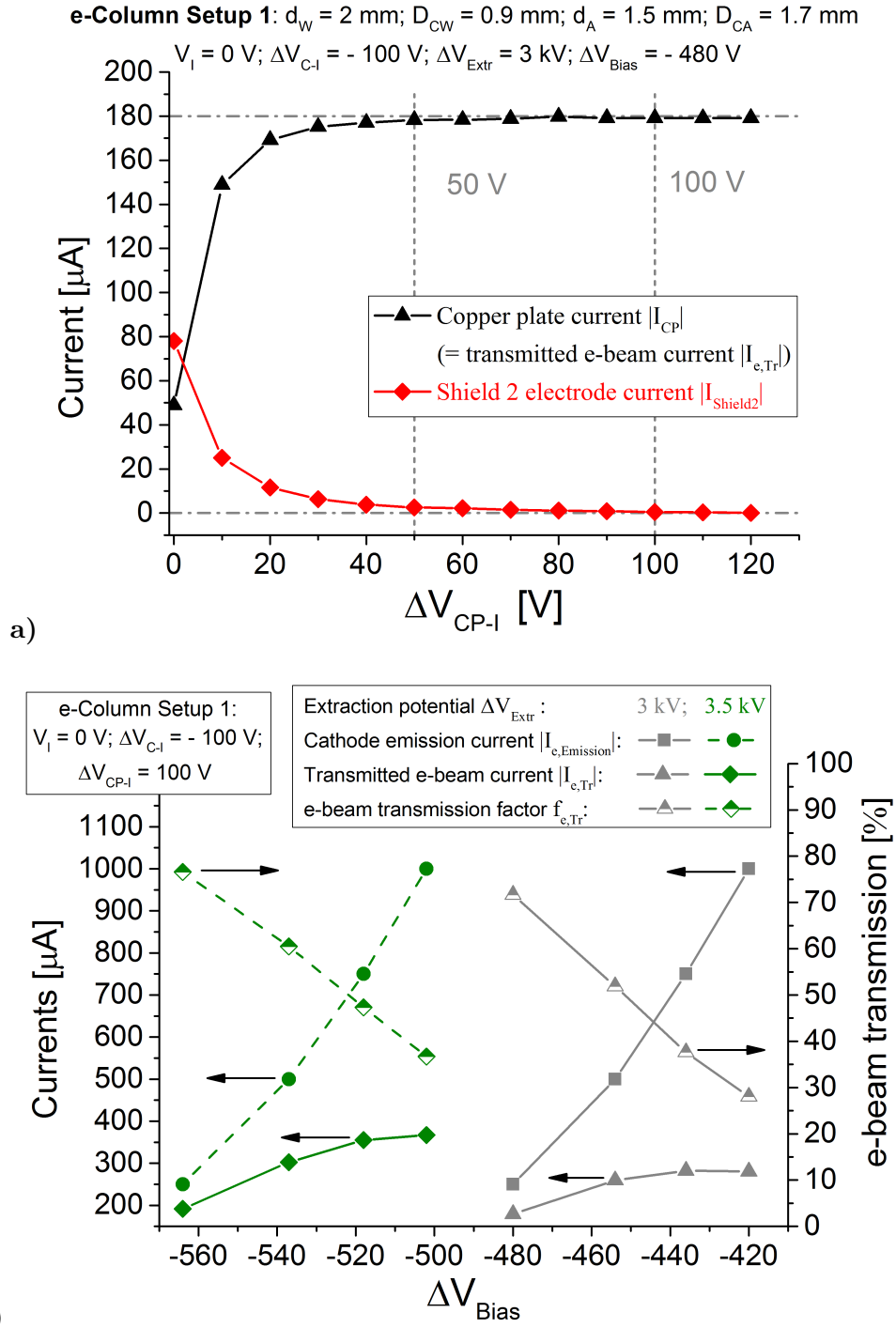


Figure 5.28: a) Suppression of the sec-e emission from the copper-plate (e-Column Setup 1);  
b) Results of the e-beam transmission tests at different extraction potentials  $\Delta V_{Extr}$  (e-Column Setup 1).

A part of the sec-e is attracted by the Shield 2 electrode as its potential is always more positive than the copper plate potential. Therefore, the continuously decreasing  $|I_{Shield2}|$  value with increasing  $\Delta V_{CP-I}$  reinforces the statement that more and more sec-e are suppressed. What can be further seen is that for  $\Delta V_{CP-I} \geq 50$  V the curve of  $|I_{e,Tr}|$  approaches a constant which means that by setting  $\Delta V_{CP-I}$  at 100 V during the e-beam transmission tests it is guaranteed that the sec-e emission is effectively suppressed. In figure 5.28b the measured e-beam transmission results are shown and at  $\Delta V_{Extr} = 3$  kV  $|I_{e,Tr}|$  varies in the range of 180 to 280  $\mu$ A with a maximal disc cathode emission current  $|I_{e,Emission}|$  of 1 mA. The value of  $|I_{e,Emission}|$  is not raised above 1 mA as the  $|I_{e,Tr}|$  curve starts reaching a plateau and it is expected that  $|I_{e,Tr}|$  will not considerably

increase when going to more positive values for  $\Delta V_{\text{Bias}}$  ( $> -420$  V). Moreover, higher  $|I_{\text{e,Emission}}|$  values mean a faster degradation of the disc cathode and a reduction of its lifetime. By increasing  $\Delta V_{\text{Extr}}$  to 3.5 kV higher  $|I_{\text{e,Tr}}|$  values are measured compared to the  $\Delta V_{\text{Extr}} = 3.0$  kV setting. **A maximum of about 370  $\mu\text{A}$  is measured at 1 mA of  $|I_{\text{e,Emission}}|$**  where the current curve starts to reach again a plateau. This result is very close to the estimation of 400  $\mu\text{A}$  made in section 5.2.1 for the e-beam current that can enter the ionisation region. In both  $\Delta V_{\text{Extr}}$  cases the experimental curves for  $f_{\text{e,Tr}}$  cannot immediately be compared to the CPO-simulation results of figure 5.7. There  $f_{\text{e,Tr}}$  is defined as ratio of the e-beam current that passes through the anode aperture to the current that enters the ionisation region and here  $f_{\text{e,Tr}}$  is equal to  $|I_{\text{e,Tr}}|/|I_{\text{e,Emission}}|$ . In the mechanical configuration of the EIRFIS prototype it is not foreseen to be able to measure directly the current passing the anode aperture, e. g. by deviating the e-beam towards a measuring plate, as it is of more importance to have a measure of the current that actually passes into the ionisation region.

### 5.5.3 Ion current generation within the ionisation region

The next experimental tests that are performed are **argon gas injection tests into the ionisation region in order to evaluate how much ion current  $I_{\text{Ions,Ar}}$  can be generated**. For this purpose a voltage supply is connected to the inlet electrode in order to be able to create a retarding field for the entering 100 eV e-beam. The setup of the e-Column is unchanged and corresponds to the e-Column Setup 1. The gas injection is gradually increased and the total current  $I_{\text{Total,CP}}$  that hits the installed copper plate is measured by the connected pico-ammeter and has different contributions as can be seen in figure 5.29a.

During these tests  $V_{\text{I}}$  is set to 100 V and the e-Column potentials adapted to still have  $\Delta V_{\text{C-I}} = -100$  V,  $\Delta V_{\text{Extr}} = 3.5$  kV and the 250  $\mu\text{A}$  e-beam emission current setting is used. In a **first step** the potential difference of  $\Delta V_{\text{CP-I}}$  is fixed at 100 V suppressing the sec-e emission and a maximum value of  $I_{\text{e,0}} = -189$   $\mu\text{A}$  is measured on the copper plate. In the used setting of the pico-ammeter a negative current value indicates that an e-beam is measured. In a **second step**  $\Delta V_{\text{CP-I}}$  is changed to -50 V to create the 1 V/mm retarding field for the e-beam. In this configuration sec-e emission occurs, no gas is yet injected into the ionisation region. The corresponding current value on the pico-ammeter is measured as  $I_{\text{CP,No-gas}} = -71$   $\mu\text{A}$  and the sec-e current contribution can be calculated by  $|I_{\text{sec-e}}| = |I_{\text{e,0}}| - |I_{\text{CP,No-gas}}|$ , meaning that in the case presented here  $|I_{\text{sec-e}}| = 118$   $\mu\text{A}$ . The corresponding sec-e emission factor can be determined to  $\gamma_{\text{sec-e}} [50 \text{ eV}] = |I_{\text{sec-e}}|/|I_{\text{e,0}}| = 0.63$  at a primary e-beam energy of 50 eV when it is hitting the copper plate. This result is very close to the value of  $\gamma_{\text{sec-e,Lit}} [50 \text{ eV}] = 0.66$  listed in [166] for copper. The **third step** consists in gradually increasing the argon gas injection so that more and more ions are created and pulled towards the copper plate. As a result a more and more positive  $I_{\text{Total,CP}}$  value is measured.  $I_{\text{Total,CP}}$  corresponds now to a sum of different contributions and is defined as:

$$I_{\text{Total,CP}} = -|I_{\text{e,0}}| \cdot f_{\text{e,CP}} + |I_{\text{e,0}}| \cdot f_{\text{e,CP}} \cdot \gamma_{\text{sec-e}} [E_{\text{e,CP}}] + I_{\text{Ions,Ar}} \quad . \quad (5.13)$$

Where  $f_{\text{e,CP}}$  accounts for the fact that due to electron gas collisions only a certain amount of the primary e-beam arrives at the copper plate with increasing  $p_{\text{IR}}$  until at higher pressures the e-beam is stopped within the ionisation region and only ions hit the copper plate. Furthermore, the energy at which the e-beam contribution arrives at the copper plate  $E_{\text{e,CP}}$  changes with  $p_{\text{IR}}$ .



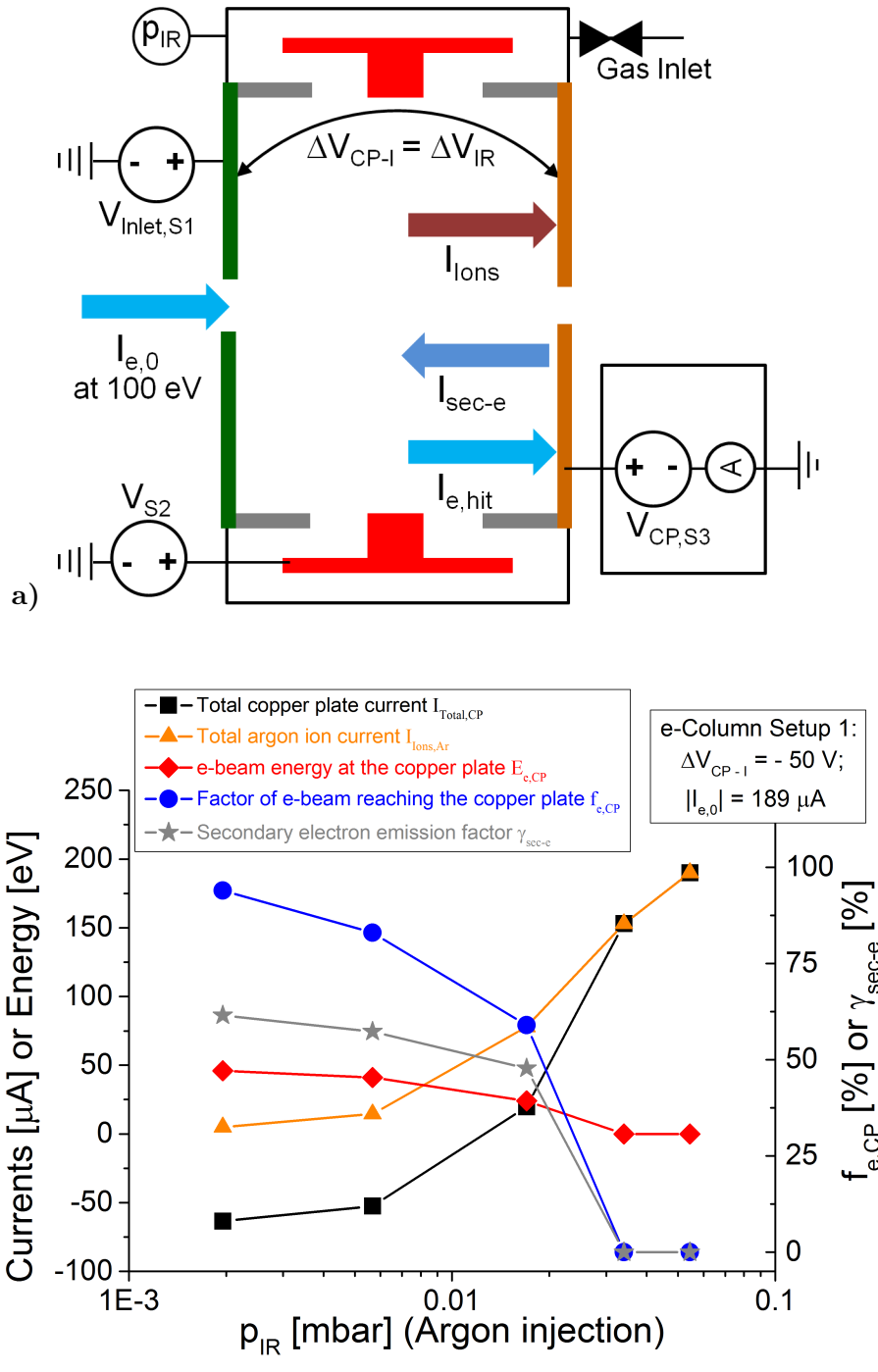


Figure 5.29: a) Illustration: Copper plate current contributions during the ion generation tests;  
 b) e-Column Setup 1: Argon ion current generation results  
 ( $\Delta V_{Extr} = 3.5$  kV;  $V_I = 100$  V;  $\Delta V_{C-I} = -100$  V).

Both quantities  $f_{e,CP}$  and  $E_{e,CP}$  are determined with the slice-approach already explained in more detail within the CPO-simulation section 5.3.1. The variation of  $E_{e,CP}$  influences as well the sec-e emission factor, this needs to be taken additionally into account. The values of  $\gamma_{sec-e}$  in the different  $E_{e,CP}$  cases ( $\gamma_{sec-e}[E_{e,CP}]$ ) are determined by comparison with the results for  $\gamma_{sec-e}$  stated in [166] for the energy range below 100 eV.

For the determination of the generated argon ion current equation 5.13 is rearranged to:

$$I_{Ions,Ar} = I_{Total,CP} + |I_{e,0}| \cdot f_{e,CP} - |I_{e,0}| \cdot f_{e,CP} \cdot \gamma_{sec-e}[E_{e,CP}] \quad . \quad (5.14)$$

Gas injection	Gas species	$p_p$ [mbar]	$p_{eC,Out}$ [mbar]	$p_{IR}$ [mbar]	$p_{Cross}$ [mbar]
YES	Ar	$1.4 \cdot 10^{-8}$	$7.9 \cdot 10^{-6}$	$1.9 \cdot 10^{-3}$	$3.3 \cdot 10^{-8}$
YES	Ar	$3.3 \cdot 10^{-8}$	$3.9 \cdot 10^{-5}$	$9.4 \cdot 10^{-3}$	$1.5 \cdot 10^{-6}$
YES	Ar	$8.2 \cdot 10^{-8}$	$1.3 \cdot 10^{-4}$	$1.9 \cdot 10^{-2}$	$2.6 \cdot 10^{-6}$
YES	Ar	$2.3 \cdot 10^{-7}$	$4.3 \cdot 10^{-4}$	$3.7 \cdot 10^{-2}$	$1.6 \cdot 10^{-5}$
YES	Ar	$3.4 \cdot 10^{-7}$	$6.7 \cdot 10^{-4}$	$5.1 \cdot 10^{-2}$	$2.5 \cdot 10^{-5}$

e-Column Setup 1 (e-beam; Correction factors for pressure gauges included).

Table 5.6: EIRFIS prototype: Pressures measured during the ion generation tests.

The different measured and deduced parameters are graphically represented in figure 5.29b in dependence of  $p_{IR}$ . The values of  $p_{IR}$  incorporate the correction factors in the case of argon for the used pressure gauge ITR90 [167]. All measured pressures during these argon ion generation tests can be found in detail in table 5.6. What can be seen in figure 5.29b is that as expected the generated amount of argon ion current increases continuously with increasing  $p_{IR}$ . At the beginning for  $p_{IR} < 1 \cdot 10^{-2}$  mbar  $I_{Total,CP}$  shows negative values which indicates that there is still a large contribution of electron current hitting the copper plate. At higher pressures  $f_{e,CP}$  starts decreasing and  $I_{Total,CP}$  becomes positive for  $p_{IR} \approx 1.8 \cdot 10^{-2}$  mbar where the determined  $I_{Ions,Ar}$  is 78  $\mu A$ . At  $p_{IR} > 3 \cdot 10^{-2}$  mbar  $f_{e,CP}$  drops to zero which indicates that the e-beam is stopped within the ionisation region and does not reach anymore the copper plate. At  $p_{IR} \approx 5 \cdot 10^{-2}$  mbar the argon ion current is determined to 180  $\mu A$ . The targeted  $p_{IR}$  of  $1 \cdot 10^{-1}$  mbar could not be reached at this point of the investigation as some charging problems occurred on the inlet and Shield 2 electrode. Going to  $p_{IR} = 1 \cdot 10^{-1}$  mbar is expected to raise  $I_{Ions,Ar}$  above 200  $\mu A$  with  $|I_{e,Emission}| = 250 \mu A$  and  $\Delta V_{Extr} = 3.5$  kV.

From the e-beam transmission test results shown in figure 5.28b it can be seen that at  $|I_{e,Emission}| = 500 \mu A$  the value of  $|I_{e,Tr}| = |I_{e,0}|$  is raised by a factor of 1.6 compared to  $|I_{e,Emission}| = 250 \mu A$  in the case of no gas injection. Taking into account that e-beam current losses due to residual gas ionisation will occur along the e-Column for  $p_{IR} = 1 \cdot 10^{-1}$  mbar, **it is expected that  $I_{Ions,Ar}$  can be further increased to the range of 250 - 300  $\mu A$** . This result is very similar to the estimation of 260  $\mu A$  performed in section 5.3.1 by using the slice-approach. To use an  $|I_{e,Emission}|$  setting above 500  $\mu A$  should be avoided as the further gain in ionising electron current is only marginal and these high values of  $|I_{e,Emission}|$  mean a faster degradation and shorter lifetime of the disc cathode.

After these ion generation tests a further adaptation of the triode extraction region assembly has been done. Additional details/explanations related to this adaptation can be found in appendix C (section 7.3). The parameters are all identical to e-Column Setup 1 with the only difference that the Wehnelt hole has been opened up to  $d_W = 3$  mm. This slight change of the e-Column will in the following be referred to as **e-Column Setup 2**.

### 5.5.4 Ion carpet incorporation and ion extraction tests

In order to evaluate the ion extraction out of the ionisation region the **PCB ion carpet** shown in figure 5.24 is **incorporated within the prototype**. These experiments are performed at  $p_{IR} = 0.1$  mbar and  $V_I = 500$  V, which currently allow to be in stable source operation conditions. The final target is to be able to raise the ionisation region to a few kV at  $p_{IR} = 0.1$  mbar and reach an energy of a few keV for the ion beam at the end of the ion column.

A special **RF-signal generation system** is developed as illustrated in figure 5.30. It incorporates an arbitrary function generator (AFG) [168] to create a low voltage sinus signal up to a frequency of 12 MHz. The AFG is connected to the input of an RF amplifier [169] with a gain of 50 dB<sup>15</sup> and a frequency range of 0.01 to 12 MHz. This amplifier measures the forward power  $P_{\text{RF,FWD}}$  and backward (reflected) power  $P_{\text{RF,BWD}}$  at its output and is rated at a maximal total output power  $P_{\text{Output}} = P_{\text{RF,FWD}} + P_{\text{RF,BWD}}$  of 40 W. The amplifier is followed by a transformer [170] that converts the single input signal into two output signals that are 180° out of phase to each other. The output impedance of this transformer is 200  $\Omega$ . Both outputs of the transformer are directly connected to a HV-decoupling box. The HV-decoupling box incorporates on each RF-signal line a total DC-blocking capacitance of 10 nF [171] in order to isolate the RF-electronics from the PCB ion carpet kept at high voltage. Furthermore, so called Transient-Voltage-Suppression (TVS) diodes [172] are installed within the HV-decoupling box to protect the system against any high voltage transition from the PCB ion carpet to the RF-electronics that can occur when electrical discharges are produced within the ion source. Moreover, a high voltage power supply is connected to the PCB ion carpet to apply  $V_{\text{IC}}$  and as well an isolated low voltage supply to apply the additional  $\Delta V_{\text{DC}}$  to create the DC-gradient across the ion carpet electrodes.

**During the argon ion extraction tests an Ex1 aperture size of  $d_{\text{Ex1}} = 100 \mu\text{m}$  is used.** As can be seen in figure 5.30 the RF-signal at the exit of the HV-decoupling box is monitored by the use of a differential voltage probe and an oscilloscope. In this way the applied amplitude  $V_{\text{Amp,RF}}$  can be measured. A faraday cup (FC) is mounted at about 90 mm behind the ground plate electrode in downstream direction in order to measure the ion current  $I_{\text{Ion-beam,Ar}}$  that passes  $d_{\text{Ex1}}$ , see figure 5.31. The Ex2 electrode is used to focus the argon ion beam into the FC and the suppressor plate of the FC is kept at - 40 V to cancel out any sec-e emission current contribution to  $I_{\text{Ion-beam,Ar}}$ . The FC is mounted on a movable XYZ-stage in order to be able to position it with respect to the ion beam.

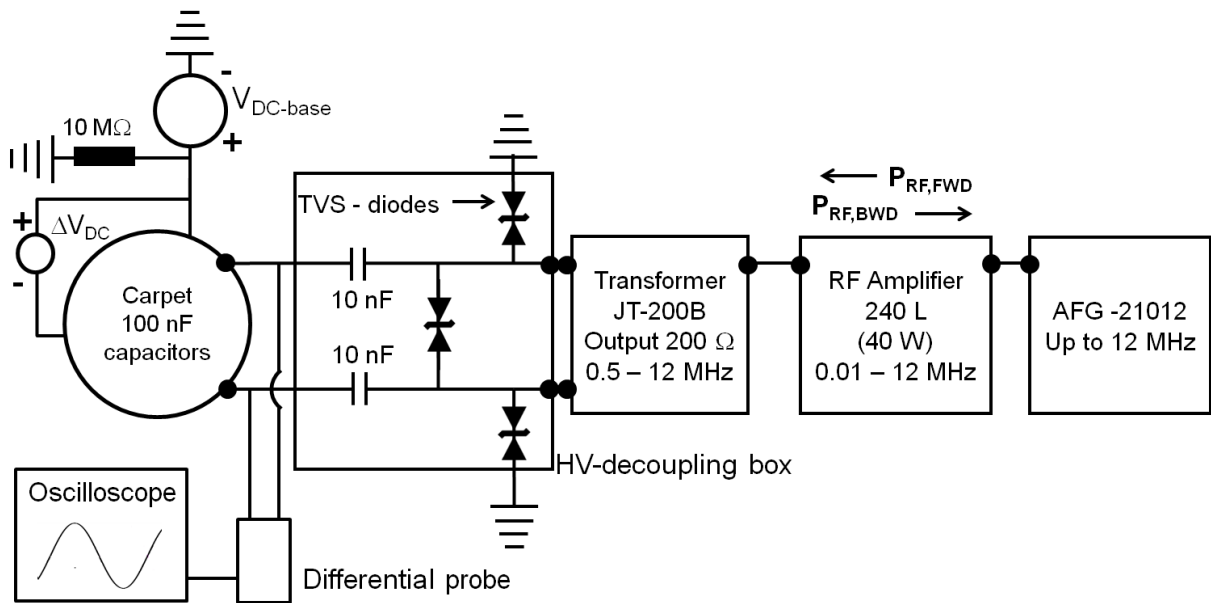


Figure 5.30: Schematic of the RF-signal generation system.

<sup>15</sup>The voltage gain can be defined as:  $\text{gain} = 20 \cdot \log(V_{\text{out}}/V_{\text{in}})$  dB.

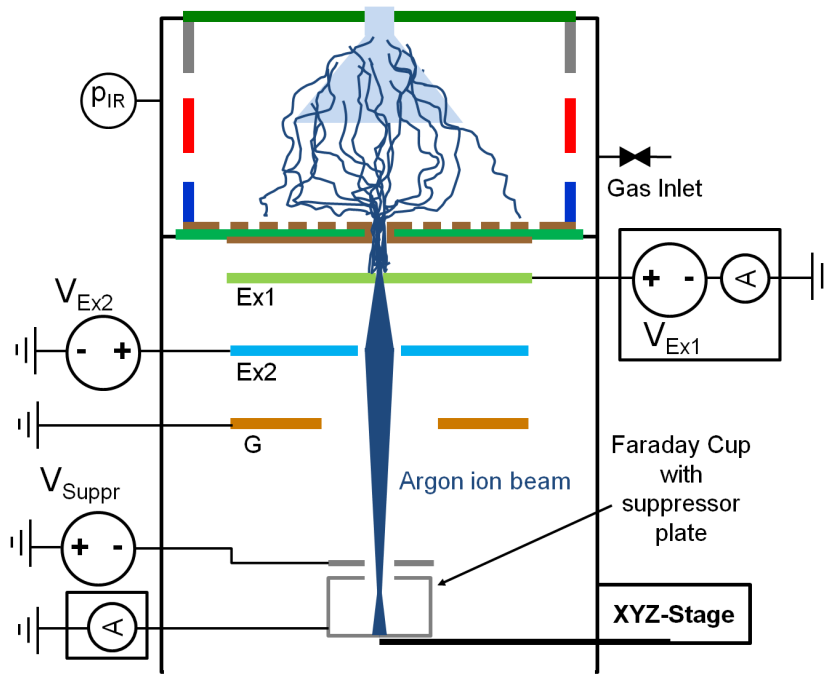
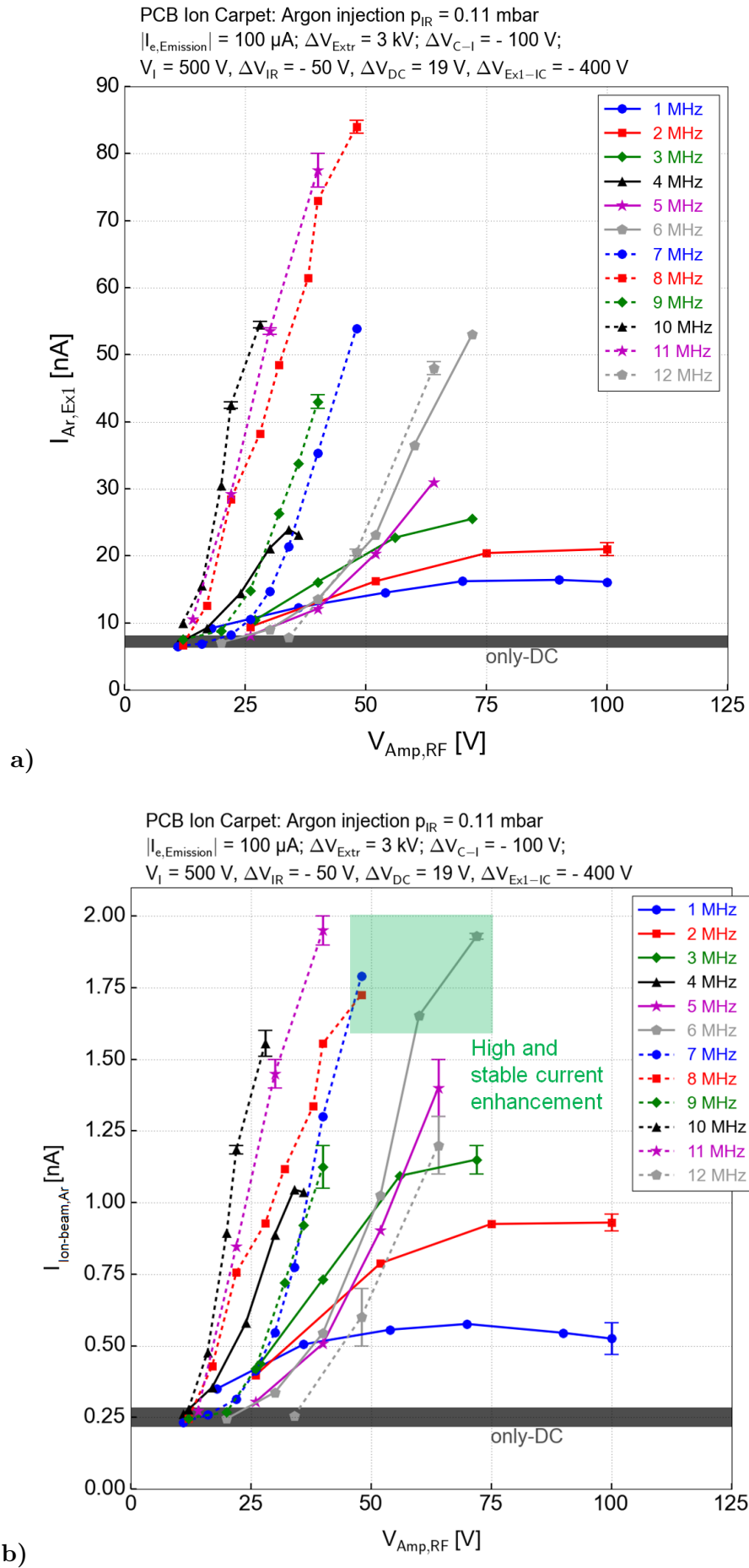


Figure 5.31: Experimental setup illustration for the ion current extraction measurements.

The FC position and the potential of Ex2 is tuned so that the maximum  $I_{\text{Ion-beam,Ar}}$  is measured. As already mentioned before the targeted pressure of  $p_{\text{IR}} = 0.1$  mbar can only be currently reached at  $V_{\text{I}} = 500$  V, this setting is as well used here. The remaining potential settings are as follows:  $\Delta V_{\text{C-I}} = -100$  V,  $\Delta V_{\text{eShield-I}} = 3$  kV,  $\Delta V_{\text{IR}} = -50$  V,  $\Delta V_{\text{Shield2-I}} = -25$  V,  $\Delta V_{\text{DC}} = 19$  V and  $\Delta V_{\text{Ex1-IC}} = -400$  V. The Ex1 electrode is connected to a pico-ammeter with internal voltage supply to accurately measure the extracted argon ion current  $I_{\text{Ar,Ex1}}$ . The Ex 2 electrode is set to 380 V, the ground electrode is earthed and the e-Column Setup 2 is used. The cathode emission current during these tests is set to  $|I_{\text{e,emission}}| = 100$   $\mu\text{A}$ , due to the fact that only in this setting the inlet electrode power supply can be operated at stable conditions. At higher  $|I_{\text{e,emission}}|$  values the measured inlet power supply current slowly increases and decreases (no fast oscillations are seen). It can happen that the measured current rises above the limit of the power supply due to which the potential  $V_{\text{I}}$  starts changing as well. Furthermore, it is noticed that due to this unstable situation electrical discharges occur which influence the other power supplies connected to the EIRFIS prototype.

As can be seen in figure 5.32 the effect on  $I_{\text{Ar,Ex1}}$  and  $I_{\text{Ion-beam,Ar}}$  when applying the RF-signals to the PCB ion carpet is evaluated up to  $f_{\text{RF}} = 12$  MHz in steps of 1 MHz. **In figure 5.32a the results are shown for  $I_{\text{Ar,Ex1}}$ .** At some data points error bars are indicated which represent current fluctuations measured at the corresponding RF setting and only fluctuations bigger than 1 nA are represented. In each  $f_{\text{RF}}$  setting the maximal reached  $V_{\text{Amp,RF}}$  corresponds to the case where the RF amplifier measures a  $P_{\text{Output}}$  of about 30 W. The region where no RF-signal is applied and only DC-potentials are present is marked in the graph as only-DC region varying between 6 to 8 nA. Already the 1, 2 and 3 MHz curves show a clear enhancement of  $I_{\text{Ar,Ex1}}$  compared to the only-DC case with shallow slopes at the beginning and plateaus for  $V_{\text{Amp,RF}} \geq 75$  V. Very similar slowly increasing curves have already been seen for the Ion Carpet B case in the 1 to 3 MHz range during the evaluation in the CPO simulation section 5.2.2, see figure 5.12. For all frequency cases above 3 MHz the experimental  $I_{\text{Ar,Ex1}}$  curves have a steeper slope and the maximal  $V_{\text{Amp,RF}}$  is always  $< 75$  V.



This steeper curve trend has as well already been observed for the simulated Ion Carpet B case. The experimental 6, 7 and 10 MHz curves in figure 5.32a show in average a maximal value for  $I_{Ar,Ex1}$  of 54 nA which corresponds to an improvement factor close to 8x with respect to the only-DC case. **The highest  $I_{Ar,Ex1}$  value is obtained at 8 MHz and  $V_{Amp,RF} \approx 50$  V with 84 nA, corresponding to an improvement factor of 12x compared to the only-DC case.** The CPO simulation results for Ion Carpet B, see figure 5.12, show that at 8 MHz and  $V_{Amp,RF} = 50$  V the improvement factor of the ion extraction efficiency is about 19 which is quite close to the here determined experimental improvement factor of 12. The experimental results in figure 5.32a show that the maximum  $I_{Ar,Ex1}$  in the 11 MHz case approaches 80 nA but higher current fluctuations appear and power supply instabilities are observed at this setting. From the e-Column transmission tests it is concluded that several tens up to hundreds of  $\mu A$  of ionising e-beam current  $|I_{e,0}|$  can reach the ionisation region. Furthermore, the ion generation tests show that with  $p_{IR} = 0.1$  mbar it is possible to produce total ion currents of several tens up to hundreds of  $\mu A$ . The simulation results for the Ion Carpet B case determine an extraction factor up to 30 % for  $V_{Amp,RF} \leq 75$  V and  $f_{RF}$  from 1 to 12 MHz, see figure 5.12. Combining all these facts justifies the expectation that at least a few  $\mu A$  of argon ion current should be extracted from the ionisation region. Currently the experimental results are still two orders of magnitude below this range.

**In figure 5.32b the experimental determined  $I_{Ion-beam,Ar}$  curves are shown** and have very similar trends to their corresponding  $I_{Ar,Ex1}$  curve in figure 5.32a. The error bars are this time shown for all data points where a current fluctuation above 0.01 nA occurred and the only-DC range is in between 0.2 and 0.3 nA. For the cases of 6, 7, 8, 10 and 11 MHz **the maximal measured  $I_{Ion-beam,Ar}$  is between 1.5 and 2 nA corresponding to improvement factors of 6x to 8x compared to the only-DC case.** Bigger current fluctuations are seen for 10 and 11 MHz so that the frequency range for a high and stable  $I_{Ion-beam,Ar}$  enhancement is determined to be from  $f_{RF} = 6$  to 8 MHz. Within this range the  $f_{RF} = 8$  MHz case represents the setting with the lowest ratio of  $P_{RF,BWD}/P_{RF,FWD} = 12$  %. This means that at 8 MHz the total impedance of the HV-decoupling box and the PCB ion carpet (the load) attached to the exits of the transformer is already close to the output impedance of  $200 \Omega^{16}$ . Therefore, the 8 MHz case probably represents a good setting where a transformer output load matching to  $200 \Omega$  can be performed by adding additional electronic components (e. g. inductors and resistances) into the HV-decoupling box. An outcome of this load matching is that it will be possible to go to higher  $V_{Amp,RF}$  values and get an even better  $I_{Ion-beam,Ar}$  enhancement within the output power range (up to 40 W) of the RF amplifier. The different measured pressures during this ion extraction evaluation can be found in table 5.7.

Argon injection			
$p_p$ [mbar]	$p_{eC,Out}$ [mbar]	$p_{IR}$ [mbar]	$p_{Cross}$ [mbar]
$8.8 \cdot 10^{-7}$	$3.0 \cdot 10^{-3}$	$1.1 \cdot 10^{-1}$	$2.6 \cdot 10^{-5}$

Table 5.7: EIRFIS prototype: Pressures measured during the argon ion extraction tests (e-Column Setup 2).

<sup>16</sup>The transformer performs the best if the attached output load is exactly  $200 \Omega$ .

What these ion extraction results clearly show is that **an enhancement of the argon ion beam current can be achieved when RF-signals of a few MHz are applied to the PCB ion carpet**. What should be mentioned is that some preliminary investigations did show that the PCB ion carpet only has an effect on the extracted argon current when  $p_{\text{IR}}$  is close to 0.1 mbar. At  $p_{\text{IR}} \leq 5 \cdot 10^{-2}$  mbar the application of the RF-signal up to  $V_{\text{Amp,RF}} = 100$  V does not have any enhancing effect. Some test simulations have shown that when  $p_{\text{IR}}$  drops to the 0.01 mbar regime the needed amplitudes  $V_{\text{Amp,RF}}$  shift to the range above 150 V to get back some benefit for  $I_{\text{Ar,Ex1}}$ .

The determined achievable reduced brightness in the order of  $B_r \approx 10^2 \text{ A}/(\text{m}^2 \text{ sr V})$  is mainly based on the fact that the EIRFIS concept can extract ion currents in the range of  $\mu\text{A}$  from the ionisation region and in this way achieve high  $I_{\text{Ion-beam}}$  values. Raising the experimentally measured extraction ion currents towards the  $\mu\text{A}$  range will result in the fact that the experimentally determinable reduced brightness of the EIRFIS prototype gets closer to the expectation of  $B_r \approx 10^2 \text{ A}/(\text{m}^2 \text{ sr V})$ .

Further improvements on the experimental setup in particular the RF-electronics should allow us to come closer to the simulated current values. In appendix C (section 7.3) some additional explanations can be found to get an idea about how the RF potentials that actually reach the different PCB ion carpet electrodes currently look like and a related improvement is discussed.

On the operational side of the ion source its lifetime is an aspect that is of interest. Most probably one of the main factors that influences the ion source lifetime is the lifetime of the used  $\text{Y}_2\text{O}_3 - \text{Ir}$  disc cathode. In [155] the lifetime of those cathodes is stated by the manufacturer as hundreds of hours with medium currents. During the experimental tests performed so far with the EIRFIS prototype a single  $\text{Y}_2\text{O}_3 - \text{Ir}$  disc cathode has been used over a period of about 100 hours without major changes in ion source performance and the cathode is still operational.

## 5.6 Summary and conclusions

- A first important result is that due to electron gas collisions combined with a retarding field of  $F_{e,Retard} = 1$  V/mm within the ionisation region, the electron stopping ranges for a 100 eV e-beam within Ne, Ar, Kr, Xe, O<sub>2</sub> and N<sub>2</sub> at  $p_{IR} = 0.1$  mbar and  $T_{IR} = 298.15$  K are below 40 mm. Therefore, the size of the EIRFIS prototype ionisation region is fixed to 50 mm in order to stop the e-beam before the integrated RF ion carpet.
- The e-Column CPO simulations show that by using as thermionic emitter an Y<sub>2</sub>O<sub>3</sub> – Ir disc cathode and by collimating the extracted e-beam the maximum injected current into the ionisation region at 100 eV through a 1.5 mm aperture leads to  $I_{e,0} \approx 400$   $\mu$ A. A special ionisation volume slice-approach is used to get an idea about the total generated ion current  $I_{Ion,total}$  at  $p_{IR} = 0.1$  mbar and is determined for Ar<sup>+</sup> ions to 260  $\mu$ A.
- Two different ion carpet setups are evaluated by CPO simulations: For Ion Carpet A the central hole electrode is kept at the DC-base potential  $V_{IC}$  superimposed with the varying RF potential and for Ion Carpet B it is fixed at  $V_{IC}$ . The extraction efficiency  $f_{Extr}$  for Ar<sup>+</sup> ions is evaluated for the conditions of:  $F_{Push} = F_{Pull} = 1$  V/mm;  $p_{IR} = 0.1$  mbar,  $T_{IR} = 298.15$  K;  $0 \text{ MHz} < f_{RF} \leq 12 \text{ MHz}$  and  $0 \text{ V} < V_{Amp,RF} \leq 150 \text{ V}$ . In the Ion Carpet A case  $f_{Extr,Ar^+}$  is at maximum about 80 % and in the Ion Carpet B case only at about 50 %. From the ion extraction evaluation it is concluded that for Ion Carpet A the settings of  $f_{RF} = 9 \text{ MHz}$  and  $V_{Amp,RF} = 100 \text{ V}$  ( $f_{Extr,Ar^+} \approx 76 \%$ ) represent a good compromise between a high  $f_{Extr,Ar^+}$  and a low risk for electrical breakdown between neighbouring carpet rings due to a too high  $V_{Amp,RF}$ . For Ion Carpet B a good choice of parameters is determined as  $f_{RF} = 7 \text{ MHz}$  and  $V_{Amp,RF} = 100 \text{ V}$  ( $f_{Extr,Ar^+} \approx 35 \%$ ).
- In order to estimate the achievable reduced brightness  $B_r$  of the EIRFIS concept, the trajectory extrapolation method is used to find the ion beam source size and half-opening angle. The evaluation is done for different ion column potential settings and an extraction aperture below the ion carpets of 100  $\mu$ m is used. For both ion carpets the determined Ar<sup>+</sup> ion beam current lies in the range of a few  $\mu$ A and the half-opening angle is always below 20 mrad. The source size is in between 50 to 80  $\mu$ m. The determined mean  $B_r$  value for the Ion Carpet A case is 526 A/(m<sup>2</sup> sr V) and for the Ion Carpet B case 95 A/(m<sup>2</sup> sr V), this lower value is mainly related to the lower extracted ion current. These determined  $B_r$  values in the 10<sup>2</sup> A/(m<sup>2</sup> sr V) range are still below the target of 10<sup>3</sup> – 10<sup>4</sup> A/(m<sup>2</sup> sr V), although for Ion Carpet A it is only a factor 2 below the lower limit of this range. An optimised electron column producing a smaller cross section of the collimated e-beam leads to a higher ionising e-beam current leading to an increase in ion beam current and further raises  $B_r$ . A conclusion that can already be drawn here is that the EIRFIS concept represents a clear improvement compared to conventional EI ion sources with  $B_r \approx 1$  A/(m<sup>2</sup> sr V).
- The evaluation of the energy distributions obtained by CPO simulations at the end of the ion column determines a large  $\Delta E$  of 30 eV (defined as FWHM) for the Ar<sup>+</sup> ion beam in the Ion Carpet A case, which is way above the target of  $\Delta E \lesssim 1$  eV. This can be mainly explained by the fact that the ions “see” a varying potential when they are extracted through the ion carpet central hole towards the extraction aperture. In the Ion Carpet B case  $\Delta E$  is clearly reduced to about 3 eV (again defined as FWHM), as in this case the central carpet hole electrode is fixed at  $V_{IC}$ . It can be concluded that less chromatic



aberration effects will arise when the Ion Carpet B case is used and the target of  $\Delta E \lesssim 1$  eV is in the same order of magnitude as the determined  $\Delta E$ .

- Gas conductance calculations/simulations are performed in parallel to the CPO simulations. It is shown that when choosing for the anode and Wehnelt aperture the sizes of  $d_A = 0.8$  mm and  $d_W = 1.5$  mm, the pressure within the Wehnelt volume drops below  $10^{-5}$  mbar in the case of Argon and Xenon injection when  $p_{IR}$  is set to 0.1 mbar. This result proves that a stable operation of the  $Y_2O_3 - Ir$  disc cathode within the EIRFIS e-Column can be realised as the needed operation vacuum level is  $< 10^{-4}$  mbar. The performed Molflow+ simulations for the ion column are used to get an estimation about the achievable pressure gradient for Argon and Xenon. The obtained results are used during the ion column CPO simulations to incorporate the effect of ion gas collisions. This leads to an ion beam spread within the simulations which is closer to the reality compared to the situation where no ion gas collision would be considered.
- The experimental e-Column characterisation shows that it is possible to guide up to  $|I_{e,Tr}| = 370$   $\mu A$  into the ionisation region at an emission current  $|I_{e,Emission}|$  of 1 mA when an inlet electrode aperture of 1.5 mm is used. This measured current value is very close to the estimation of  $|I_{e,Tr}| = 400$   $\mu A$  obtained by using CPO simulations. The increase in  $|I_{e,Tr}|$  for settings above  $|I_{e,Emission}| = 500$   $\mu A$  is only marginal. Therefore, it is recommended to limit  $|I_{e,Emission}|$  to 500  $\mu A$  as slower degradation of the disc cathode will occur resulting in an increased lifetime.
- Argon gas injection tests and related total ion current measurements show that the range of 250 to 300  $\mu A$  for  $I_{Ions,Ar}$  can be reached with the ionisation region kept at  $p_{IR} = 0.1$  mbar. Preliminary tests in order to get a stable source operation highlighted that currently  $p_{IR} = 0.1$  mbar can only be achieved when the ionisation region is set to about 500 V.
- The incorporation of the PCB ion carpet has been realised with a central hole diameter of  $d_0 = 1$  mm. Enhancements of the extracted argon ion current  $I_{Ar,Ex1}$  are measured over the complete frequency range up to 12 MHz when  $p_{IR} = 0.1$  mbar compared to the situation where no RF-signal is applied. The measured values of  $I_{Ar,Ex1}$  go up to 80 - 90 nA and the ion beam current that passes through a 100  $\mu m$  extraction aperture is determined to be at maximum in between 1.5 and 2 nA, which correspond to enhancement factors of 6 to 8 times compared to the situation where no RF is applied. The result for  $I_{Ar,Ex1}$  is still two orders of magnitude below the expected  $\mu A$  range. The estimation for  $B_r \approx 10^2$  A/(m<sup>2</sup> sr V) is mainly based on a high value of  $I_{Ar,Ex1}$ . Therefore, it is concluded that as long as the EIRFIS concept does not achieve the  $\mu A$  range for  $I_{Ar,Ex1}$  the experimental determinable  $B_r$  will not reach the estimation. By further improving the experimental setup and in particular the RF-electronics we should be able to come closer to the simulated extracted ion current values. Currently the 8 MHz case creates a very low reflected RF power in the designed RF-signal generation system and represents a good setting to perform an output load matching for the used transformer to 200  $\Omega$ . This will result in being able to apply even higher RF-signal amplitudes to the PCB ion carpet (e. g. currently limited to 50 V at 8 MHz) which should further raise the ion extraction efficiency.

## 6 Conclusions and Outlook

For FIB nano-applications it is mandatory to use high-brightness ion sources in order to be able to achieve finely focused ion beam probes for a high lateral resolution while having sufficiently high ion beam currents to obtain reasonable erosion rates as well as large secondary electron/ion yields. Furthermore, in order to minimise the chromatic aberrations within the ion focussing columns the ion beam energy spread should be kept as small as possible.

During this thesis, we worked on the development of an electron impact (EI) ion source with a targeted reduced brightness  $B_r$  of  $10^3 - 10^4 \text{ A m}^{-2} \text{ sr}^{-1} \text{ V}^{-1}$  giving a versatile choice in provided ion species and an energy spread of  $\Delta E \lesssim 1 \text{ eV}$ . The ion source setup is based on conventional mechanical fabrication techniques and it targets a compact design in order to be able to use it as add-on tool for existing FIB instruments. Two different design approaches have been evaluated and related conclusions as well as an outlook will be given in the following.

### 6.1 Conclusions

#### 6.1.1 Miniature ionisation volume electron impact ion source

This first investigated EI ion source concept is based on the idea to combine a compact thermionic emitter e-Column with an ionisation region of mm-dimensions within which the electron beam (e-beam) is focused above an ion extraction aperture creating an orthogonal setup of the electron and ion beam axis. By combining an ionisation volume (IV) size in the  $\mu\text{m}$  range with an electrode plate spacing of  $D_{\text{Plates}} \leq 1 \text{ mm}$  and a plate potential difference  $\Delta V_{\text{Plates}} < 10 \text{ V}$ , it is possible to extract ion beams with an energy spread  $\Delta E \lesssim 1 \text{ eV}$ . Different conclusions related to the evaluation of this ion source concept can be drawn:

- Charged particle optics (CPO) simulations were carried out for a compact hairpin filament e-Column (length  $\approx 70 \text{ mm}$ ) consisting of a triode extraction region combined with an electrostatic two lens system. It is determined that at  $1 \text{ keV}$  the focussed e-beam results in a cylindrical IV with a FW50 diameter of  $100 \mu\text{m}$  above the ion extraction aperture containing  $50 \mu\text{A}$  of current. Exchanging the hairpin filament with a  $\text{LaB}_6$  emitter decreases the IV diameter by a factor of 2.5 while the e-beam current is comparable.
- Related ion column CPO simulations have been performed with  $D_{\text{Plates}} = 1 \text{ mm}$ ,  $\Delta V_{\text{Plates}} = 10 \text{ V}$  and the ionisation region extraction electrode is followed by two additional electrodes. The hairpin filament e-Column is combined with an extraction aperture of  $100 \mu\text{m}$  and  $B_r$  is determined in between  $50 - 65 \text{ A}/(\text{m}^2 \text{ sr V})$  for  $\text{Ar}^+$ ,  $\text{Xe}^+$  and  $\text{O}_2^+$  ions for an ionisation region pressure of  $p_{\text{IR}} = 0.1 \text{ mbar}$ . The achieved ion beam FW50 source size lies within  $5 - 25 \mu\text{m}$ , the half-opening beam angle range is  $5 - 20 \text{ mrad}$  and the beam current is in between  $20 - 45 \text{ nA}$ . These parameter ranges are related to different investigated ion column potential settings. The determined energy spread (defined as FWHM) is  $\Delta E \approx 1 \text{ eV}$  which meets the objective. During the simulations no ion gas collisions within the ion column are considered. As the gas conductance through the small extraction aperture will not be very significant it is concluded that the ion beam broadening due to ion gas collisions will in reality not be a strongly degrading performance factor. Further possible degrading factors are space charge effects, electrodes misalignment or imperfections of their shape which have not been included in the performed CPO simulations.

- The LaB<sub>6</sub> emitter e-Column is combined with an extraction aperture of 40  $\mu\text{m}$  so that it matches the reduced IV size. The determined  $B_r$  is increased to 150 - 180  $\text{A}/(\text{m}^2 \text{sr V})$  for  $\text{Ar}^+$  with  $p_{\text{IR}} = 0.1 \text{ mbar}$ . The half-opening beam angle is reduced to 3 - 10 mrad, the sources size to 4 - 14  $\mu\text{m}$  and the ion beam current drops to 5 nA. The energy spread is as well decreased due to the smaller IV size and is determined to be  $< 0.5 \text{ eV}$  which clearly meets the objective for  $\Delta E$ . A similar improvement of ion source performance can be expected for  $\text{Xe}^+$  and  $\text{O}_2^+$  ions.
- One challenge to get in reality a stable ion source operation is that the LaB<sub>6</sub> emitter needs a vacuum level of  $< 1 \cdot 10^{-6} \text{ mbar}$  which means that across the compact e-Column more than five orders of magnitude in pressure difference need to be achieved as  $p_{\text{IR}} = 0.1 \text{ mbar}$  is targeted. A mechanical setup for the e-Column has been developed and related gas conductance simulations as well as experimental investigations demonstrate that in the current configuration it is possible to reach the low  $1 \cdot 10^{-5} \text{ mbar}$  regime. This allows to operate a hairpin filament but for a LaB<sub>6</sub> emitter an optimisation is still needed. The integration of gas impermeable electron transparent graphene grids within the compact e-Column has been tested. The related pressure tests indicate that it is possible to get a further improvement factor of 10 for the pressure difference between ionisation and Wehnelt region, which means that in this setup a LaB<sub>6</sub> emitter can be operated. Unfortunately, transmission tests show that when the graphene grids are placed right in front of the ionisation region where the e-beam has an energy of about 1 keV only 25 % of the incident beam current will pass through. It can be concluded that the afore mentioned improvement of the reduced brightness by the use of a LaB<sub>6</sub> emitter will be partially counteracted as less ion current is generated. Furthermore, the graphene grids are extremely fragile during handling so that the final mechanical setup of the e-Column would face further challenges to be realised.
- During the performed CPO simulations for the LaB<sub>6</sub> e-Column the emitter was inserted into the identical triode extraction system as used for the hairpin filament. It is expected that if a better tailored geometrical setup of the triode extraction system for the use of a LaB<sub>6</sub> emitter is realised, the reduction in IV size can be pushed towards a factor of 10 compared to the hairpin filament e-Column. With an adaptation of the ionisation region to  $D_{\text{Plates}} = 0.1 \text{ mm}$ ,  $\Delta V_{\text{Plates}} = 10 \text{ V}$  and with an extraction aperture of 10  $\mu\text{m}$  it is expected that the ion source  $B_r$  can be further increased to the upper  $10^2 \text{ A m}^{-2} \text{sr}^{-1} \text{V}^{-1}$  range and the ion beam source size will be in the low  $\mu\text{m}$  range while maintaining an extracted ion current of a few nA. Furthermore, in this configuration the energy spread can still be kept at  $\Delta E \lesssim 1 \text{ eV}$ . Nevertheless, the higher electric field of 100 V/mm within the ionisation region leads to a stronger deviation of the 1 keV e-beam away from the ion extraction aperture. An adaptation of the until now evaluated simple parallel plate concept is needed to still get a reasonably good ion extraction efficiency.
- Due to the fact that the estimated brightness performance is still below the objective of  $10^3 - 10^4 \text{ A m}^{-2} \text{sr}^{-1} \text{V}^{-1}$  and due to the mentioned difficulties to achieve the needed pressure difference across the compact e-Column it has been decided to not proceed to a prototype construction at this point of development.

### 6.1.2 Electron impact radio frequency ion source

The second investigated ion source concept is based on the idea to stop a 100 eV e-beam containing a few hundreds of  $\mu\text{A}$  within the ionisation region by a combination of electron gas collisions and a retarding electric field. As a result a large amount of ion current is generated within an IV of mm-dimensions. A radio frequency (RF) ion carpet is used to efficiently extract the ions through a hole in its centre. By placing an extraction aperture with a diameter of  $d = 100 \mu\text{m}$  close to the backside of the ion carpet it is possible to achieve ion source sizes in the  $\mu\text{m}$  range, half-opening angles in the low mrad range while having  $\mu\text{A}$  of ion beam current. By using an yttria-coated iridium ( $\text{Y}_2\text{O}_3 - \text{Ir}$ ) disc cathode emitter the pressure requirements of the Wehnelt region with  $p_w < 1 \cdot 10^{-4}$  mbar are less restrictive compared to the miniature IV EI ion source concept. The following conclusions can be drawn for the developed and experimentally tested prototype of the Electron Impact Radio Frequency Ion Source (EIRFIS) concept:

- The determined stopping range for the 100 eV e-beam in an ionisation region at 0.1 mbar combined with a retarding field of 1 V/mm is below 40 mm for the gases Ne, Ar, Kr, Xe,  $\text{O}_2$  and  $\text{N}_2$ . This leads to the decision to set the size of the ionisation region to 50 mm in order to stop the e-beam in front of the ion carpet.
- The evaluation by CPO simulations of an electrostatic collimating single lens e-Column shows that up to 400  $\mu\text{A}$  of electron current can enter the ionisation region through a 1.5 mm inlet aperture in combination with a 0.8 mm anode aperture. In parallel performed gas conductance calculations highlight that this aperture combination leads to a  $p_w < 1 \cdot 10^{-5}$  mbar for Argon and Xenon allowing a stable disc cathode operation.
- During ion column CPO simulations, with collinear ion and electron beam axes, two different RF ion carpets have been investigated. The ionisation region is kept at 0.1 mbar of argon gas and  $\text{Ar}^+$  ions are generated inside of a large conical volume. Neighbouring RF ring electrodes are kept at RF-signals with the same frequency/amplitude but  $180^\circ$  out of phase. The ions are pushed towards the carpet and pulled to the central region by DC-fields of 1 V/mm. The extraction efficiency ( $f_{\text{Extr}}$ ) evaluation is done up to 12 MHz and 150 V in amplitude. For Ion Carpet A the metallised central hole is electrically isolated from the backside plane and is kept at a DC-RF-potential. The 9 MHz, 100 V amplitude case most probably represents a good compromise between a high  $f_{\text{Extr}}$  of 75 % and a low risk to get in reality any voltage breakdown problems between neighbouring rings due to a too high RF amplitude. For Ion Carpet B the central hole electrode is connected to the backside plane and kept at a fixed DC-potential. A drop in  $f_{\text{Extr}}$  for  $\text{Ar}^+$  ions is clearly seen compared to Ion Carpet A. The 7 MHz, 100 V amplitude case with  $f_{\text{Extr}} = 35 \%$  turns out to be a good choice for the experimental tests with Ion Carpet B.
- For both ion carpets different ion column potential settings have been investigated by CPO simulations resulting in FW50 source sizes in between 50 to 80  $\mu\text{m}$ , half-opening beam angles in between 10 - 20 mrad and ion beam currents of a few  $\mu\text{A}$  reaching the end of the extraction column. The determined reduced brightness  $B_r$  in the Ion Carpet B case is about  $1 \cdot 10^2 \text{ A m}^{-2} \text{ sr}^{-1} \text{ V}^{-1}$  for  $\text{Ar}^+$  ions; mainly due to the higher  $f_{\text{Extr}}$  it increases to about  $5 \cdot 10^2 \text{ A m}^{-2} \text{ sr}^{-1} \text{ V}^{-1}$  for Ion Carpet A. An advantage of Ion Carpet B is the 10 times lower energy spread for  $\text{Ar}^+$  ions of  $\Delta E \approx 3 \text{ eV}$  (FWHM) compared to Ion Carpet A. This is related to the central hole electrode kept at a fixed DC potential compared to a

varying DC-RF-potential, respectively. The value of  $\Delta E \approx 3$  eV is still above the objective of  $\Delta E \lesssim 1$  eV but already in the same order of magnitude.

- Molecular flow simulations have been used to determine an ion column pressure gradient which is incorporated into the CPO simulations to be as close as possible to the real situation where ion gas collisions will lead to a broadening of the ion beam. Ion column misalignments, electrode shape imperfections as well as space charge effects can still have an additional degrading effect on the EIRFIS prototype performance.
- The experimental characterisation of the EIRFIS prototype e-Column has shown that about 300  $\mu\text{A}$  of electron current enters the ionisation region at a disc emission current setting of 500  $\mu\text{A}$ , which represents the author's recommended maximal setting for the disc cathodes. At higher emission currents the increase in ionising e-beam current is close to 30 % saturating at about 400  $\mu\text{A}$ . Nevertheless, a faster degradation and a reduction of the disc cathode lifetime will occur, whereas the increasing effect on the produced ion current and related ion source performance is only marginally. A better adapted triode extraction region for the use of the high emission current disc cathodes can lead to a smaller cross section of the collimated e-beam. This would allow to transmit already at lower disc emission settings higher e-beam currents into the ionisation region compared to the currently used e-Column. As a result the same total generated ion current could be obtained at emission conditions that will lead to a longer lifetime.
- Measurements of the total generated ion current show that up to 300  $\mu\text{A}$  of argon current can be produced for  $p_{\text{IR}} = 0.1$  mbar. The produced Printed Circuit Board (PCB) Ion Carpet is similar to Ion Carpet B. Experiments did show that an improving effect on the argon ion beam current (6 to 8 times more) occurs for all frequencies up to 12 MHz compared to the situation where no RF-signal is applied. The 8 MHz setting is determined to combine a good enhancement factor with a stable ion beam current situation. Furthermore, in this setting the measured reflected RF-power in the self-designed signal generation system is very low. Most probably a load matching at 8 MHz for the used transformer can improve the ion source performance. The load matching consists of placing within the HV-decoupling box suitable inductors to cancel out the capacitive contribution of the current transformer load and to use resistors to obtain a total resistance of 200  $\Omega$ . This will have a positive effect on the maximum reachable RF-amplitude (currently limited to  $\leq 100$  V) and will lead to even better ion extraction enhancement factors. So far the maximal argon ion currents measured at the extraction electrode goes up to about 100 nA and the ion beam currents passing the aperture of 100  $\mu\text{m}$  go up to a few nA.
- It has been determined that an ion current enhancing effect occurs only if  $p_{\text{IR}}$  can be raised to 0.1 mbar. Currently, a stable source operation at this targeted pressure is only reachable if the ionisation region electrode potentials are kept below 1 kV and if a low cathode emission current setting ( $\lesssim 100$   $\mu\text{A}$ ) is used. Further investigations (i. e. more precise voltage breakdown tests; reconfigurations of the power supply system) are needed to be able to keep the ionisation region at a few kV to get an ion beam energy of a few keV and to be able to generate up to a few hundred  $\mu\text{A}$  of ion current. The production of such large ion currents is one of the main aspect on which the EIRFIS concept performance is based.

- The experimentally tested PCB ion carpet is based on Ion Carpet B for which the central ring is kept at a fixed DC-potential generating a small ion beam  $\Delta E$ . Electrical measurements indicate that currently a quite large RF-contribution is applied to the central ring. It has been seen that by a simple modification of the electrical circuit layout (i. e. by removing a capacitor) the central ring will be closer to a complete DC-potential situation, being favourable to obtain a small  $\Delta E$ . Furthermore the RF-amplitudes on neighbouring carpet ring electrodes are better equilibrated to each other which is assumed to additionally lead to a higher extracted ion current.
- It can as well be concluded that the EIRFIS concept will work with other gases as e. g. xenon, oxygen or nitrogen but most probably the best extraction situation will be obtained at a different RF-setting compared to argon. Currently the measured ion currents are still one or two orders of magnitude below the expected  $\mu\text{A}$  range. By performing the several optimisations for the EIRFIS prototype setup mentioned before, the expected  $B_r$  range of  $10^2 - 10^3 \text{ A m}^{-2} \text{ sr}^{-1} \text{ V}^{-1}$  will be reached and FIB nano-applications become possible.

### 6.1.3 General conclusions

Table 6.1 gives a synoptic overview of the performance of the two evaluated EI ion source concepts together with state-of-the-art ion sources used for FIB applications.

	Electron impact IS	Duoplasmatron	Miniature IV EI ion source	EIRFIS
Ion species	Ar, Xe, O <sub>2</sub> , C <sub>60</sub> , ...	Ar, Xe, O <sub>2</sub> , ...	Ar, Xe, O <sub>2</sub> , ...	Ar, Xe, O <sub>2</sub> , ...
Source size	100 - 500 $\mu\text{m}$	30 - 500 $\mu\text{m}$	1 - 25 $\mu\text{m}$	50 - 80 $\mu\text{m}$
Extraction current	1 - 1000 $\mu\text{A}$	1 - 500 $\mu\text{A}$	nA range	up to a few 10 $\mu\text{A}$
Reduced brightness $\text{A}/(\text{m}^2 \text{ sr V})$	1	$10^2 - 10^3$	$10 - 10^2 \text{ A}$ $10^2 - 10^3 \text{ B}$	$\approx 1 \cdot 10^2 \text{ \#}$ $\approx 5 \cdot 10^2 \text{ \#\#}$
Energy spread	1 - 10 eV	5 - 20 eV	$\approx 1 \text{ eV}^{\text{A}}; < 0.5 \text{ eV}^{\text{B}}$	$\approx 3 \text{ eV}^{\text{\#}}; \approx 30 \text{ eV}^{\text{\#\#}}$

	Hyperion plasma source	MOTIS	LMIS	NAIS	GFIS
Ion species	H, He, O <sub>2</sub> , Ar, Xe, Ne, Kr	Ar, Xe, Ne, Kr, Na, K, Rb, Cs, Mg, Ca, ...	Ga, In, Au <sub>n</sub> , Bi <sub>n</sub>	He, Ne, Ar, Kr, Xe	He, Ne, N <sub>2</sub> , H <sub>2</sub>
Source size	10 - 20 $\mu\text{m}$	10 - 50 $\mu\text{m}$	10 - 50 nm	< 100 nm	< 1 nm
Extraction current	10 - 50 $\mu\text{A}$	1 - 200 pA	1 - 500 $\mu\text{A}$	1 - 400 pA	1 fA - 100 nA
Reduced brightness $\text{A}/(\text{m}^2 \text{ sr V})$	$10^3 - 10^4$	$10^4$	$10^6 - 10^7$	$10^7 \text{ *}$ ( $10^2 - 10^4 \text{ **}$ )	$10^{10}$
Energy spread	5 - 6 eV	$\lesssim 0.1 \text{ eV}$	5 - 50 eV	< 5 eV	$\lesssim 1 \text{ eV}$

\* estimated range taken from [22], \*\* experimental determined values taken from [25, 54].

<sup>A</sup> hairpin filament, <sup>B</sup> LaB<sub>6</sub> emitter; <sup>\#</sup> Ion Carpet B, <sup>\#\#</sup> Ion Carpet A.

Table 6.1: Main characteristics of different ion source types used for FIB applications.

- In the case of the miniature IV EI ion source concept the determined  $B_r$  values of a few tens of  $\text{A}/(\text{m}^2 \text{sr V})$  when using a hairpin filament e-Column represent already a clear improvement compared to conventional EI ion sources with  $B_r \approx 1 \text{ A}/(\text{m}^2 \text{sr V})$ . By using a  $\text{LaB}_6$  emitter the performance in terms of  $B_r$  reaches the lower  $10^2$  range and the source concept is comparable to the Duoplasmatron source and has clearly smaller ion beam source sizes as well as a far lower energy spread. This would allow to obtain ion beam probe sizes in the range of a few nanometres by means of primary ion beam columns of existing SIMS instruments. With an optimised e-Column for the use of the  $\text{LaB}_6$  emitter the  $B_r$  can be pushed to the upper  $10^2$  range and the source starts approaching the performance of the Hyperion plasma source with very similar source sizes. Moreover, the very low  $\Delta E$  below 0.5 eV makes the miniature IV EI ion source suitable for low energy applications. One of the major challenges to realise a prototype setup is to obtain the needed differential pumping capability of the compact e-Column to be able to operate the  $\text{LaB}_6$  emitter as the ionisation region pressure needs to be kept at 0.1 mbar.
- The EIRFIS concept is far less restrictive in terms of operation pressure requirements for the electron emitter as  $\text{Y}_2\text{O}_3 - \text{Ir}$  disc cathodes ( $p_{\text{needed}} < 1 \cdot 10^{-4} \text{ mbar}$ ) are used compared to the miniature IV EI ion source. Currently, with the determined  $B_r$  in the  $10^2 \text{ A m}^{-2} \text{sr}^{-1} \text{V}^{-1}$  range its performance is clearly better than the one of conventional EI ion sources. Furthermore, the EIRFIS is comparable in terms of  $B_r$  to Duoplasmatrons used in different SIMS instruments and has smaller ion beam source sizes and a lower  $\Delta E$  which makes it more suitable for low energy applications. In the currently investigated source setup the objective of  $B_r = 10^3 - 10^4 \text{ A m}^{-2} \text{sr}^{-1} \text{V}^{-1}$  can not be reached and further optimisations would be needed to become, for example, comparable to the Hyperion plasma source, but with a lower  $\Delta E$ .

## 6.2 Outlook

The evaluations performed during this thesis related to the miniature IV EI ion source concept indicated that the maximal reachable reduced brightness  $B_r$  lies in the upper  $10^2 \text{ A m}^{-2} \text{sr}^{-1} \text{V}^{-1}$  range when using a single  $\text{LaB}_6$  emitter e-Column. An idea to even raise further the reduced brightness is to combine the ionisation region with several compact  $\text{LaB}_6$  emitter e-Columns. In this way a higher amount of ionising e-beam current can be used for the ion production while the performance in terms of ion beam source size and half-opening beam angle will be unchanged. This further increase in reduced brightness is expected to be at maximum close to a factor 5 for an optimal configuration of the ion source so that it can be concluded that a maximum value of  $B_r \approx 5 \cdot 10^3 \text{ A m}^{-2} \text{sr}^{-1} \text{V}^{-1}$  would be achievable. It is obvious that the requirements for the realisation of the mechanical setup of such a multiple e-Column EI ion source are pushed to an even more challenging level.

After having performed the detailed investigations related to this ion source concept idea we can say that they prove the assumption that the performance of conventional EI ion sources can be clearly enhanced by using an ionisation volume of  $\mu\text{m}$  dimensions. Nevertheless, the results showed that it seems to be difficult to push the ion source performance above the limit of  $B_r = 1 \cdot 10^4 \text{ A m}^{-2} \text{sr}^{-1} \text{V}^{-1}$ . When using conventional mechanical setup configurations the dimensions of the ionisation region plate spacing as well as the ion extraction aperture size will be limited to 10  $\mu\text{m}$  or above. In this way ion beam source sizes of a few  $\mu\text{m}$  are reachable

with reasonable ion beam currents of a few nA. In order to go to even lower source sizes and reach a  $B_r > 1 \cdot 10^4 \text{ A m}^{-2} \text{ sr}^{-1} \text{ V}^{-1}$ , a further reduction of the ionisation region dimensions is needed so that it becomes more and more difficult to use conventional fabrication techniques. Furthermore, the extraction fields within the ionisation region would need to be raised  $> 100 \text{ V/mm}$  in order to keep reasonable ion beam currents. This introduces as already mentioned before additional difficulties for the orthogonal setup of electron and ion beam axis due to a strong deviation of the used low energy e-beam away from the ion extraction aperture.

In the case of the EIRFIS ion source concept a first outlook can be given by consideration of the CPO simulation results. A further improvement of the reduced brightness of the ion source to the upper  $10^2 \text{ A m}^{-2} \text{ sr}^{-1} \text{ V}^{-1}$  range while keeping an ion beam  $\Delta E$  of a few eV could be realised if the PCB ion carpet configuration is a merging of Ion Carpet A and Ion Carpet B. An idea to achieve this is to use a non-metallised central hole while keeping at its surrounding on the ionisation region side the smallest RF-ring. On the backside the GND electrode will touch the border of the central hole to get a fixed potential situation at the exit. Nevertheless, one challenge of such a setup is to be able to apply the RF-signal to the smallest RF-ring by using a via connection of the PCB technology in close vicinity to the central opening.

Currently the EIRFIS prototype has dimensions of  $42 \text{ cm} \times 20 \text{ cm}$  (vacuum pumps and pressure gauges not included) which does not really represent a compact ion source design. As the e-Column as well as the ion extraction column is only based on the application of electrostatic potentials their dimension can be reduced by scaling down all elements by the same geometrical factor without influencing the current determined source performance. The overall size of the ion source can be reduced in this way and a setup that fits more the requirements for a compact add-on tool for existing FIB instruments can be realised.

A further raise of the EIRFIS  $B_r$  towards  $10^3 - 10^4 \text{ A m}^{-2} \text{ sr}^{-1} \text{ V}^{-1}$  can most probably be obtained by a combined reduction of the central hole diameter and of the extraction aperture, resulting in smaller virtual source sizes. In order to still get a reasonable amount of extracted ion current it is expected that the aspect ratio of the central hole diameter to its length needs to be carefully chosen. The hole length is given by the standard thickness of  $0.8 \text{ mm}$  for the insulating layer of the PCB ion carpet. A strongly reduced ion beam current will partially counteract the benefit of getting smaller virtual source sizes. The EIRFIS concept evaluation indicates as well that it will be difficult to go beyond  $B_r = 1 \cdot 10^4 \text{ A m}^{-2} \text{ sr}^{-1} \text{ V}^{-1}$  as the minimal reachable source size seems to be limited to a few tens of  $\mu\text{m}$  resulting from the fact that the large ionisation volume size can only be, to some extent, counteracted by the used RF ion carpet.

The current determined EIRFIS prototype performance makes it suitable for FIB nano-applications (e. g. for SIMS) where ion probe beam currents in the pA to nA-range are used. Finally, the designed ion column allows an easy exchange of the extraction aperture in size and hole configuration. It can therefore as well be used in the future for higher current ion probe applications where the probe size does not need to be in the nm-range or for multi-ion beam applications by the use of an extraction aperture with multiple holes generating for each extracted ion beam a current in the order of  $1 \mu\text{A}$ .



## 7 Appendices

### 7.1 Appendix A: General theory and simulation software

#### Molflow+ simulation software

The kind of gas particles used for a Molflow+ simulation is chosen in the global parameters by setting the corresponding molecular mass  $M$ . For each facet certain parameters can be chosen via corresponding dialogue boxes. Parameters as the opacity, the facet temperature or the particle reflection type on the facet can be chosen. Furthermore, it is possible to set a facet as 1-sided or 2-sided. The 1-sided facets are opaque for the gas particles from the side where the facet normal is pointing to and 2-sided facets are opaque from both sides. An individual facet of the system can serve as gas injection facet by choosing between the different desorption types uniform, cosine, or  $\cos^N$  (please see [128] for more details) and by setting a certain out-gassing rate. Furthermore, a facet can also be set as pumping facet when a pumping speed  $S$  different from 0 is chosen and the software calculates by itself the related sticking factor  $F_{\text{Stick}}$  by using:

$$F_{\text{Stick}} = \frac{4 \cdot S}{A_F \cdot v_{\text{mean}}} \quad , \quad (7.1)$$

where  $A_F$  represents the corresponding facet area.

Every facet has its own direction vectors  $\vec{u}$  and  $\vec{v}$  as is illustrated in figure 7.1a and for example a pressure profile along one of the directions can be displayed as shown. During the simulation the evolution of different profiles on different facets can be monitored by the use of the profile plotter and by choosing the desired profile from the corresponding drop down list. Not only 1D but also 2D profiles can be visualised during the simulation on any facet of the structure, as can be seen in figure 7.1b. The user has to choose what kind of parameter should be recorded to create the 2D-profile. In the case shown in figure 7.1b side wall facets have been selected and here in order to record the pressure on these the user needs to select the “count reflection” option within the facet mesh setting box shown in figure 7.2a. During the simulation different 2D-profile visualisation settings can be chosen within the texture scaling box.

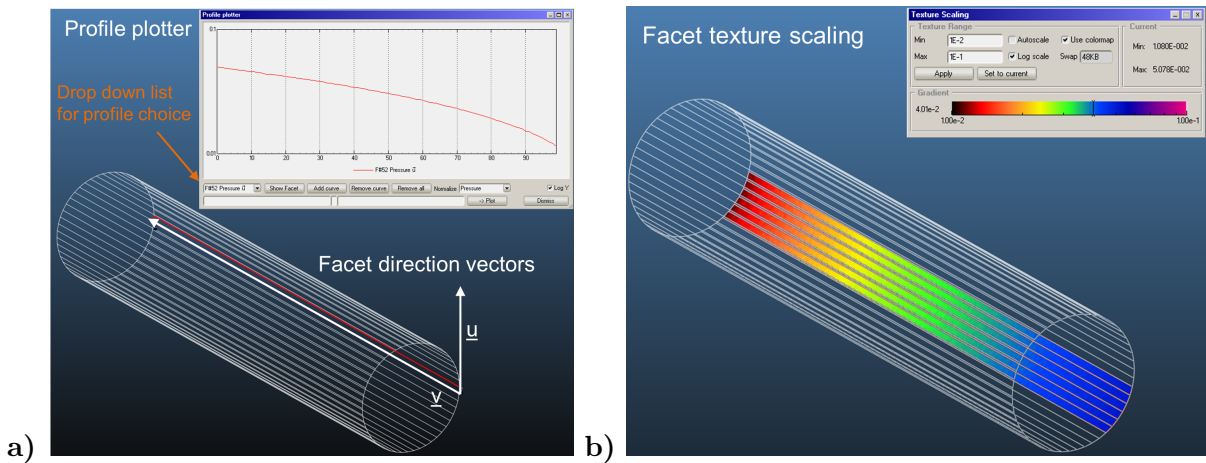


Figure 7.1: a) Illustration of the Molflow+ profile plotter feature and facet direction vectors;  
b) Illustration of the 2D texture scaling in Molflow+ (here on the tube side walls).

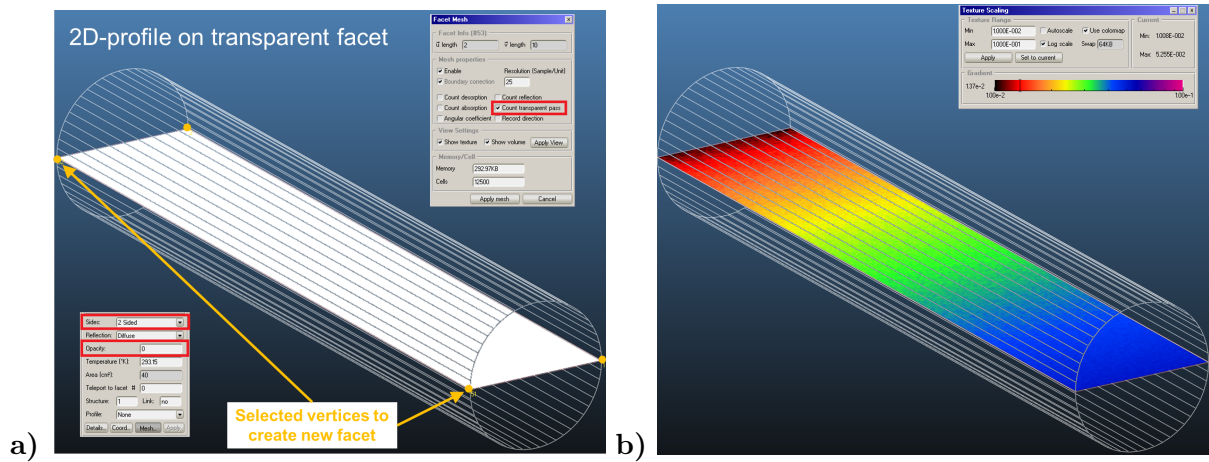


Figure 7.2: a) Illustration of a new transparent facet created within Molflow+;  
b) Illustration of the pressure 2D-profile on the transparent facet.

Very often it is interesting to record the pressure distribution within the empty volume of the structure. For this purpose it is necessary to create a new facet by selecting within Molflow+ existing vertices or creating new vertices. After that the new facet has been created it has to be set as 2-sided and its opacity to zero in order to make it transparent. In this case the parameter to be recorded needs to be set to “Count transparent pass” in order to record the 2D-pressure profile on the new created transparent facet, see figure 7.2a and 7.2b.

## SREM - CASINO simulation software

The selection of physical models shown in figure 7.3 is the one that is used during all SREM simulation related results presented within this manuscript.

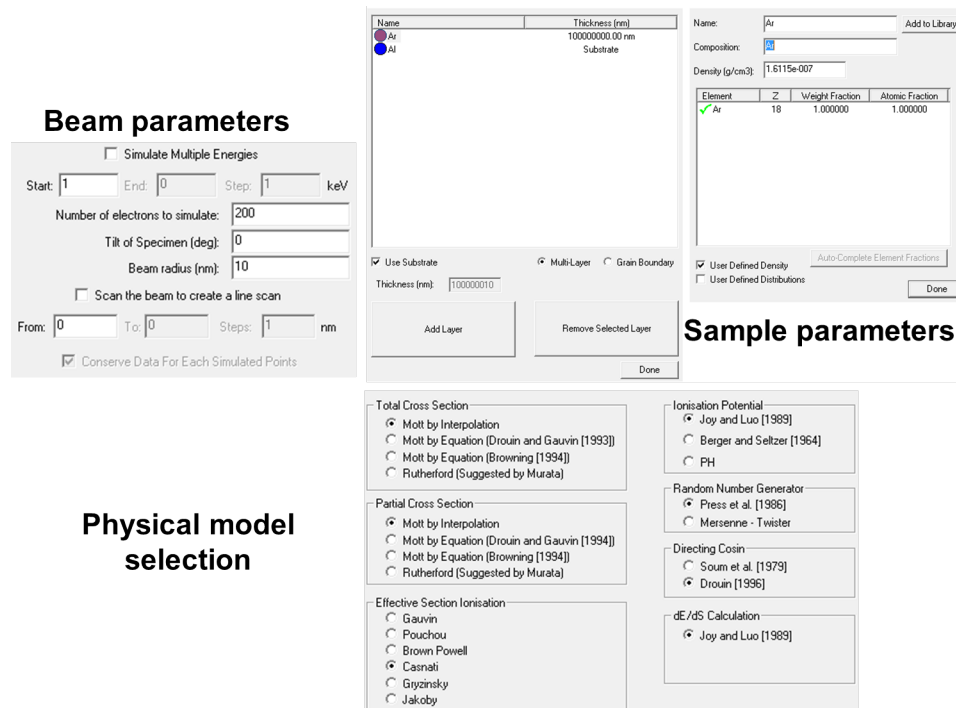


Figure 7.3: Dialogue boxes for the CASINO simulation parameter selection.

## 7.2 Appendix B: Miniature ionisation volume EI - ion source

### Box-Muller Method

This method is mentioned in section 4.2 in order to generate standard normal distributions for a random deviate and will be described here in detail. In the basic form two uniform distributed variables  $a_1$  and  $a_2$  are generated on the interval (0,1). They can then be used to calculate the two following quantities  $b_1$  and  $b_2$ :

$$\begin{aligned} b_1 &= \sqrt{-2 \ln(a_1)} \cos(2\pi a_2) \quad , \\ b_2 &= \sqrt{-2 \ln(a_1)} \sin(2\pi a_2) \quad . \end{aligned} \quad (7.2)$$

From these expressions it is possible to obtain the following expression for  $a_1$  and  $a_2$ :

$$\begin{aligned} a_1 &= \exp\left(-\frac{1}{2}(b_1^2 + b_2^2)\right) \quad , \\ a_2 &= \frac{1}{2\pi} \arctan\left(\frac{b_2}{b_1}\right) \quad . \end{aligned} \quad (7.3)$$

When calculating with the expressions in equation 7.3 the Jacobian determinant a product of a function only depending on  $b_1$  and of a function only depending on  $b_2$  is obtained:

$$\left| \begin{array}{cc} \frac{\partial a_1}{\partial b_1} & \frac{\partial a_1}{\partial b_2} \\ \frac{\partial a_2}{\partial b_1} & \frac{\partial a_2}{\partial b_2} \end{array} \right| = \frac{\partial a_1}{\partial b_1} \cdot \frac{\partial a_2}{\partial b_2} - \frac{\partial a_2}{\partial b_1} \cdot \frac{\partial a_1}{\partial b_2} = -\frac{1}{\sqrt{2\pi}} \cdot \exp\left(-\frac{b_1^2}{2}\right) \cdot \frac{1}{\sqrt{2\pi}} \cdot \exp\left(-\frac{b_2^2}{2}\right) \quad . \quad (7.4)$$

Therefore,  $b_1$  and  $b_2$  are independently distributed with a standard normal distribution (equation 4.5 with  $\mu = 0$  and  $\sigma = 1$ ).

The more often used form of the Box-Muller method is its polar form. Therefore two independently and uniformly distributed quantities  $g_1$  and  $g_2$  are generated in the closed interval of [-1,1]. After this the value  $G = R^2 = g_1^2 + g_2^2$  is being calculated. In the case that  $G = 0$  or  $G \geq 1$  is obtained a new pair of  $g_1$  and  $g_2$  is generated. This will be repeated until  $G \neq 0$  or  $G < 1$  is found. In this way  $g_1$  and  $g_2$  represent the coordinates of a point within the unit circle (see figure 7.4) and the value  $s$  represents a uniform deviate which can be used in the expressions of equation 7.2 as  $a_1$ . Furthermore, the angle  $\theta$  shown in figure can be used as  $2\pi a_2$  in equation 7.2, representing a random angle. This allows it to rewrite equation 7.2 in the following way:

$$\begin{aligned} b_1 &= \sqrt{-2 \ln(G)} \cos(\theta) = \sqrt{-2 \ln(G)} \frac{g_1}{\sqrt{G}} \quad , \\ b_2 &= \sqrt{-2 \ln(G)} \sin(\theta) = \sqrt{-2 \ln(G)} \frac{g_2}{\sqrt{G}} \quad . \end{aligned} \quad (7.5)$$

Equation 7.5 is used in the SIMION workbench user programme to generate the correct normal distributions for  $v_x$ ,  $v_y$  and  $v_z$  within the electron emission algorithm. As a proof that the Box-Muller method works it can be seen in the left of figure 7.5 that a standard normal distribution is generated for the deviate  $b_1$  ( $10^6$  values for  $b_1$  have been generated).

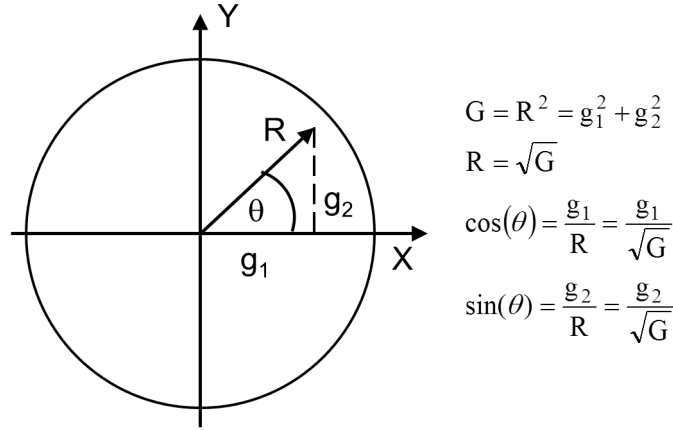


Figure 7.4: Schematic of the uniform deviates  $g_1$  and  $g_2$  that are used to generate a random point within the unit circle.

By multiplying then the values obtained for  $b_1$  with  $\sigma = \sqrt{\frac{k_B T}{m_e}}$  the wanted Maxwell Boltzmann distribution function for the velocity components  $v_i$  is obtained (right side of figure 7.5).

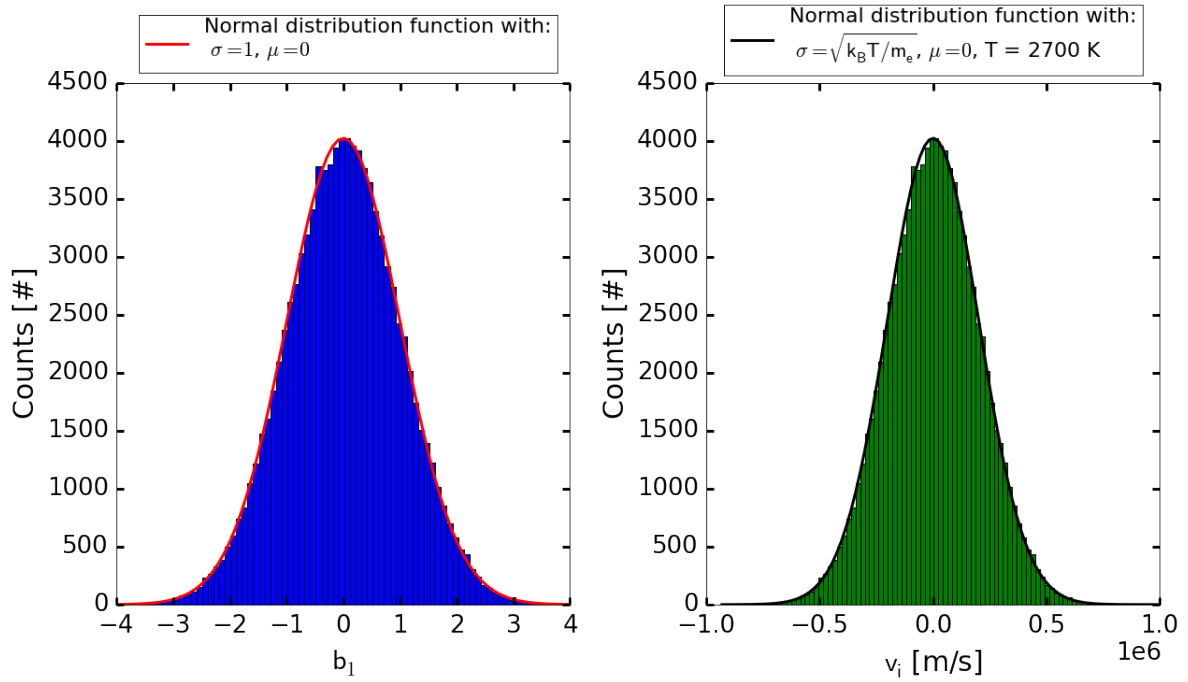


Figure 7.5: Left: Standard normal distribution of  $b_1$  generated with the Box-Muller method; Right: Example of Maxwell-Boltzmann distribution function for  $v_i$  by multiplying the  $b_1$  values with  $\sigma = \sqrt{\frac{k_B T}{m_e}}$  (Here:  $T = 2700$  K).

### Boundary matching technique between SIMION potential arrays

The boundary matching technique is used to match the potential values between the different potential arrays that are overlapped within the SIMION workbench for the e-Column simulation. For example the boundary matching in the filament region of the e-Column is done between two 3D-PA files. The virtual electrodes VE 1, VE 2, VE 3 and VE 4 represented as lines in the left of figure 7.6 correspond in 3D to the sides of a virtual electrode box surrounding the filament tip, middle of figure 7.6. In order to explain the boundary matching in more detail VE 2 is used as an example. In figure 7.7 the blue bigger points belong to the coarser grid unit system, here identified as the triode region PA, and the smaller green points belong to the finer grid unit system, here identified as the filament tip PA, involved in the boundary matching. The point P on VE 2 has the coordinates  $(z_{gu}, y_{gu})$  within the finer GU-system. The following equation can be used to transform  $(z_{gu}, y_{gu})$  into the corresponding coordinates  $(Z_{gu}, Y_{gu})$  within the coarser GU-system:

$$(Z_{gu}, Y_{gu}) = \frac{f_{GU,coarse}}{f_{GU,fine}} \cdot (z_{gu}, y_{gu}) \quad , \quad (7.6)$$

where  $f_{GU,coarse}$  and  $f_{GU,fine}$  represent the GU per mm ratios set for the coarser or finer PA-file respectively. After the coarser PA-file is refined with SIMION the potential values are known for each of its GU points (e. g. for point P1:  $V(Z_{gu1}, Y_{gu1}) = V_1$ , for point P2:  $V(Z_{gu1}, Y_{gu2}) = V_2$ , for point P3:  $V(Z_{gu2}, Y_{gu2}) = V_3$  and for point P4:  $V(Z_{gu2}, Y_{gu1}) = V_4$ ). For the point P which lies within the square having its corners at P1, P2, P3 and P4 the correct potential value is calculated by using a bilinear interpolation method [138]. Two variables that are used for this interpolation are defined by:

$$t = Z_{gu} - Z_{gu1} \text{ and } u = Y_{gu} - Y_{gu1} \quad . \quad (7.7)$$

The potential at the point P can be determined by:

$$V(Z_{gu}, Y_{gu}) = (1 - t) \cdot (1 - u) \cdot V_1 + t \cdot (1 - u) \cdot V_2 + t \cdot u \cdot V_3 + (1 - t) \cdot u \cdot V_4 \quad . \quad (7.8)$$

A Lua<sup>17</sup> programme is then used to calculate with equation 7.8 the interpolated potential value and assign it to each corresponding grid unit point of the finer PA that lies on the boundary surface VE 2. The same procedure is applied to all six virtual electrodes VE 1, 2, 3, 4, 5 and 6 (see the top of figure 7.8) of the filament tip PA. The determined potential value at each point P on these side walls is kept fixed during the last stage of the boundary matching technique when the finer PA-file is being refined by using SIMION. The here explained technique of boundary matching is very important for the correct simulation of charged particle trajectories when a SIMION workbench is composed of several overlapping PA-files.

<sup>17</sup>Lua is one of the programming languages that can be used for writing the SIMION user workbench programmes or other programmes that can manipulate the used SIMION PA files.

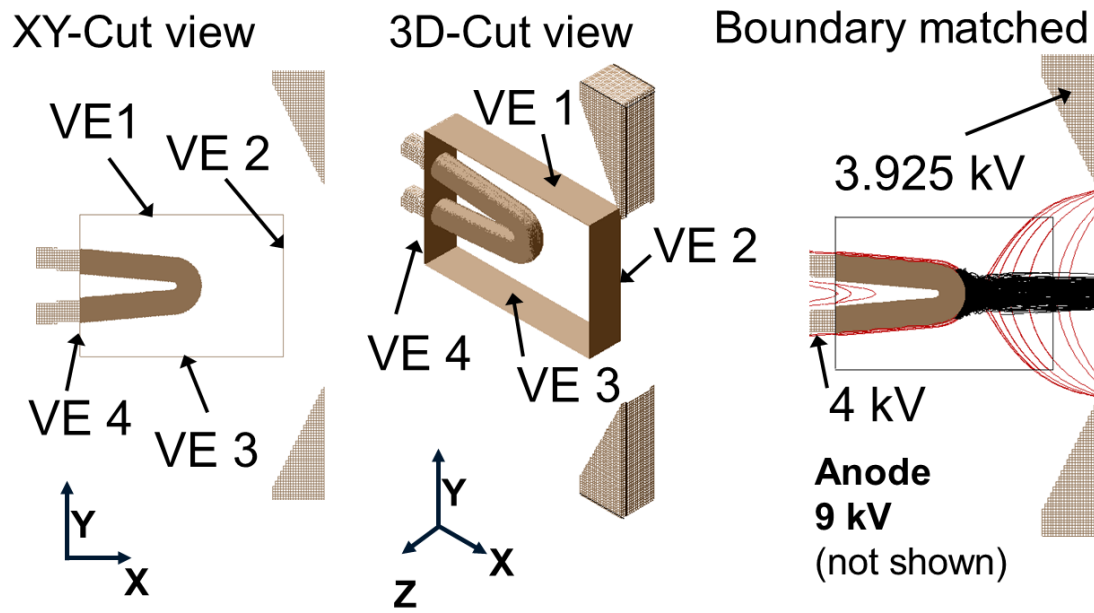


Figure 7.6: Boundary matching illustration within the hairpin filament region.

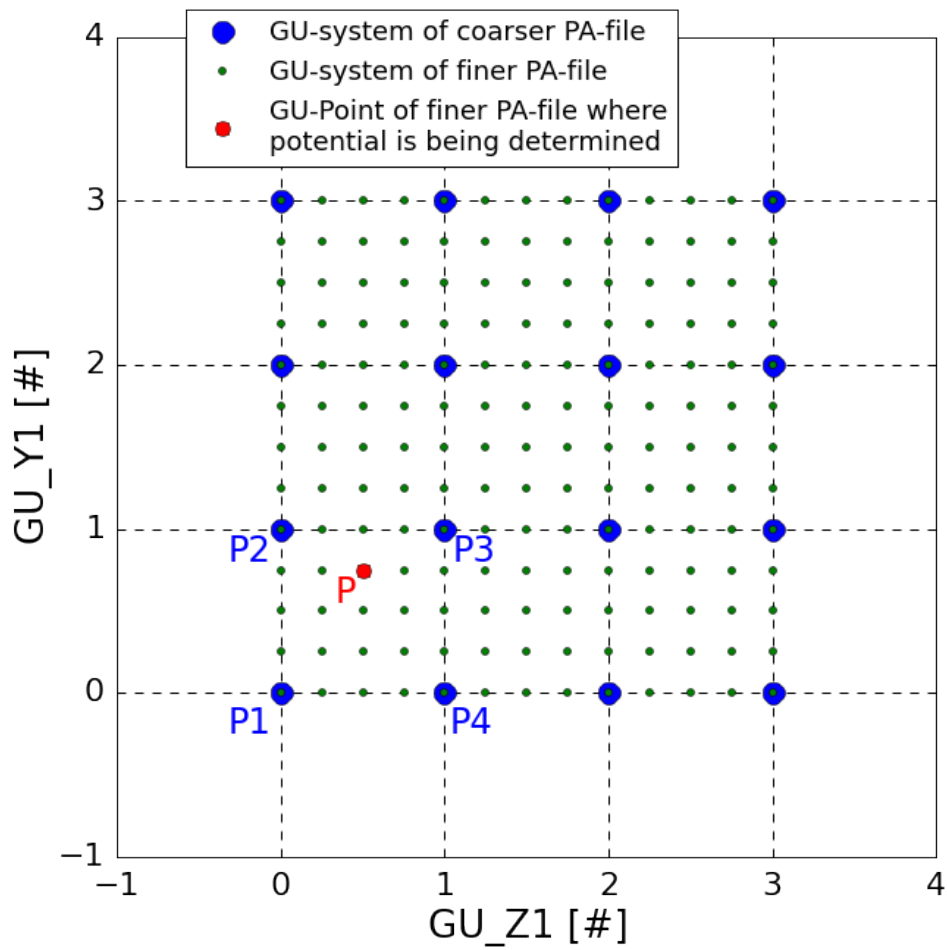


Figure 7.7: Illustration of two grid systems used within the bilinear interpolation of the boundary matching technique.

### The SIMION electron column workbench PA-composition

The complete workbench for the electron column simulation is composed of four different 3D-PA files. In the top of figure 7.8 the filament tip PA is shown. It contains the filament tip itself and the 6 virtual electrodes (VE) as explained in the afore paragraph for boundary matching purposes are forming a rectangular box that surrounds the filament tip. Furthermore, the triode PA is shown in the bottom of figure 7.8 and it contains the filament, the Wehnelt electrode, the anode and a small circular virtual electrode right behind the anode opening in positive X-direction.

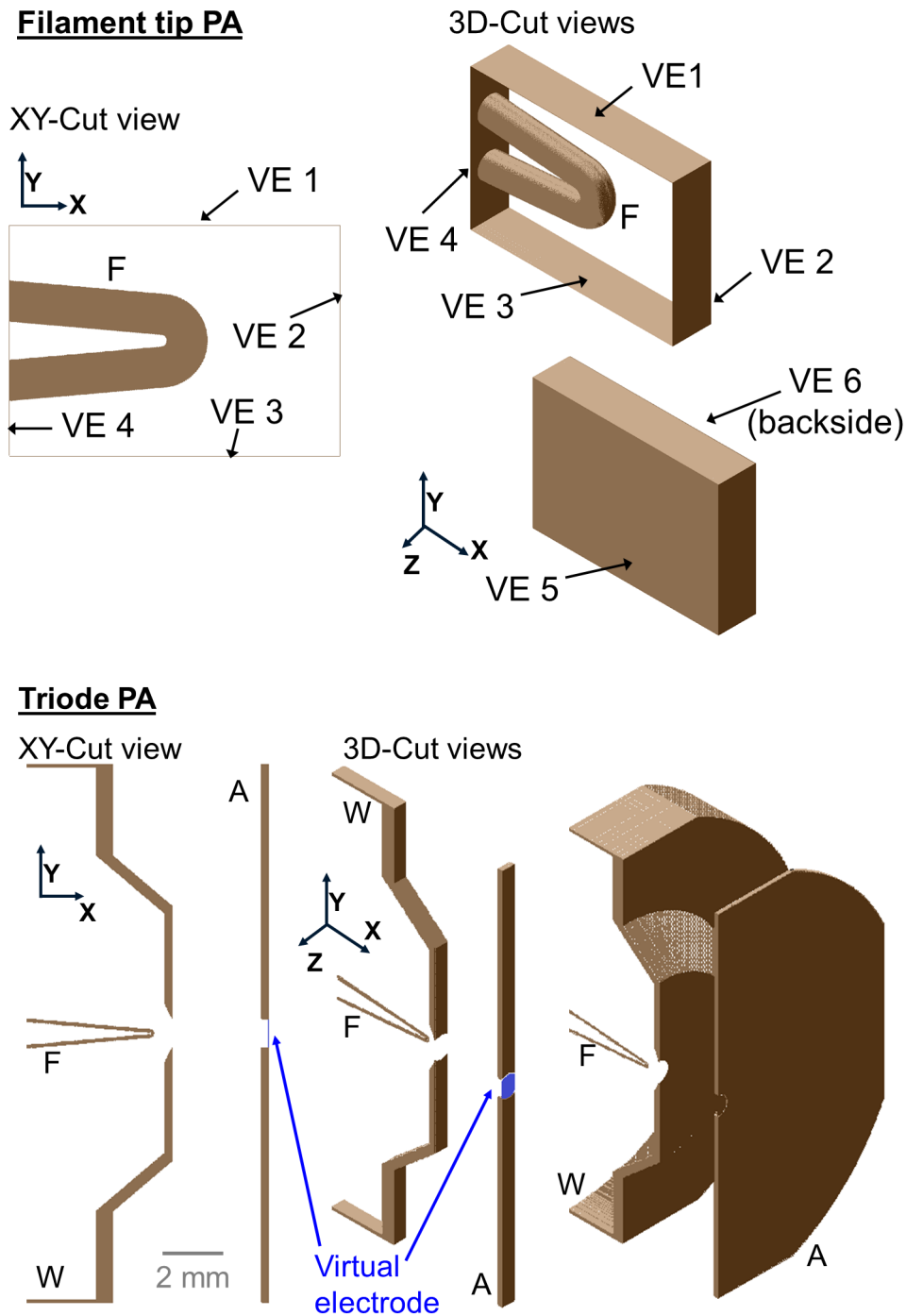


Figure 7.8: Filament tip PA and triode PA elements.

This virtual electrode is needed to perform the boundary matching between the deflection region PA and the triode PA. The mentioned deflection region PA is shown in figure 7.9, illustrating here the example of the asymmetric Lens 1. In this PA file a virtual electrode, expanding over the complete PA YZ-cross section, is introduced right behind the first element of the second lens ( $L_{2Start}$ ) in order to match the boundary between the ionisation region PA and the deflection region PA. The exact configuration of the deflector is also shown in figure 7.9. It consists of 4 electrodes forming a cylindrical quadrupole in between the two elements  $L_{1End}$  and  $L_{2Start}$ . In the 3D views of figure 7.8 and 7.9 some electrode sides show flat surfaces and not a complete round outer shape as it is expected from their cylindrical symmetry about the X-axis. This is due to the fact that the width and height of the 3D-PA files in Y- and Z-direction is smaller than the actual outer diameter of the electrodes. The electrode outer shapes are therefore cut by the PA box sides and appear as flat electrode surfaces. It is expected that these features have no influence on the expected cylindrical symmetry of the electric field close to the optical axis during the simulation of the e-beam as they are located quite far away from it.

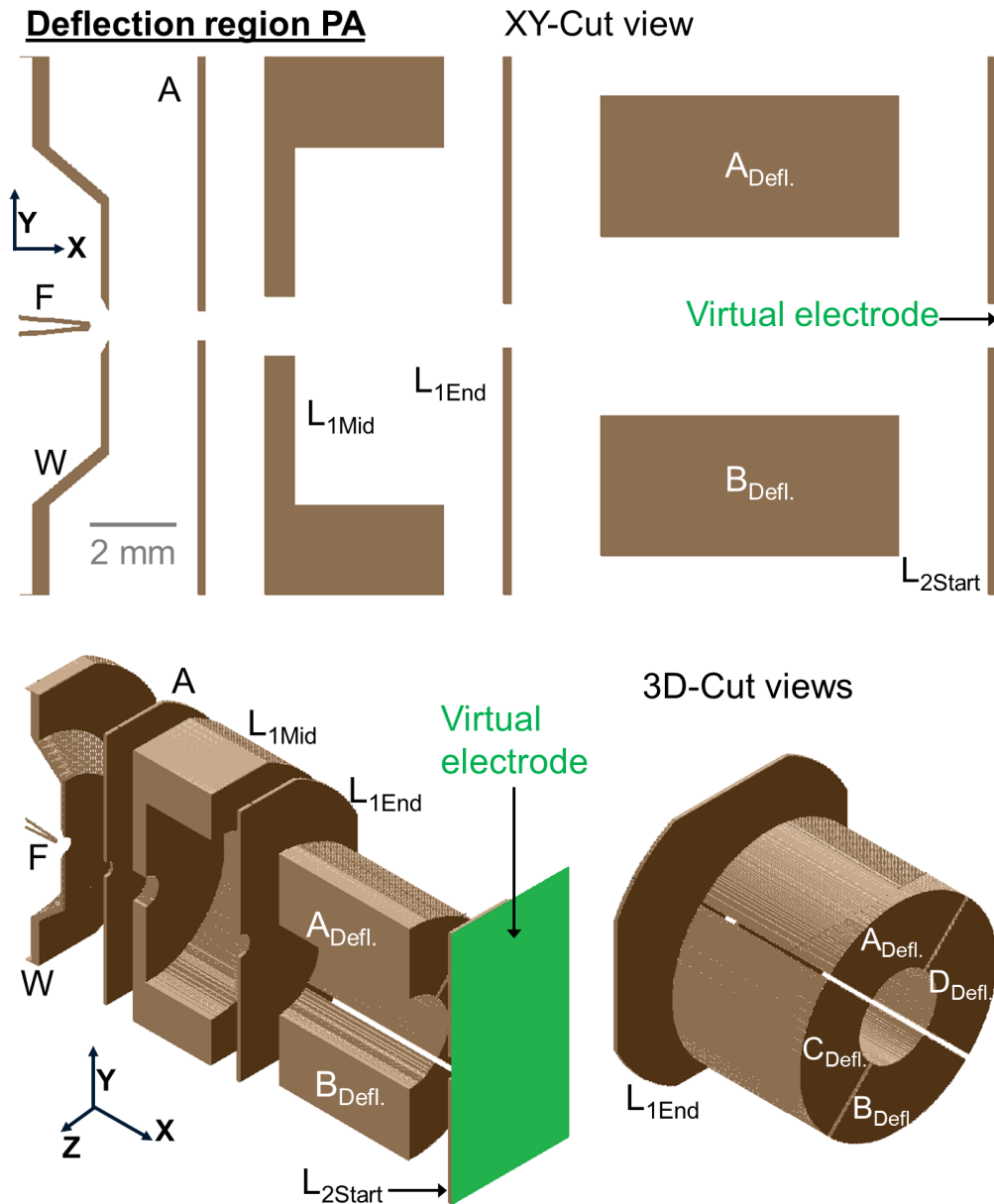


Figure 7.9: Deflection region PA elements.



The ionisation region PA can be seen in figure 7.10. A small part of the cylindrical quadrupole is incorporated into the ionisation region PA in order to simulate correctly its influence within the lens 2 region and at the entrance of the ionisation region. Furthermore, this incorporation is needed to be able to correctly perform the boundary matching at the virtual electrode of the deflection region PA.

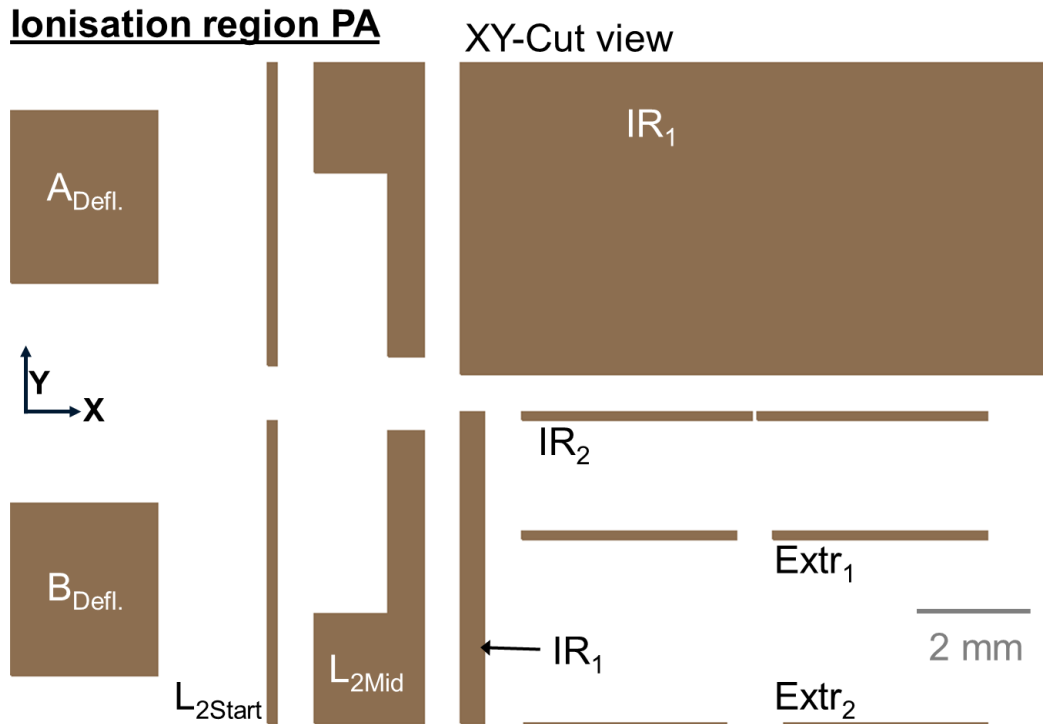


Figure 7.10: Ionisation region PA elements.

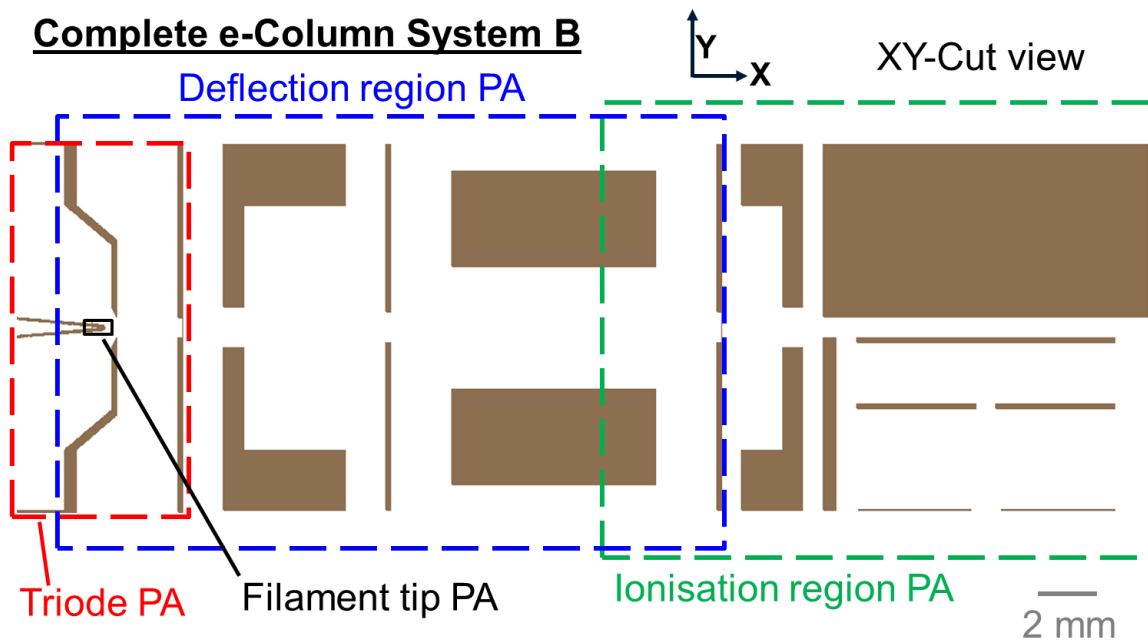


Figure 7.11: Complete e-Column System B with overlapping PAs.

All here presented PA files are overlapped within the SIMION workbench for the electron column simulations as it is shown as an example in figure 7.11 for e-Column System B. The procedure that is always applied before an electron column simulation is performed is the following:

1. Potential values are set to all elements of the ionisation region PA and it is then refined
2. Boundary matching between the ionisation region and the deflection region PA
3. Refining the deflection region PA
4. Boundary matching between the deflection region PA and the triode PA
5. Refining of the triode PA
6. Boundary matching between the triode PA and the filament tip PA
7. Refining of the filament tip PA
8. Electron beam generation, extraction, transportation and focalisation simulation

### Electrode potentials for the simulations of : e-Column system A and B

#### **e-Column System A:** Asymmetric Lens 1 and Symmetric Lens 2

$E_{e,End}$ [eV]	$V_F$ [kV]	$V_W$ [kV]	$V_A$ [kV]	$V_{L1Mid}$ [kV]	$V_{L1End} = V_{Defl.} = V_{L2Start}$ [kV]
100	4.9	4.825	9.9	5.5	5.6
250	4.75	4.675	9.75	5.35	6.2
500	4.5	4.425	9.5	5.1	7.6
750	4.25	4.125	9.25	4.85	9.25
1000	4	3.925	9	5	9

$E_{e,End}$ [eV]	$V_{L2Mid}$ [kV]	$V_{IR1} = V_{IR2}$ [kV]	$Extr_1 = Extr_2$ [kV]
100	5.05	5	5
250	5.5	5	5
500	5.07	5	5
750	5.12	5	5
1000	5.1	5	5

#### **e-Column System B:** Asymmetric Lens 1 and Asymmetric Lens 2

$E_{e,End}$ [eV]	$V_F$ [kV]	$V_W$ [kV]	$V_A$ [kV]	$V_{L1Mid}$ [kV]	$V_{L1End} = V_{Defl.} = V_{L2Start}$ [kV]
100	4.9	4.825	9.9	5.5	5.6
250	4.75	4.675	9.75	5.35	6.2
500	4.5	4.425	9.5	5.1	7.6
750	4.25	4.125	9.25	4.85	9.25
1000	4	3.925	9	5	9

$E_{e,End}$ [eV]	$V_{L2Mid}$ [kV]	$V_{IR1} = V_{IR2}$ [kV]	$Extr_1 = Extr_2$ [kV]
100	5.08	5	5
250	5.07	5	5
500	5.15	5	5
750	5.075	5	5
1000	5.25	5	5

Table 7.1: Electrode potential values for the simulations with e-Column System A and B.

### Ion column CPO simulations

In contrast to the ionisation region 3D PA-file used within the electron column simulations (see figure 7.10) the PA-files used here for the ion column simulations are 2D PA-files with cylindrical symmetry about the axis  $Y_{Axis,IR}$  (see figure 7.12). The entrance region where the e-beam is supposed to enter the ionisation region is modified compared to the geometry shown in figure 7.10. This is related to the fact that some test simulations have been performed between the e-Column and ion column simulations. These tests have shown that by increasing the space between the electrodes  $IR_1$  and  $IR_2$  in the entrance region a smaller proportion of particles hits the electrode  $IR_1$  and more e-beam current can reach the middle of the ionisation region. What should be further noticed here is that no entrance hole for the e-beam is present in the PA-files for the ion column simulations. Both afore mentioned electrode modifications compared to the

e-Column simulations are assumed to have no direct impact on the field distributions close to  $Y_{\text{Axis,IR}}$  and so no impact on the ion beam extraction. Moreover, additional features have been added to the ion column electrodes  $IR_2$ ,  $IR_{2B}$ ,  $\text{Extr}_1$  and  $G$ , see figure 7.12a. As the electrode  $IR_1$  extends along the complete Y-length of the ion column geometry, these features are necessary to shield the  $Y_{\text{Axis,IR}}$  region from the effect of the  $IR_1$  - potential.

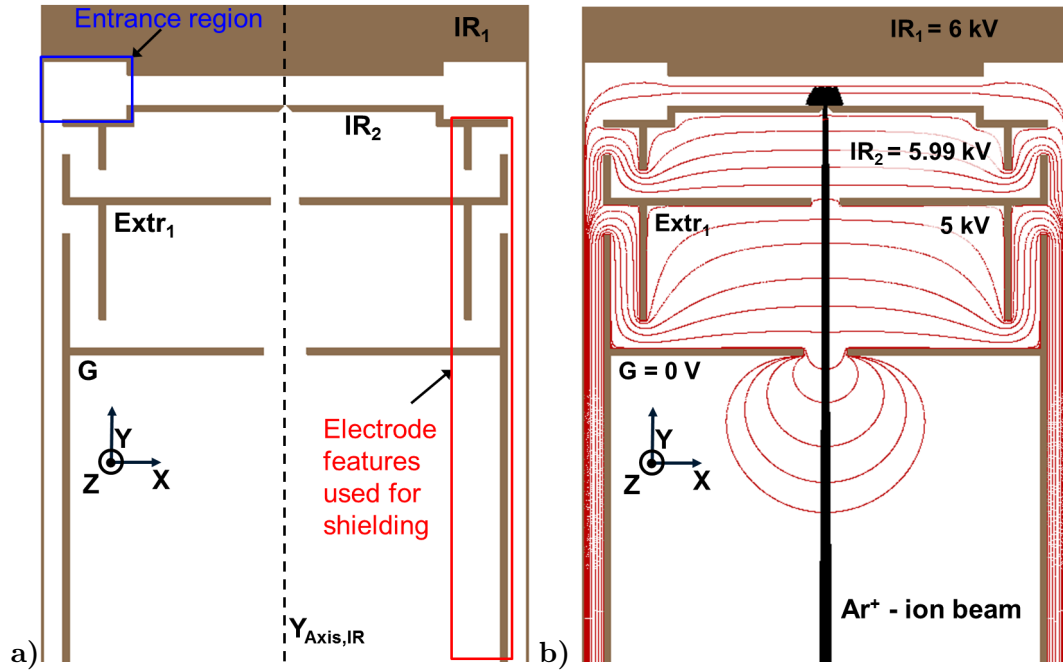


Figure 7.12: a) Complete PA-File used in the ion column CPO simulations;  
b)  $\text{Ar}^+$  simulation: IV-hairpin filament,  $p_{\text{IR}} = 0.1 \text{ mbar}$ ,  $d_{\text{Extr}} = 100 \text{ }\mu\text{m}$ .

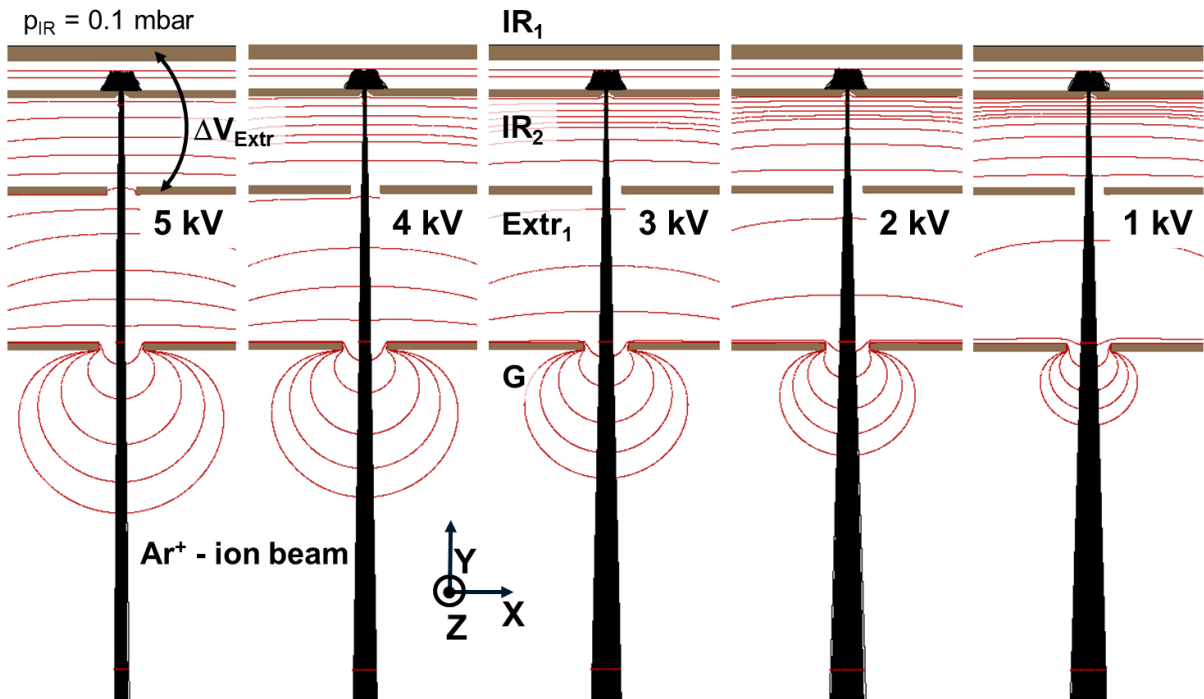


Figure 7.13:  $\text{Ar}^+$  - ion beam simulation, IV-hairpin filament,  $p_{\text{IR}} = 0.1 \text{ mbar}$ ,  $d_{\text{Extr}} = 100 \text{ }\mu\text{m}$ .  
Potentials:  $V_{\text{IR}_1} = 6 \text{ kV}$ ,  $V_{\text{IR}_2} = 5.99 \text{ kV}$ ,  $V_G = 0 \text{ V}$  and variation of  $V_{\text{Extr}_1}$ .

### GaussAmp fitting function

The **fitting function** that is used during the evaluation of the ion beam energy distributions in section 4.2 and 5.3.2 is a special kind of Gaussian distribution function defined here as GaussAmp function and expressed by:

$$f(y) = y_0 + A \cdot \exp\left(\frac{-(y - y_c)^2}{2 \cdot w^2}\right) \quad . \quad (7.9)$$

Here  $y_0$  is the background parameter,  $A$  the amplitude,  $y_c$  the location parameter and  $w$  the scale parameter [173]. Furthermore, the FWHM value of the GaussAmp distribution function can be calculated by  $\text{FWHM} = \sqrt{\ln(4)} \cdot 2 \cdot w$ . The name GaussAmp comes from the fact that the multiplication factor of the exponential in equation 7.9 is simply represented by an amplitude value  $A$  and not as a fraction as it is the case for the normal distribution function of equation 4.5.

### Ionisation region zoom

In figure 7.14 here below a closer view of the ionisation region and the near ion extraction aperture region is shown with the IV-hairpin filament setting used. The pressure within the ionisation region has been simulated as 0.1 mbar of Argon.

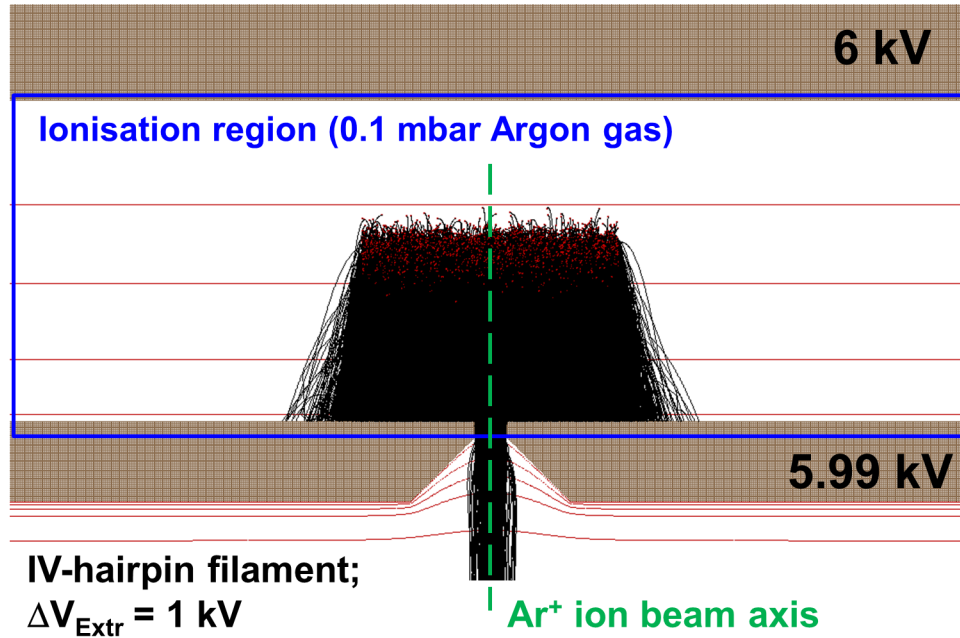


Figure 7.14: Zoom of the  $\text{Ar}^+$  - ion beam extraction from the ionisation region at 0.1 mbar of Argon gas (IV-hairpin filament;  $\Delta V_{\text{Ext}} = 1 \text{ kV}$ ).

### Molecular flow simulations for the e-Column

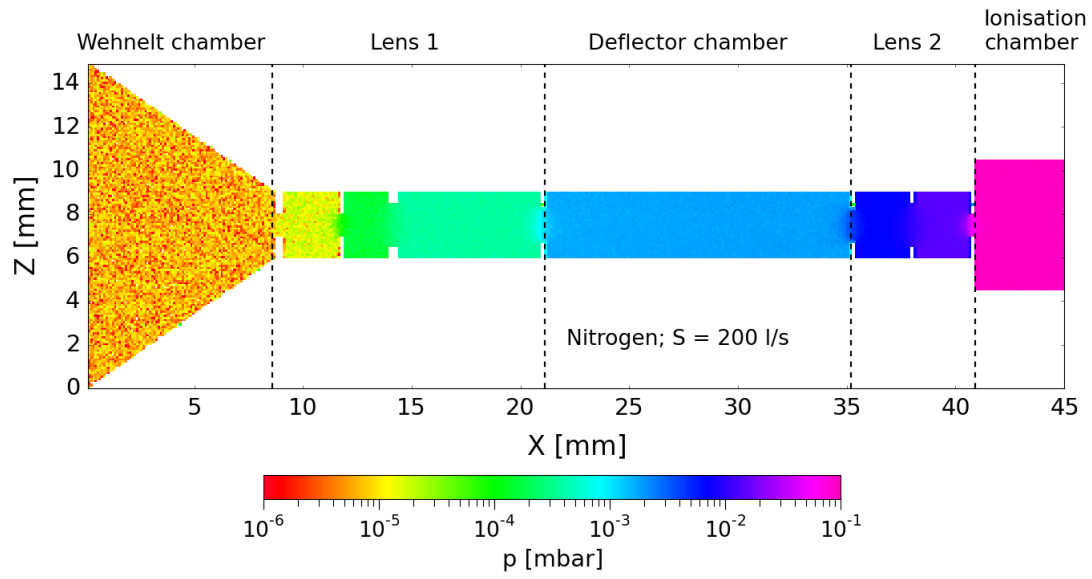


Figure 7.15: Pressure distribution along e-Column Model A (Nitrogen,  $S = 200$  l/s).

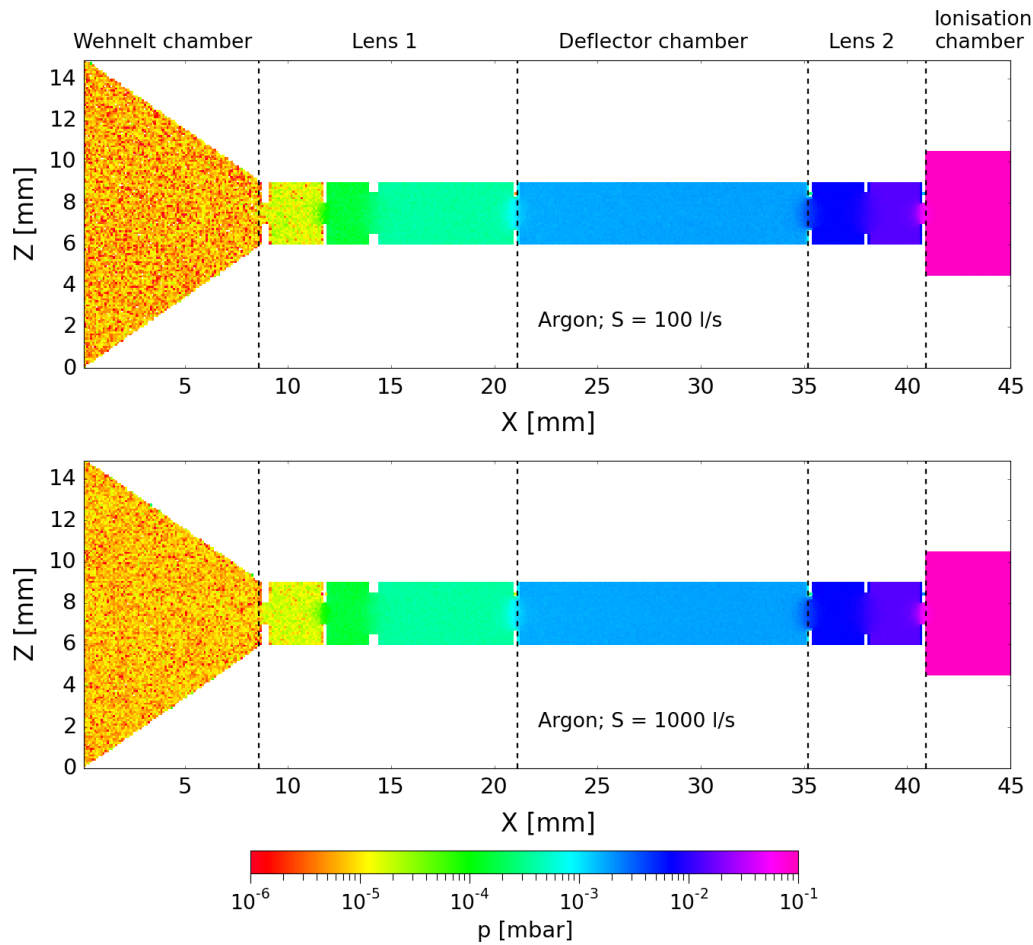


Figure 7.16: Pressure distributions along e-Column Model A (Argon,  $S = 100$  l/s and 1000 l/s).

### Experimental investigations: transmission definition of graphene grids

In section 4.4.2 experimental gas pressure difference tests and e-beam transmission tests are described that are performed with the 300 mesh copper grids illustrated in figure 7.17 and commercially available from TED PELLA INC. [174]. The carbon support film has a cobweb like structure (see figure 7.18b) with a hole size varying in the range of less than 250 nm to 10  $\mu\text{m}$  (specifications given by the manufacturer [175]). The graphene film that is chosen for the experimental tests is a 2 ML-film (thickness 0.68 nm). The e-beam transmission of the graphene film can be theoretically estimated by the following equation stated in [146] and [176]:

$$\text{Tr}_{\text{Graphene}} = \frac{I_T}{I_0} = \exp\left(\frac{-t_{\text{Graphene}}}{\lambda_{\text{IMFP}} \cdot \cos(\Theta)}\right) \quad . \quad (7.10)$$

The incident and transmitted beam current are represented by  $I_0$  and  $I_T$  respectively. The thickness of the graphene film is represented by  $t_{\text{Graphene}}$  and  $\Theta$  is the angle between the grid surface normal and the beam axis direction. The inelastic mean free path (IMFP) is represented by  $\lambda_{\text{IMFP}}$ . A theoretical estimation of  $\lambda_{\text{IMFP}}$  in  $\text{\AA}$  can be done with the following equation which has been stated in [177] and [178]:

$$\lambda_{\text{IMFP}} = \frac{E_{\text{Beam}}}{E_p^2 [\beta \ln(\gamma E_{\text{Beam}}) - (C/E_{\text{Beam}}) + (D/E_{\text{Beam}}^2)]} \quad . \quad (7.11)$$

$E_{\text{Beam}}$  is the beam energy in eV and  $E_p$  is the bulk plasmon energy in eV of the material of interest. The parameters  $\beta$ ,  $\gamma$ ,  $C$  and  $D$  are listed for various elemental solids in table 5 of reference [178].

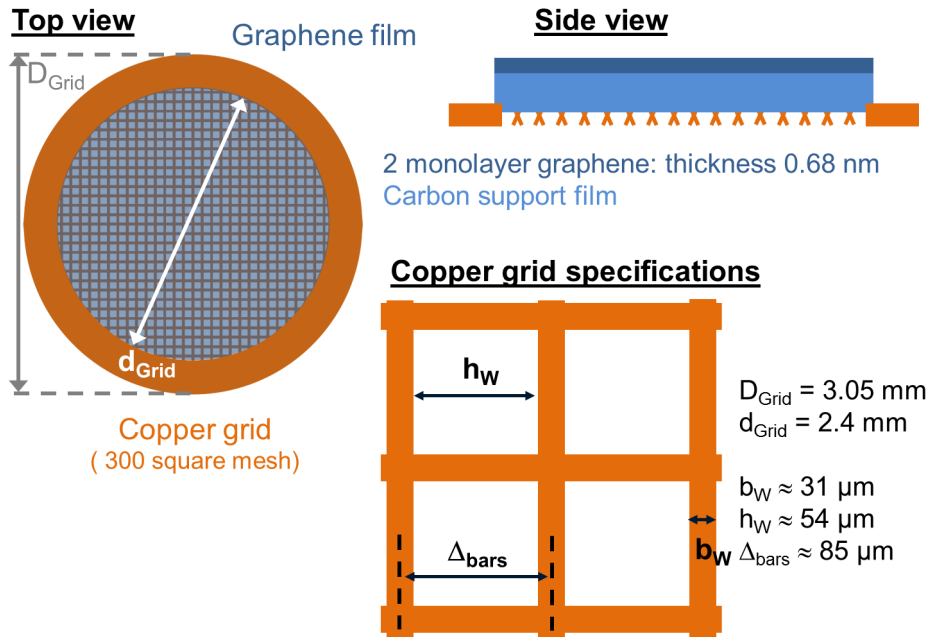


Figure 7.17: Illustration of the 300 square mesh copper grid covered by a carbon support/graphene film ( $D_{\text{Grid}}$ ,  $d_{\text{Grid}}$ ,  $b_w$ ,  $h_w$  and  $\Delta_{\text{bars}}$ : specifications of the manufacturer [179]).

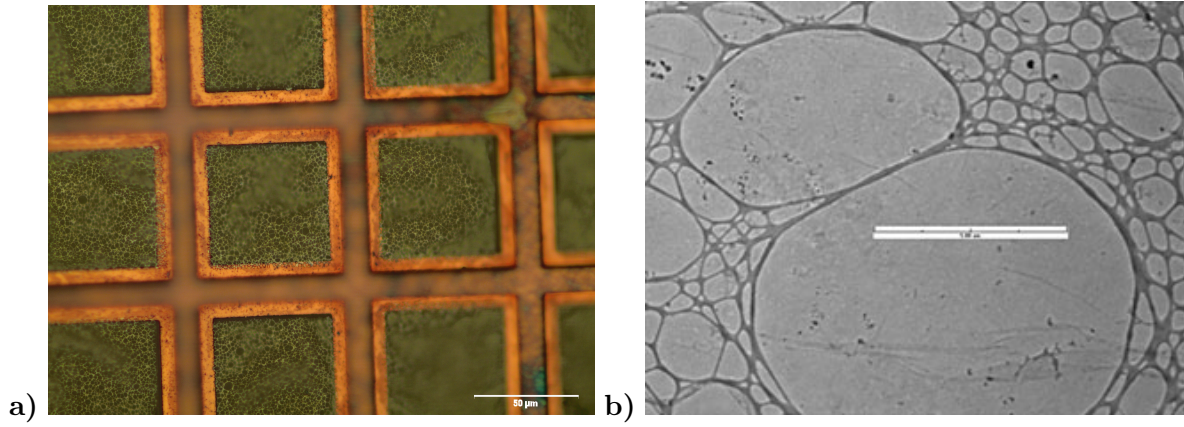


Figure 7.18: a) Optical microscopy image of 300 mesh square copper grid covered by a carbon support and 2 monolayer graphene film;  
b) Carbon support film and 3-5 ML-graphene (bar = 5 μm, taken from [174]).

In order to calculate the energy dependent values of  $\lambda_{\text{IMFP}}$  for the graphene films the following parameter values have been used (stated as the values for graphite in [178]):  $\beta = 0.0183 \text{ (eV \AA)}^{-1}$ ,  $\gamma = 0.1333 \text{ (eV)}^{-1}$ ,  $C = 1.365 \text{ (\AA)}^{-1}$ ,  $D = 23.6 \text{ eV (\AA)}^{-1}$  and  $E_p = 24.93 \text{ eV}$ .

In figure 7.19a a graphical representation of the result obtained for the  $\lambda_{\text{IMFP}}$  of graphene can be seen over the energy range of 50 eV to 10 keV. For the purpose of comparison the thickness sizes of 1, 2, 3 or 4 ML-graphene films are shown as greyed out areas. The e-beam transmission curves calculated by using equation 7.10 for graphene films with  $t_{\text{Graphene}}$  in the range of 1 to 4 monolayers are shown in figure 7.19b for a normal incident e-beam ( $\Theta = 0^\circ$ ). As expected the transmission goes down with an increase in film thickness. All 4 curves have their minimum in the range of 50 eV to 100 eV and the transmission is above 50 % for all 4 curves in the range  $E > 1 \text{ keV}$ . In the 2 ML-graphene film case the estimated e-beam transmission is 53.4 % at 500 eV, 68.9 % at 1 keV and 80.7 % at 2 keV. What should be mentioned is that the here presented e-beam transmission estimation does not include the elastic scattering contribution. Therefore, it should be kept in mind that experimental obtained results will be below the here estimated values.

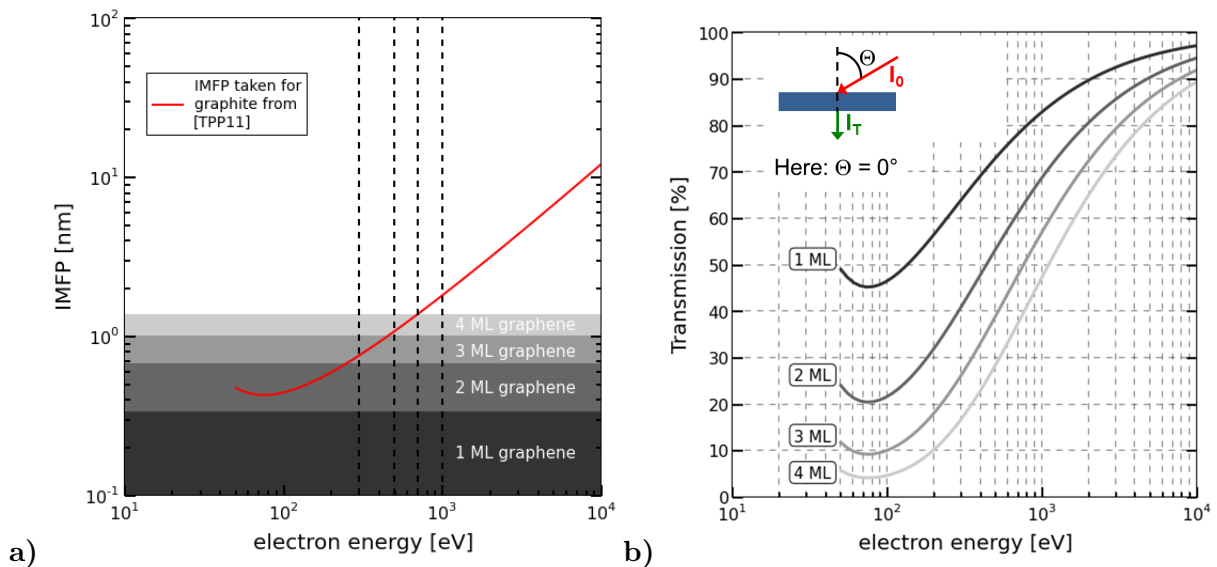


Figure 7.19: a) Electron IMFP for graphite (Used equation 7.11 and parameters from [178]);  
b) Electron transmission curves, used equation 7.10 for a normal incident beam.



### 7.3 Appendix C: EIRFIS

#### EIRFIS e-Column CPO simulations

$V_W$ [kV]	$V_L$ [kV]	Fixed: $V_C = 5.9$ kV; $V_A = V_{e\text{-Shield}} = 8.9$ kV; $V_I = V_{S1} = 6$ kV; $V_{S2} = 5.975$ kV; $V_{IC} = V_{S3} = 5.95$ kV and $V_{VT} = 0$ kV.
4.2	5.675	
4.3	5.700	
4.4	5.700	
4.5	5.725	
4.6	5.725	

Table 7.2: Potential settings for the EIRFIS e-Column simulations (Related results in figure 5.7).

The YZ-cross sections of the e-beam at the inlet electrode, at 3 mm behind the inlet electrode close to the e-beam focus and at the middle of the ionisation region are shown in figure 7.20. These are related to the simulation case already shown in figure 5.6a. Furthermore, the corresponding 2D-histograms are shown in order to visualise in more detail the electron distributions within the YZ-cross sections. At the inlet electrode and close to the e-beam focus plane the 2D-histograms show maximum intensity regions in proximity of the Y-axis at radial values ( $r = \sqrt{Y^2 + Z^2}$ ) of about 0.4 mm for the inlet plane and 0.1 mm close to the e-beam focus plane. Furthermore, at the same radial values higher intensity rings are visible. Compared to this at the YZ-cross section in the middle of the ionisation the e-beam distribution changes and the maximum intensity region is found close to the e-beam axis with a continuously decreasing intensity when going outwards in radial direction.

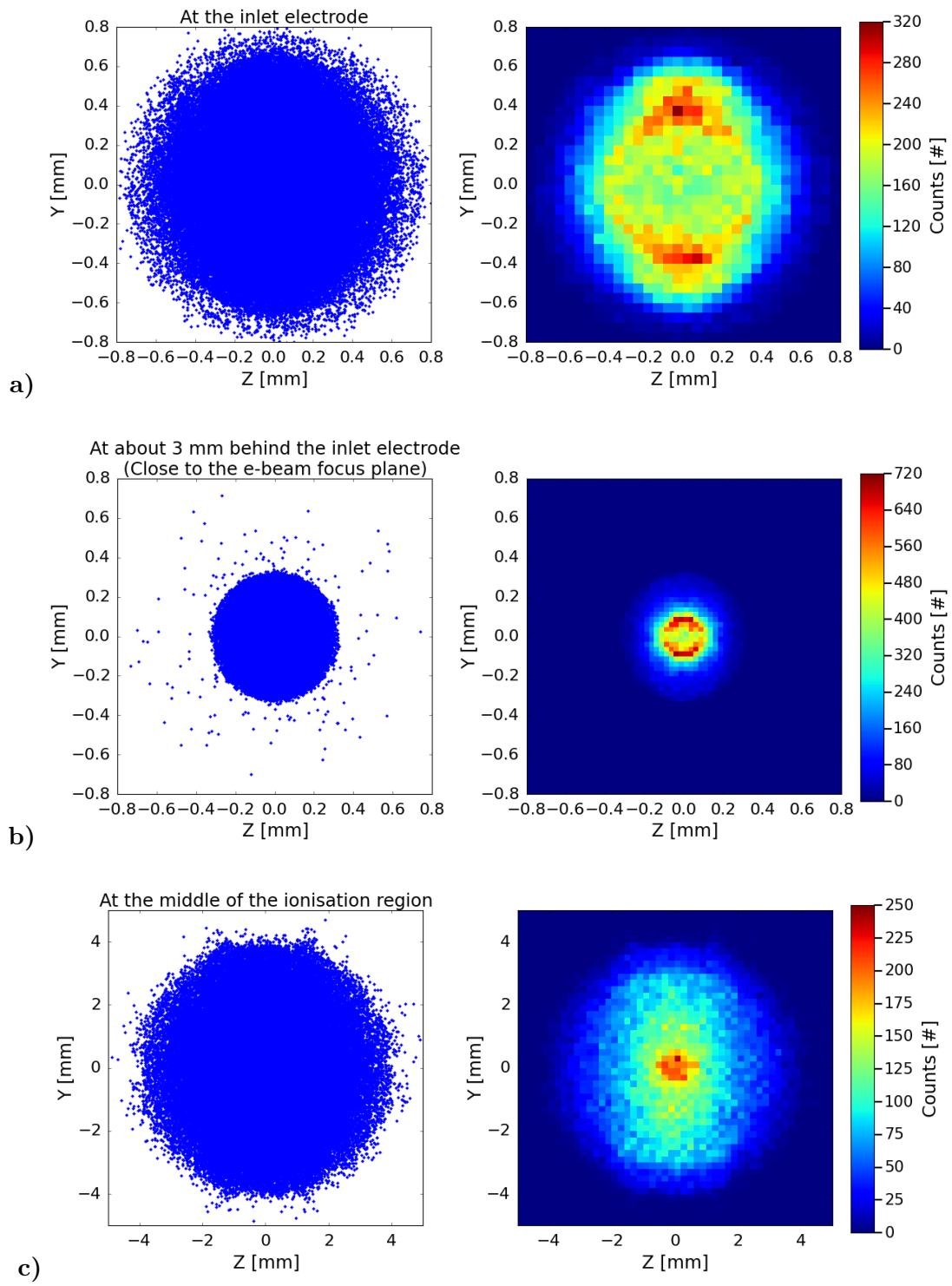


Figure 7.20: e-beam YZ-cross sections and corresponding 2D-histograms for the EIRFIS e-Column simulation of figure 5.6a:

- a) At the inlet electrode;
- b) At 3 mm behind the inlet electrode (close to the e-beam focus plane);
- c) At the middle of the ionisation region.

### EIRFIS ionisation region and ion column CPO simulations

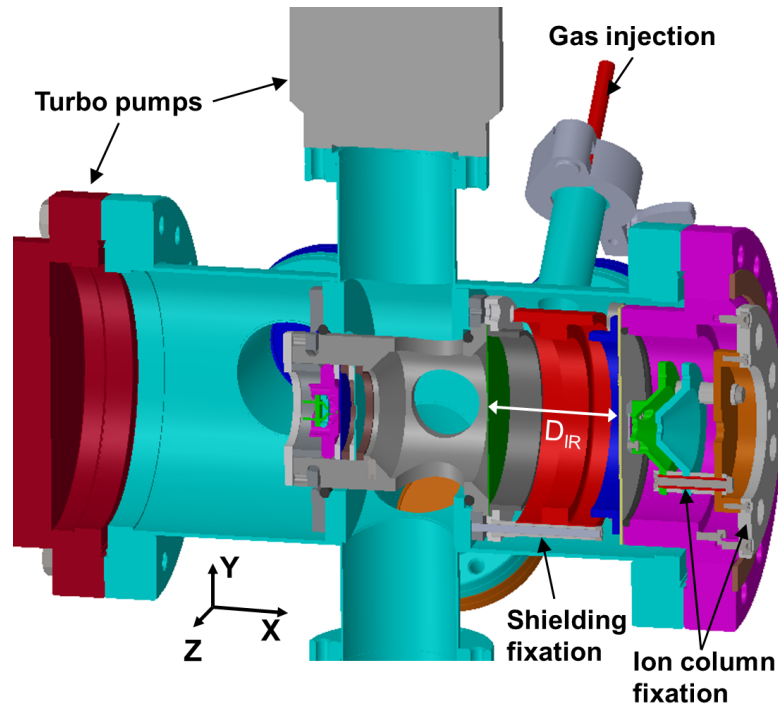


Figure 7.21: EIRFIS mechanical model schematic: ionisation region (with shielding) and ion extraction column (3D view).

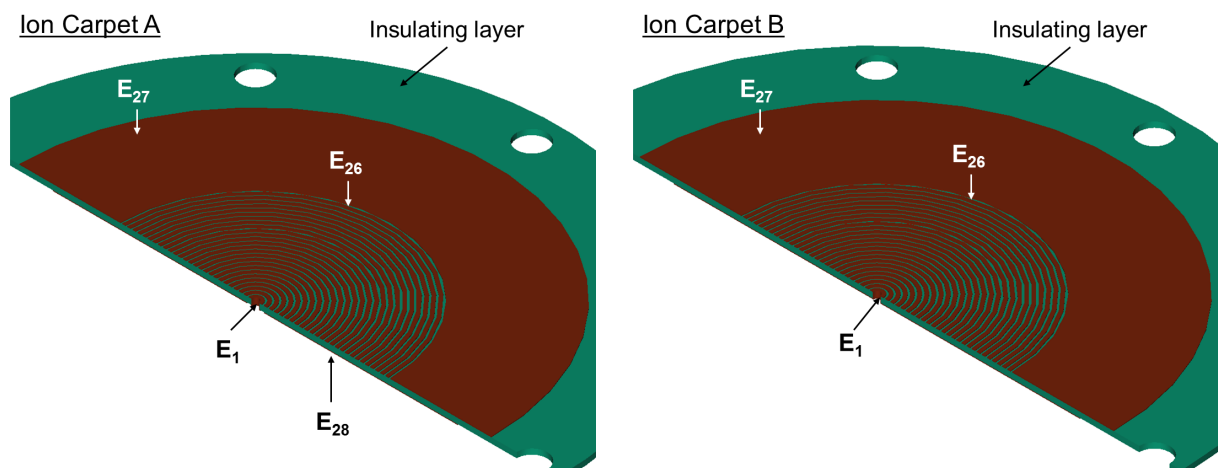


Figure 7.22: 3D illustration of Ion Carpet A and B (including insulating layer).

During the CPO ion column evaluation the ions are generated within an ionisation volume above the Ion Carpets A and B which has a truncated cone shape. This can be seen in figure 7.23 which is related to the simulation case shown in figure 5.11 of section 5.2.2. The initial positions of the ions are generated programmatically within the corresponding SIMION workbench programmes and the parametrisation that is used is:

$$dX = h \cdot u_{\text{rand}} \quad \text{and} \quad r_{dX} = r_s + \tan(\alpha) \cdot dX$$

$$r_{\text{rand}} = r_{dX} \cdot v_{\text{rand}} \quad \text{and} \quad \theta_{\text{rand}} = t_{\text{rand}} \cdot 2\pi \quad (7.12)$$

$$X_{\text{ion}} = X_0 + dX \quad \text{and} \quad Y_{\text{ion}} = r_{\text{rand}} \cdot \sin(\theta_{\text{rand}}) \quad \text{and} \quad Z_{\text{ion}} = r_{\text{rand}} \cdot \cos(\theta_{\text{rand}}) \quad .$$

Here  $u_{\text{rand}}$ ,  $v_{\text{rand}}$  and  $t_{\text{rand}}$  represent random numbers generated between 0 and 1. For each ion firstly a random value for  $dX$  is generated in between 0 and  $h$ . The outside radius  $r_{dX}$  of the truncated cone at  $dX$  is then calculated, followed by a random generation of a radius  $r_{\text{rand}}$  and angle  $\theta_{\text{rand}}$  within the circular cross section of the truncated cone at  $dX$ .

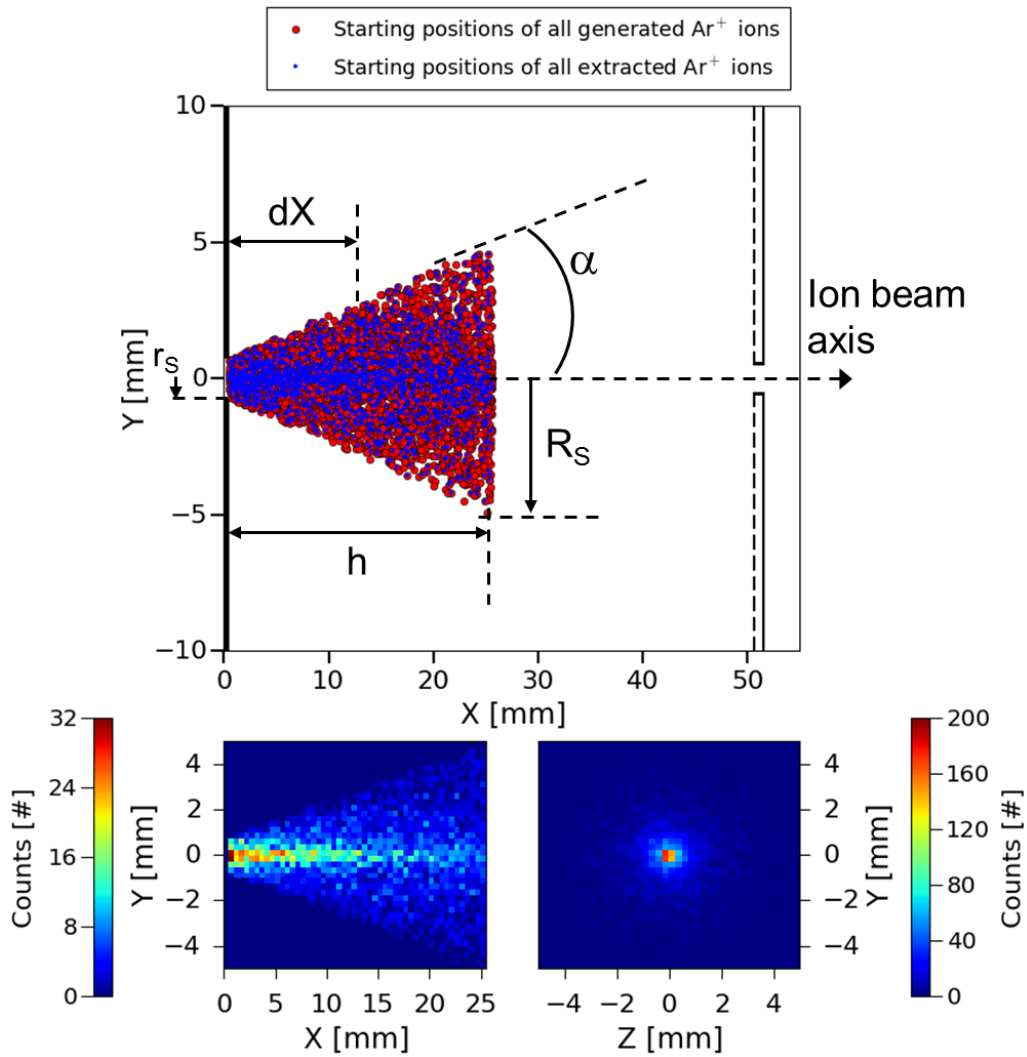


Figure 7.23: Starting volume illustration for the EIRFIS ion column simulations ( $\text{Ar}^+$  ions).

At the end  $dX$ ,  $r_{\text{rand}}$  and  $\theta_{\text{rand}}$  are used to calculate the initial starting position of the ion ( $X_{\text{ion}}$ ,  $Y_{\text{ion}}$ ,  $Z_{\text{ion}}$ ) in the SIMION workbench coordinates. As can be seen in the 2D-histograms of figure 7.23 the density of ions close to the ion beam axis is higher, within each YZ-cross section along the truncated cone volume, compared to the regions further away in radial direction

( $r = \sqrt{Y^2 + Z^2}$ ). Moreover, it can be seen that within the smaller YZ-cross sections the overall ion density is higher compared to bigger YZ-cross sections. This is related to the fact that if the same number of ions is generated within both cross sections the ions are packed denser in the cross section having the smaller area. No correction for this unequal density of ion position generation is currently taken into account. Furthermore, when having a look at the e-beam cross sections shown in figure 7.20 it can be concluded that as a general approximation the e-beam density is higher close to the ion beam axis (which is equal to the e-beam axis) within the ionisation region. Therefore, the chosen parametrisation of equation 7.12 for the initial ion positions is related in good approximation to the results of the e-beam density distributions. Moreover, it can be concluded that it is not necessary to perform a more precise relation between the initial ion positions and the e-beam distributions as the EIRFIS e-Column CPO evaluations do not take into account any electron gas collisions which will affect the e-beam distribution.

In figure 7.24 all frequency cases used for the extraction efficiency evaluation of Ion Carpet A and B in the case of  $\text{Ar}^+$  ions are shown to complete the data shown in figure 5.12 of section 5.2.2.

In figure 7.25 the variation of different parameters used during the slice-approach to calculate the total generated and extracted ion current (explained in detail in section 5.3.1) is shown. The parameter curves are related to the simulation case shown in figure 5.11. What can be seen is that as expected from equation 5.6 the energy of the e-beam drops linearly when going from slice to slice within the truncated cone volume. The extraction efficiency per slice  $f_{\text{Extr,slice-i,Ar}^+}$  is varying between 10 to 70 % with a mean value of about 36 %. The generated  $\text{Ar}^+$  current per slice  $I_{\text{slice-i,Ar}^+}$  is higher within the slices close to the inlet electrode (slice number < 100) as the energy is in the range of 60 to 100 eV for which the EI cross section is the highest. For slice numbers > 150 the EI cross section starts decreasing quite fast related to the fact that the energy drops below 40 eV, this fast drop is as well seen in the related curve of  $I_{\text{slice-i,Ar}^+}$ .

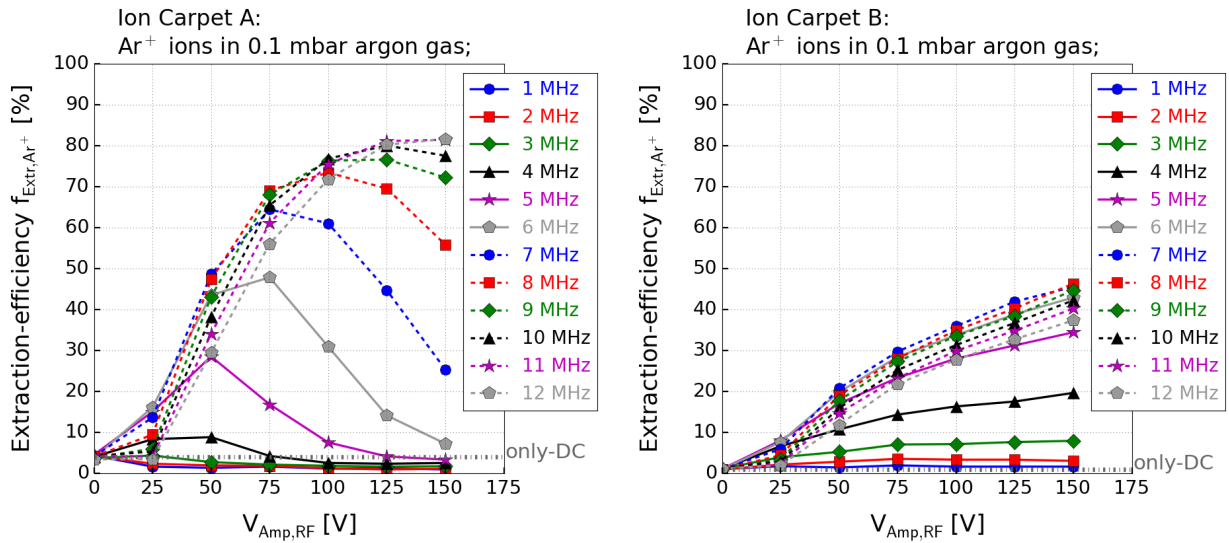


Figure 7.24: Extraction efficiency Ion Carpet A/B:  $\text{Ar}^+$  in argon (IV-Ar;  $p_{\text{IR}} = 0.1$  mbar,  $T_{\text{IR}} = 298.15$  K;  $d_0 = 1$  mm;  $d_{\text{Ex1}} = 0.1$  mm;  $\Delta V_{\text{IC-Ex1}} = 500$  V; Use of the Test-pressure-gradient).

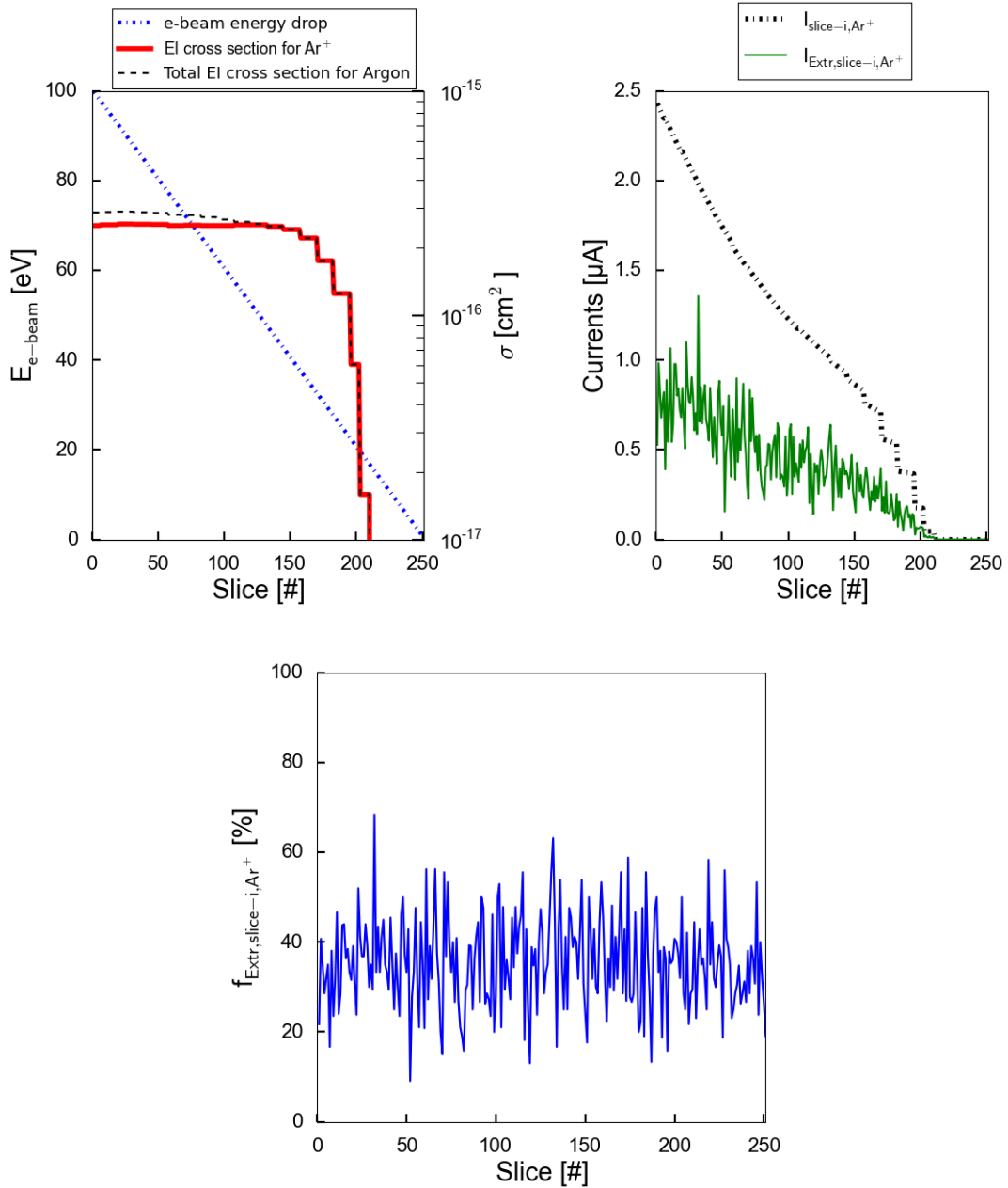


Figure 7.25: Ion current determination by the slice-approach: Variation of different parameters (Ion Carpet B:  $f_{RF} = 8$  MHz,  $V_{Amp,RF} = 100$  V;  $p_{IR} = 0.1$  mbar,  $T_{IR} = 298.15$  K).

At slice numbers  $> 200$   $I_{\text{slice-i,Ar}^+}$  goes to zero as the e-beam energy drops below the threshold for ionisation (in the case of  $\text{Ar}^+ \approx 17$  eV [45]). The combination of  $I_{\text{slice-i,Ar}^+}$  and  $f_{\text{Ext,slice-i,Ar}^+}$  results in the curve shown for the extracted  $\text{Ar}^+$  current per slice  $I_{\text{Ext,slice-i,Ar}^+}$ .

In figure 7.26 a complete ion column simulation for  $\text{Ar}^+$  ions for the case of Ion Carpet A is shown as an illustration. Related evaluations of the ion beam profile at the Rec-Plane and source location plane can be found in figure 7.27. The ion beam profile at the Rec-Plane represents the evaluation of the ion positions directly obtained within the CPO simulation. What can be seen in the corresponding 2D- (zoomed views) and 1D-histograms (representing projections in Z- and Y-direction) is that a Gaussian-like profile is obtained with a FW50 diameter of about 2 mm. In the source location plane the beam size is clearly smaller compared to the Rec-Plane and the represented ion positions are the result of the trajectory extrapolation method used in X-direction. The FW50 diameter in the source plane is 65  $\mu\text{m}$  and the corresponding 2D- and 1D-histograms show here a more top hat shape like profile. When having a look at the 2D-



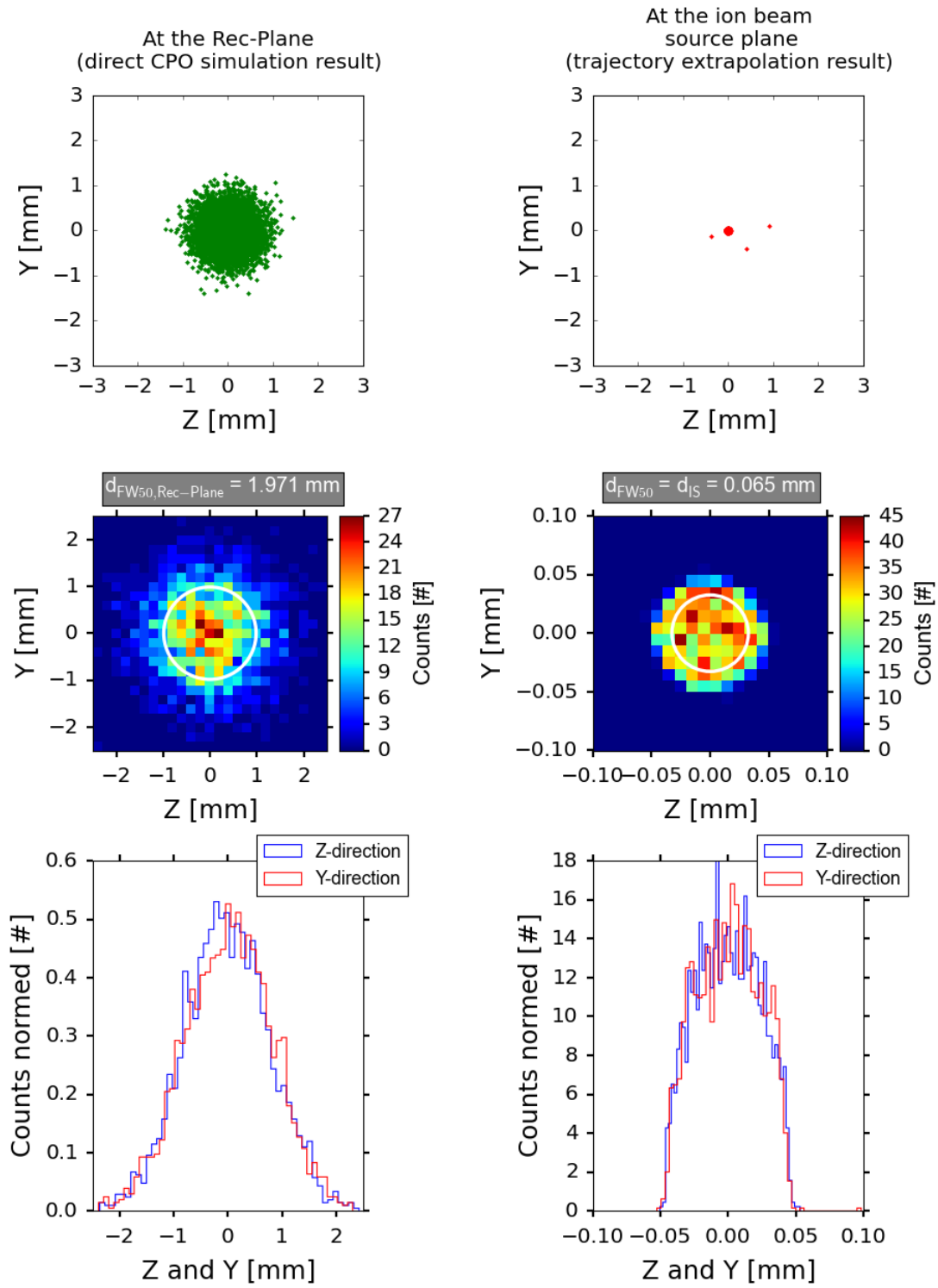


Figure 7.27:  $\text{Ar}^+$  ion beam profile evaluation at the Rec-Plane and source location plane for the simulation case of figure 7.26.



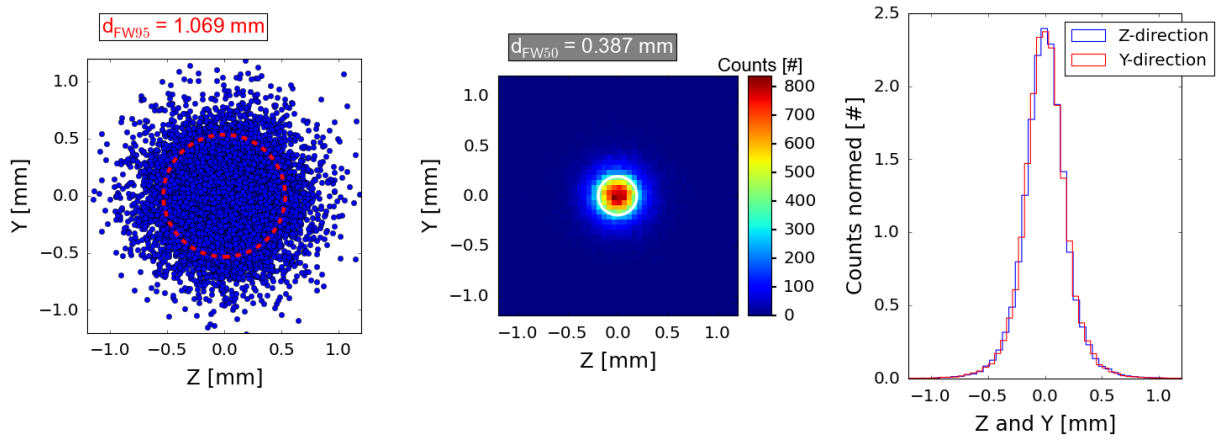


Figure 7.28:  $\text{Ar}^+$  ion beam profile evaluation at the extraction aperture plane for the simulation case of figure 7.26.

### Gas conductance calculations for the e-Column

More details about the different pV-flow equations mentioned in section 5.4.1 will be given here. For the inner ceramic region the following pV-flow equation can be established:

$$q_1 = q_2 + q_3 \iff (p_{\text{IR}} - p_{\text{eC,In}}) \cdot C_1 = (p_{\text{eC,In}} - p_{\text{eC,Out}}) \cdot C_2 + (p_{\text{eC,In}} - p_{\text{W}}) \cdot C_3 \quad . \quad (7.13)$$

Three additional pV-flow equations can be established:

$$\text{Outside of the ceramic: } q_2 = q_{\text{eC}} \iff (p_{\text{eC,In}} - p_{\text{eC,Out}}) \cdot C_2 = p_{\text{eC,Out}} \cdot S_{\text{eff,eC}} \quad . \quad (7.14)$$

$$\text{Wehnelt volume: } q_3 = q_4 \iff (p_{\text{eC,In}} - p_{\text{W}}) \cdot C_3 = (p_{\text{W}} - p_{\text{P}}) \cdot C_4 \quad . \quad (7.15)$$

$$\text{Pump chamber: } q_4 = q_{\text{P}} \iff (p_{\text{W}} - p_{\text{P}}) \cdot C_4 = p_{\text{P}} \cdot S_{\text{eff,P}} \quad . \quad (7.16)$$

Rearranging/combining of the different pV-flow equations is needed in order to find the pressure expressions of equation 5.10. By simply rearranging the pV-flow equations 7.14 and 7.16 it is possible to obtain:

$$p_{\text{eC,Out}} = p_{\text{eC,In}} \cdot \frac{C_2}{S_{\text{eff,eC}} + C_2} \quad \text{and} \quad p_{\text{P}} = p_{\text{W}} \cdot \frac{C_4}{S_{\text{eff,P}} + C_4} \quad . \quad (7.17)$$

By inserting the expression for  $p_{\text{P}}$  into equation 7.15 and rearranging, the following is obtained:

$$\begin{aligned} (p_{\text{eC,In}} - p_{\text{W}}) \cdot C_3 &= \left( p_{\text{W}} - p_{\text{W}} \cdot \frac{C_4}{S_{\text{eff,P}} + C_4} \right) \cdot C_4 \\ \iff p_{\text{eC,In}} \cdot C_3 &= p_{\text{W}} \cdot \left[ \left( 1 - \frac{C_4}{S_{\text{eff,P}} + C_4} \right) \cdot C_4 + C_3 \right] \\ \iff p_{\text{eC,In}} \cdot C_3 &= p_{\text{W}} \cdot K_{\text{A}} \\ \iff p_{\text{W}} &= p_{\text{eC,In}} \cdot \frac{C_3}{K_{\text{A}}} \quad . \end{aligned} \quad (7.18)$$

Furthermore by inserting the obtained expressions for  $p_{eC,Out}$  and  $p_W$  into equation 7.13 the expression for  $p_{eC,In}$  can be obtained:

$$\begin{aligned}
 (p_{IR} - p_{eC,In}) \cdot C_1 &= \left( p_{eC,In} - p_{eC,In} \cdot \frac{C_2}{S_{eff,eC} + C_2} \right) \cdot C_2 + \left( p_{eC,In} - p_{eC,In} \cdot \frac{C_3}{K_A} \right) \cdot C_3 \\
 \iff p_{IR} \cdot C_1 &= p_{eC,In} \cdot \left[ \left( 1 - \frac{C_2}{S_{eff,eC} + C_2} \right) \cdot C_2 + \left( 1 - \frac{C_3}{K_A} \right) \cdot C_3 + C_1 \right] \\
 \iff p_{IR} \cdot C_1 &= p_{eC,In} \cdot K_B \\
 \iff p_{eC,In} &= p_{IR} \cdot \frac{C_1}{K_B} \quad .
 \end{aligned} \tag{7.19}$$

The quantities  $K_A$  and  $K_B$  have the same unit as gas conductances ( $m^3/s$  or  $l/s$  or ...).

As also mentioned in section 5.4.1 the expression for the conductance  $C_3$  (series connection of several elements) is evaluated here below in more detail. The following can be written for the elements cross sections  $A_i$  - and the  $\delta_{i,i+1}$  - values needed in order to use equation 3.32 for the calculation of  $C_3$  :

Element	i	
L	1	$A_2 \geq A_1 \Rightarrow \delta_{12} = 0$
Sp <sub>LA</sub>	2	$A_3 < A_2 \Rightarrow \delta_{23} = 1$
A	3	$A_4 \geq A_3 \Rightarrow \delta_{34} = 0$
Sp <sub>AW</sub>	4	$A_5 < A_4 \Rightarrow \delta_{45} = 1$
W	5	

With this knowledge it can be written for  $C_3$  that:

$$\begin{aligned}
 \frac{1}{C_3} &= \frac{1}{C_L} + \frac{1}{C_{SpLA}} + \frac{1}{C_A} + \frac{1}{C_{SpAW}} + \frac{1}{C_W} - \frac{4}{v_{mean}} \cdot \left( \frac{1}{A_L} + \frac{1}{A_{SpLA}} + \frac{1}{A_A} + \frac{1}{A_{SpAW}} + \frac{1}{A_W} \right) + \dots \\
 &\quad \dots + \frac{4}{v_{mean}} \cdot \left( \frac{1}{A_A} - \frac{1}{A_{SpLA}} \right) + \frac{4}{v_{mean}} \cdot \left( \frac{1}{A_W} - \frac{1}{A_{SpAW}} \right) + \frac{4}{v_{mean} A_L} \\
 \iff \frac{1}{C_3} &= \frac{1}{C_L} + \frac{1}{C_{SpLA}} + \frac{1}{C_A} + \frac{1}{C_{SpAW}} + \frac{1}{C_W} - \frac{8}{v_{mean}} \cdot \left( \frac{1}{A_{SpLA}} + \frac{1}{A_{SpAW}} \right) \quad .
 \end{aligned} \tag{7.20}$$

### Molecular flow simulations for the ion column

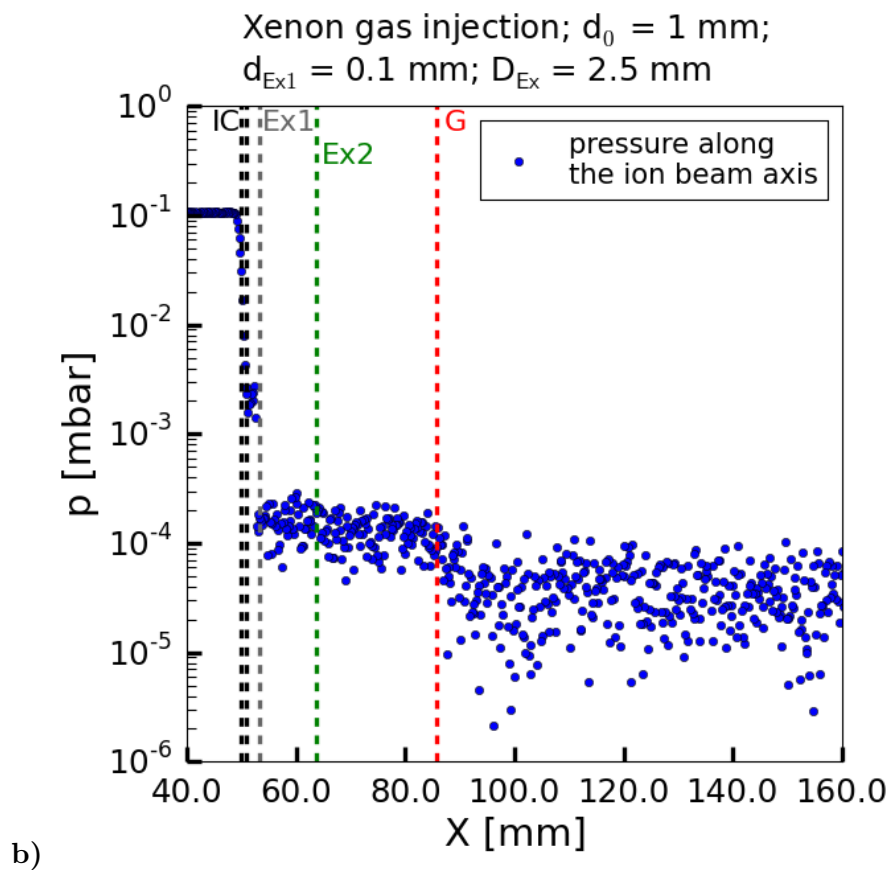
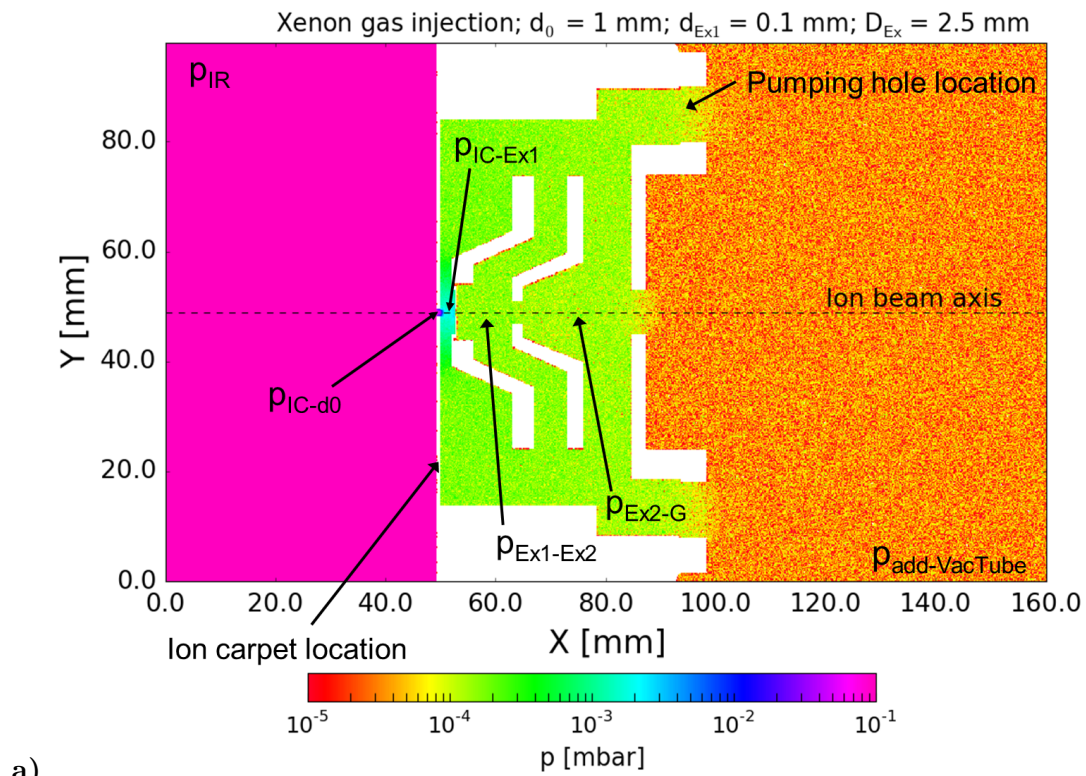


Figure 7.29: Molflow+ EIRFIS ion column simulation ( $d_0 = 1$  mm,  $d_{Ex1} = 100$   $\mu$ m):

- a) 2D pressure distribution (Xe,  $S_{eff,IC} = 75$  l/s,  $T = 298.15$  K);
- b) Pressure gradient along the ion beam axis (Xe,  $S_{eff,IC} = 75$  l/s,  $T = 298.15$  K).

### Experimental investigations

The distance  $D_{CW}$  between the disc cathode and the Wehnelt electrode used within the EIRFIS prototype e-Column Setup 1 is increased to 0.9 mm compared to the value of  $D_{CW} = 0.2$  mm used during the e-Column CPO simulations and during some preliminary experimental e-Column tests. The increase of  $D_{CW}$  is related to the fact that after some time of operation it appeared that the potentials of the disc cathode and the Wehnelt electrode are not independent any more and discharge problems between those elements are being seen. According to the cathodes manufacturer Kimball Physics Inc., it can be that a value of  $D_{CW} = 0.2$  mm is chosen to small as there will be some expansion of the small heating wires attached to the disc cathode which will further reduce  $D_{CW}$ . Therefore, the advice of the manufacturer is it to increase the value of  $D_{CW}$  and simultaneously slightly the Wehnelt hole diameter ( $d_W$  has been increased to 2.0 mm compared to 1.5 mm before) to avoid any charging problems. Very flat discs have been introduced in between the cathode base and the Wehnelt electrode to increase  $D_{CW}$  to 0.9 mm, as illustrated in figure 7.30.

At some point the Wehnelt hole is opened up even further to  $d_W = 3$  mm (e-Column Setup 2). This is related to the fact that it has been noticed that a misalignment of the Wehnelt hole with respect to the anode aperture was existing. As can be seen in figure 7.31, by increasing  $d_W$  to 3 mm a concentric alignment of these two apertures could again be realised.

The charging problems between disc cathode and Wehnelt electrode appeared again after some time even if  $D_{CW}$  and  $d_W$  have been increased. Therefore, a further modification that is done in order to avoid these charging problems is shown in figure 7.32. In the top left picture of figure 7.32 a circular deposition layer can be clearly seen. This is the result of the electrode configuration shown in figure 7.30 and the material that is deposited is most probably evaporated from the heater wires. During the operation the deposition layer grows and at one point an electrical contact is produced between the heater wires and the Wehnelt electrode.

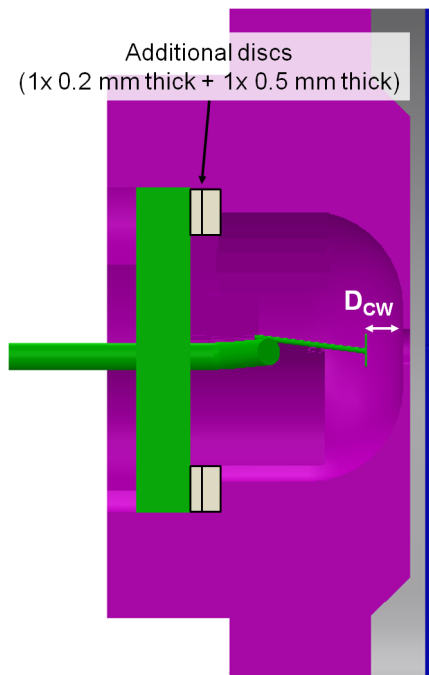


Figure 7.30: Illustration of the increase in  $D_{CW}$  by inserting additional small very flat discs in between the cathode ceramic base and the Wehnelt electrode.

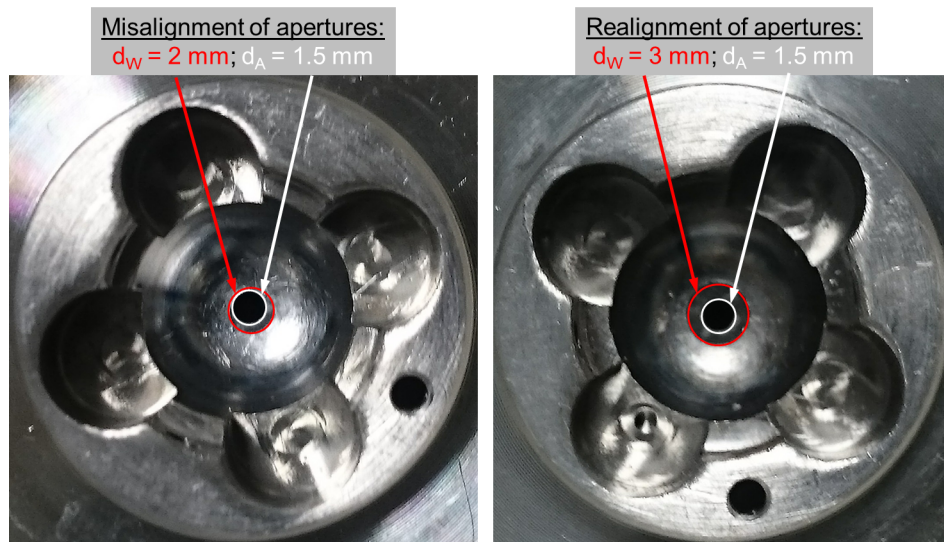


Figure 7.31: Illustration of the realignment of the Wehnelt and anode aperture.

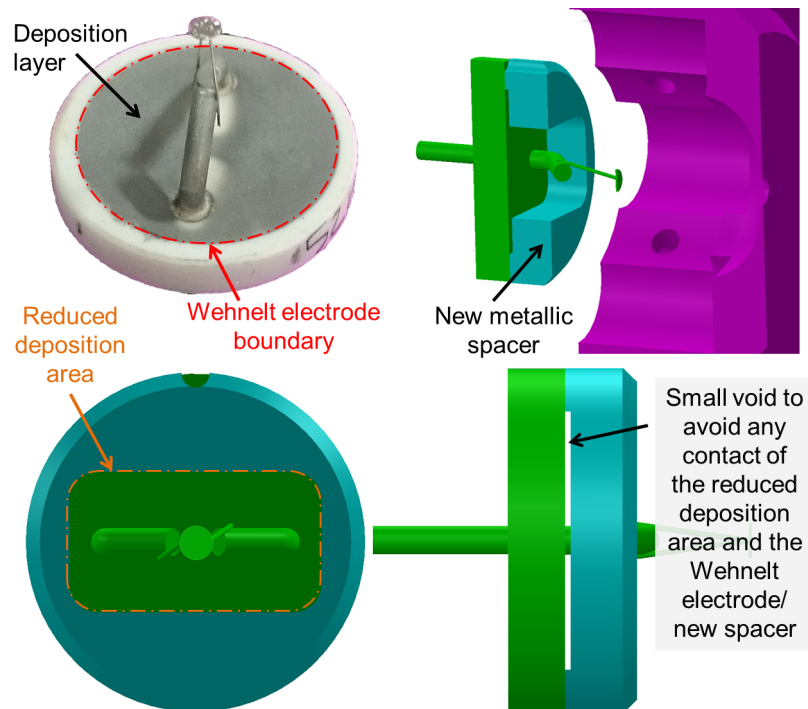


Figure 7.32: Illustration of the realignment of the Wehnelt and anode aperture.

The Wehnelt electrode boundary touching the deposition layer is shown in the top left picture of figure 7.32. A new metallic spacer piece is introduced in between the ceramic base of the cathode and the Wehnelt electrode, top right picture of figure 7.32. This spacer has a special shape so that the deposition layer is limited to a rectangular area around the centre of the ceramic base. Additionally a small void exists in between the new spacer and the ceramic base, see bottom pictures of figure 7.32. In this way the reduced deposition layer is nowhere in contact with any metal boundary and the electrical contact between cathode and Wehnelt electrode is avoided. The experienced charging problems can be suppressed with this new electrode configuration which was used as well for the e-Column Setup 2.

Further improvements of the RF electronics are expected to increase the extractable ion current out of the ionisation region to the targeted  $\mu\text{A}$  range. One aspect which is expected to have a clear effect on the extractable ion current is discussed in more detail in the following. The RF-signal amplitudes  $V_{\text{Amp,RF},i}$  generated at the different electrodes of the PCB ion carpet are measured by using a differential voltage probe and an oscilloscope. These measurements are performed under air when the ion carpet is not mounted within the EIRFIS prototype. Two different cases are compared: The first case has the same electrical circuit layout as shown in figure 5.25 and the second case has an identical circuit layout except that the capacitor C1 is removed. In both cases the AFG together with the transformer is used to apply low amplitude RF-signals to the ion carpet.

The measured  $V_{\text{Amp,RF},i}$  values can be seen in figure 7.33 for both cases (with and without C1). When having a look at the case with C1, figure 7.33a, it is visible that on E26 has a quite large  $V_{\text{Amp,RF},i}$ . This means that even if E26 has no direct connection to one of the RF-signal lines there is some passage of RF through the resistances in between E26 and its neighbouring electrodes. Moreover, on E1 and E27 an even larger  $V_{\text{Amp,RF},i}$  is measured even if it is expected that no varying potential contribution should be generated on these electrodes. This is due to the fact that C1 is connected to E1 which itself is connected via the GND of the ion carpet to E27. Another unexpected situation that shows up is that the  $V_{\text{Amp,RF},i}$  values measured on even and odd ring electrodes are unbalanced. It is assumed that this effect can create an unstable ion motion above the PCB ion carpet and lead to a quite low ion extraction through the central ion carpet hole as seen during the argon ion extraction tests.

In the PCB ion carpet case without C1, figure 7.33b, the measured RF amplitudes are quite different compared to the case with C1. A first result that can be seen is that now on E1, E26 and E27 only a very small  $V_{\text{Amp,RF},i}$  value can be measured. In this electrical circuit situation the central ion carpet hole potential is closer to a complete DC-potential situation which has been determined by the CPO simulations to be favourable to get a low  $\Delta E$  for the generated ion beam. Furthermore, the  $V_{\text{Amp,RF},i}$  value measured on even and odd ring electrodes is far more equilibrated compared to the case with C1. Even if the absolute values of  $V_{\text{Amp,RF},i}$  on the rings are lower compared to the case with C1, it is assumed that the case without C1 will create a more stable ion motion above the PCB ion carpet and be favourable for the ion extraction. This assumption still needs to be tested by experimental investigations.

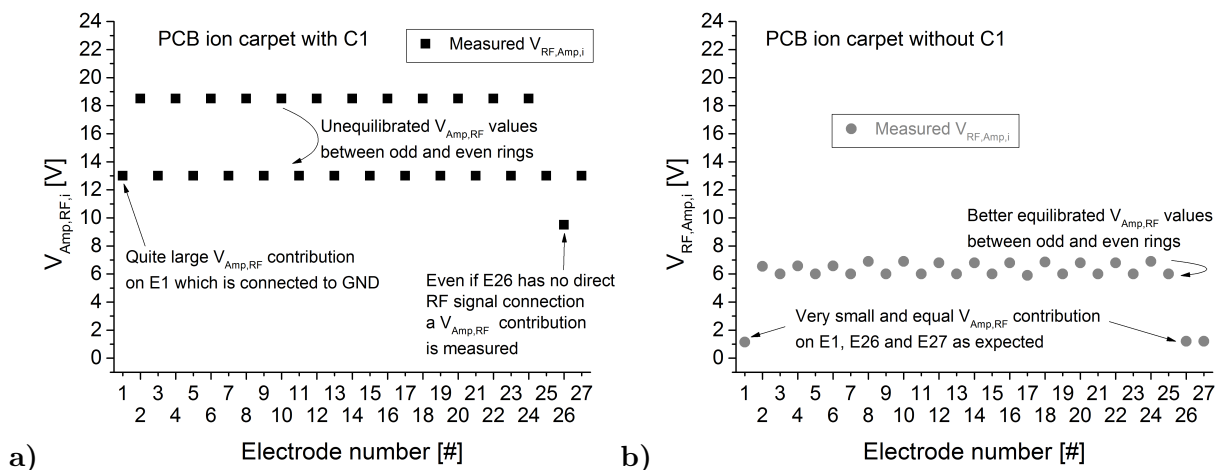


Figure 7.33: Measured RF amplitudes  $V_{\text{Amp,RF},i}$  on the PCB ion carpet:

a) Electrical circuit layout with C1; b) Electrical circuit layout without C1.



## 7.4 Appendix D: Résumé français de la thèse

### 7.4.1 Introduction et objectifs

Différentes techniques à l'échelle nanométrique utilisant des faisceaux d'ions focalisés (FIB: acronyme anglais de Focused Ion Beam) existent de nos jours: la **nano-fabrication par FIB** [1, 2, 3, 4, 5], la **nano-imagerie par FIB** (pas d'information chimique) [6, 7, 8], la **nano-analyse par FIB** (information chimique) [9, 10, 11, 84].

Un aspect commun de **toutes ces nano-applications par FIB** est qu'elles **nécessitent des sources d'ions à haute brillance** ayant une faible dispersion en énergie  $\Delta E$  pour obtenir une excellente résolution latérale et un courant d'ions suffisamment élevé pour induire des vitesses d'érosion raisonnables et des rendements élevés d'émission électronique et ionique secondaire. Une faible valeur de  $\Delta E$  est désirée pour minimiser les effets d'aberrations chromatiques dans la colonne ionique qui élargissent la taille du faisceau dans le plan d'analyse et ainsi limitent la résolution.

Pour évaluer la qualité d'un faisceau d'ions et comparer la performance de différentes sources d'ions la **brillance réduite  $B_r$**  est utilisée et est calculée avec:

$$B_r = \frac{I_{\text{Ionique}}}{A_{\text{Source}} \cdot \Omega \cdot V_{\text{Faisceau}}} \quad (7.21)$$

où  $A_{\text{Source}}$  représente la surface de la source ionique,  $I_{\text{Ionique}}$  le courant ionique,  $\Omega$  l'angle solide et  $V_{\text{Faisceau}}$  le potentiel d'accélération du faisceau [20, 32, 33]. Les différents paramètres sont illustrés sur la figure 7.34.

Un aspect important pour les applications par FIB est le type d'ions délivré qui a un fort impact sur des paramètres comme les rendements de pulvérisation, la modification des propriétés du matériel, les rendements d'émission d'électrons/d'ions secondaires [3, 12, 14, 15, 16, 17, 18, 19]).

La source d'ions à métal liquide (LMIS: acronyme anglais de Liquid Metal Ion Source) de gallium est le plus souvent utilisée à cause de sa grande brillance réduite dans la gamme de  $B_r = 10^6 - 10^7 \text{ A m}^{-2} \text{ sr}^{-1} \text{ V}^{-1}$  et son fonctionnement stable et fiable. Un désavantage est l'implantation du Ga dans les échantillons ce qui cause des changements non-désirés de propriétés des matériaux [15, 64, 65], donc une utilisation de faisceaux d'ions de gaz nobles serait avantageuse. D'autres sources d'ions à haute brillance existent et sont aussi utilisées pour des nano-applications par FIB.

Les sources à impact électronique (IE) ont des caractéristiques très intéressantes, dont la flexibilité des espèces ioniques, mais sont limitées par une très basse brillance réduite dans leur configuration conventionnelle avec  $B_r \approx 1 \text{ A}/(\text{m}^2 \text{ sr V})$ .

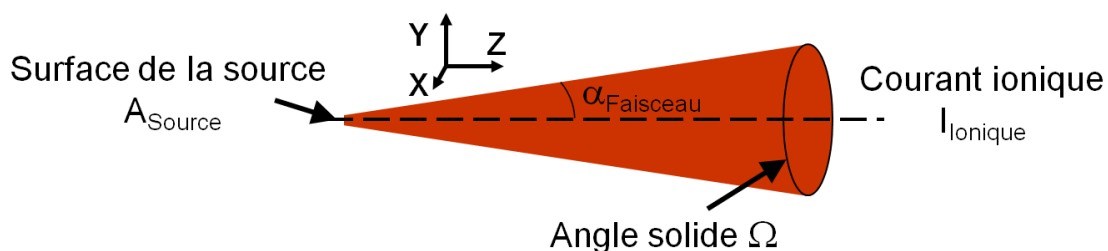


Figure 7.34: Illustration des paramètres géométriques d'un faisceau d'ions.

Les objectifs de la thèse sont les suivants:

- **Le développement d'une source d'ions gazeuse à haute brillance basée sur l'impact électronique.** L'objectif est d'obtenir une brillance réduite dans la gamme de  $B_r = 10^3 - 10^4 \text{ A m}^{-2} \text{ sr}^{-1} \text{ V}^{-1}$ .
- **La création de faisceaux d'ions avec une basse dispersion en énergie** pour minimiser l'élargissement du faisceau dû aux aberrations chromatiques dans la colonne ionique d'un instrument FIB. L'objectif pour la dispersion en énergie est  $\Delta E \lesssim 1 \text{ eV}$ .
- **Un choix polyvalent de l'espèce d'ions**, obtenu essentiellement par un simple changement du gaz injecté dans la source.
- **Un concept mécanique le plus compact possible** afin de faciliter l'utiliser sur des instruments à FIB existants.

#### 7.4.2 Source d'ions à impact électronique et volume d'ionisation micrométrique

Le premier concept de source d'ions à IE évalué est basé sur l'idée d'utiliser une **colonne électronique à émetteur thermoïonique** pour focaliser le faisceau d'électrons avec une énergie inférieure à 1 keV entre deux électrodes parallèles distantes de  $D_{RI} \leq 1 \text{ mm}$ . Ainsi un **volume d'ionisation micrométrique** est formé au-dessus d'une ouverture d'extraction d'ions avec un diamètre de  $d_{\text{Extr}} \leq 100 \text{ }\mu\text{m}$  (voir la figure 7.35). L'extraction du faisceau d'ions est perpendiculaire à l'axe de la colonne électronique. Le volume d'ionisation d'où sont extraits les ions peut être représenté par un petit cylindre de diamètre  $d_{VI}$ . La combinaison d'un volume d'ionisation micrométrique avec le bon choix de  $D_{RI}$  et de la différence en potentiel des électrodes  $\Delta V_{RI}$ , permet d'obtenir des faisceaux d'ions avec une **basse dispersion en énergie**. Par exemple pour des ions mono-chargés avec les paramètres  $D_{RI} = 1 \text{ mm}$ ,  $\Delta V_{RI} = 10 \text{ V}$  et  $d_{VI} = 100 \text{ }\mu\text{m}$  la dispersion en énergie est estimée à  $\Delta E = 1 \text{ eV}$ .

#### Simulations de particules chargées: Colonne électronique

Pour évaluer les performances de la source d'ions des **simulations de particules chargées ont été réalisées avec le logiciel SIMION**. La colonne électronique consiste en une région d'extraction avec un **filament de tungstène** à la pointe duquel sont générés les électrons, d'une première lentille unipotentielle pour paralléliser le faisceau d'électrons, suivi d'un déflecteur et enfin d'une deuxième lentille qui focalise le faisceau d'électrons au dessus de l'ouverture d'extraction d'ions au centre de la région d'ionisation.

La taille du point focal  $d_{\text{Focus}}$  a été déterminée pour différentes énergies du faisceau  $E_{e,\text{End}}$  à l'intérieur de la région d'ionisation, voir figure 7.36. L'énergie  $E_{e,\text{End}}$  est progressivement augmentée jusqu'à 1 keV et  $d_{\text{Focus}}$  est définie comme diamètre du volume d'ionisation cylindrique qui contient 50 % du courant total  $d_{\text{FW50}}$  (FW50: acronyme anglais de Full Width 50). Les résultats montrent qu'une réduction d'un facteur  $\approx 2$  est obtenu en augmentant  $E_{e,\text{End}}$  de 100 eV à 1 keV, où  $d_{\text{Focus}}$  est de  $95 \text{ }\mu\text{m}$ . La situation avec  $E_{e,\text{End}} = 1 \text{ keV}$  représente un bon compromis entre un petit point focal, donc un petit volume d'ionisation, et une bonne efficacité pour la génération d'ions par IE. Le courant électronique  $I_{e,\text{Extr}}$  est d'environ  $80 \text{ }\mu\text{A}$ , c'est une bonne approximation du courant qui entre dans la région d'ionisation.



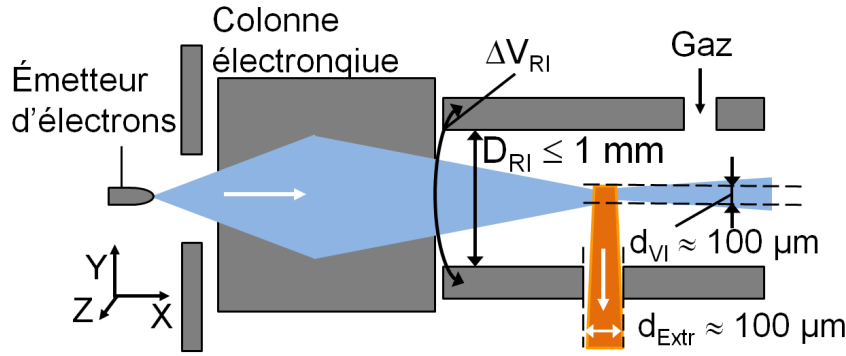


Figure 7.35: Illustration: source d'ions à IE et volume d'ionisation micrométrique.

### Simulations de particules chargées: Colonne ionique

De façon analogue à la focalisation du faisceau d'électrons, la **simulation du faisceau de particules chargées est fait pour une colonne ionique** composée de deux électrodes parallèles de la région d'ionisation ( $RI_1$ ,  $RI_2$ ) et de deux électrodes supplémentaires ( $Extr_1$ ,  $G$ ). Comme il est montré dans la figure 7.37, les ions sont générés dans un petit volume cylindrique au-dessus de l'ouverture d'extraction avec un diamètre légèrement plus grand que la taille du point focal du faisceau d'électrons de 1 keV. Ceci prend donc en compte qu'en réalité des aberrations dans la colonne électronique peuvent légèrement agrandir la taille du point focal et donc du volume d'ionisation. Une pression uniforme de  $p_{RI} = 0.1$  mbar est utilisée dans la région d'ionisation où un **simple modèle de collision de sphères dures** est pris en considération pour les collisions entre les ions et les particules du gaz. Aucun effet de collisions n'est pris en considération dans la colonne ionique pour obtenir une première estimation de la performance du concept de la source d'ions. Le courant ionique total d'ions produit dans le volume d'ionisation est déterminé en considérant le courant électronique  $I_e$ , la densité du gaz  $n_{Gaz}$ , la longueur  $L_{Gen}$  du volume d'ionisation et la section efficace d'ionisation par impact électronique  $\sigma_{IE}$  à 1 keV d'énergie. Un courant électronique  $I_e$  de 50  $\mu A$  est utilisé qui est inférieur aux 80  $\mu A$  déterminés dans le paragraphe précédent et prend en compte des pertes de transmission le long de la colonne électronique.

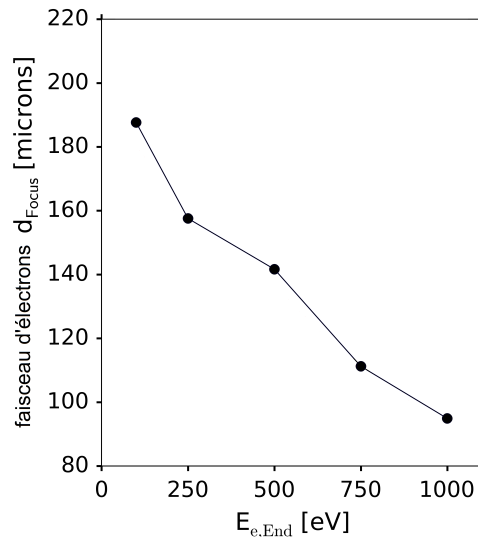


Figure 7.36: Résultats de la focalisation du faisceau d'électrons.

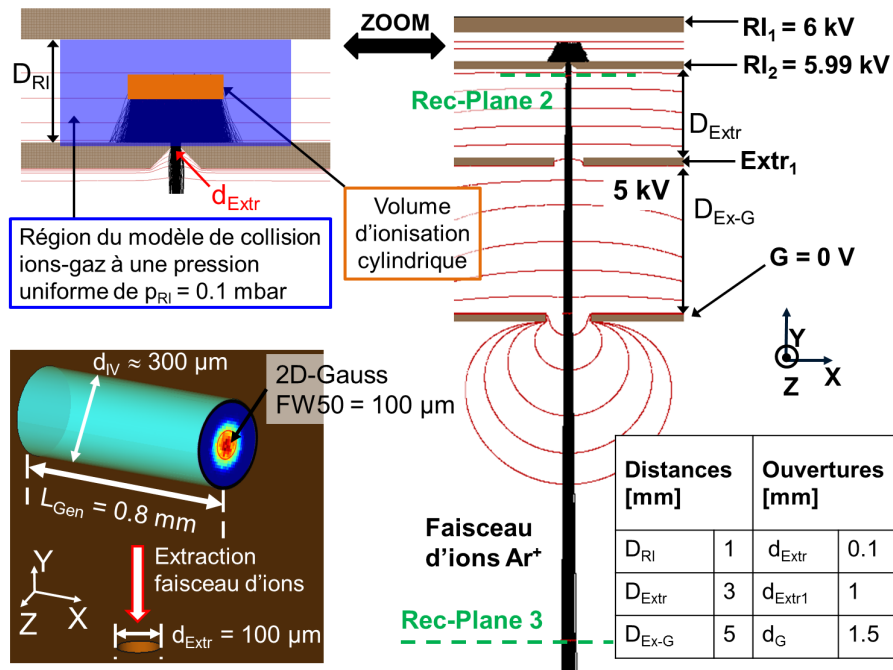


Figure 7.37: Illustration de l'extraction du faisceau d'ions  $\text{Ar}^+$  dans la colonne ionique.

Des simulations sont réalisées pour les ions  $\text{Ar}^+$ ,  $\text{Xe}^+$  et  $\text{O}_2^+$  en variant le potentiel de l'électrode d'extraction  $\text{Extr}_1$  et en gardant les autres potentiels fixés aux valeurs indiquées dans la figure 7.37. Une méthode d'extrapolation des trajectoires ioniques est utilisée à partir du plan XZ nommé Rec-Plane 3 le long de l'axe Y pour déterminer la taille de la source du faisceau d'ions  $d_{\text{Source}}$  (valeur minimale de  $d_{\text{FW50}}$  le long de l'axe Y) et de plus le demi-angle d'ouverture  $\alpha_{\text{Faisceau}}$ . En définissant  $d_{\text{Source}}$  comme  $d_{\text{FW50}}$  un facteur 0.5 est pris en compte pour calculer la brillance réduite avec l'équation 7.21. Les résultats déterminés sont représentés dans le tableau 7.3 et sont les valeurs moyennes de toutes les situations de potentiel évaluées pour chaque espèce d'ions. Dans tous les cas  $d_{\text{Source}}$  est inférieur à 15  $\mu\text{m}$  et  $\alpha_{\text{Faisceau}}$  est d'environ 15 mrad ( $\approx 0.9^\circ$ ). Le courant ionique est dans la gamme des 20 - 45 nA et **la brillance réduite se situe entre 50 - 65  $\text{A}/(\text{m}^2 \text{sr V})$  pour  $\text{Ar}^+$ ,  $\text{Xe}^+$  et  $\text{O}_2^+$ .**

Une façon d'augmenter la brillance réduite est de diminuer  $d_{\text{VI}}$  et donc  $d_{\text{Source}}$  tout en gardant un courant électronique similaire pour le processus d'ionisation. Ceci peut être réalisé en utilisant comme émetteur thermoionique un petit monocristal d'hexaborure de lanthane ( $\text{LaB}_6$ ). Des simulations avec la colonne électronique intégrant un  $\text{LaB}_6$  ont montré que  $d_{\text{VI}}$  peut être diminué d'un facteur 2.5 par rapport à l'utilisation du filament de tungstène. Des simulations correspondantes avec la colonne ionique ont été faites pour un faisceau d'ions  $\text{Ar}^+$  en adaptant la taille de l'ouverture d'extraction de  $d_{\text{Extr}} = 100 \mu\text{m}$  à 40  $\mu\text{m}$ . **La brillance réduite est augmentée d'un facteur proche de 3 pour obtenir  $B_r = 1.6 \cdot 10^2 \text{ A m}^{-2} \text{sr}^{-1} \text{V}^{-1}$  qui est encore toujours inférieur à l'objectif de  $B_r = 10^3 - 10^4 \text{ A m}^{-2} \text{sr}^{-1} \text{V}^{-1}$ .**

Espèce d'ions	$d_{\text{Source}}$ [ $\mu\text{m}$ ]	$\alpha_{\text{Faisceau}}$ [mrad]	$I_{\text{Ionique}}$ [nA]	$B_r$ [ $\text{A m}^{-2} \text{sr}^{-1} \text{V}^{-1}$ ]
$\text{Ar}^+$	11	14	29	54
$\text{Xe}^+$	13	14	43	63
$\text{O}_2^+$	9	15	21	61

Table 7.3: Résultats des simulations de la colonne ionique ( $I_e = 50 \mu\text{A}$ ,  $p_{\text{RI}} = 0.1 \text{ mbar}$ ).

Néanmoins ce résultat présente clairement une amélioration par rapport à  $B_r \approx 1 \text{ A}/(\text{m}^2 \text{ sr V})$  pour les sources conventionnelles à IE. L'évaluation de la dispersion en énergie  $\Delta E$  du faisceau d'ions d' $\text{Ar}^+$ , défini comme largeur à mi-hauteur, est déterminé à 0.4 eV en utilisant l'émetteur  $\text{LaB}_6$  et des résultats similaires peuvent être attendus pour les faisceaux de  $\text{Xe}^+$  et  $\text{O}_2^+$ . Ceci montre clairement que l'objectif de  $\Delta E \lesssim 1 \text{ eV}$  est atteint avec ce concept de source à IE.

### Considérations techniques

Un point critique est d'obtenir la basse pression de fonctionnement du  $\text{LaB}_6$  du côté émetteur de la colonne électronique,  $p_{\text{nécessaire}} < 10^{-6} \text{ mbar}$ . Un modèle mécanique a été conçu sur base duquel ont été réalisés des simulations de conductance de gaz et des mesures expérimentales. Les résultats ont montré que la pression du côté émetteur est d'environ  $1 \cdot 10^{-5} \text{ mbar}$  pour une pression d'azote de  $p_{\text{RI}} = 0.1 \text{ mbar}$ . Un résultat très similaire peut être attendu pour l'injection d'argon. En conclusion le fonctionnement d'un  $\text{LaB}_6$  au sein de la colonne électronique reste critique. Différentes méthodes ont été évaluées pour diminuer la pression dans la chambre de l'émetteur. Malheureusement, jusqu'à présent aucune solution a été trouvée pour réaliser ceci, avec une configuration compacte de la colonne électronique, tout en gardant la performance de la source déterminée dans le paragraphe précédent. À cause de ces difficultés et du fait que  $B_r \approx 2 \cdot 10^2 \text{ A m}^{-2} \text{ sr}^{-1} \text{ V}^{-1}$  est inférieur à la valeur minimum de notre objectif, nous avons décidé de ne pas construire un prototype de ce concept de source.

#### 7.4.3 Source d'ions radio-fréquence à impact électronique

Le deuxième concept de source d'ions est basé sur l'idée d'obtenir un faisceau ionique à fort courant avec une taille de source et un demi-angle d'ouverture similaire aux résultats du premier concept de source, mais en changeant l'interaction électron-gaz et la collection des ions. La figure 7.38 présente cette nouvelle structure; pour générer les ions un faisceau d'électrons à fort courant entre dans la région d'ionisation avec une énergie de 100 eV et est arrêté par les collisions avec le gaz et un champ décélérateur  $F_{e,\text{décél.}}$ .

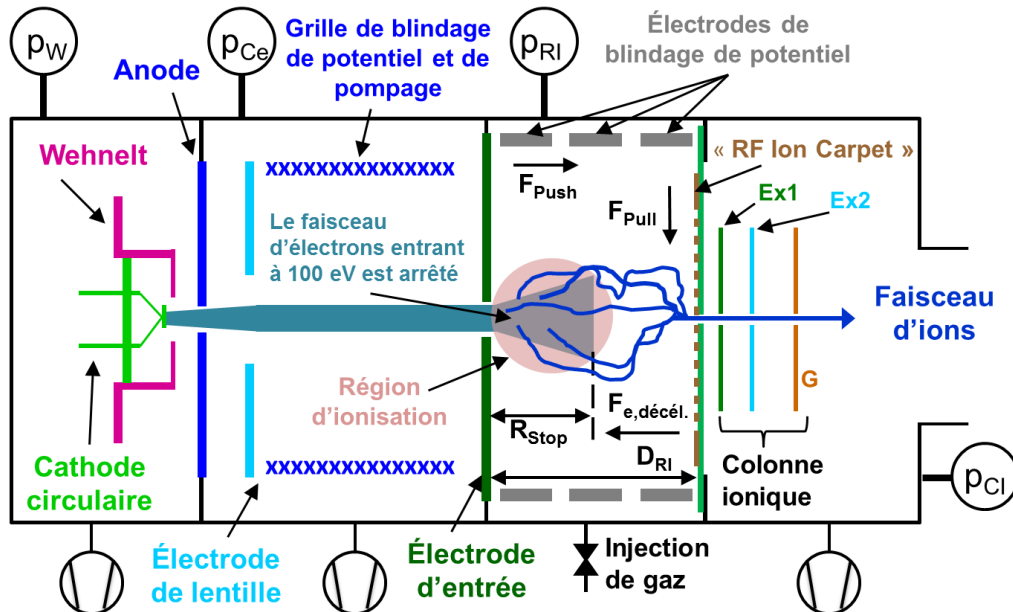


Figure 7.38: Illustration: source d'ions radio-fréquence à impact électronique.

Avec des électrons d'énergie inférieure ou égale à 100 eV, les sections efficaces par IE de la plupart des gaz atteignent leur maximum, ainsi une ionisation très efficace est obtenue dans un volume d'ionisation millimétrique. Un **élément spécial d'optique ionique radio-fréquence (RF) nommé « RF Ion Carpet »** est utilisé pour diriger et extraire efficacement les ions à travers d'un canal central.

Le type d'émetteur **thermoionique à fort courant** qui est utilisé est une **cathode circulaire d'iridium enduit d'ytterbium ( $\text{Y}_2\text{O}_3 - \text{Ir}$ )** [155], qui a l'avantage d'avoir une pression de fonctionnement inférieur à  $1 \cdot 10^{-4}$  mbar; le gradient de pression nécessaire à travers la colonne électronique est moins élevé que celui du premier concept de source d'ions évalué. Proche de la sortie du canal central du « RF Ion Carpet » une électrode d'extraction est positionnée avec un diamètre d'ouverture de  $d_{\text{Ex1}} = 100 \mu\text{m}$ . Cette disposition sélectionne que la partie centrale du faisceau d'ions ce qui permettra d'atteindre les objectifs en taille de source et de demi-angle d'ouverture du faisceau.

### Simulations de particules chargées: Colonne électronique

Des simulations de particules chargées ont été faites pour la colonne électronique illustrée sur la figure 7.38. Les électrons sont générés très près de la surface de la cathode circulaire. Une lentille unipotentielle composée de l'anode, de l'électrode de lentille et de la grille de blindage est utilisée pour paralléliser le faisceau d'électrons qui passe ensuite à travers l'électrode d'entrée de la région d'ionisation. La grille de blindage est nécessaire pour éviter les perturbations sur le faisceau d'électrons du potentiel nul du tube à vide. De plus la grille permet un pompage efficace de la colonne qui garantit le fonctionnement de la source. À l'aide des résultats des simulations il est estimé que le faisceau d'électrons à 100 eV passe dans la région d'ionisation avec un courant  $I_{e,0}$  maximal d'environ 400  $\mu\text{A}$  à travers une ouverture de 1.5 mm en diamètre.

### Simulations de particules chargées: Colonne ionique

**Deux configurations différentes du « RF Ion Carpet »** avec un canal central d'un diamètre de  $d_0 = 1 \text{ mm}$  ont été évaluées (voir figure 7.39). Pour le **Ion Carpet A** un potentiel RF est appliqué à l'électrode centrale (E1) pour obtenir une extraction très efficace des ions. Malheureusement un faisceau d'ions avec un large  $\Delta E$  est généré à cause d'une région d'extraction avec un potentiel non fixé. Pour cette raison la configuration du **Ion Carpet B** ne présente plus de signal RF sur l'électrode centrale (E1). L'Ion Carpet B crée des rendements d'extraction d'ions moins élevés comparé à l'Ion Carpet A, mais la dispersion  $\Delta E$  est inférieure. Pour les deux dispositifs les signaux RF appliqués sur les électrodes circulaires adjacentes à la face avant ont la même fréquence  $f_{\text{RF}}$  et amplitude  $V_{\text{Amp,RF}}$  mais ils sont déphasés de  $180^\circ$ . Un champ électrique  $F_{\text{Push}}$  créé dans la région d'ionisation pousse les ions vers le « RF Ion Carpet » et de plus un gradient DC est superposé aux signaux RF ce qui crée un champ électrique  $F_{\text{Pull}}$  qui tire les ions vers l'axe central.

**Les rendements d'extraction d'ions  $f_{\text{Extr}}$  ont été évalués** pour des ions d' $\text{Ar}^+$  en gardant la région d'ionisation à  $p_{\text{RI}} = 0.1 \text{ mbar}$ ,  $T_{\text{RI}} = 298.15 \text{ K}$ ,  $F_{\text{Push}} = 1 \text{ V/mm}$  et  $F_{\text{Pull}} \approx 1 \text{ V/mm}$ . Les collisions des ions avec les particules du gaz sont pris en considération à l'intérieur de la région d'ionisation mais aussi tout le long de la colonne ionique.

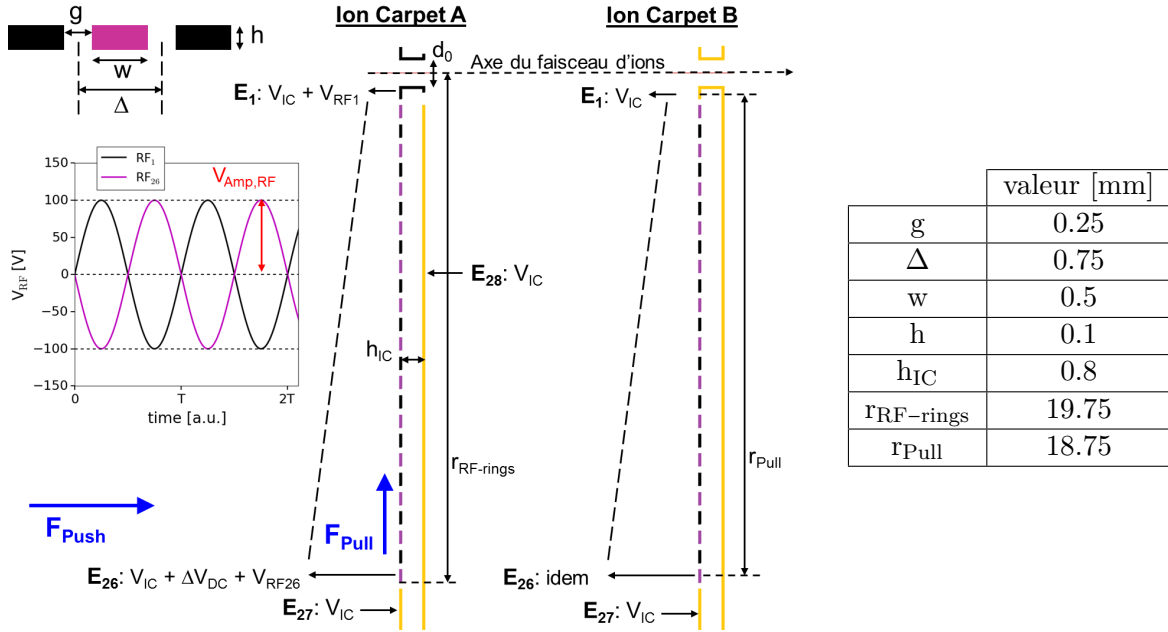


Figure 7.39: Illustration: configuration du Ion Carpet A et B, dimensions et potentiels appliqués.

Le gradient de pression le long de la colonne a été déterminé par des simulations de conductance de gaz comme approximation de la situation réelle dans le prototype de la source. En variant  $f_{RF}$  entre 1 - 12 MHz et  $V_{Amp,RF}$  entre 0 - 150 V le rendement d'extraction  $f_{Extr,Ar^+}$  peut atteindre jusqu'à  $\approx 80\%$  pour le cas du Ion Carpet A et jusqu'à  $\approx 50\%$  pour le cas du Ion Carpet B qui comme attendu mène à des valeurs de  $f_{Extr,Ar^+}$  plus basses que l'Ion Carpet A. Il est estimé qu'en utilisant un courant électronique de  $I_{e,0} = 400 \mu A$  le courant ionique total  $I_{Ar^+,total}$  généré dans le volume d'ionisation millimétrique est entre 200 et 300  $\mu A$ . Le courant du faisceau d'ions  $I_{ionique}$  est déterminé en multipliant  $I_{Ar^+,total}$  avec le facteur de transmission d'ions à travers l'électrode d'extraction Ex1. La taille de source et le demi-angle d'ouverture du faisceau ont aussi été estimés.

Différentes combinaisons de potentiels de la colonne ionique ont été évaluées pour la configuration des Ion Carpet A et B. Les résultats des simulations peuvent être trouvés dans le tableau 7.4 et représentent la valeur moyenne de toutes les combinaisons de potentiels évaluées. Le courant ionique est environ 2 à 3 fois plus élevé pour l'Ion Carpet A comparé à l'Ion Carpet B ce qui est dû à la différence du rendement d'extraction. La taille de source  $d_{Source}$  est pour les deux configurations proche de 60  $\mu m$ . En utilisant l'Ion Carpet B  $\alpha_{Faisceau}$  est légèrement plus grand comparé à l'utilisation du Ion Carpet A mais reste en dessous de 15 mrad. Globalement la configuration avec l'Ion Carpet A génère une brillance réduite de  $B_r \approx 5 \cdot 10^2 A m^{-2} sr^{-1} V^{-1}$  et celle avec l'Ion Carpet B  $B_r \approx 1 \cdot 10^2 A m^{-2} sr^{-1} V^{-1}$  principalement suite à une plus petite valeur de  $I_{ionique}$ . L'évaluation des distributions d'énergie du faisceau d'ions d' $Ar^+$  montre que comme prévu le cas du Ion Carpet A induit une large dispersion en énergie de  $\Delta E \approx 30 eV$  qui est clairement réduite en utilisant la configuration du Ion Carpet B qui donne  $\Delta E \approx 3 eV$ .

La performance de ce concept de la source d'ions en terme de brillance réduite est encore inférieure de l'objectif de  $B_r = 10^3 - 10^4 A m^{-2} sr^{-1} V^{-1}$ , dans le cas du Ion Carpet A la valeur est seulement d'un facteur 2 en-dessous du minimum ciblé. Malheureusement  $\Delta E$  est largement au-dessus de l'objectif de  $\Delta E \lesssim 1 eV$  et seulement le cas du Ion Carpet B permet d'atteindre presque cet objectif.

Ion Carpet	$d_{\text{Source}}$ [ $\mu\text{m}$ ]	$\alpha_{\text{Faisceau}}$ [mrad]	$I_{\text{Ionique}}$ [ $\mu\text{A}$ ]	$B_r$ [ $\text{A m}^{-2} \text{sr}^{-1} \text{V}^{-1}$ ]
A	61.0	12.5	8.7	$5.3 \cdot 10^2$
B	61.6	14.6	2.2	$9.5 \cdot 10^1$

Table 7.4: Résultats des simulations de la colonne ionique avec des ions d'Ar<sup>+</sup>  
( $I_{e,0} = 400 \mu\text{A}$ ,  $p_{\text{RI}} = 0.1 \text{ mbar}$ , gradient-pression-Ar).

### Considérations techniques

Des **calculs de conductance de gaz** ont été faits pour la colonne électronique en la considérant comme système isotherme à 298.15 K. Une combinaison de  $d_A = 0.8 \text{ mm}$  (ouverture de l'anode) et  $d_E = 1.5 \text{ mm}$  (ouverture de l'électrode d'entrée) génère une pression de  $p \approx 5 \cdot 10^{-6} \text{ mbar}$  proche de la cathode pour une pression  $p_{\text{RI}} = 0.1 \text{ mbar}$  dans le cas d'injection d'argon. Cette combinaison d'ouvertures a aussi été utilisée pour les simulations de particules chargées. La pression déterminée montre que le fonctionnement de la cathode est clairement réalisable. Il faut noter qu'en réalité la cathode sera à une température plus élevée lors du fonctionnement de la source qui induit une pression réelle légèrement plus élevée que l'estimation.

Des **simulations de conductance de gaz** ont été faites pour la **colonne ionique** pour pouvoir incorporer un gradient de pression lors des simulations de particules chargées correspondantes. Le résultat du gradient de pression pour l'injection d'argon montre que la pression dans la région proche de l'électrode d'extraction est déjà deux ordres de grandeur en-dessous de la pression de la région d'ionisation, soit  $10^{-3} \text{ mbar}$ .

### Investigations expérimentales

La figure 7.40 présente la réalisation mécanique complète 3D du prototype de la source d'ions radio-fréquence à IE. Le « RF Ion Carpet » utilisé est fabriqué comme un circuit imprimé et sa configuration est similaire à la configuration de l'Ion Carpet B simulée. Un circuit d'alimentation RF a été développé et il est principalement composé d'un générateur de formes d'onde arbitraires, d'un amplificateur RF et d'un transformateur.

Des mesures du courant électronique qui passe à travers l'électrode d'entrée avec  $d_E = 1.5 \text{ mm}$  ont montré qu'une valeur d'environ  $190 \mu\text{A}$  est atteinte. En injectant du gaz d'argon un courant total ionique de  $200 - 250 \mu\text{A}$  généré dans la région d'ionisation est déterminé avec  $p_{\text{RI}} = 0.1 \text{ mbar}$ . Ceci est en accord avec les résultats des simulations de particules chargées qui ont montré que quelques centaines de  $\mu\text{A}$  peuvent être atteint.

L'utilisation du « RF Ion Carpet » a été évaluée en mesurant le courant ionique qui heurte l'électrode d'extraction  $\text{Ex1 } I_{\text{Ar,Ex1}}$  et le courant du faisceau d'argon  $I_{\text{Faisceau,Ar}}$  transmis à travers l'électrode d'extraction. Pour ces mesures les potentiels de la région d'ionisation étaient d'environ  $500 \text{ V}$  et seulement quelques dizaines de  $\mu\text{A}$  de courant électronique entrent dans la région d'ionisation. Ces paramètres permettent un fonctionnement stable de la source pour une pression de  $p_{\text{RI}} = 0.1 \text{ mbar}$ . Les conditions suivantes ont été utilisées pendant les mesures de courant ionique:  $F_{\text{Push}} = 1 \text{ V/mm}$ ,  $\Delta V_{\text{DC}} = 19 \text{ V}$ ,  $F_{\text{Pull}} \approx 1 \text{ V/mm}$  et  $d_{\text{Ex1}} = 100 \mu\text{m}$ . L'évaluation des effets de l'application des signaux RF sur  $I_{\text{Ar,Ex1}}$  et  $I_{\text{Faisceau,Ar}}$  a été faite jusqu'à une fréquence  $f_{\text{RF}} = 12 \text{ MHz}$  et l'augmentation du courant ionique par rapport à la situation sans signal RF a pu être mesurée sur toute la gamme de fréquence couverte.

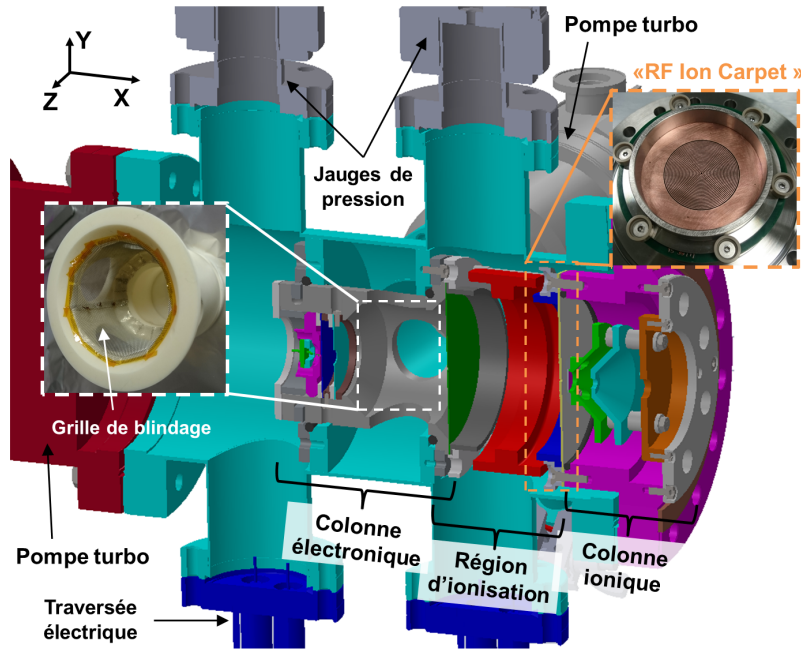


Figure 7.40: Réalisation mécanique de la source d'ions radio-fréquence à impact électronique.

La valeur stable la plus élevée de  $I_{Ar,Ex1}$  est obtenue à 8 MHz et  $V_{Amp,RF} \approx 50$  V avec 84 nA, ceci correspond à une augmentation d'un facteur 12 comparé à la situation sans RF. Le courant du faisceau d'argon  $I_{Faisceau,Ar}$  correspondant se situe entre 1.5 et 2 nA. Le cas de  $f_{RF} = 8$  MHz produit une très faible puissance réfléchi dans le système de génération du signal RF et représente donc un bon choix pour faire une adaptation de l'impédance de charge à la sortie du transformateur. Le bénéfice d'une telle adaptation est qu'il sera possible d'augmenter davantage la valeur maximale de l'amplitude RF appliquée et ainsi d'augmenter aussi  $I_{Faisceau,Ar}$ .

La brillance réduite de  $B_r \approx 10^2$  A/(m<sup>2</sup> sr V) déterminée par simulation est principalement basée sur le fait que des courants ioniques dans la gamme du  $\mu$ A peuvent être extraits de la région d'ionisation ce qui génère des hautes valeurs de  $I_{Faisceau,Ar}$ . Actuellement, cette valeur de courant n'est pas atteinte expérimentalement. Des optimisations pour améliorer la performance de la source ont été identifiées et vont être intégrés dans le futur pour atteindre  $B_r \approx 10^2$  A/(m<sup>2</sup> sr V).

#### 7.4.4 Conclusions finales et perspectives

- L'évaluation du premier concept de la source d'ions à IE utilisant un volume d'ionisation micrométrique a montré qu'avec une colonne électronique qui intègre un émetteur LaB<sub>6</sub> une brillance réduite  $B_r \approx 2 \cdot 10^2$  A/(m<sup>2</sup> sr V) et une dispersion en énergie de  $\Delta E < 0.5$  eV est obtenue pour des faisceaux d'Ar<sup>+</sup>, Xe<sup>+</sup> ou O<sub>2</sub><sup>+</sup>. Avec une telle performance le concept est comparable aux sources Duoplasmatrons avec  $B_r = 10^2 - 10^3$  A m<sup>-2</sup> sr<sup>-1</sup> V<sup>-1</sup> en ayant même une plus faible dispersion en énergie ( $\Delta E$  des Duoplasmatrons 5 - 20 eV). Il est estimé qu'avec une colonne électronique mieux optimisée pour l'utilisation du LaB<sub>6</sub> et une combinaison d'une seule région d'ionisation et de plusieurs colonnes électronique, il devient possible d'améliorer les performances de ce concept de source. Néanmoins un des points critiques pour la réalisation d'un prototype reste le gradient de pression nécessaire pour faire fonctionner les LaB<sub>6</sub> dans des conditions stables. Après avoir fait les investigations détaillées de ce concept de source nous pouvons dire qu'atteindre une brillance réduite de  $B_r \geq 1 \cdot 10^4$  A/(m<sup>2</sup> sr V) sera très difficile. Pour ceci une réalisation mécanique devrait

permettre d'obtenir une taille de source pour le faisceau d'ion  $< 1 \mu\text{m}$  et ainsi l'utilisation de techniques de fabrication conventionnelles n'est plus adaptée car les dimensions de la région d'ionisation devront aussi être sub-micrométriques.

- Pour le concept de la source d'ions radio-fréquence à IE il a été montré par simulation qu'en intégrant dans la région d'ionisation un « RF Ion Carpet » qui n'applique pas de signal RF au canal central métallisé il est possible d'atteindre des rendements d'extraction d'ions de quelques dizaines de pourcent. La performance de la source est autour de  $B_r \approx 10^2 \text{ A}/(\text{m}^2 \text{ sr V})$  avec une dispersion d'énergie de  $\Delta E \approx 3 \text{ eV}$  pour des ions  $\text{Ar}^+$ . Cette performance est de nouveau comparable aux sources Duoplasmatrons en terme de brillance réduite en ayant une plus faible dispersion en énergie. Malheureusement, les mesures expérimentales avec le prototype ont montré que le courant ionique extrait est encore en-dessous de la gamme du  $\mu\text{A}$  attendue sur base des résultats de simulations. L'augmentation de la performance du concept de source radio-fréquence à IE vers la gamme de  $B_r = 10^3 - 10^4 \text{ A}/(\text{m}^2 \text{ sr V})$  tout en gardant  $\Delta E$  de quelques eV, peut probablement être réalisée en utilisant une configuration du « RF Ion Carpet » intégré dans le prototype qui est une fusion du Ion Carpet A et B. De même en diminuant le diamètre du canal central parallèlement à une réduction du diamètre de l'électrode d'extraction les performances du concept peuvent être optimisées. Par contre en vue de toujours obtenir un courant ionique raisonnable il sera nécessaire de choisir avec prudence le rapport longueur/diamètre du canal.



## 8 Glossary

Abbreviation	Meaning
AFG	Arbitrary Function Generator
AFM	Atomic Force Microscopy
ALIS	Atomic Level Ion Source
ASCII	American Standard Code for Information Interchange
CAD	Computer Aided Design
CI	Coulomb Interactions
CP	Copper Plate
CPO	Charged Particle Optics
CsBr - screen	Caesium Bromide screen
CSDA	Continuous Slowing Down Approximation
CVD	Chemical Vapour Deposition
DC	Direct Current
DUV LED	Deep UltraViolet Light-Emitting Diode
e-beam	Electron beam
e-Column	Electron column
e-Gun	Electron gun
EI	Electron Impact
EIRFIS	Electron Impact Radio Frequency Ion Source
ESA	Electrostatic Sector Analyser
FC	Faraday Cup
FDM	Finite Difference Method
FIB	Focused Ion Beam
FIBAE	Focused Ion Beam Assisted Etching
FIBID	Focused Ion Beam Induced Deposition
FOFEM	First Order Finite Element Method
FW50	Full Width 50
FWHM	Full Width Half Maximum
GFIS	Gas Field Ionisation Source
GO-film	Graphene Oxide film
GU	Grid Units
HIM	Helium Ion Microscope
IC	Ion Carpet
IMFP	Inelastic Mean Free Path
IV	Ionisation Volume
LEIS	Low Energy Ion Scattering
LMIS	Liquid Metal Ion Source
MC	Monte Carlo
MCP	Multi Channel Plates
ML	MonoLayer
MOTIS	Magneto-Optical Trap Ion Source
MRTOF-MS	Multi Reflector Time-Of-Flight Mass Spectrometer

Abbreviation	Meaning
MSA	Magnetic Sector Analyser
NAIS	Nano-Aperture Ion Source
PA	Potential Array
PCB	Printed Circuit Board
QMS	Quadrupole Mass Separator
RAM	Read-Access-Memory
RF	Radio Frequency
ROC	Radius Of Curvature
SCC	Single Collision Condition
SE	Secondary Electrons
SEM	Scanning Electron Microscope
SI	Secondary Ions
SIM	Scanning Ion Microscope
SIMS	Secondary Ion Mass Spectrometry
SOFEM	Second Order Finite Element Method
SREM	Stopping and Range of Electrons in Matter
STEM	Scanning Transmission Electron Microscopy
STL-file	STereoLithography-file
TEM	Transmission Electron Microscopy
TVS	Transient Voltage Suppression
VE	Virtual Electrode

Symbol	Meaning
A	Atomic number
$A_E$	Entrance cross sectional area
$A_{\text{Extr}}$	Effective electron extraction area
$A_F, A_S$	Facet and surface area (Molflow+)
$A_{\text{Gen}}$	Electron generation area
$A_L, A_{\text{SpLA}}, A_{\text{SpAW}}, A_A, A_W,$ $A_{\text{Open,W,pump-holes}}$	Cross-sectional areas used during the gas conductance calculations/simulations (EIRFIS; section 5.4.1 and 5.4.2)
$A_R$	Richardson constant
$A_{\text{Surface-Ellipsoid}}$	Surface area of ellipsoid
$A_{\text{Source}}$	Source area
a, b and c	half axes values of ellipsoid
$a_1, a_2, b_1, b_2, g_1, g_2$ and G	Deviates used in Box-Muller method
$\alpha_{\text{half}}, \alpha_{\text{Ion-beam}}$	half-opening angle and ion beam half opening angle
$\alpha_{\text{Inc}}$	Incidence angle of particle beam
$\alpha_0$	Particle trajectory angle
$\alpha_x, \alpha_y$	transverse beam angle in x- and y-direction
B	Brightness
$\vec{B}$	Magnetic field vector
$B_r, B_{r,\text{Ion-beam}}$	Reduced brightness and ion beam reduced brightness
$\beta, \gamma, C$ and D	Parameters for the determination of the inelastic mean free path within elemental solids
c	Speed of light
$C_{\text{chr}}, C_{\text{sph}}$	Chromatic and spherical aberration coefficient
$C_{\text{Vac,Chamber}}, C_{\text{V81,eC}}, C_{\text{pump-hole,eC}},$	Conductances used in the experimental gas conductance measurement section 4.4.2
$C_{12}, C_{\text{mol}},$ $C_{\text{mol,arb,cyl-tube}}, C_{\text{mol,cir-aperture}},$ $C_{\text{mol,cyl-elbow90}}, C_{\text{Total}}, C_i, C_{\text{element}}$	Conductances used in the vacuum technology theory section (see section 3.3)
$C_1, C_2, C_3, C_4, C_{\text{eC,pumphole}}, C_{\text{eC,total}},$ $C_{\text{V81,eC}}, C_{\text{V301,P}}, C_L, C_{\text{SpLA}}, C_{\text{SpAW}},$ $C_W, C_A$	Conductances used during the gas conductance calculations/simulations (EIRFIS; section 5.4.1 and 5.4.2)
$C_{\text{Opening}}$	Conductance of an opening
d	Diameter
$d_{\text{characteristic}}$	Characteristic length within a vacuum structure
$D_C$	Critical distance
$d_C, d_W, d_{W2}, d_A, d_I, d_L, d_{\text{e-Shield}}$	Diameters used for the e-Column CPO simulations (EIRFIS; section 5.2.1)
$D_{\text{critical}}$	Critical voltage breakdown distance

Symbol	Meaning
$D_{AL}, D_{LI}, D_{CA}, D_{CW}, D_{IC}, D_{e-Shield,I}$	Distances used for the e-Column CPO simulations (EIRFIS; section 5.2.1)
$D_{EA}$	Distance between emitter and anode
$d_{Extr}$	Ion extraction aperture diameter
$D_{Extr}, D_{Ex,G}$	Distance between electrode IR2 and Extr <sub>1</sub> , Extr <sub>1</sub> and ground electrode (section 4.2)
$d_F$	Filament diameter
$d_{Focus}$	Beam focus
$d_{FW50}, d_{FW90}, d_{FW95}$	Full width 50, Full width 90 and Full width 95 diameter
$d_{FW50,Ion-beam}$	Full width 50 diameter of ion beam
$d_{FW50,Rec-Plane}$	Full width 50 diameter of ion beam at Rec-Plane (EIRFIS concept)
$D_{FA}, D_{WA}$	Distance between filament and anode, Wehnelt and anode
$D_{Grid}, d_{Grid}$	Copper grid outside and inside diameter
$d_{Extr}, d_{Extr1}, d_G$	Ion column aperture diameters of the electrodes IR2, Extr1 and ground (section 4.2)
$d_{IR}, d_{Ex1}, d_{Ex2}, d_G, d_0, d_{RF-rings}$	Diameters used within the ion column CPO simulations (EIRFIS concept; section 5)
$D_{IR}, D_A, D_B, D_{Ex}, h_{IC}$	Distances used within the ion column CPO simulations (EIRFIS concept; section 5)
$d_{IS}$	Ion beam source size
$d_{IV}$	Ionisation volume diameter
$D_{L1}, D_{LD}, d_1, d_{1b}, d_2, d_3, d_D, l_{Lens1}, l_{Lens1b}$	Geometrical parameters for distances, diameters and lengths within the e-Column setup (section 4.2)
$d_m$	Molecular diameter
$D_{Plates}$	Parallel plate spacing within the ionisation region
$d_S, D_s, h, \alpha$	Parameters of the truncated cone ionisation volume
$d_{VS,simul}$	Simulated virtual source diameter
$d_{Virtual,Aperture}$	Diameter of virtual aperture
$d_W$	Wehnelt hole diameter
$\delta_{i,i+1},$	Parameter used in total conductance calculation for a series connection of several elements with varying cross section
$\Delta$	Pitch distance (Ion carpets)
$\Delta_{bars}, b_W$ and $h_W$	Copper grid bar spacing, bar and hole width
$\Delta E$	Energy spread (difference)
$\Delta p$	Pressure difference
$\Delta r_{chr}, \Delta r_{sph}$	Chromatic and spherical aberration disc radius

Symbol	Meaning
$\Delta V_{\text{Bias}}$ or $\Delta V_{\text{bias}}$	Potential difference between Wehnelt and emitter
$\Delta V_{\text{CA}}$	Potential difference between cathode and anode
$\Delta V_{\text{CP-I}}, \Delta V_{\text{C-I}}, \Delta V_{\text{eShield-I}}, \Delta V_{\text{Shield2-I}}, \Delta V_{\text{Ex1-IC}}, \Delta V_{\text{DC,i}}$	Potential differences used within the experimental investigation section 5.5 (EIRFIS)
$\Delta V_{\text{Plates}}$	Potential difference of ionisation region plates
$\Delta V_{\text{EA}}, \Delta V_{\text{Extr}}$	Potential difference between emitter and anode, extraction potential difference
$\Delta V_{\text{IG}}, \Delta V_{\text{DC}}, \Delta V_{\text{IC-Ex1}}, \Delta V_{\text{Ex1-Ex2}}, \Delta V_{\text{rings}}$	Ion column potential differences used within CPO simulations (EIRFIS; section 5.2.2 to 5.3.2)
$\Delta V_{\text{WC}}$	Potential difference between Wehnelt and Cathode
$\Delta X$	Difference/distance of two YZ-planes in X-direction
$dX$	Step size in X-direction
$e$	Elementary charge
$\vec{E}$	Electric field vector
$E$ and $E_p$	Energy and bulk plasmon energy
$E_{\text{Beam}}$	Beam energy
$E_{\text{e-beam}}$	Electron beam energy
$E_{\text{e,CP}}$	Electron beam current at copper plate
$\epsilon_0$	Electric constant
$E_{\text{e,0}}$	Electron beam start energy
$E_{\text{e,End}}$	Electron beam end energy
$E_{\text{field}}, E_{\text{Field}}, E_1, E_2$	Electric field strengths
$E_i$	Electrode i
$E_{\text{I,i}}$	Energy of ion number i
$E_r, E_z$	Radial and axial electric field component
$E_{\text{Total}}, E_{\text{kinetic}}$	Total and kinetic energy
$E(X_0), E(\Delta X)$	Energy at position $X_0$ and $\Delta X$
$E_{\text{slice-i,Out}}, E_{\text{slice-i,In}}, E_{\text{slice-(i+1),In}}, E_{\text{slice-i,mean}}$	Energies used during the ionisation volume slice-approach (EIRFIS; section 5.3.1)
$\mathcal{E}, \mathcal{E}_{\text{x,norm}}, \mathcal{E}_{\text{y,norm}}$	Emittance and normalised transverse emittances
$F, W, A, L_{1\text{Mid}}, L_{1\text{End}}, A_{\text{Defl.}}, B_{\text{Defl.}}, C_{\text{Defl.}}, D_{\text{Defl.}}, L_{2\text{Start}}, L_{2\text{Mid}}$	Symbols used to describe electrodes within the electron column setups (section 4.2)
$f, f_v$	General and gas speed distribution function
$f_A$	Focal length
$F_{\text{Damp}}$	Damping factor (Ion carpets)
$F_{\text{Deflection}}$	Deflection force magnitude

Symbol	Meaning
$F_E$	Electrical field magnitude
$f_{\text{ellipse,axis}}$	Size ratio of ellipse axes
$f_{e,CP}, f_{\gamma_{\text{sec-e,Lit}}}$	Factors used within the EIRFIS experimental investigation section 5.5
$f_{\text{Extr}}, f_{e,\text{Extr}}, f_{\text{Extr,Ion}}, f_{\text{Extr,Ar}^+}, f_{\text{Extr,slice-i}}, f_{\text{Extr,slice-i,Ar}^+}$	Extraction factor in general; electron beam and ion beam/ $\text{Ar}^+$ extraction factor; Extraction factors from slice-i (EIRFIS)
$f_M$	Material factor
$f_{OR}$	Over-relaxation correction parameter
$F_{\text{Push}}, F_{\text{Pull}}$	Electric push and pull field strength (Ion carpets)
$F_{\text{Rep}}$	Repelling force strength (Ion carpets)
$F_{e,\text{retard}}$	Retarding field strength for e-beam
$f_{RF}$	Radio frequency signal frequency
$F_{\text{Stick}}$	Sticking factor in Molflow+
$f_{e,\text{Tr}}, f_{\text{Ar}^+,\text{Tr}}$	Electron beam and $\text{Ar}^+$ transmission factor
$\phi$	Work function
$\varphi(z)$	Axial potential
$\gamma_{SI}$	Secondary Ion emission coefficient
$\gamma_{SE}, \gamma_{\text{sec-e}}$	Secondary Electron emission coefficients
$g$	Gap size (Ion carpets)
$H$	Cathode height
$h$	Planck constant
$h$ and $W$	Height and width
$ I_{CP} ,  I_{e,\text{Tr}} ,  I_{e,\text{Emission}} ,  I_{CP,\text{No-gas}} ,  I_{\text{sec-e}} ,  I_{e,0} , I_{CP,\text{No-gas}}, I_{\text{Total,CP}}, I_{\text{Ion-beam,Ar}}, I_{\text{Ions,Ar}}, I_{\text{Ar,Ex1}}$	Current values used within the EIRFIS experimental investigation section 5.5
$I_{e,\text{Extr}}, I_{e,\text{Tr}}$	Extracted and transmitted electron current
$I_e, I_{\text{Ion,Total}}, I_{\text{Ion,beam}}, I_{a,\text{Ar}}$	Electron, total ion, ion beam and axial Argon ion beam current
$I_{e,0}, I_{e,\text{slice-i,Out}}, I_{e,\text{slice-i,In}}, I_{e,\text{slice-i,mean}}, I_{e,\text{slice-(i+1),In}},$	Electron currents used during the slice-approach for the ionisation volume in order to calculate the total generated ion current (EIRFIS; section 5.3.1)
$I_{\text{slice-i,Ar}^+}, I_{\text{Extr,slice-i,Ar}^+}$	$\text{Ar}^+$ ion current generated within and extracted from slice-i (EIRFIS; section 7.3)
$I_{\text{Ion,IV}}$	Total ion current within the ionisation volume
$I_{\text{Ion,total}}, I_{\text{Ion,Ex1}}, I_{\text{Ar}^+,\text{total}}, I_{\text{Ar}^+,\text{Ex1}}$	Total ion currents and ion currents at the extraction aperture Ex1 (EIRFIS; section 5)
$I_{\text{Ion,transmitted}}$	Transmitted ion beam current
$I_T, I_0$	Primary and transmitted electron beam current
$J_{e,\text{thermionic}}, J_{e,\text{Schottky}}$	Thermionic and Schottky current density

Symbol	Meaning
$J_{\text{Ion-beam}}$	Ion beam current density
$J_{\text{LC}}$	Space charge limited current density
$K_A, K_B$	Parameters related to the gas conductance calculations for the EIRFIS prototype
$K_{2\text{DGauss},50}$	Constant used for 2D elliptical Gaussian
$k_B$	Boltzmann constant
$K, K_0$	Ion mobility and reduced ion mobility
$K_n$	Knudsen Number
$\kappa, \zeta, Q_d, Q_{pr}$	Parameters used for the stability region evaluation of ion carpets
$L_{\text{Drift}}, L_{\text{UF}}$	Length of drift space and uniform field region
$L_{\text{Gen}}$	Ion generation length
$l$	Length
$\lambda_{\text{IMFP}}, \lambda_{\text{free,gas}}$	Inelastic mean free path, gas inter-particle collisional mean free path
$M$	Molecular mass
$M_A, M_{\text{Drift}}, M_{\text{UF,para}}$	Aperture, drift space and uniform field (paraaxial case) matrix
$m, \Delta m$	Mass and mass difference
$m_e$	Electron mass
$m_{\text{Gas}}$	Gas particle mass
$m_I$	Ion mass
$M_L$	Linear magnification
$m_0, m_{\text{CP}}$	Particle rest mass and charged particle mass
$N_{\text{Gen,Ion}}, N_{\text{Extr,Ion}}$	Total generated and total extracted ion number
$N_{\text{Hits,S}}, N_{\text{MC}}$	Number of hits on surface, number of MC-particles (Molflow+)
$N_{\text{Ions,gen}}, N_{\text{Ions,Ex1}}, N_{\text{Ions,gen,slice-i}}, N_{\text{Ions,Ex1,slice-i}}$	Total number of ions generated within the ionisation volume and extracted through the central carpet hole; Number of generated ions within and of extracted ions from slice-i (EIRFIS, section 5.2.2 and 7.3)
$N_{\text{Plane,End}}$	Maximal number of planes in trajectory extrapolation
$n, n_{\text{Gas}}$	Particle and gas particle density
$N_{\text{rings}}$	Number of ring electrodes
$\eta$	Dynamic viscosity
$\Omega$	Solid angle
$\Omega_{\text{Ion-beam}}$	Ion beam solid angle
$\phi, \Phi_{1,i}$	Work function and first ionisation potential
$\Phi$	Scalar potential
$P, P_{\text{mol,elbow}90^\circ}$	Particle pass probabilities
$P_i$	Particle pass probability of element i

Symbol	Meaning
$p, p_1, p_2, p_i$	Pressures
$(p \cdot d)_{\text{critical}}$	Critical product of pressure and distance related to voltage breakdowns and Paschen curves
$PW_{\text{needed}}, PW_{\text{optimised}}, PeC$	Pressures used in the experimental gas conductance measurement of section 4.4.2
$p_{\text{Calc}}$	Calculated pressure in Molflow+
$p_{\text{Cross}}, p_{\text{IR,max-stable}}$	Pressures used within the experimental investigation section (EIRFIS; section 5.5)
$PeC_{\text{In}}, PeC_{\text{Out}}, PW, PP, p_{\text{Ex1-Ex2}}, p_{\text{Ex2-G}}, p_{\text{add-VacTube}}$	Pressures related to the gas conductance calculations/simulations for the EIRFIS prototype
$p_I, p_W$	Ionisation and Wehnelt chamber pressure
$p_{\text{Inlet}}$	Ionisation region pressure
$p_{\text{IR}}, p_{\text{IC}}, p_{\text{IC-d}_0}, p_{\text{IC-Ex1}}$	Ionisation region pressure, ion column pressure, pressure within the central ion carpet hole, pressure between the ion carpet and the Ex1 electrode (EIRFIS; section 5)
$Pot_{\text{Ion}}$	Potential at local ion position
$P_{\text{Output}}, P_{\text{RF,FWD}}, P_{\text{RF,BWD}}$	Powers used within the experimental investigation section (EIRFIS; section 5.5)
$P_{\text{Stop}}$	Stopping power
$p_0$	Standard pressure
$p_x, p_y, p_z$	Momentums in x-, y- and z-direction
$\chi, \psi$	Angle values for torus segment generation
$q$	Charge
$q_{Li}$	Charge of ion number i
$q_{pV}, q_{1in}, q_{1out}, q_{2in}, q_{2out}, q_{iout}$	pV-flows
$q_{In}, q_1, q_2, q_3, q_4$	pV-flows (gas conductance calculations/simulations EIRFIS)
$q_n$	Charge of a n-times ionised ion
$q_{\text{Ion}}$	Ion charge
$Q_{\text{outgassing}}$	Total outgassing in Molflow+
$r, r_{dX}, r_S, R_S, r_{\text{rand}}, u_{\text{rand}}, v_{\text{rand}}, t_{\text{rand}}, \theta_{\text{rand}}$	Radii values and random parameters/radom ion positions related to the truncated cone ionisation volume (EIRFIS; section 5)
$R, r, r_1, r_2, r_{\text{End}}, r_{\text{Start}}$	Radii values
$r', r'_1, r'_2, r'_{\text{End}}, r'_{\text{Start}}$	Particle trajectory slopes
$r_A, r_B$	Radius of particle species A and B
$\rho, \rho_0, \rho_C$	Density, standard density and charge density
$R_{\text{Ex}}, R_{\text{Ex,Fit}}$	Extrapolated and fitted extrapolated range



Symbol	Meaning
$r_{\text{eff, Extr}}$	Effective emission area radius
$r_{\text{e-beam, 90\%, inlet}}$	90 % e-beam radius at the inlet electrode
$r_{\text{FW50}}, r_{90}$ and $r_{\text{max}}$	Full Width 50 radius, 90 % radius and maximal radius
$r_i, r_{2i}$	Individual particle radius values
$r_{\text{Pull}}$	Radius/distance over which the pull field is applied
$\bar{R}$	Universal gas constant
$R_{\text{Stop}}$	Stopping range
$S, S_{\text{eff}}$	Pumping speed and effective pumping speed
$S_{\text{eff, W}}, S_{\text{eff, pump-hole}}, S_{\text{eff, outside, eC}}, S_{V1001}, S_{V81}$	Pumping speeds and effective pumping speeds used in the experimental gas conductance measurement section 4.4.2
$S_{\text{eff, P}}, S_{\text{eff, eC}}, S_{\text{eff, IC}}, S_{V81}, S_{V301}, S_{V361}$	Pumping speeds and effective pumping speeds used during the gas conductance calculations and simulations (EIRFIS; section 5.4.1 and 5.4.2)
$S_{\text{PLA}}, S_{\text{PAW}}$	Spacer label for the gas conductance model of the EIRFIS e-Column
$\sigma$ and $\mu$	Standard deviation and mean value of the normal distribution function
$\sigma_{\text{C}}, \sigma_{\text{t}}, \sigma_{\text{Individual}}, \sigma_{\text{EI}}$	Electron impact counting, total, individual (partial) and general cross section
$\sigma_{\text{t, slice-i}}, \sigma_{\text{Individual, slice-i}}, \sigma_{\text{Ar}^+}$	Total/individual electron impact cross section within slice-i; individual electron impact cross section for $\text{Ar}^+$ (EIRFIS; section 5)
$t$	Time
$T, T_{\text{Operating}}, T_{\text{MP}}$	Temperature, operating and melting point temperature
$T_{\text{IR}}$	Ionisation region temperature
$T_0$	Standard temperature
$\text{Tr}_{\text{Graphene}}$ and $t_{\text{Graphene}}$	Graphene film transmission and graphene film thickness
$\text{Tr}_{\text{exp}}, \text{Tr}_{\text{Grid}}, \text{Tr}_{\text{theo}}, \text{Tr}_{2\text{ML-graphene}}$	Transmissions used in the graphene grid e-beam transmission paragraph of section 4.4.2
$t$ and $u$	Variables used for the boundary matching technique
$\Theta$	Beam incident angle between surface normal and beam axis
$\vec{v}, v$	Velocity and speed
$V_{\text{Accel}}, V_{\text{Ion, Accel}}$	Acceleration and ion acceleration potential
$V_{\text{A}}, V_{\text{B}}$	Aperture and beam potential
$V_{\text{Amp, RF}}, V_{\text{Amp, RF, i}}$	Radio frequency signal amplitudes

Symbol	Meaning
$V_{\text{Bottom}}$	Bottom plate potential
$V_{\text{Beam}}$	Beam potential
$v_x, v_y, v_z$ and $v$	Gas particle velocity components and speed
$V_i$	Potential value at location $Y_i$
$V_I, V_{IC}, V_{DC,E_i}, V_{E_i}, V_{RF_i}, V_{S1}, V_{S2}, V_{S3}, V_A, V_L, V_{VT}, V_{e\text{-Shield}}$	Potentials used within the e-Column and ion column CPO simulations (EIRFIS; section 5.2.1 to 5.3.2)
$V_{\text{Inlet},S1}, V_{\text{CP},S3}$	Potentials used within the experimental investigation section (EIRFIS; section 5)
$v_{\text{mean}}$ and $v_{\text{mp}}$	Mean and most probable speed
$v_{\text{mean},BG}$	Background gas mean velocity
$v_i$	velocity component ( $i = x, y$ or $z$ )
$V_{\text{Top}}$	Top plate potential
$V_1, V_2, V_3$	Electrode potentials
$V_{P0}, V_{P1}, V_{P2}, V_{P3}, V_{P4}, V_{P5}, V_{P6}$	Grid points potential values
$w_{Z,\text{Focus}}, w_{Y,\text{Focus}}$	Ellipse axis sizes of e-beam focus
$w$	Width of ion carpet electrodes
$x, y, z$	Coordinates or directions
$X_1, X_2, Y_1, Y_2, Z_1, Z_2$	Coordinates used in trajectory extrapolation explanation
$X_0$	Starting X-position
$X_{\text{ion}}, Y_{\text{ion}}, Z_{\text{ion}}$	Ion starting positions
$X_{\text{IR},\text{MID}}$	X-position of ionisation region middle
$Y_{\text{gu}}, Y_{\text{gu1}}, Y_{\text{gu2}}, Y_{\text{gu}}$	Grid unit coordinates used for the boundary matching technique
$Y_i$	Location at which ion $i$ has been created
$Y_S$	Sputtering Yield
$Y_0$	Y-Position of centre of ionisation region
$Y_{\text{Axis},\text{IR}}$	Ion beam axis and ionisation region PA Y-Axis
$Z$	Atomic number
$Z_{\text{gu}}, Z_{\text{gu1}}, Z_{\text{gu2}}, Z_{\text{gu}}$	Grid unit coordinates used for the boundary matching technique

## 9 List of Tables

2.1	Product $A_R \cdot f_M$ and work function $\phi$ for various materials [29]. . . . .	8
2.2	Main characteristics of different ion source types used for FIB applications. . . .	22
3.1	Small probe electron emitter properties (taken from [100]). . . . .	28
3.2	Extrapolated range values for 100 eV electrons within different gases (Calculations by using equations 3.38 and 3.40). . . . .	45
4.1	Geometrical parameters of the two optical systems presented in figure 4.7. . . .	56
4.2	Obtained statistical radii values for the e-beam at d <sub>3</sub> -YZ-Plane. . . . .	57
4.3	Additional geometrical parameters for the two optical systems presented in figure 4.9. . . . .	59
4.4	Molflow+ simulation results related to the e-Column Model A ( $T = 298.15$ K). . .	76
4.5	Experimental gas conductance tests with Nitrogen injection: dummy model of e-Column Model A and the experimental setup configuration shown in figure 4.30a. . . . .	80
4.6	Estimated optimised gas conductance results when adding an additional cylindrical tube into the already designed e-Column setup. . . . .	81
4.7	Pressure test results for graphene Grid B glued to a 2 mm aperture. . . . .	83
4.8	e-beam transmission test results for graphene Grid C. . . . .	84
5.1	Comparison: $P_{\text{Stop}}$ vs $e \cdot F_{e,\text{retard}}$ and $R_{\text{Ex}}$ vs $R_{\text{Stop}}$ ( $P_{\text{Stop}}$ and $R_{\text{Ex}}$ as in table 3.2). . .	91
5.2	Geometrical parameters for the designed EIRFIS e-Column and ionisation region. . .	95
5.3	Gas conductance calculation results for the EIRFIS e-Column. . . . .	112
5.4	Results of the Molflow+ pressure gradient simulations for the EIRFIS ion column. . .	115
5.5	EIRFIS prototype: Pressures measured just before the e-beam transmission tests. . .	121
5.6	EIRFIS prototype: Pressures measured during the ion generation tests. . . . .	125
5.7	EIRFIS prototype: Pressures measured during the argon ion extraction tests (e-Column Setup 2). . . . .	129
6.1	Main characteristics of different ion source types used for FIB applications. . . .	137
7.1	Electrode potential values for the simulations with e-Column System A and B. . .	150
7.2	Potential settings for the EIRFIS e-Column simulations (Related results in figure 5.7). . . . .	156
7.3	Résultats des simulations de la colonne ionique ( $I_e = 50$ $\mu\text{A}$ , $p_{\text{RI}} = 0.1$ mbar). . .	173
7.4	Résultats des simulations de la colonne ionique avec des ions d'Ar <sup>+</sup> ( $I_{e,0} = 400$ $\mu\text{A}$ , $p_{\text{RI}} = 0.1$ mbar, gradient-pression-Ar). . . . .	177

## 10 List of Figures

2.1	Schematic of a typical FIB instrument setup. . . . .	4
2.2	Illustration of the interaction between an energetic ion beam and a solid (modified from [28]). . . . .	4
2.3	Illustration of the characteristic geometrical parameters of an ion beam. . . . .	5
2.4	Schematic of a conventional Nier-type ion source (taken from [38]). . . . .	7
2.5	a) NAIS: microchip as ionisation cell in SEM (taken from [22]). b) Estimated achievable $B_r$ values by the NAIS from TU Delft (taken from [22]).	9
2.6	Emitter tip of a conventional GFIS on the left and a supertip GFIS with a nano-metric protrusion on top of a regular emitter on the right (modified from [56]). . . . .	11
2.7	Illustration of the sharp tungsten needle and the attached metal reservoir within a LMIS (modified from [26]). . . . .	12
2.8	a) Schematic of a duoplasmatron ion source with expansion cup (taken from [29]); b) Schematic of a cold cathode Penning type ion source (taken from [29]). . . .	13
2.9	Illustration of the MOTIS working principle (taken from [31]). . . . .	14
2.10	a) FIB milled nano-holes in Silicon (30 keV $\text{Ga}^+$ FIB at 1 pA; taken from [3]). b) HIM image of a bow-tie nano-antenna produced by a combined process of $\text{Ga}^+$ and $\text{He}^+$ FIB milling (ROC = Radius Of Curvature; modified from [76]); c) Micro-sized cross-cantilever made by ion implantation in Silicon and subsequent etching with KOH (30 keV $\text{Ga}^+$ FIB at 100 pA; modified from [3]); d) SIM image of a FIBID produced diamond-like carbon micro-bellow (30 keV $\text{Ga}^+$ FIB, 7 nm diameter beam, aromatic hydrocarbon precursor gas; modified from [3]). . . . .	17
2.11	HIM image of an asbestos fibre on top of a carbon film (edge resolution of 0.35 nm; taken from [6]). . . . .	19
2.12	Schematic of the recently developed HIM-SIMS instrument. . . . .	20
3.1	Charged particle multiple element cylindrical electrostatic lenses (taken from [94]).	25
3.2	a) Field free drift space effect on a charged particle trajectory (taken from [95]); b) Electrostatic uniform field effect on a charged particle trajectory (accelerating paraxial case; taken from [95]). . . . .	26
3.3	a) Schematic of a typical triode extraction setup, E: Emitter, W: Wehnelt, A: Anode (modified from [40]); b) Schematic of a general ion source extraction column. . . . .	28
3.4	a) Schematic of a parallel plate deflector (taken from [95]); b) Schematic of a quadrupole (left) and octopole (right) cylindrical deflector. . .	29
3.5	a) Illustration of spherical aberration produced by a 2 electrode electrostatic lens (modified from [97]); b) Illustration of chromatic aberration produced by a 2 electrode electrostatic lens (modified from [97]). . . . .	30
3.6	a) Illustration of a cylindrical symmetric 2D-PA for a simple three electrode lens; b) Corresponding volume view which shows the intended cylindrical Einzel lens.	32
3.7	a) Illustration of nearest neighbour grid points of point $P_0$ ; b) Illustration of circular electrode surface in 2D-PA. . . . .	33

3.8	Illustration of the hard sphere collision of gas species A and B. . . . .	35
3.9	a) Schematic and picture of an ion guide/funnel (modified from [111]); b) Ion carpets used in gas stopping cells (taken from: Top [116]; Bottom [117, 118]); c) Ion carpet in an electrospray ion source for mass spectrometry (taken from [119]). . . . .	36
3.10	Illustration of the parameter plot $Q_d/\kappa$ vs $Q_{pr}$ (data points taken from [122]). . .	38
3.11	Maxwell-Boltzmann distribution of gas particle speeds (Air at $T = 298.15$ K). . .	40
3.12	Illustration of pV-flows within a connected two chamber system: a) Vacuum pump immediately connected to chamber 2; b) Vacuum pump indirectly connected to chamber 2 by an intermediate tube. . .	42
3.13	CASINO simulation: Incident e-beam 100 eV, 5 mm; Argon gas 298.15 K, 0.1 mbar.	46
3.14	a) Examples of CASINO transmission probability curves and related linear fits; b) Extrapolated range values for a 100 eV electron beam within different kind of gases at 298.15 K and 0.1 mbar. . . . .	47
4.1	a) Schematic of a Nier type EI ion source with ionisation volume of cubic mm size; b) Schematic of the intended design for the new EI ion source with a micron scale ionisation volume size. . . . .	50
4.2	Illustration of the positive ion acceleration within the ionisation region when $V_{Top} > V_{Bottom}$ . . . . .	50
4.3	Optical images of a hairpin filament, front and side view with additional zoom images of the filament front tip region. . . . .	52
4.4	a) Schematic of a torus surface point parametrisation; b) 3D-Plot of the filament tip surface and the electron starting positions within the generation area $A_{Gen}$ , here $\chi_{Lim} = 60^\circ$ and $\psi_{Lim} = 35^\circ$ . . . . .	52
4.5	a) SIMION PA of the triode PA used in the e-Column CPO-simulations; b) Zoom of the filament tip region within the triode PA; c) Top: Triode PA (80 GU/mm) overlapped with filament tip PA (2000 GU/mm; VE 1, 2, 3 and 4 are side wall virtual electrodes); Bottom: Extraction of the e-beam, F: 4 kV, W: 3.925 kV, A: 9 kV (not shown). The equipotential lines are shown in red. . . . .	53
4.6	a) Initial starting positions of the extracted electrons on the filament tip surface ( $\Delta V_{Bias} = -75$ V, $\frac{dW}{H} = 1.6$ , $D_{WA} = 3$ mm and $\Delta V_{FA} = 5$ kV); b) Schematic of the ellipsoidal extraction area $A_{Extr}$ . . . . .	54
4.7	a) XY-middle plane cut view: Lens 1 as symmetric Einzel lens; b) XY-middle plane cut view: Lens 1 as asymmetric Einzel lens. . . . .	55
4.8	2D-histogram of the e-beam cross section at $d_3$ YZ-plane: a) Symmetric Lens 1 case; b) Asymmetric Lens 1 case. . . . .	57
4.9	a) XY-middle plane cut view: Lens 2 as symmetric Einzel lens (For all potentials not listed here please see figure 4.7); b) XY-middle plane cut view: Lens 2 as asymmetric Einzel lens (For all potentials not listed here please see figure 4.7). . . . .	58
4.10	3D-Cut view of the ionisation region PA used for the complete e-Column CPO simulations. . . . .	58

4.11	Illustration for the trajectory extrapolation in a field free region. . . . .	59
4.12	a) Statistical radii variations along the X-axis related to the simulation case shown in figure 4.9b;	
	b) Corresponding 2D-histogram and 1D-projections of the YZ-cross-plane at the X-position of the e-beam focus (minimal $r_{FW50}$ position). . . . .	61
4.13	Focussing results for e-Column System A and B. FW50 circle and ellipse results.	62
4.14	Energy dependent EI ionisation cross sections for $Ar^+$ , $Xe^+$ and $O_2^+$ (values taken from [45, 48]). . . . .	63
4.15	Illustration of the $Ar^+$ - ion beam extraction within the ion column (XY-cut view).	64
4.16	a) Cylindrical ionisation volume illustration. Starting positions of all generated and extracted $Ar^+$ ions;	
	b) Starting position distributions of all generated $Ar^+$ within the ionisation volume;	
	c) Starting position distributions of all extracted $Ar^+$ within the ionisation volume.	65
4.17	IV-hairpin filament with $Ar^+$ : $f_{Extr,Ion}$ , $I_{Ion,IV}$ and $I_{Ion,Extr}$ in dependence of $p_{IR}$ . .	66
4.18	Trajectory extrapolation results for the simulation of figure 4.15:	
	a) $Ar^+$ ion beam FW50 variation;	
	b) $Ar^+$ ion beam half-opening angle variation. . . . .	67
4.19	Illustration of the $Ar^+$ ion beam simulation with a variation of $V_{Extr1}$ (IV-hairpin filament, $p_{IR} = 0.1$ mbar, $d_{Extr} = 100$ $\mu m$ ). . . . .	68
4.20	Results of the reduced brightness $B_{r,Ion-beam}$ determination and related parameters	
	(IV-hairpin filament, $p_{IR} = 0.1$ mbar, $d_{Extr} = 100$ $\mu m$ ). . . . .	69
4.21	Illustration of a $LaB_6$ thermionic emitter (taken from [143]). . . . .	70
4.22	a) Bottom view into the ionisation region: Different IV-settings; $d_{Extr} = 100$ $\mu m$ ;	
	b) Bottom view into the ionisation region: Different IV-settings; $d_{Extr} = 40$ $\mu m$ . .	71
4.23	IV-Setting/ $d_{Extr}$ combination comparison: Results of the determination of $B_{r,Ion-beam}$ and related parameters ( $Ar^+$ ion beam, $p_{IR} = 0.1$ mbar). . . . .	71
4.24	Total energy distribution of all transmitted $Ar^+$ ions:	
	a) IV-hairpin filament setting, $d_{Extr} = 100$ $\mu m$ and $\Delta V_{Extr} = 3$ kV;	
	b) IV- $LaB_6$ setting, $d_{Extr} = 100$ $\mu m$ and $\Delta V_{Extr} = 3$ kV;	
	c) IV- $LaB_6$ setting, $d_{Extr} = 40$ $\mu m$ and $\Delta V_{Extr} = 3$ kV. . . . .	73
4.25	Illustration of the designed mechanical setup for e-Column model A. . . . .	74
4.26	a) Free space volume of the mechanical e-Column Model A loaded into Molflow+;	
	b) Injection of gas particles (Facet-view; particles represented as green points)	
	c) Pumping channels available along the e-Column Model A. . . . .	75
4.27	2D pressure distribution along the e-Column Model A (Argon, $S = 200$ l/s). . .	76
4.28	Schematic of the e-Column dummy model for the gas conductance measurements related to e-Column Model A. . . . .	77
4.29	Elements of the e-Column dummy model used to perform the experimental gas conductance measurements. . . . .	78
4.30	a) Schematic of the experimental gas conductance measurement setup;	
	b) Experimental gas conductance measurement setup for the tests with Nitrogen.	79

4.31	a) Optical microscopy images of two graphene grids in their initial state; b) Illustration of the pressure test setup with Grid B; c) Optical microscopy images of Grid B glued to the 2 mm aperture before and after the pressure tests (Numbers 1, 2 and 3 are shown for orientation purposes).	82
4.32	a) Illustration of the e-beam transmission measurement setup; b) More precise illustration of the transmission measuring rod; c) Optical microscopy image of the graphene grid (Grid C) inserted below the 1.8 mm hole of the measuring rod. . . . .	85
4.33	Illustration of the copper grids covered by the graphene film. . . . .	86
5.1	Illustration of the yttria-coated iridium disc cathode (modified from [156]). . . .	89
5.2	a) Illustration of the electron impact radio frequency ion source (EIRFIS) concept; b) More detailed representation of the electric fields within the ionisation region.	90
5.3	Electron extrapolated ranges $R_{Ex}$ and total stopping ranges $R_{Stop}$ for different gases ( $p_{IR} = 0.1$ mbar, $T_{IR} = 298.15$ , $F_{e,retard} = 10$ V/cm and $E_{e,0} = 100$ eV). . .	91
5.4	EIRFIS mechanical model schematic: a) e-Column and ionisation region (XY-cut view); b) e-Column and ionisation region (3D view). . . . .	93
5.5	a) EIRFIS e-Column simulation with vacuum tube included; b) EIRFIS e-Column simulation with vacuum tube and shielding included (The geometrical parameters can be found in table 5.2). . . . .	94
5.6	EIRFIS e-Column simulation with vacuum tube and shielding: 3D-cut view of the 3D-PA file with Y- and Z-symmetry. . . . .	96
5.7	Results of the EIRFIS e-Column simulations: a) Extraction area radius and 90 % e-beam radius at the inlet electrode; b) Extraction and transmission factor; c) Estimated extraction and transmission e-beam current. . . . .	97
5.8	EIRFIS mechanical model schematic: Ionisation region (with shielding) and ion extraction column (XY-cut view). . . . .	98
5.9	a) PA-file of the EIRFIS ionisation region and ion extraction column (XY-cut view); b) Illustration of the Ion Carpet A and B setups, dimensions and applied potentials. . . . .	99
5.10	Evaluation of the $Ar^+$ motion above Ion Carpet A/B (parameters shown in figure).	100
5.11	Illustration of the $Ar^+$ ion generation volume and the extraction towards Ex1 (Ion Carpet B; $p_{IR} = 0.1$ mbar and the Test-pressure-gradient is applied). . . .	101
5.12	Extraction efficiency Ion Carpet A/B: $Ar^+$ in argon (IV- $Ar$ ; $p_{IR} = 0.1$ mbar, $T_{IR} = 298.15$ K; $d_0 = 1$ mm; $d_{Ex1} = 0.1$ mm; $\Delta V_{IC-Ex1} = 500$ V; Use of the Test-pressure-gradient). . . . .	102
5.13	Illustration of the IV slice approach for the total ion current calculation. . . .	103
5.14	Illustration of a complete EIRFIS ion column simulation for $Ar^+$ ions (Ion Carpet B; IV- $Ar$ ; $p_{IR} = 0.1$ mbar, $T_{IR} = 298.15$ K; $Ar$ -pressure-gradient used). . . . .	105
5.15	Brightness calculation for $Ar^+$ ions: Left Ion Carpet A; Right Ion Carpet B; (IV- $Ar$ ; $p_{IR} = 0.1$ mbar, $T_{IR} = 298.15$ K; $Ar$ -pressure-gradient used). . . . .	107

5.16	Total energy distributions at the Rec-Plane for $\text{Ar}^+$ ions:	
	a) Ion Carpet A case; b) Ion Carpet B case; (related to the simulation cases shown in figure 5.14 and figure 7.26 of appendix C (section 7.3)).	109
5.17	a) Simplified EIRFIS e-Column model used for the gas conductance calculations;	
	b) Illustration of the Wehnelt volume pumping holes.	111
5.18	a) Illustration of the ion column pumping within the EIRFIS prototype;	
	b) Molflow+ setup illustration for the EIRFIS ion column simulation.	113
5.19	Molflow+ EIRFIS ion column simulation ( $d_0 = 1 \text{ mm}$ , $d_{\text{Ex1}} = 100 \text{ }\mu\text{m}$ ):	
	2D pressure distribution ( $\text{Ar}$ , $S_{\text{eff,IC}} = 116 \text{ l/s}$ , $T = 298.15 \text{ K}$ ).	114
5.20	Molflow+ EIRFIS ion column simulation ( $d_0 = 1 \text{ mm}$ , $d_{\text{Ex1}} = 100 \text{ }\mu\text{m}$ ):	
	Pressure gradient along the ion beam axis ( $\text{Ar}$ , $S_{\text{eff,IC}} = 116 \text{ l/s}$ , $T = 298.15 \text{ K}$ ).	115
5.21	Illustration/pictures of the EIRFIS prototype e-Column and its assemblage.	116
5.22	Illustration/pictures of the EIRFIS prototype ionisation region and its assemblage.	117
5.23	Illustration/pictures of the EIRFIS prototype ion column and its assemblage.	118
5.24	Illustration/pictures of the PCB ion carpet (front- and backside).	118
5.25	Electrical circuit layout of the PCB ion carpet.	119
5.26	Illustration of the EIRFIS prototype test bench setup for the first e-Column/ionisation region tests.	120
5.27	Illustration of the different parameters of the EIRFIS prototype e-Column disc cathode region.	120
5.28	a) Suppression of the sec-e emission from the copper-plate (e-Column Setup 1);	
	b) Results of the e-beam transmission tests at different extraction potentials $\Delta V_{\text{Extr}}$ (e-Column Setup 1).	122
5.29	a) Illustration: Copper plate current contributions during the ion generation tests;	
	b) e-Column Setup 1: Argon ion current generation results ( $\Delta V_{\text{Extr}} = 3.5 \text{ kV}$ ; $V_{\text{I}} = 100 \text{ V}$ ; $\Delta V_{\text{C-I}} = -100 \text{ V}$ ).	124
5.30	Schematic of the RF-signal generation system.	126
5.31	Experimental setup illustration for the ion current extraction measurements.	127
5.32	a) Results: $I_{\text{Ar,Ex1}}$ measurements in dependence of the applied $V_{\text{Amp,RF}}$ ;	
	b) Results: $I_{\text{Ion-beam,Ar}}$ measurements in dependence of the applied $V_{\text{Amp,RF}}$ .	128
7.1	a) Illustration of the Molflow+ profile plotter feature and facet direction vectors;	
	b) Illustration of the 2D texture scaling in Molflow+ (here on the tube side walls).	140
7.2	a) Illustration of a new transparent facet created within Molflow+;	
	b) Illustration of the pressure 2D-profile on the transparent facet.	141
7.3	Dialogue boxes for the CASINO simulation parameter selection.	141
7.4	Schematic of the uniform deviates $g_1$ and $g_2$ that are used to generate a random point within the unit circle.	143
7.5	Left: Standard normal distribution of $b_1$ generated with the Box-Muller method;	
	Right: Example of Maxwell-Boltzmann distribution function for $v_i$ by multiplying the $b_1$ values with $\sigma = \sqrt{\frac{k_B T}{m_e}}$ (Here: $T = 2700 \text{ K}$ ).	143
7.6	Boundary matching illustration within the hairpin filament region.	145
7.7	Illustration of two grid systems used within the bilinear interpolation of the boundary matching technique.	145
7.8	Filament tip PA and triode PA elements.	146



7.9	Deflection region PA elements. . . . .	147
7.10	Ionisation region PA elements. . . . .	148
7.11	Complete e-Column System B with overlapping PAs. . . . .	148
7.12	a) Complete PA-File used in the ion column CPO simulations;	
	b) Ar <sup>+</sup> simulation: IV-hairpin filament, p <sub>IR</sub> = 0.1 mbar, d <sub>Extr</sub> = 100 μm. . . . .	151
7.13	Ar <sup>+</sup> - ion beam simulation, IV-hairpin filament, p <sub>IR</sub> = 0.1 mbar, d <sub>Extr</sub> = 100 μm. Potentials: V <sub>IR1</sub> = 6 kV, V <sub>IR2</sub> = 5.99 kV, V <sub>G</sub> = 0 V and variation of V <sub>Extr1</sub> . . .	151
7.14	Zoom of the Ar <sup>+</sup> - ion beam extraction from the ionisation region at 0.1 mbar of Argon gas (IV-hairpin filament; ΔV <sub>Extr</sub> = 1 kV). . . . .	152
7.15	Pressure distribution along e-Column Model A (Nitrogen, S = 200 l/s). . . . .	153
7.16	Pressure distributions along e-Column Model A (Argon, S = 100 l/s and 1000 l/s). . . . .	153
7.17	Illustration of the 300 square mesh copper grid covered by a carbon support/graphene film (D <sub>Grid</sub> , d <sub>Grid</sub> , b <sub>W</sub> , h <sub>W</sub> and Δ <sub>bars</sub> : specifications of the manufacturer [179]). . . . .	154
7.18	a) Optical microscopy image of 300 mesh square copper grid covered by a carbon support and 2 monolayer graphene film;	
	b) Carbon support film and 3-5 ML-graphene (bar = 5 μm, taken from [174]). . . . .	155
7.19	a) Electron IMFP for graphite (Used equation 7.11 and parameters from [178]);	
	b) Electron transmission curves, used equation 7.10 for a normal incident beam. . . . .	155
7.20	e-beam YZ-cross sections and corresponding 2D-histograms for the EIRFIS e- Column simulation of figure 5.6a:	
	a) At the inlet electrode;	
	b) At 3 mm behind the inlet electrode (close to the e-beam focus plane);	
	c) At the middle of the ionisation region. . . . .	157
7.21	EIRFIS mechanical model schematic: ionisation region (with shielding) and ion extraction column (3D view). . . . .	158
7.22	3D illustration of Ion Carpet A and B (including insulating layer). . . . .	158
7.23	Starting volume illustration for the EIRFIS ion column simulations (Ar <sup>+</sup> ions). . . . .	159
7.24	Extraction efficiency Ion Carpet A/B: Ar <sup>+</sup> in argon (IV-Ar; p <sub>IR</sub> = 0.1 mbar, T <sub>IR</sub> = 298.15 K; d <sub>0</sub> = 1 mm; d <sub>Ex1</sub> = 0.1 mm; ΔV <sub>IC-Ex1</sub> = 500 V; Use of the Test-pressure-gradient). . . . .	160
7.25	Ion current determination by the slice-approach: Variation of different parameters (Ion Carpet B: f <sub>RF</sub> = 8 MHz, V <sub>Amp,RF</sub> = 100 V; p <sub>IR</sub> = 0.1 mbar, T <sub>IR</sub> = 298.15 K). . . . .	161
7.26	Illustration of a complete EIRFIS ion column simulation for Ar <sup>+</sup> ions (Ion Carpet A; IV-Ar; p <sub>IR</sub> = 0.1 mbar, T <sub>IR</sub> = 298.15 K; Ar-pressure-gradient used). . . . .	162
7.27	Ar <sup>+</sup> ion beam profile evaluation at the Rec-Plane and source location plane for the simulation case of figure 7.26. . . . .	163
7.28	Ar <sup>+</sup> ion beam profile evaluation at the extraction aperture plane for the simulation case of figure 7.26. . . . .	164
7.29	Molflow+ EIRFIS ion column simulation (d <sub>0</sub> = 1 mm, d <sub>Ex1</sub> = 100 μm):	
	a) 2D pressure distribution (Xe, S <sub>eff,IC</sub> = 75 l/s, T = 298.15 K);	
	b) Pressure gradient along the ion beam axis (Xe, S <sub>eff,IC</sub> = 75 l/s, T = 298.15 K). . . . .	166
7.30	Illustration of the increase in D <sub>CW</sub> by inserting additional small very flat discs in between the cathode ceramic base and the Wehnelt electrode. . . . .	167
7.31	Illustration of the realignment of the Wehnelt and anode aperture. . . . .	168
7.32	Illustration of the realignment of the Wehnelt and anode aperture. . . . .	168

---

7.33	Measured RF amplitudes $V_{\text{Amp,RF,i}}$ on the PCB ion carpet:	
	a) Electrical circuit layout with C1; b) Electrical circuit layout without C1. . . . .	169
7.34	Illustration des paramètres géométriques d'un faisceau d'ions. . . . .	170
7.35	Illustration: source d'ions à IE et volume d'ionisation micrométrique. . . . .	172
7.36	Résultats de la focalisation du faisceau d'électrons. . . . .	172
7.37	Illustration de l'extraction du faisceau d'ions $\text{Ar}^+$ dans la colonne ionique. . . . .	173
7.38	Illustration: source d'ions radio-fréquence à impact électronique. . . . .	174
7.39	Illustration: configuration du Ion Carpet A et B, dimensions et potentiels appliqués. . . . .	176
7.40	Réalisation mécanique de la source d'ions radio-fréquence à impact électronique. . . . .	178

## 11 References

- [1] A. A. G. Bruzzone, H. L. Costa, P. M. Lonardo, and D. A. Lucca, “Advances in engineered surfaces for functional performance,” *CIRP Annals - Manufacturing Technology*, vol. 57, pp. 750 – 769, 2008.
- [2] K. Gamo, “Nanofabrication by FIB,” *Microelectronic Engineering*, vol. 32, pp. 159 – 171, 1996.
- [3] A. A. Tseng, “Recent developments in nanofabrication using focused ion beams,” *Small*, vol. 1, no. 10, pp. 924 – 939, 2005.
- [4] L. A. Giannuzzi and F. A. Stevie, “A review of focused ion beam milling techniques for TEM specimen preparation,” *Micron*, vol. 30, pp. 197 – 204, 1999.
- [5] M. Sugiyama and G. Sigisato, “A review of focused ion beam technology and its applications in transmission electron microscopy,” *Journal of Electron Microscopy*, vol. 53, no. 5, pp. 527 – 536, 2004.
- [6] N. P. Economou, J. A. Notte, and W. B. Thompson, “The history and development of the helium ion microscope,” *SCANNING*, vol. 34, no. 2, pp. 83 – 89, 2012.
- [7] F. H. M. Rahman, S. McVey, L. Farkas, J. A. Notte, S. Tan, and R. H. Livengood, “The prospects of a subnanometer focused neon ion beam,” *Scanning*, vol. 34, pp. 129 – 134, 2012.
- [8] W. B. Thompson, J. Notte, L. Scipioni, M. Ananth, L. Stern, S. Sijbrandij, and C. Sanford, “Advances in helium ion microscopy for high resolution imaging, analysis and materials modification,” *NSTI-Nanotech*, vol. 1, pp. 25 – 28, 2010.
- [9] D. S. McPhail, “Applications of secondary ion mass spectrometry (SIMS) in materials science,” *Journal of Materials Science*, vol. 41, pp. 873 – 903, 2006.
- [10] P. C. Zalm, “Secondary ion mass spectrometry,” *Vacuum*, vol. 45, no. 6-7, pp. 753 – 772, 1994.
- [11] H. N. Migeon, F. Saldi, Y. Gao, and M. Schuhmacher, “Ion microscope and ion microprobe analysis under oxygen, cesium and gallium bombardment,” *International Journal of Mass Spectrometry and Ion Processes*, vol. 143, pp. 51 – 63, 1995.
- [12] P. Weber, E. Guibert, S. Mikhailov, J. Brügger, and G. Villanueva, “Ion beam etching: Replication of micro nano structured 3D stencil masks,” *AIP Conference Proceedings*, vol. 1099, pp. 539 – 541, 2009.
- [13] C. Mansilla, P. Philipp, and T. Wirtz, “Roughening of silicon (1 0 0) surface during low energy Cs<sup>+</sup> ion bombardment,” *Nuclear Instruments & Methods in Physics Research, Section B: Beam Interactions with Materials and Atoms*, vol. 269, pp. 905 – 908, 2011.
- [14] P. Sigmund, “Theory of sputtering. I. sputtering yield of amorphous and polycrystalline targets,” *Physical Review*, vol. 184, pp. 383 – 416, 1969.

- [15] A. V. Crewe, P. W. Hawkes, P. Kruit, G. H. Jansen, B. Lencová., G. L. R. Mair, E. Munro, M. T. Postek, M. Sato, G. A. Schwind, L. W. Swanson, K. Tsuno, and M. Utlaut, *Handbook of Charged Particle Optics*. CRC Press LLC, 1997.
- [16] L. A. Dietz and J. C. Sheffield, “Secondary electron emission induced by 5 to 30 keV monatomic ions striking thin oxide films,” *Journal of applied Physics*, vol. 46, pp. 4361 – 4370, 1975.
- [17] P. Philipp, T. Wirtz, H. N. Migeon, and H. Scherrer, “SIMS analysis with neutral cesium deposition: Negative secondary ion sensitivity increase and quantification aspects,” *International Journal of Mass Spectrometry*, vol. 253, pp. 71 – 78, 2006.
- [18] K. Wittmaack, *Physical and Chemical Parameters Determining Ion Yields in SIMS Analyses: A Closer Look at the Oxygen-Induced Yield Enhancement in Secondary Ion Mass Spectrometry SIMS XI*. JOHN WILEY & SONS, 1998.
- [19] A. Wucher, “Formation of atomic secondary ions in sputtering,” *Applied Surface Science*, vol. 255, pp. 1194 – 1200, 2008.
- [20] V. N. Tondare, “Quest for high brightness, monochromatic noble gas ion sources,” *Journal of Vacuum Science & Technology A*, vol. 23, no. 6, pp. 1498 – 1508, 2005.
- [21] J. E. Barth, C. B. de Gruyter, E. Koets, P. Kruit, P. E. van der Leeden, J. B. Le Poole, and K. D. van der Mast, “Gas ion source for focused beams,” *Microelectronic Engineering*, vol. 3, pp. 147 – 152, 1985.
- [22] D. S. Jun, V. G. Kutchoukov, and P. Kruit, “Ion beams in SEM: An experiment towards a high brightness low energy spread electron impact gas ion source,” *Journal of Vacuum Science & Technology B*, vol. 29, no. 06F603, pp. 1 – 7, 2011.
- [23] P. Kruit and V. N. Tondare, “Particle-optical apparatus equipped with a gas ion source,” August 2010.
- [24] N. Liu, P. S. Raman, X. Xu, H. M. Tan, A. Khursheed, and J. A. van Kan, “Development of ion sources: Towards high brightness for proton beam writing applications,” *Nuclear Instruments and Methods in Physics Research B*, vol. 348, pp. 23 – 28, 2015.
- [25] N. Liu, X. Xu, R. Pang, P. S. Raman, A. Khursheed, and J. A. van Kan, “Brightness measurement of an electron impact gas ion source for proton beam writing applications,” *Review of Scientific Instruments*, vol. 87, no. 02A903, pp. 1 – 3, 2016.
- [26] L. A. Giannuzzi and F. A. Stevie, eds., *INTRODUCTION TO FOCUSED ION BEAMS: Instrumentation, Theory, Techniques and Practice*. Springer Science+Business Media, Inc., 2005.
- [27] H. H. Andersen, H. L. Bay, R. Behrisch, M. T. Robinson, H. E. Roosendaal, and P. Sigmund, *Sputtering by Particle Bombardment: I Physical Sputtering of Single-Element Solids*. Springer-Verlag Berlin Heidelberg, 1981.
- [28] T. Wirtz, L. Pillatsch, N. Vanhove, D. Dowsett, S. Sijbrandij, and J. Notte, “Towards secondary ion mass spectrometry on the helium ion microscope,” *Microscopy and Microanalysis*, vol. 18 (Suppl 2), pp. 812 – 813, July 2012.

- [29] B. Wolf, G. D. Alton, R. Becker, F. Bourg, I. G. Brown, H. Horneff, J. Ishikawa., T. W. Jolly, K. Leung, B. Sharkov, P. Späedtke, and P. Strehl, *Handbook of Ion Sources*. CRC Press, Inc., 1995.
- [30] I. Brown, M. Farley, N. Gavrilov, R. Hollinger, J. Ishikawa, J. Kwan, D. Leitner, K. Leung, C. Lyneis, E. Oks, P. Rose, G. Ryding, N. Sakudo, B. Sharkov, P. Späedtke, and Y. Takeiri, *The Physics and Technology of Ion Sources*. WILEY-VCH Verlag GmbH & Co. KGaA, Weinheim, 2004.
- [31] J. L. Hanssen, S. Hill, J. Orloff, and J. J. McClelland, “Magneto-Optica-Trap-Based, high brightness ion source for use as a nanoscale probe,” *Nano Letters*, vol. 8, no. 9, pp. 2844 – 2850, 2008.
- [32] S. Fujita, T. R. C. Wells, W. Ushio, H. Sato, and M. M. El-Gomati, “Enhanced angular current intensity from Schottky emitters,” *Journal of Microscopy*, vol. 239, no. 3, pp. 215 – 222, 2010.
- [33] M. S. Bronsgeest, *PHYSICS OF SCHOTTKY ELECTRON SOURCES*. PhD thesis, Technische Universiteit Delft, 2009.
- [34] H. Zhang, *Ion Sources*. Springer-Verlag Berlin Heidelberg New York and Science Press Beijing, 1999.
- [35] T. D. Maerk and G. H. Dunn, eds., *Electron Ionization*. Innsbruck University Press, 2010.
- [36] J. R. Ahn, S. G. Lee, and C. J. Park, “Measurement of ion kinetic-energy distributions in electron-impact ion sources of a quadrupole mass spectrometer,” *Journal of the Korean Physical Society*, vol. 59, no. 4, pp. 2670 – 2675, 2011.
- [37] A. O. Nier, “A mass spectrometer for isotope and gas analysis,” *Review of Scientific Instruments*, vol. 18, pp. 398 – 410, June 1947.
- [38] C. J. Park and J. R. Ahn, “A closed ion source with a cylindrical repeller for sensitivity enhancement in quadrupole mass spectrometry,” *Review of Scientific Instruments*, vol. 76, no. 044101, pp. 1 – 5, 2005.
- [39] T. B. Angerer, P. Blenkinsopp, and J. S. Fletcher, “High energy gas cluster ions for organic and biological analysis by time-of-flight secondary ion mass spectrometry,” *Intern*, vol. 377, pp. 591–598, 2015.
- [40] R. F. Egerton, *Physical Principles of Electron Microscopy: An Introduction to TEM, SEM, and AEM*. Springer Science+Business Media, Inc., 2005.
- [41] R. O. Jenkins, “A review of thermionic cathodes,” *Vacuum*, vol. 19, no. 8, pp. 353 – 359, 1969.
- [42] S. Yamamoto, “Fundamental physics of vacuum electron sources,” *Reports on Progress in Physics*, vol. 69, pp. 181 – 232, 2006.
- [43] T. D. Maerk, “Fundamental aspects of electron impact ionization,” *International Journal of Mass Spectrometry and Ion Physics*, vol. 45, pp. 125 – 145, 1982.

- [44] T. D. Maerk, “Ionization by electron impact,” *Plasma Physics and Controlled Fusion*, vol. 34, no. 13, pp. 2083 – 2090., 1992.
- [45] R. Rejoub, B. G. Lindsay, and R. F. Stebbings, “Determination of the absolute partial and total cross sections for electron-impact ionization of the rare gases,” *Physical Review A: Atomic, Molecular, and Optical Physics*, vol. 65, no. 042713, pp. 1 – 8, 2002.
- [46] D. Rapp and P. Englander-Golden, “Total cross sections for ionization and attachment in gases by electron impact. I. Positive ionization,” *Journal of Chemical Physics*, vol. 43, pp. 1464 – 1479, 1965.
- [47] H. C. Straub, P. Renault, B. G. Lindsay, K. A. Smith, and R. F. Stebbings, “Absolute partial and total cross sections for electron-impact ionization of argon from threshold to 1000 eV,” *Physical Review A: Atomic, Molecular, and Optical Physics*, vol. 52, no. 2, pp. 1115 – 1124, 1995.
- [48] H. C. Straub, P. Renault, B. G. Lindsay, K. A. Smith, and R. F. Stebbings, “Absolute partial cross sections for electron-impact ionization of H<sub>2</sub>, N<sub>2</sub>, and O<sub>2</sub> from threshold to 1000 eV,” *Physical Review A*, vol. 54, pp. 2146 – 2153, September 1996.
- [49] Y. K. Kim and M. E. Rudd, “Binary-encounter-dipole model for electron-impact ionization,” *Physical Review*, vol. 50, pp. 3954 – 3967, 1994.
- [50] M. R. H. Rudge, “Theory of the ionization of atoms by electron impact,” *Review of Modern Physics*, vol. 40, pp. 564 – 590, July 1968.
- [51] P. M. Stone and Y. K. Kim, “An overview of the BEB method for electron-impact ionization of atoms and molecules,” *Surface and Interface Analysis*, vol. 37, pp. 966 – 968, 2005.
- [52] D. S. Jun, V. G. Kutchoukov, C. T. H. Heerkens, and P. Kruit, “Design and fabrication of a miniaturized gas ionization chamber for production of high quality ion beams,” *Microelectronic Engineering*, vol. 97, pp. 134 – 137, 2012.
- [53] V. N. Tondare, *Towards a High Brightness, Monochromatic Electron Impact Gas Ion Source*. PhD thesis, Technische Universiteit Delft, 2006.
- [54] D. S. Jun, *Development of the Nano-Aperture Ion Source (NAIS)*. PhD thesis, TU Delft, Netherlands, 2014.
- [55] G. L. Allan and G. J. F. Legge, “Characteristics of a hydrogen gas field ion source for muprobe application,” *Nuclear Instruments and Methods in Physics Research B*, vol. 34, pp. 122 – 126, July 1988.
- [56] S. Kalbitzer, “Bright ion beams for the nuclear microprobe,” *Nuclear Instruments and Methods in Physics Research B*, vol. 158, pp. 53 – 60, 1999.
- [57] R. Hill, J. Notte, and B. Ward, “The ALIS He ion source and its application to high resolution microscopy,” *Physics Procedia*, vol. 1, pp. 135 – 141, 2008.
- [58] R. Hill and F. H. M. F. Rahman, “Advances in helium ion microscopy,” *Nuclear Instruments & Methods in Physics Research, Section A*, vol. 645, pp. 96 – 101, 2011.

- [59] J. Notte, F. H. M. F. Rahman, S. McVey, S. Tan, and R. H. Livengood, “Neon gas field ion source - stability and lifetime,” *Microscopy and Microanalysis*, vol. 16, pp. 28 – 29, July 2010.
- [60] F. Aramaki, T. Kozakai, O. Matsuda, O. Takaoda, Y. Sugiyama, H. Oba, K. Aita, and A. Yasaka, “Photomask repair technology by using gas field ion source,” *SPIE Proceedings, Photomask and Next-Generation Lithography Mask Technology XIX*, vol. 8441, April 2012.
- [61] A. Yasaka, F. Aramaki, T. Kozakai, and O. Matsuda, “Nanoscale imaging, material removal and deposition for fabrication of cutting-edge semiconductor devices,” *Hitachi Review*, vol. 65, no. 7, pp. 233 – 237, 2016.
- [62] R. G. Forbes, “Understanding how the liquid-metal ion source works,” *Vacuum*, vol. 48, pp. 85 – 97, 1997.
- [63] L. W. Swanson, “Use of the liquid metal ion source for focused beam applications,” *Applied Surface Science*, vol. 76/77, pp. 80 – 88, 1994.
- [64] Z. Cui, P. D. Prewett, and J. G. Watson, “Focused ion beam biased repair of conventional and phase shift masks,” *Journal of Vacuum Science & Technology B*, vol. 14, pp. 3942 – 3946, 1996.
- [65] S. Khizroev and D. Litvinov, “Focused-ion-beam-based rapid prototyping of nanoscale magnetic devices,” *Nanotechnology*, vol. 15, pp. R7 – R15, 2004.
- [66] L. Pillatsch, T. Wirtz, H. N. Migeon, and H. Scherrer, “Use of a duoplasmatron ion source for negative ion generation,” *Nuclear Instruments and Methods in Physics Research B*, vol. 269, pp. 1036 – 1040, 2011.
- [67] N. S. Smith, P. P. Tesch, N. P. Martin, and D. E. Kinion, “A high brightness source for nano-probe secondary ion mass spectrometry,” *Applied Surface Science*, vol. 255, pp. 1606 – 1609, 2008.
- [68] C. D. Coath and J. V. P. Long, “A high brightness duoplasmatron ion source for microprobe secondary ion mass spectrometry,” *Review of Scientific Instruments*, vol. 66, pp. 1018 – 1023, 1995.
- [69] S. K. Guharay, S. Douglass, and J. Orloff, “High-resolution primary ion beam probe for SIMS,” *Applied Surface Science*, vol. 926-929, pp. 231 – 232, 2004.
- [70] N. S. Smith, W. P. Skoczylas, S. M. Kellogg, D. E. Kinion, and P. P. Tesch, “High brightness inductively coupled plasma source for high current focused ion beam applications,” *Journal of Vacuum Science & Technology B*, vol. 24, pp. 2902 – 2906, Nov/Dec 2006.
- [71] Oregon Physics, “Hyperion I Positive Ion Source.” <http://www.oregon-physics.com/hyperion1.php>, May 2016.
- [72] Oregon Physics, “Hyperion II Dual Polarity Ion Source.” <http://www.oregon-physics.com/hyperion2.php>, May 2016.
- [73] B. Knuffman, A. V. Steele, J. Orloff, and J. J. McClelland, “Nanoscale focused ion beam from laser-cooled lithium atoms,” *New Journal of Physics*, vol. 13, no. 103035, pp. 1 – 9, 2011.

- [74] K. A. Twedt, L. Chen, and J. J. McClelland, “Scanning ion microscopy with low energy lithium ions,” *Ultramicroscopy*, vol. 142, pp. 24 – 31, 2014.
- [75] A. V. Steele, B. Knuffman, J. J. McClelland, and J. Orloff, “Focused chromium ion beam,” *Journal of Vacuum Science & Technology B*, vol. 28, pp. C6F1 – C6F5, 2010.
- [76] H. Kollmann, X. Piao, M. Esmann, S. F. Becker, D. Hou, C. Huynh, L.-O. Kautschor, G. Bösker, H. Vieker, A. Beyer, A. Götzhäuser, N. Park, R. Vogelgesang, M. Silies, and C. Lienau, “Toward plasmonics with nanometer precision: Nonlinear optics of helium-ion milled gold nanoantennas,” *Nano Letters*, vol. 14, pp. 4778 – 4784, 2014.
- [77] H. Guo, S. Dong, P. D. Rack, J. D. Budai, C. Beekman, Z. Gai, W. Siemons, C. M. Gonzalez, R. Timilsina, A. T. Wong, A. Herklotz, P. C. Snijders, E. Dagotto, and T. Z. Ward, “Strain doping: Reversible single-axis control of a complex oxide lattice via helium implantation,” *Physical Review Letters*, vol. 114, no. 256801, pp. 1 – 6, 2015.
- [78] Z. Wang, T. Kato, T. Hirayama, N. Kato, K. Sasaki, and H. Saka, “Surface damage induced by focused-ion-beam milling in a Si/Si p-n junction cross-sectional specimen,” *Applied Surface Science*, vol. 241, pp. 80 – 86, 2005.
- [79] P. D. Prewett, A. W. Eastwood, G. S. Turner, and J. G. Watson, “Gallium staining in FIB repair of photomasks,” *Microelectronic Engineering*, vol. 21, pp. 191–196, 1993.
- [80] M. K. Miller, K. F. Russell, and G. B. Thompson, “Strategies for fabricating atom probe specimens with a dual beam FIB,” *Ultramicroscopy*, vol. 102, pp. 287 – 298, 2005.
- [81] G. B. Thompson, M. K. Miller, and H. L. Fraser, “Some aspects of atom probe specimen preparation and analysis of thin film materials,” *Ultramicroscopy*, vol. 100, pp. 25 – 34, 2004.
- [82] A. Delobbe, O. Salord, T. Hrncir, A. David, P. Sudraud, and F. Lopour, “High speed TEM sample preparation by Xe FIB,” *Microscopy and Microanalysis*, vol. 20 (Suppl 3), pp. 298 – 299, August 2004.
- [83] T. L. Burnett, R. Kelley, B. Winiarski, L. Contreras, M. Daly, A. M. G. Burke, and P. J. Withers, “Large volume serial section tomography by Xe Plasma FIB dual beam microscopy,” *Ultramicroscopy*, vol. 161, pp. 119 – 129, 2016.
- [84] T. Wirtz, P. Philipp, J.-N. Audinot, D. Dowsett, and S. Eswara, “High-resolution high-sensitivity elemental imaging by secondary ion mass spectrometry: from traditional 2D and 3D imaging to correlative microscopy,” *Nanotechnology*, vol. 26, no. 434001, pp. 1 – 22, 2015.
- [85] L. Yedra, S. Eswara, D. Dowsett, and T. Wirtz, “In-situ isotopic analysis at nanoscale using parallel ion electron spectrometry: A powerful new paradigm for correlative microscopy,” *Scientific Reports*, vol. 6, no. 28705, pp. 1 – 7, 2016.
- [86] T. Wirtz and H.-N. Migeon, “Cation mass spectrometry: towards an optimisation of SIMS analyses performed in the MCs+x mode,” *Spectroscopy Europe*, vol. 15, no. 4, pp. 16 – 22, 2003.



- [87] D. Dowsett, T. Wirtz, N. Vanhove, L. Pillatsch, S. Sijbrandij, and J. Notte, “Secondary ion mass spectrometry on the helium ion microscope: A feasibility study of ion extraction,” *Journal of Vacuum Science & Technology B*, vol. 30, no. 06F602, pp. 1 – 7, 2012.
- [88] G. Hlawacek and A. Götzhäuser, eds., *Helium Ion Microscopy*. NanoScience and Technology, Springer International Publishing, 2016.
- [89] L. Pillatsch, T. Wirtz, H. N. Migeon, and H. Scherrer, “SIMS using negative primary ion bombardment,” *Surface and Interface Analysis*, vol. 42, pp. 645 – 648, 2010.
- [90] P. Philipp, T. B. Angerer, S. Sämfors, P. Blenkinsopp, J. S. Fletcher, and T. Wirtz, “Significant enhancement of negative secondary ion yields by cluster ion bombardment combined with cesium flooding,” *Analytical Chemistry*, vol. 87, pp. 10025 – 10032, 2015.
- [91] D. Boussard, G. R. Brewer, R. Castaing, H. A. Enge, J. Fronteau, A. Galejs, J. F. Hennequin, L. Henry, R. Hutter, L. Jackson Laslett, P. H. Rose, A. Septier, G. Slodzian, and H. Wollnik, *Focusing of Charged Particles*, vol. II. Academic Press Inc. - New York, London, 1967.
- [92] P. Grivet, M. Y. Bernard, F. Bertein, R. Castaing, M. Gauzit, and A. Septier, *Electron Optics*. Pergamon Press - Oxford, London, Edinburgh, New York, Paris, Frankfurt, 1965.
- [93] J. Großer, *Einführung in die Teilchenoptik*. B. G. Teubner Stuttgart, 1983.
- [94] O. Sise, M. Ulu, and M. Dogan, “Characterization and modeling of multi-element electrostatic lens systems,” *Radiation Phys*, vol. 76, pp. 593 – 598, 2007.
- [95] H. Liebl, *Applied Charged Particle Optics*. Springer Berlin Heidelberg, 2008.
- [96] O. Sise, M. Ulu, and M. Dogan, “Multi-element cylindrical electrostatic lens systems for focusing and controlling charged particles,” *Nuclear Instruments & Methods in Physics Research, Section A: Accelerators, Spectrometers, Detectors, and Associated Equipment*, vol. 554, pp. 114 – 131, 2005.
- [97] O. Sise, M. Ulu, and M. Dogan, “Aberration coefficients of multi-element cylindrical electrostatic lens systems for charged particle beam applications,” *Nuclear Instruments & Methods in Physics Research, Section A: Accelerators, Spectrometers, Detectors, and Associated Equipment*, vol. 573, pp. 329 – 339, 2007.
- [98] G. H. N. Riddle, “Electrostatic einzel lenses with reduced Cs for use in field emission guns,” *Journal of Vacuum Science & Technology*, vol. 15, pp. 857 – 860, May/June 1978.
- [99] M. E. Haine and P. A. Einstein, “Characteristics of the hot cathode electron microscope gun,” *British Journal of Applied Physics*, vol. 3, pp. 40 – 46, 1952.
- [100] D. B. Williams and C. B. Carter, *Transmission Electron Microscopy: A Textbook for Materials Science*. Springer Science/Business Media, 2009.
- [101] R. F. Bunshah, L. A. Harris, L. H. Leonard, G. F. Barber, R. Bakish, R. X. Masse, T. Kraus, O. Winkler, H. R. Smith Jr., A. Lawley, S. S. White, E. B. Bas, C. K. Crawford, O. C. Wells, D. W. Moore, and W. E. Glenn, *Introduction to electron beam technology*. John Wiley & Sons, Inc., New York London, 1962.

- [102] M. Iqbal, M. Rafiq, S. A. Bhatti, and F. e-Aleem, “The electron beam gun with thermionic hairpin-like cathode for welding and surface modifications,” *Vacuum*, vol. 77, pp. 19 – 26, 2004.
- [103] Kimball Physics Inc., *User Manual of Kimball Physics electron gun EMG-4212*. Kimball Physics Inc., 311 Kimball Hill Road Wilton, New Hampshire 03086-5715 USA.
- [104] J. R. Ahn and C. J. Park, “Computer simulation of electron and ion trajectories in electron-impact ion sources of a quadrupole mass spectrometer,” *Nuclear Instruments and Methods in Physics Research A*, vol. 645, pp. 345 – 349, 2011.
- [105] G. Martínez and M. Sancho, “Accurate calculation of geometric aberrations in electrostatic lenses,” *Nuclear Instruments & Methods in Physics Research, Section A: Accelerators, Spectrometers, Detectors, and Associated Equipment*, vol. 363, pp. 198 – 204, 1995.
- [106] M. Oral and B. Lencová, “Calculation of aberration coefficients by ray tracing,” *Ultramicroscopy*, vol. 109, pp. 1365 – 1373, 2009.
- [107] J. Orloff and L. W. Swanson, “An asymmetric electrostatic lens for field emission microprobe applications,” *Journal of Applied Physics*, vol. 50, pp. 2494 – 2501, April 1979.
- [108] G. F. Rempfer, “Unipotential electrostatic lenses: Paraxial properties and aberrations of focal length and focal point,” *Journal of Applied Physics*, vol. 57, no. 7, pp. 2385 – 2401, 1985.
- [109] D. J. Manura and D. A. Dahl, *SIMION Version 8.0 User Manual*. Scientific Instrument Services Inc., 1027 Old York Rd, Ringoes, NJ 08551 USA, document revision 4 ed., 2008.
- [110] Scientific Instrument Services Inc., *SIMION 8.1 Supplemental Documentation*. Scientific Instrument Services Inc., 1027 Old York Rd, Ringoes, NJ 08551 USA, 2004 - 2012.
- [111] R. R. Julian, S. R. Mabbett, and M. F. Jarrold, “Ion funnels for the masses: Experiments and simulations with a simplified ion funnel,” *Journal of the American Society for Mass Spectrometry*, vol. 16, pp. 1708 – 1712, 2005.
- [112] T. Kim, A. V. Tolmachev, R. Harkewicz, D. C. Prior, G. Anderson, H. R. Udseth, and R. D. Smith, “Design and implementation of a new electrodynamic ion funnel,” *Analytical Chemistry*, vol. 72, pp. 2247 – 2255, 2000.
- [113] E. C. Lynn, M.-C. Chung, and C.-C. Han, “Characterizing the transmission properties of an ion funnel,” *Rapid communications in mass spectrometry*, vol. 14, pp. 2129 – 2134, 2000.
- [114] S. C. Shaffer, D. C. Prior, G. A. Anderson, H. R. Udseth, and R. D. Smith, “An ion funnel interface for improved ion focusing and sensitivity using electrospray ionization mass spectrometry,” *Analytical Chemistry*, vol. 70, pp. 4111 – 4119, 1998.
- [115] S. C. Shaffer, K. Tang, G. A. Anderson, D. C. Prior, H. R. Udseth, and R. D. Smith, “A novel ion funnel for focusing ions at elevated pressures using electrospray ionization mass spectrometry,” *Rapid Communications in Mass Spectrometry*, vol. 11, pp. 1813 – 1817, 1997.

- [116] M. Wada, Y. Ishida, T. Nakamura, Y. Yamazaki, T. Kambara, H. Ohyama, Y. Kanai, T. M. Kojima, Y. Nakai, N. Ohshima, A. Yoshida, T. Kubo, Y. Matsuo, Y. Fukuyama, K. Okada, T. Sonoda, S. Ohtani, K. Noda, H. Kawakami, and I. Katayama, “Slow RI-beams from projectile fragment separators,” *Nuclear Instruments & Methods in Physics Research Section B: Beam Interactions with Materials and Atoms*, vol. 204, pp. 570 – 581, 2003.
- [117] M. Ranjan, P. Dendooven, S. Purushothaman, T. Dickel, M. P. Reiter, S. Ayet, E. Haettner, I. D. Moore, N. Kalantar-Nayestanaki, H. Geissel, W. R. Plaß, D. Schäfer, C. Scheidenberger, F. Schreuder, H. Timersma, J. Van de Walle, and H. Weick, “Design, construction and cooling system performance of a prototype cryogenic stopping cell for the super-FRS at FAIR,” *Nuclear Instruments & Methods in Physics Research Section A: Accelerators, Spectrometers, Detectors and Associated Equipment*, vol. 770, pp. 87 – 97, 2015.
- [118] M. Ranjan, S. Purushothaman, T. Dickel, H. Geissel, W. R. Plaß, D. Schäfer, C. Scheidenberger, J. Van de Walle, H. Weick, and P. Dendooven, “New stopping cell capabilities: RF carpet performance at high gas density and cryogenic operation,” *Europhysics Letters*, vol. 96, no. 52001, pp. 1 – 6, 2011.
- [119] S. Naimia, S. Nakamura, Y. Ito, H. Mita, K. Okada, A. Ozawa, P. Schury, T. Sonoda, A. Takamine, M. Wada, and H. Wollnik, “An RF-carpet electrospray ion source to provide isobaric mass calibrants for trans-uranium elements,” *International Journal of Mass Spectrometry*, vol. 337, pp. 24 – 28, 2013.
- [120] S. N. Anthony, D. L. Shinholt, and M. F. Jarrold, “A simple electrospray interface based on a DC ion carpet,” *International Journal of Mass Spectrometry*, vol. 371, pp. 1 – 7, 2014.
- [121] A. Chaudhary, F. H. W. van Amerom, and R. T. Short, “A novel planar ion funnel design for miniature ion optics,” *Review of Scientific Instruments*, vol. 85, no. 105101, pp. 1 – 5, 2014.
- [122] G. K. Pang, *Development of radiofrequency carpets for ion transport at the NSCL*. Chemistry, Michigan State University, 2011.
- [123] S. Schwarz, “RF ion carpets: The electric field, the effective potential, operational parameters and an analysis of stability,” *International Journal of Mass Spectrometry*, vol. 299, pp. 71 – 77, 2011.
- [124] A. A. Shvartsburg, *Differential Ion Mobility Spectrometry - Nonlinear Ion Transport and Fundamentals of FAIMS*. CRC Press, Taylor & Francis Group LLC, 2009.
- [125] K. Jousten, ed., *Wutz Handbuch Vakuumtechnik; Theorie und Praxis 9. Auflage*. Friedr. Vieweg und Sohn Verlag, 2006.
- [126] J. M. Lafferty, *Foundations of Vacuum Science and Technology*. John Wiley and Sons, Inc., 1998.
- [127] J. F. O’Hanlon, *A Users’s Guide to Vacuum Technology*. JOHN WILEY & SONS, INC., 2003.

- [128] M. Ady and R. Kersevan, *MolFlow+ user guide for version 2.3.5.2*. CERN - Conseil Européen pour la Recherche Nucléaire, CH-1211 Geneva 23, Switzerland, May 2013.
- [129] R. Kersevan and J. L. Pons, “Introduction to MOLFLOW+: New graphical processing unit-based Monte Carlo code for simulating molecular flows and for calculating angular coefficients in the compute unified device architecture environment,” *Journal of Vacuum Science & Technology, A: Vacuum, Surfaces, and Films*, vol. 27, no. 4, pp. 1017 – 1023, 2009.
- [130] A. Cengiz and C. Özmütlu, “Range distribution of electrons,” *Nuclear Instruments and Methods in Physics Research B*, vol. 84, pp. 310 – 318, 1994.
- [131] O. Güler, S. Yalçın, A. Gültekin, and G. Kaynak, “Calculation of projected range of electrons in some elemental solids and gases,” *Japanese Journal of Applied Physics*, vol. 44, no. 12, pp. 8630 – 8634, 2005.
- [132] H. Iskef, J. W. Cunningham, and D. E. Watt, “Projected ranges and effective stopping powers of electrons with energy between 20 eV and 10 keV,” *Physics in Medecine and Biology*, vol. 28, no. 5, pp. 535 – 545, 1983.
- [133] T. Tabata, V. Moskvina, P. Andreo, V. Lazurik, and Y. Rogov, “Extrapolated ranges of electrons determined from transmission and projected-range straggling curves,” *Radiation Physics and Chemistry*, vol. 64, pp. 161 – 167, 2002.
- [134] C. Inguibert, M. Belhaj, J. Puech, and J. Pierron, “Monte carlo simulation of the electron range/energy relationship in the sub-keV energy domain,” in *The international workshop on Multipactor Corona and Passive Intermodulation 2014*, pp. 1–8, 2014.
- [135] J. A. LaVerne and A. Mozumder, “Range and range straggling of low-energy electrons in the rare gases,” *Journal of Physical Chemistry*, vol. 89, pp. 4219 – 4225, 1985.
- [136] A. R. Couture and D. Drouin, “Casino.” <http://www.gel.usherbrooke.ca/casino/What.html>, 2015.
- [137] A. R. Couture and D. Drouin, “The stopping and range of electrons in matter.” <http://www.srim.org/SREM.htm>, 2015.
- [138] W. H. Press, S. A. Teukolsky, W. T. Vetterling, and B. P. Flannery, *Numerical Recipes in C: The Art of Scientific Computing*. CAMBRIDGE UNIVERSITY PRESS, 2nd ed., 1992.
- [139] D. Kusswurm, *Modern X86 Assembly Language Programming: 32-bit, 64-bit, SSE, and AVX*. Apress, 2014.
- [140] Kimball Physics Inc., *Tungsten Filaments, Hairpin Thermionic Emitters*, November 2013.
- [141] I. Ribeiro, “Gaussian probability density functions: Properties and error characterization,” Institute for Systems and Robotics, Lisboa, Portugal, February 2004.
- [142] R. F. Berg and W. C. Burton, “Noble gas viscosities at 25 °C,” tech. rep., National Institute of Standards and Technology, July 2012.

- [143] Kimball Physics Inc., *LaB6 Cathodes Single-Crystal Lanthanum Hexaboride*, November 2013.
- [144] Agilent Technologies, *Agilent turbo pumps*. 5301 Stevens Creek Blvd. Santa Clara, CA 95051 United States, December 2008.
- [145] MKS Instruments Deutschland GmbH, *Digital Mass Flow Controller - Type 1179B / 1479B / 2179B and Digital Mass Flow Meter 179B - Instruction Manual*. MKS Instruments Deutschland GmbH, Schatzbogen 43, 81829 München, 2003.
- [146] J. D. Stoll and A. Kolmakov, “Electron transparent graphene windows for environmental scanning electron microscopy in liquids and dense gases,” *Nanotechnology*, vol. 23, no. 505704, pp. 1 – 8, 2012.
- [147] M. Krueger, S. Berg, D. Stone, E. Strelcov, D. A. Dikin, J. Kim, L. J. Cote, J. Huang, and A. Kolmakov, “Drop-casted self-assembling graphene oxide membranes for scanning electron microscopy on wet and dense gaseous samples,” *ACS Nano*, vol. 5, pp. 10047 – 10054, November 2011.
- [148] I. Müllerová, M. Hovorka, R. Hanzlíková, and L. Frank, “Very low energy scanning electron microscopy of free-standing ultrathin films,” *Materials Transactions*, vol. 51, no. 2, pp. 265 – 270, 2010.
- [149] J. Y. Mutus, L. Livadaru, J. T. Robinson, R. Urban, M. H. Salomons, M. Cloutier, and R. A. Wolkow, “Low-energy electron point projection microscopy of suspended graphene, the ultimate microscope slide,” *New Journal of Physics*, vol. 13, no. 063011, pp. 1 – 11, 2011.
- [150] J. S. Bunch, S. S. Verbridge, J. S. Alden, A. M. van der Zande, J. M. Parpia, H. G. Craighead, and P. L. McEuen, “Impermeable atomic membranes from graphene sheets,” *Nano Letters*, vol. 8, no. 8, pp. 2458 – 2462, 2008.
- [151] T. J. Booth, P. Blake, R. R. Nair, D. Jiang, E. W. Hill, U. Bangert, A. Bleloch, M. Gass, K. S. Novoselov, M. I. Katsnelson, and A. K. Geim, “Macroscopic graphene membranes and their extraordinary stiffness,” *Nano Letters*, vol. 8, no. 8, pp. 2442 – 2446, 2008.
- [152] C. Lee, X. Wei, J. W. Kysar, and J. Hone, “Measurement of the elastic properties and intrinsic strength of monolayer graphene,” *Science*, vol. 321, pp. 385 – 387, July 2008.
- [153] I. Müllerová, M. Hovorka, I. Konvalina, M. Uncovský, and L. Frank, “Scanning transmission low-energy electron microscopy,” *IBM Journal of Research and Development*, vol. 55, pp. 2:1 – 2:6, July-August 2011.
- [154] O. De Castro, D. Dowsett, T. Wirtz, and S. Della Negra, “Towards a high brightness electron impact ion source for nano-applications,” *Microscopy and Microanalysis*, vol. 21, no. Issue S4, pp. 94 – 99, 2015.
- [155] Kimball Physics Inc., *Yttria-coated iridium cathodes - rugged thermionic emitters*, July 2015.
- [156] Kimball Physics Inc., “Yttria coated iridium disc cathode.” <http://www.kimballphysics.com/yttria-coated-iridium-discs>, July 2015.

- [157] F. H. W. van Amerom, A. Chaudhary, and R. T. Short, “Planar ion funnel,” May 2013.
- [158] Advanced Circuit Boards, “Printed circuit boards technology.” <http://www.acb.be/index.php/fr/technologie>, August 2016.
- [159] National Physical Laboratory, “Kaye&laby tables of physical & chemical constants: 4.4 free electrons and ions in gases - 4.4.1 ionic mobility.” [http://www.kayelaby.npl.co.uk/atomic\\_and\\_nuclear\\_physics/4\\_4/4\\_4\\_1.html](http://www.kayelaby.npl.co.uk/atomic_and_nuclear_physics/4_4/4_4_1.html), August 2015.
- [160] Agar Scientific, “Platinum/iridium high quality disc apertures for electron microscopes, focus ion beam, microprobe and x-ray systems.” <http://www.agarscientific.com/sem/apertures/apertures-17994.html>, August 2016.
- [161] Agilent Technologies, *The New Turbo-V 301 Navigator*. 5301 Stevens Creek Blvd. Santa Clara, CA 95051 United States, July 2001.
- [162] F. J. McQuillan, J. R. Culham, and M. M. Yovanovich, “Properties of some gases and liquids at one atmosphere,” tech. rep., Microelectronics Heat Transfer Lab, University of Waterloo, Ontario, July 1984.
- [163] Oerlikon Leybold Vacuum GmbH, *Technical Datasheet TurboVac 361*, 2015.
- [164] Kimball Physics Inc., *ES-526 Y2O3 Disc Cathode Care and Operating Instructions*, March 2015.
- [165] Kimball Physics Inc., “Private operational data communication for the ES-526 yttria disc cathode.” September 2015.
- [166] V. Baglin, I. Collins, B. Henrist, N. Hilleret, and G. Vorlaufer, “A summary of main experimental results concerning the secondary electron emission of copper,” LHC project report 472, LHC Division, CERN, Switzerland, June 2002.
- [167] Oerlikon Leybold Vacuum Inc., *Operating manual for IoniVac ITR 90 pressure sensor*. Oerlikon Leybold Vacuum Inc., 5700 Mellon Road Export, PA 15632-8900, United States, 2008.
- [168] ISOTECH, *Aribitrary function generator - AFG-21000 Series*. ISOTECH, P. O. Box 99 Corby, Northants NN17 9RS, England, 2016.
- [169] Electronics and Innovation Ltd., *Usermanual 240L Broadband Power Amplifier*, August 2012.
- [170] Electronics and Innovation Ltd., *Datasheet JT-200 Matching Transformer*, 2015.
- [171] Murata Manufacturing Co., Ltd., *Datasheet High Voltage Ceramic Capacitor, DHR4E4C102K2FB*, 2016.
- [172] STMicroelectronics, *Datasheet TRANSIL diode, 1.5KE6V8A/440A; 1.5KE6V8CA/440CA*, 2003.
- [173] M. Abramowitz and I. A. Stegun, eds., *Handbook of Mathematical functions with Formulas, Graphs and Mathematical Tables*. National Bureau of Standards, 10 ed., December 1972.

- [174] TED PELLA INC., “PELCO graphene & graphene oxide films; PELCO graphene TEM support films & substrates.” [https://www.tedpella.com/Support\\_Films\\_html/Graphene-TEM-Support-Film.htm.aspx](https://www.tedpella.com/Support_Films_html/Graphene-TEM-Support-Film.htm.aspx), March 2016.
- [175] TED PELLA INC., “Lacey support films - netmesh grids.” [https://www.tedpella.com/Support\\_Films\\_html/Support\\_Films\\_and\\_Substrates\\_Overview.htm](https://www.tedpella.com/Support_Films_html/Support_Films_and_Substrates_Overview.htm), March 2016.
- [176] A. Kolmakov, D. A. Dikin, L. J. Cote, J. Huang, M. K. Abyaneh, M. Amati, L. Gregoratti, S. Guenther, and M. Kiskinova, “Graphene oxide windows for in situ environmental cell photoelectron spectroscopy,” *Nature Nanotechnology*, vol. 6, pp. 651 – 657, October 2011.
- [177] S. Tanuma, C. J. Powell, and D. R. Penn, “Calculations of electron inelastic mean free paths. II. Data for 27 elements over the 50-2000 eV range,” *Surface and Interface Analysis*, vol. 17, pp. 911 – 926, 1991.
- [178] S. Tanuma, C. J. Powell, and D. R. Penn, “Calculations of electron inelastic mean free paths. IX. Data for 41 elemental solids over the 50 eV to 30 keV range,” *Surface and Interface Analysis*, vol. 43, pp. 689 – 713, 2011.
- [179] TED PELLA INC., “PELCO 300 mesh grids.” [https://www.tedpella.com/grids\\_html/Pelco-TEM-Grids.htm](https://www.tedpella.com/grids_html/Pelco-TEM-Grids.htm), March 2016.





**Titre:** Développement d'une source d'ions polyvalente à haute brillance basée sur l'impact électronique pour la nano-fabrication, la nano-imagerie et la nano-analyse

**Mots clés:** Sources d'ions à haute brillance, impact électronique, nano-applications, radio-fréquence, faisceaux d'ions focalisés

**Résumé:** Les nano-applications utilisant des faisceaux d'ions focalisés nécessitent des sources d'ions à haute brillance avec une faible dispersion en énergie ( $\Delta E$ ) ce qui permet une excellente résolution latérale et un courant d'ions suffisamment élevé pour induire des vitesses d'érosion raisonnables et des rendements élevés d'émission électronique et ionique. Les objectifs de cette thèse sont le développement d'une source d'ions basée sur l'impact électronique ayant une brillance réduite  $B_r$  de  $10^3 - 10^4 \text{ A m}^{-2} \text{ sr}^{-1} \text{ V}^{-1}$ , une dispersion en énergie  $\Delta E \lesssim 1 \text{ eV}$  et un choix polyvalent d'ions. Le premier concept évalué consiste à focaliser un faisceau d'électrons à une énergie de 1 keV entre deux électrodes parallèles distant de moins d'un millimètre. Le volume d'ionisation « micrométrique » est formé au-dessus d'une ouverture d'extraction de quelques dizaines de  $\mu\text{m}$ . En utilisant un émetteur d'électrons  $\text{LaB}_6$  et une pression de 0.1 mbar dans la région d'ionisation,  $B_r$  est proche de  $2 \cdot 10^2 \text{ A m}^{-2} \text{ sr}^{-1} \text{ V}^{-1}$  avec des tailles de source de quelques  $\mu\text{m}$ , des courants de quelques nA pour  $\text{Ar}^+/\text{Xe}^+/\text{O}_2^+$  et une dispersion en énergie  $\Delta E < 0.5 \text{ eV}$ . La brillance réduite  $B_r$  est encore en dessous de la valeur minimum de notre objectif et la pression de fonctionnement très faible nécessaire pour l'émetteur  $\text{LaB}_6$  ne peut être obtenue avec une colonne d'électrons compacte, donc ce prototype n'a pas été construit.

Le deuxième concept évalué est basé sur un faisceau d'électrons à fort courant et de 100 eV d'énergie qui est arrêté dans une région d'ionisation sous une pression de 0.1 mbar et ayant un champ électrique décélérateur de 1 V/mm. Des courants d'ions de quelques 100  $\mu\text{A}$  sont produits dans un volume d'ionisation millimétrique. Afin d'extraire efficacement les ions de façon coaxiale au faisceau électronique et de garder des tailles de source dans le domaine du  $\mu\text{m}$ , un élément spécial d'optique ionique radio-fréquence nommé « RF Ion Carpet » est utilisé pour guider les ions vers un canal central d'un mm suivi d'une extraction de 100  $\mu\text{m}$  d'ouverture. La brillance réduite  $B_r$  est déterminée autour de  $10^2 \text{ A m}^{-2} \text{ sr}^{-1} \text{ V}^{-1}$  ce qui est inférieur à notre objectif initial pour un faisceau d' $\text{Ar}^+$  avec une dispersion  $\Delta E \approx 3 \text{ eV}$  qui est dans le même ordre de grandeur que l'objectif et un courant d'ions de quelques  $\mu\text{A}$  qui compense la faible brillance et une dispersion en énergie un peu élevée. Des études expérimentales avec un prototype de la source d'ions ont montrées que l'extraction d'ions d'argon est clairement améliorée en utilisant le dispositif « RF Ion Carpet ». Malheureusement, les courants d'ions mesurés sont actuellement encore un à deux ordres de grandeur en dessous de la gamme du  $\mu\text{A}$ . Des moyens d'optimisation pour améliorer d'avantage les performances de la source ont été identifiés et vont être intégrés dans le futur.

**Title:** Development of a Versatile High-Brightness Electron Impact Ion Source for Nano-Machining, Nano-Imaging and Nano-Analysis

**Keywords:** High brightness ion sources, electron impact, nano-applications, radio frequency, focused ion beam

**Abstract:** High brightness low energy spread ( $\Delta E$ ) ion sources are needed for focused ion beam nano-applications in order to get a high lateral resolution while having sufficiently high ion beam currents to obtain reasonable erosion rates and large secondary electron/ion yields. The objectives of this thesis are: the design of an electron impact ion source, a reduced brightness  $B_r$  of  $10^3 - 10^4 \text{ A m}^{-2} \text{ sr}^{-1} \text{ V}^{-1}$  with an energy distribution spread  $\Delta E \lesssim 1 \text{ eV}$  and a versatile ion species choice. In a first evaluated concept an electron beam is focussed in between two parallel plates spaced by  $\leq 1 \text{ mm}$ . A micron sized ionisation volume is created above an extraction aperture of a few tens of  $\mu\text{m}$ . By using a  $\text{LaB}_6$  electron emitter and the ionisation region with a pressure around 0.1 mbar,  $B_r$  is close to  $2 \cdot 10^2 \text{ A m}^{-2} \text{ sr}^{-1} \text{ V}^{-1}$  with source sizes of a few  $\mu\text{m}$ , ionic currents of a few nA for  $\text{Ar}^+/\text{Xe}^+/\text{O}_2^+$  and the energy spread being  $\Delta E < 0.5 \text{ eV}$ . The determined  $B_r$  value is still below the minimum targeted value and furthermore the main difficulty is that the needed operation pressure for the  $\text{LaB}_6$  emitter cannot be achieved across the compact electron column and therefore a prototype has not been constructed.

The second evaluated source concept is based on stopping a 100 eV high current electron beam within a 1 V/mm retarding field ionisation region kept at a pressure of 0.1 mbar. Ion currents up to hundreds of  $\mu\text{A}$  are created within an ionisation volume of mm dimensions. In order to obtain an efficient ion extraction, which is done coaxially to the electron beam, and keep the ion beam source size in the  $\mu\text{m}$  range a radio frequency ion carpet is used to funnel the ions through a central 1 mm opening followed by an extraction aperture of 100  $\mu\text{m}$  in diameter. The determined  $B_r$  is in the lower  $10^2 \text{ A m}^{-2} \text{ sr}^{-1} \text{ V}^{-1}$  range for  $\text{Ar}^+$  ions with  $\Delta E \approx 3 \text{ eV}$ . The reduced brightness is lower than the original goal but a few  $\mu\text{A}$  of ion beam current are available and  $\Delta E$  is in the same order of magnitude as the objective. Experimental prototype tests have shown that the argon ion extraction is clearly raised by using the radio frequency ion carpet. Unfortunately, the measured ion currents are still one or two orders of magnitude below the  $\mu\text{A}$  range. Further optimisations to further enhance the source performance have been identified and will be implemented in the future.